REPORT DOCUMENTATION PAGE

AFRL-SR-BL-TR-98-

U805

Public reporting burden for this collection of information is estimated to average 1 hour per response, incluc —s, gathering and maintaining the data needed, and completing and reviewing the collection of information. Send cor collection of information, including suggestions for reducing this burden, to Washington Headquarters Services, Director hway, Suite 1204, Arlington, VA 22202-4302, and to the Office of management and Budget, Paperwork Reduction Projec

1. AGENCY USE ONLY (Leave Blank)	2. REPORT DATE December, 1995	3. RE Final

4. TITLE AND SUBTITLE
USAF Summer Research Program - 1995 Graduate Student Research Program
Final Reports, Volume 10A, Wright Laboratory

5. FUNDING NUMBERS

6. AUTHORS
Gary Moore

7. PERFORMING ORGANIZATION NAME(S) AND ADDRESS(ES)
Research and Development Labs, Culver City, CA

8. PERFORMING ORGANIZATION REPORT NUMBER

9. SPONSORING/MONITORING AGENCY NAME(S) AND ADDRESS(ES)
AFOSR/NI
4040 Fairfax Dr, Suite 500
Arlington, VA 22203-1613

10. SPONSORING/MONITORING AGENCY REPORT NUMBER

11. SUPPLEMENTARY NOTES
Contract Number: F49620-93-C-0063

12a. DISTRIBUTION AVAILABILITY STATEMENT
Approved for Public Release

12b. DISTRIBUTION CODE

13. ABSTRACT *(Maximum 200 words)*
The United States Air Force Graduate Student Research Program (USAF- GSRP) is designed to introduce university, college, and technical institute graduate students to Air Force research. This is accomplished by the graduate students being selected on a nationally advertised competitive basis during the summer intersession period to perform research at Air Force Research Laboratory Technical Directorates and Air Force Air Logistics Centers. Each participant provided a report of their research, and these reports are consolidated into this annual report.

14. SUBJECT TERMS
AIR FORCE RESEARCH, AIR FORCE, ENGINEERING, LABORATORIES, REPORTS, SUMMER, UNIVERSITIES

15. NUMBER OF PAGES

16. PRICE CODE

17. SECURITY CLASSIFICATION OF REPORT	18. SECURITY CLASSIFICATION OF THIS PAGE	19. SECURITY CLASSIFICATION OF ABSTRACT	20. LIMITATION OF ABSTRACT
Unclassified	Unclassified	Unclassified	UL

Standard Form 298 (Rev. 2-89)
Prescribed by ANSI Std. 239.18
Designed using WordPerfect 6.1, AFOSR/XPP, Oct 96

1998124071

UNITED STATES AIR FORCE

SUMMER RESEARCH PROGRAM -- 1995

GRADUATE STUDENT RESEARCH PROGRAM FINAL REPORTS

VOLUME 10A

WRIGHT LABORATORY

RESEARCH & DEVELOPMENT LABORATORIES

5800 Uplander Way

Culver City, CA 90230-6608

Program Director, RDL
Gary Moore

Program Manager, AFOSR
Major David Hart

Program Manager, RDL
Scott Licoscos

Program Administrator, RDL
Gwendolyn Smith

Submitted to:

AIR FORCE OFFICE OF SCIENTIFIC RESEARCH

Bolling Air Force Base

Washington, D.C.

December 1995

PREFACE

Reports in this volume are numbered consecutively beginning with number 1. Each report is paginated with the report number followed by consecutive page numbers, e.g., 1-1, 1-2, 1-3; 2-1, 2-2, 2-3.

Due to its length, Volume 10 is bound in two parts, 10A and 10B. Volume 10A contains #1-20, and Volume 10B contains reports #21-37. The Table of Contents for Volume 10 is included in both parts.

This document is one of a set of 16 volumes describing the 1995 AFOSR Summer Research Program. The following volumes comprise the set:

VOLUME	TITLE
1	Program Management Report
	Summer Faculty Research Program (SFRP) Reports
2A & 2B	Armstrong Laboratory
3A & 3B	Phillips Laboratory
4	Rome Laboratory
5A, 5B, & 5C	Wright Laboratory
6A & 6B	Arnold Engineering Development Center, Wilford Hall Medical Center and Air Logistics Centers
	Graduate Student Research Program (GSRP) Reports
7A & 7B	Armstrong Laboratory
8	Phillips Laboratory
9	Rome Laboratory
10A & 10B	Wright Laboratory
11	Arnold Engineering Development Center, Wilford Hall Medical Center and Air Logistics Centers
	High School Apprenticeship Program (HSAP) Reports
12A & 12B	Armstrong Laboratory
13	Phillips Laboratory
14	Rome Laboratory
15A&15B	Wright Laboratory
16	Arnold Engineering Development Center

GSRP FINAL REPORT TABLE OF CONTENTS

APPENDICIES:

GSRP FINAL REPORTS

COMPARISON OF DIRECT AND DOWNCONVERTED DIGITIZATION
IN GPS RECEIVER FRONT END DESIGNS

James B. Y. Tsui
WL/AAWP-1
Hanger 4B
WPAFB, OH 45433

Dennis M. Akos
Avionics Engineering Center
Ohio University
215 Stocker Center
Athens, OH 45701

COMPARISON OF DIRECT AND DOWNCONVERTED DIGITIZATION
IN GPS RECEIVER FRONT END DESIGNS

James B. Y. Tsui
WL/AAWP-1

Dennis M. Akos
Ohio University

Abstract

This paper compares two front end designs of a global positioning system (GPS) receiver. The first approach is the direct digitization of the input signal and the second approach is to downconvert the input signal to an intermediate frequency (IF) then digitize it. Theoretically, these two methods should produce similar results and our experimental data support this argument.

COMPARISON OF DIRECT AND DOWNCONVERTED DIGITIZATION
IN GPS RECEIVER FRONT END DESIGNS

James B. Y. Tsui
Dennis M. Akos

Introduction

The signal of interest in this study is the GPS L1 band signal modulated with the coarse/acquisition (C/A) code and navigation data. A majority of the GPS receivers digitized the input signal and use digital signal processing to perform the necessary functions.

The conventional approach used in the frond end of a GPS receiver is to amplify the input signal, then downconvert it to an IF. The IF signal is further amplified and digitized[1]. In this approach, the radio frequency (RF) chain in front of the analog-to-digital converter (ADC) contains amplifiers, filters, a mixer and a local oscillator. The advantages of this approach are: 1) The requirements of the ADC are less stringent, because the input frequency is only required to accommodate the reduced IF. 2) The filter after the IF requires a lower Q value to cover the same bandwidth. The disadvantage is that a local oscillator and a mixer are required, or even additional components if multiple stages are used, to downconvert the input frequency before digitization.

Theoretically, the input signal can be digitized directly and similar results should be obtained. In this approach, the mixer and local oscillator are no longer needed. The disadvantages are: 1) The ADC must accommodate the input L1 frequency of 1.57542 GHz, although the sampling frequency is much lower at 5 MHz. 2) The filter centered at the L1 frequency with a desired bandwidth of approximately 2 MHz requires a very high Q.

In this paper both direct digitization and downconverted approaches are discussed with experimental results presented. A direct digitization approach has been published by Brown[2]. In that work the ADC operates at 800 MHz but only with one bit sampling. In this experiment, the ADC operates at 5 MHz with 8 bit sampling. Off line processing was used to detect the signals.

In the next section, the experimental set-up will be presented. In Section III, results obtained using true GPS signals will be discussed. In Section IV, a continuous wave (CW) is used to determined the signal-to-noise ratio and the results are compared with the theoretically predicted ones. The paper concludes with a summary of the results.

Experimental Set-up

The guaranteed minimum power level of the L1 band C/A code GPS signal is at -130 dBm. A Tektronix TDS 684A digital scope was used as the ADC which has a minimum sensitivity of 1 mv (about -50 dBm). Therefore, the input signal must be amplified at least by 80 dB. In both the direct and downconverted digitization experiments over 90 dB gain was used. The input bandwidth of the scope is specified as 1 GHz and 8 bit amplitude resolution, but it can digitize the L1 frequency without problems. One of the disadvantages of using the scope as the

digitizer is that the sampling frequency can only be set at certain fixed values. Under this condition, the input frequency may not be aliased to a desired frequency. This problem will be further discussed later in this section.

In the direct digitization, the experimental set-up is shown in Figure 1. The input signal was amplified

Figure 1: Experimental Set-up for Direct Digitization
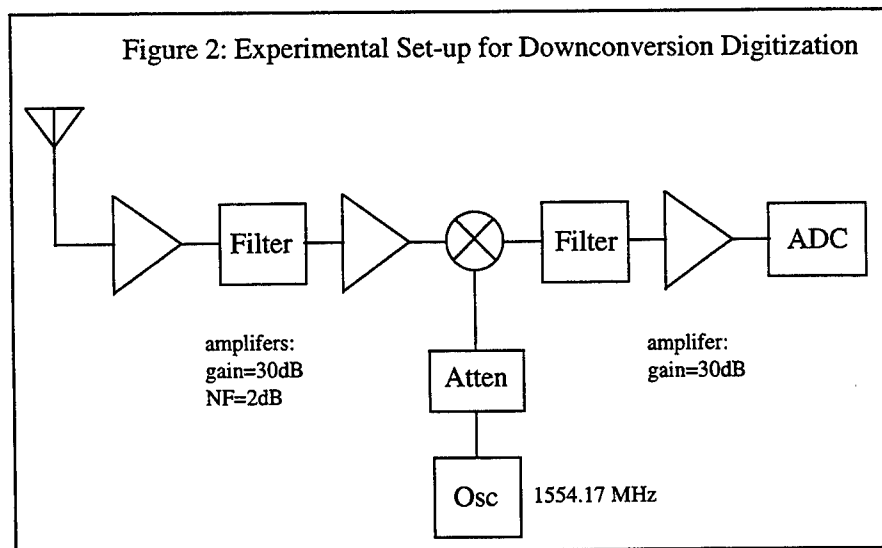
amplifers: gain=30dB & NF=2dB each
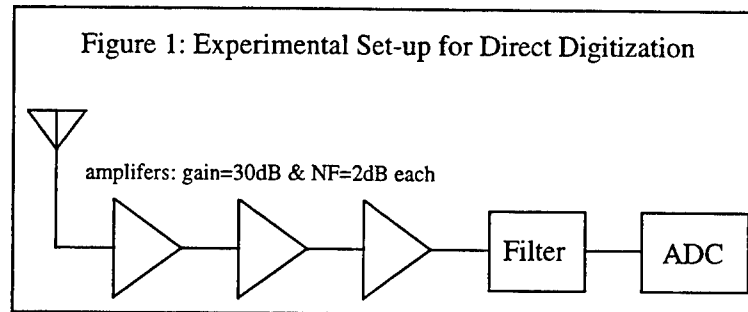
using 3 amplifiers with a nominal gain of 30 dB and noise figure of 2 dB. A total of 92 dB of gain was measured from three amplifiers combined. The filter following the amplifier chain has an insertion loss of 3.2 dB and 3 dB and 30 dB bandwidths of 3.4 MHz and 10.3 MHz, respectively. It is difficult to build a filter with a narrower bandwidth, because of the relatively high center frequency. The filter dimension is 3x6x14 cm^3.

The null-to-null bandwidth of the C/A signal is about 2 MHz. Theoretically a minimum sampling frequency of 4 MHz will accommodate the signal, although the center frequency is close to 1.6 GHz. In this experiment, a 5 MHz sampling frequency was used which should accommodate the 2 MHz bandwidth without spectrum overlap. This sampling frequency will alias the 1575.42 MHz into 420 kHz. It is desirable to alias the input frequency close to 1.25 MHz, the center of the band, because the sideband will have less interference. Since the input data is real, in contrast to complex, one single frequency will produce two outputs through the FFT. If the frequency is close to an alias zone boundary, the sideband of the two outputs may interference with each other. If the sampling frequency can be changed to 4.99737 MHz, the input frequency will be alias close to 1.25 MHz. However, the sampling frequency cannot be changed arbitrarily and 5 MHz was used to sample the input signal.

In this arrangement, one can consider that there are four disadvantages: 1) The filter has a bandwidth of 3.2 MHz which is wider than the minimum required of 2.0 MHz. As a result, additional noise will be aliased into the digitized data and the sensitivity of the receiver will suffer. 2) The physical dimensions of the filter are rather bulky. 3) The input frequency range of the ADC must be high enough to accommodate the input signal. 4) The input signal is aliased close to a zone boundary, but this problem is not an essential one in the general case as it can be corrected if the proper sampling frequency is used.

The downconverted arrangement is shown in Figure 2. In this figure about 30 dB of gain is placed in front of the first filter which has a center frequency of 1575.42 MHz and an insertion loss of 2.2 dB with 3 dB and 30 dB bandwidth of 86 MHz and 280 MHz respectively. The physical dimension of the filter is 1x2.5x3.5 cm^3. The mixer has an insertion loss of 6 dB. The local oscillator generates a 1554.17 MHz frequency which is applied to the mixer through a 3 dB attenuator. The downconverted frequency is at 21.25 MHz. The second filter has a center frequency of 21.4 MHz which is slightly off from the desired frequency. It has an insertion loss of 2 dB with 3 dB and 30 dB

Figure 2: Experimental Set-up for Downconversion Digitization

amplifers:
gain=30dB
NF=2dB

Atten

amplifer:
gain=30dB

Osc   1554.17 MHz

bandwidth of 2.25 and 5.16 MHz respectively. The filter dimension is 1x1.3x4.5 cm³. These two filters are much smaller than the one used in the direct digitization. The 21.25 MHz signal sampled at 5 MHz will alias to 1.25 MHz, the center of the alias zone. The input frequency of the ADC required to digitize this IF signal is only in the 20 MHz range instead in the GHz range.

The disadvantage of this approach is the amount of hardware. A mixer and a local oscillator are needed. However, the filters are small in size and the IF filter has better selectivity.

CW Test Results

Two types of signals were applied to the input of the receiver front end. A GPS antenna was used to collect actual GPS signals. However, under this condition it is difficult to obtain quantitative results to compare the performance of the two front end designs. Rather, a CW signal is used to determine the signal-to-noise ratio of both front end designs. This approach can provide a comparative level of performance. In this section the results of the CW test will be reported.

The digital scope used as the ADC can perform near real time FFT operation. The FFT output was used to determine the signal-to-noise ratio. For the direct digitization approach, a CW signal with frequency close to 1575.42 MHz and amplitude of -110 dBm was used as the input signal. The scope performed a 10,000 point FFT. Since the sampling frequency is 5 MHz, a 10,000 point FFT will span 2 ms which corresponds to a frequency resolution of 500 Hz. The input frequency was adjusted slightly so that the energy of the CW signal was contained within a single frequency bin. Figure 3 shows the results of a 5000 point FFT and an enlarged view of only 21 points centered about the frequency bin of the CW signal. It appears that the signal only occupies one frequency bin.

Figure 3: 10000 Point FFT of Sampled CW Signal (Direct Digitization)
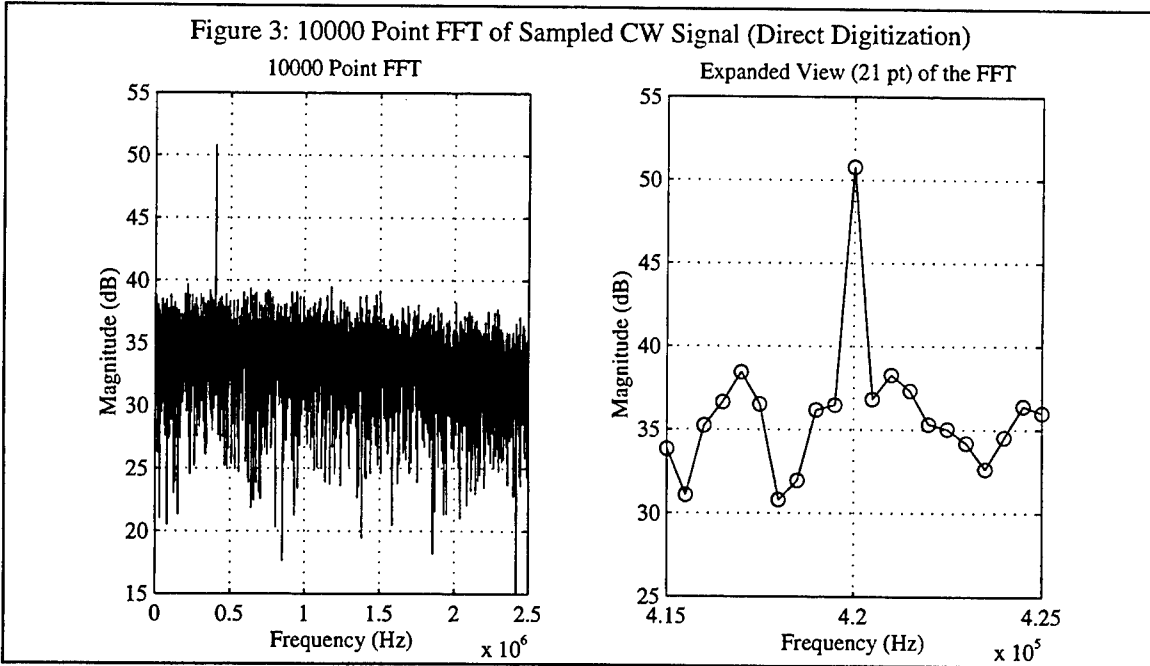
The signal power is calculated from the square of the signal amplitude and the noise power is calculated from averaging the square of the remaining data points. The signal-to-noise ratio measured is 31.99 dB.

For the downconverted case a similar approach was performed. The input frequency was adjusted to correspond with one output frequency bin. The only difference is output from the mixer is close to 21.25 MHz. The signal-to-noise ratio measured under this condition is 32.64 dB.

The expected signal-to-noise ratio can be found from the following procedure. The noise floor of a 500 Hz bandwidth system with 3 dB noise (including 1 dB insertion loss of the input cable) is:

$$NoiseFloor = -174 + 10\log(500) + 3 = -174 + 27 + 3 = -144 \quad dBm$$

The corresponding signal-to-noise ratio (S/N) is:

$$S / N = InputSignal - NoiseFloor = -110 + 144 = 34 \quad dB$$

This result is about 1.4 dB lower than the predicted one. This error might be a result of the measurement equipment, e.g., there is no known equipment in our laboratory to measure the input power directly at -110 dBm. The other possibility is that filter bandwidth (2.25 MHz) is very close to the Nyquist sampling frequency (2.5 MHz), thus additional noise is folded into the desired band. However, the relative measurement, i.e. the results obtained from the downconversion method and direct digitization, should be accurate.

The signal-to-noise ratio of the down converted approach is .65 dB (32.64-31.99) better than the direct digitization. This difference can be ascribed as that the RF filter bandwidth (3.4 MHz) is wider than the Nyquist sampling frequency of 2.5 MHz and more noise will fold in the desired band. If a filter with narrower bandwidth can be built, the signal-to-noise ratio of both approaches should be equal.

Results Against True GPS Signals

       In this experiment, an antennas was placed at the input of the receiver front end to collect data from the GPS satellites. A GEC Plessey GPS receiver was used to determine which satellites were visible. The two antennas of the two systems were placed next to each other. The direct digitization configuration, depicted in Figure 1, has been modified slightly by the inclusion of an additional filter after the first amplifier to suppress out-of-band signals. A total of 15,000 data points were collected and Figure 4 shows the collected data from direct digitization in the time domain.

Figure 4: Time/Frequency Plots for a Direct Digitized Data Set
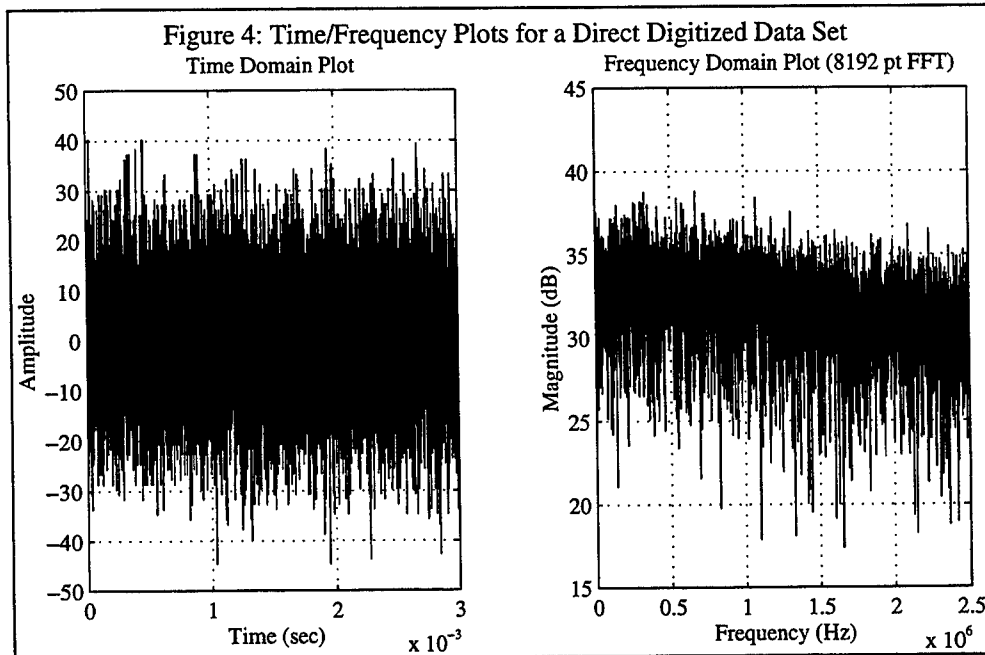
Data obtained from the downconverted case, similar in appearance, is not shown. Only 8192 points were used in the signal search which corresponds to about 1.64 ms of time. The digital data collected were processed through the following procedure:

1) The Gold code of a certain satellite was digitized at 5 MHz to generate 13192 (8192+5000) points of data. Because the Gold code will repeat every millisecond, only 1 millisecond of data were needed which corresponds to 5000 data points. Only the Gold codes of the satellites received by the Plessey receiver were digitized.

2) The first 8192 digitized Gold code data were multiplied by the input signal point by point. This procedure was trying to strip off the biphase modulation of the spreading code[3].

3) A 8192 point FFT was performed on the multiplied data and the highest frequency component was recorded.

4) Repeat steps 2 and 3 by shifting the digitized Gold code one data point at a time, until all possible phases of the Gold code data set were used. In this procedure, the 8192 point FFT will be performed 5000 times. A typical result is shown in Figure 5.

Figure 5: Results of Search for SV#15 in Two Data Sets
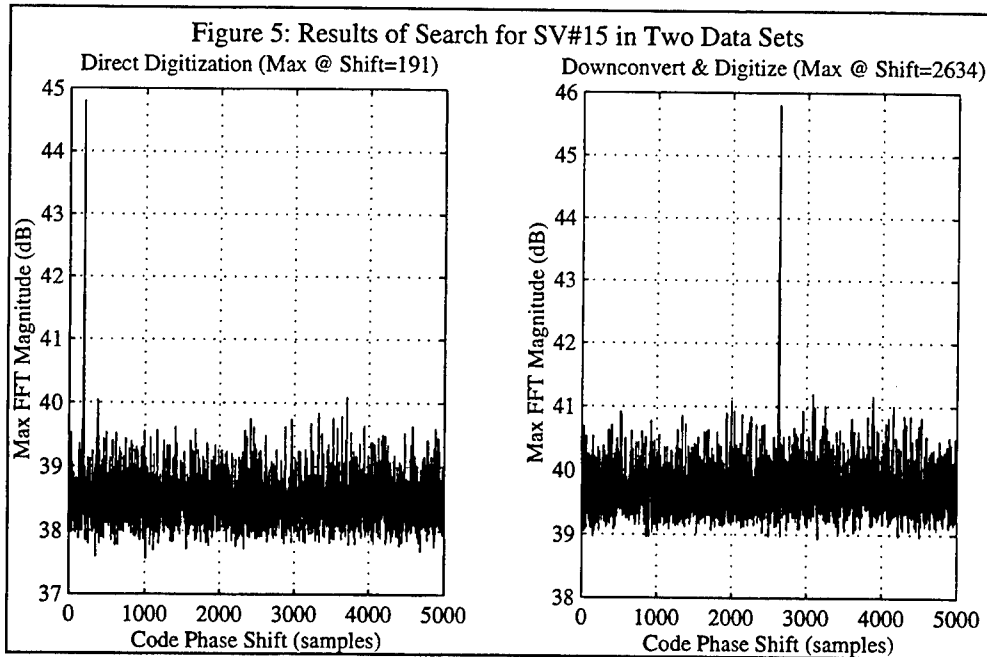
One should note that the horizontal axis represents the relative phase of the Gold code and the input data. The highest peak represents that location of the Gold code is correctly matched to the input signal.

5) The last step was to check whether the peak found in step 4 was the correct one. In this stage, the FFT result of the matched Gold code and input signal was calculated as illustrated in Figure 6.

If the output frequency is at the desired bin, which is close the 420 kHz for the direct digitization and 1.25 MHz for the downconversion case, the correlation peak is considered the correct one. The frequency may not be exactly at these frequency bins, because of the Doppler effect. If the frequency is far from the expected value, the correlation peak is regarded as an erroneous detection of the true signal.

When using the direct digitization front end, the Plessey receiver tracked four satellites with PRN numbers: 4, 7, 18 and 29. The experimental arrangement identified all four in the data set. For the downconversion case, the Plessey receiver tracked satellite PRN numbers: 4, 12, 16 and 18; and the experimental set-up detected: 4, 16 and 18. It should be noted that that in the experimental case, no threshold was set. The highest correlation peak was assumed to represent the correct code phase alignment. The signals were recognized from visual display as shown in Figures 5 and 6. Also, the Plessey receiver receives the signal in a continuous manner, it may spend a relative longer time to search the signal. The experimental set-up only used 1.64 ms of data. That might be the reason the experimental arrangement receives only a subset of those signals being tracked by the Plessey receiver. For the direct digitization case, as mentioned in Section II, the sideband of the signals may be distorted, because the signal is not aliased into the center of the band. Although not evident through our results, this interference may degrade the signal identification capability.

The same digitized data were truncated to 1 bit with identical processing applied. Similar results were

Figure 6: Corresponding FFTs (Post SV#15 C/A Code Correlation)
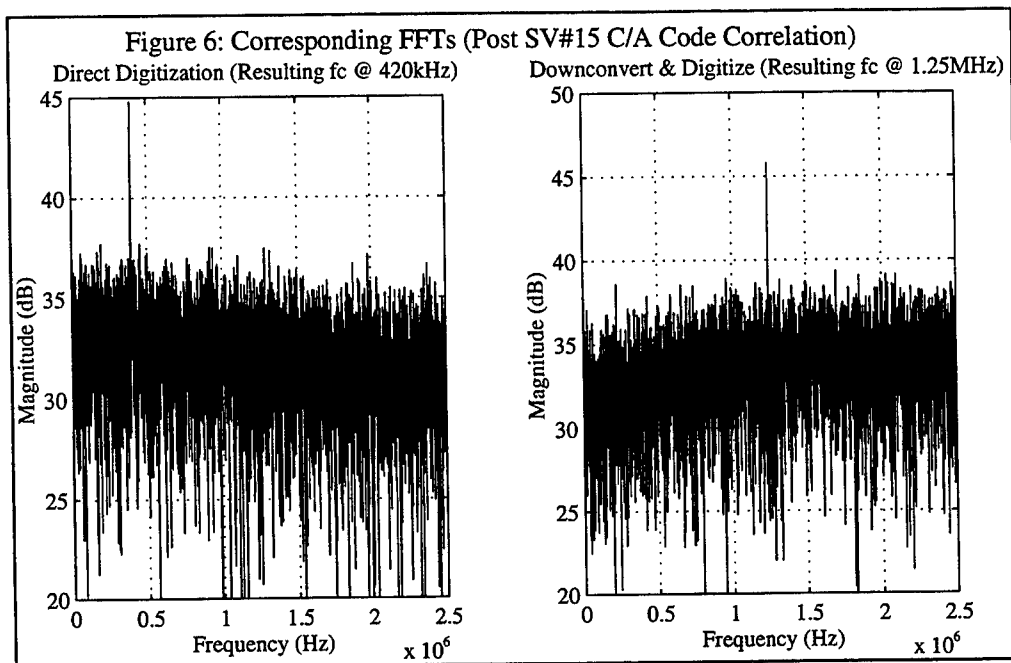
obtained without significant degradation of performance. This result is shown in Figure 7. This verifies that the ADC can use single bit sampling, which indicates it might be easier to achieve a wider input bandwidth.

Summary

This paper compares the results of two GPS front end designs: a direct digitization against downconversion. Theoretically, there is no difference in performance, and the measured results support this claim. The selection of the designs should base on the availability of hardware and cost. In the direct digitization, the requirements of the filter and ADC are more stringent. In the downconversion case, a mixer and local oscillator are needed.

References

1. Tsui, James B. Y., Digital Techniques for Wideband Receivers, Artech House, Norwood, MA, 1995.

2. Brown, Alison, and Wolt, Barry, "Digital L-Band Receiver Architecture with Direct RF Sampling", IEEE Position Location and Navigation Symposium, Las Vegas, April 1994, pp. 209-215.

3. van Nee, D. R. J., and Coenen, A. J. R. M., "New Fast GPS Code Acquistion Technique Using FFT", Electronic Letters, Vol. 27, No. 2, January 17, 1991, pp. 158-160.

Figure 7: Comparison of Eight Bit Sampling & One Bit Sampling
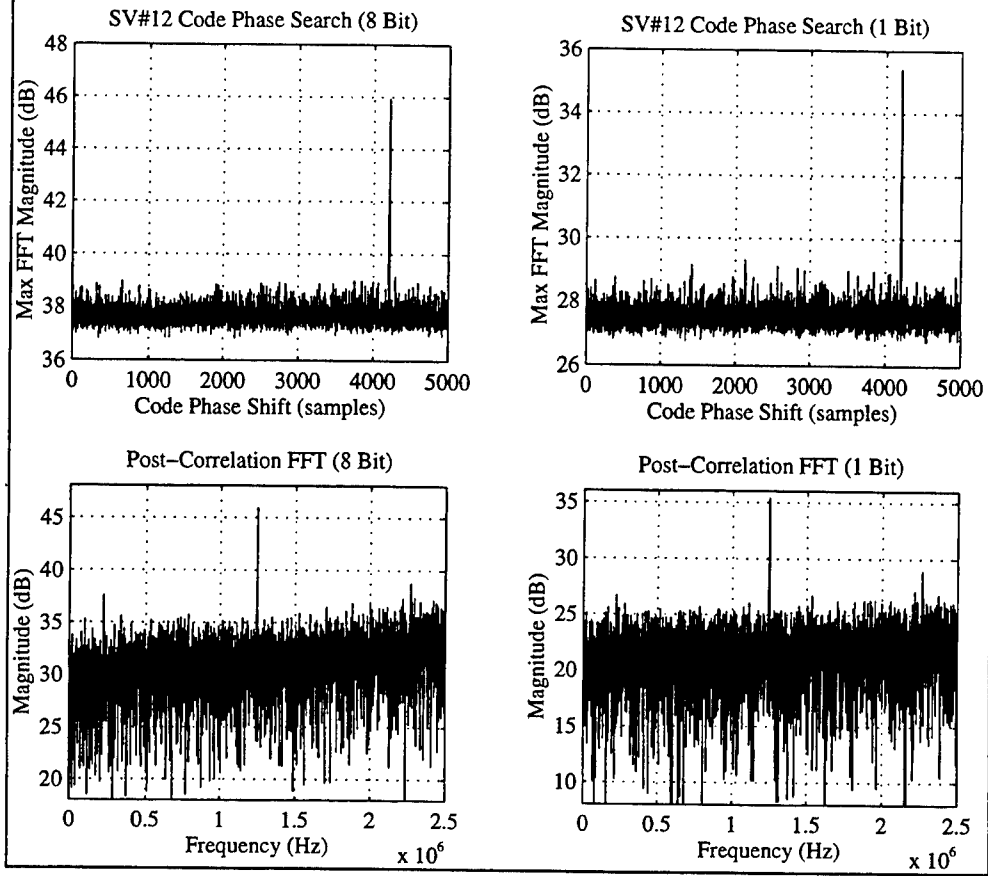
CONSTRUCTION AND USE OF A WAVEFRONT SENSOR FOR ADAPTIVE OPTICS

Wesley A. Bernard
Department of Electro-Optical Engineering

University of Dayton
300 College Park
Dayton, OH 45469-0227

CONSTRUCTION AND USE OF A WAVEFRONT SENSOR FOR ADAPTIVE OPTICS

Wesley A. Bernard
Department of Electro-Optical Engineering
University of Dayton

Abstract

The effects of atmospheric turbulence on the propagation of light, and information that may be encoded on this light, were studied. A Hartmann Wavefront sensor was constructed to sample incoming light using a CCD camera and an array of small lenslets. This enabled the creation of phase screens to express how light from a distant source had been altered by variations in the refractive index of the intervening medium. Experimental data was taken, and is currently being processed. Deformable mirrors may eventually be used in the optical path of the light to conjugate out the effects of turbulence, leaving the signal in its original state. This is the goal of adaptive optics.

CONSTRUCTION AND USE OF A WAVEFRONT
SENSOR FOR ADAPTIVE OPTICS

Wesley A. Bernard

Introduction

The existence of local variations in the index of refraction in the earth's atmosphere has long been understood. The twinkling of a star and the hazy shimmer that rises above a hot road are everyday examples of this phenomenon. One current area of study involves detecting and characterizing the consequences of this turbulence on light and then correcting for it. This is termed 'adaptive optics', and leads to improvements in such areas as astronomical observations and optical communications. In viewing objects outside the atmosphere, a strong light source (bright star) near an object to be studied provides light that should be nearly a plane wave. Correcting this light will also correct the signal from the object under study, whose light passes through approximately the same turbulence {2}. Similarly, if a plane-wave source is used in communications than this light can be studied for any departure from a flat phase front upon reaching a detector. Because of the relatively simple design of a Hartmann wavefront sensor, it is an ideal piece equipment for studying phase. The design is also more stable and easier to maintain at operating performance than some alternatives (i.e.. a shearing interferometer). Setting up a sensor and characterizing the effects on light in such a system is the first step. Correction can then ensure that a signal encoded on the beam will be accurately interpreted.

Methodology

The atmosphere of the earth is comprised of constantly shifting regions of air. Temperature variations due to the heating and cooling of the earth, as well as changes is atmospheric pressure, give rise to variously sized pockets of turbulent air at different temperatures. Difference in kinetic energy of the air molecules causes the index of refraction to be temperature sensitive, and thus to vary with these pockets. When light from outside the atmosphere enters the earth's surrounding layer of air it encounters these different regions, thus arriving at the planet's surface having gone through different optical paths (an optical path being the sum of spatial distances traveled through

each region times the index of refraction in each region) {1}. This means that the arriving light contains variations in phase. An element sensing the light, be it a telescope or a person's eye, will see a distorted signal. Light from distant objects, such as stars, arrives planar in phase due to the spreading out of the phase over the long distances traveled. Similarly, a light beam can be generated to be planar in phase. When this light passes through the atmosphere different portions become out of phase with other portions, resulting in a difference between the actual and ideal light signals.

To achieve a corrected optical signal, a method has been developed to compensate for the previously discussed deviation of the wavefront. In general, the wavefront variations coming to the sensor are monitored, and a deformable mirror used to impart the conjugate deformation on the signal. The light is then returned to the state in which it existed before encountering the atmosphere {2}. The first step in this process is analysis of the turbulent effects, and this is done by using a Hartmann wavefront sensor {3}.

A Hartmann sensor consists of an array of very small lenslets that divide the light signal into sub divisions of the original entrance pupil. These divisions are called sub-apertures. Beyond the array a CCD camera collects the light being focused. Because the phase front entering this lenslet array is not uniformly flat and parallel to the array, these small lenses will not always focus the light to a spot centered in the sub-aperture. A slight tilt in phase at the lens will cause the spot to appear shifted away from center to a location (xc,yc), taken with respect to the center of the sub-aperture. By determining these xc and yc values, and knowing the spacing between the lens and the CCD, the angles in the x and y directions formed by the spot are found. These angles give two slopes of the wavefront (one per direction) at that lenslet {1}. Finally these slopes are converted into phase values using a reconstruction matrix. One makes a map of these phases and the result is a phase screen that ideally would be flat, but in actuality has been corrupted by turbulence into a tilted plane of peaks and valleys.

One of the advantages of a Hartmann sensor is the simplicity of the physical design. A system of lenses magnifies the incoming light to a small, collimated beam that strikes a lenslet array and then falls on a CCD camera (see Figure 1). The initial lens is chosen as large as possible

because this lens places a limit on the amount of light that gets through the system. In this case, a 15 cm. plano-convex lens with a 45 cm. focal length was used. This first lens focuses the beam to a point. Slightly beyond this focal plane a collimating lens is placed to capture the diverging signal and return it to its initial state, diminished in size. This is again a relatively planar
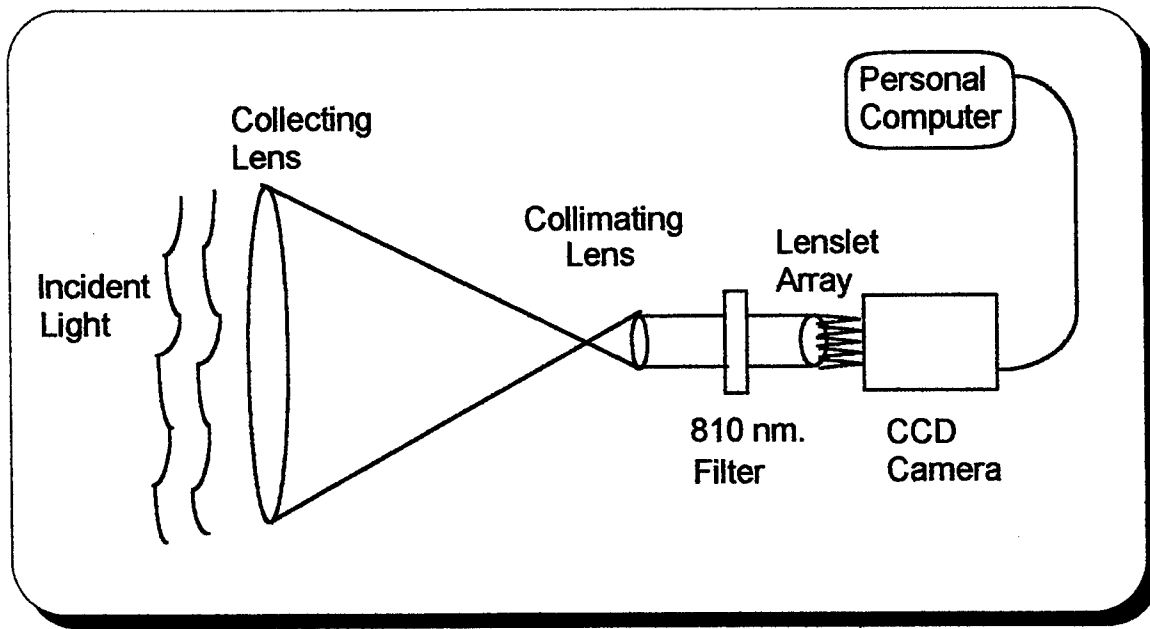

Figure 1: Schematic setup of Hartmann sensor apparatus.

wave, and when it strikes the lenslet array it is focused to the focal plane of the individual lenslets 7.8 mm away. A charge coupling device is placed in this plane to receive the light. The lenslets used are spherical in nature, with diameters of 203 micrometers and a fill factor of 100%. The number of sub-apertures actually used depends on the size of the newly collimated beam and the size of the CCD. The camera used consists of an array of 256 x 256 pixels, each 16 microns on a side, for a total active size of 4.098 mm. on a side. Thus there are 20 x 20 sub-apertures focusing light onto the CCD. A personal computer controls the camera and stores the images. One problem that exists in choosing the initial lens and the collimating lens is that all the light that gets through the first lens must also get collimated so that no loss of information occurs. To do this, the numerical apertures of the two lenses must be matched and the collimating lens must be the desired size of the beam at the CCD. The result of this setup is that light collected by the first

lens, complete with slight phase irregularities, appears at the lenslet array to be focused to the CCD and recorded.

Portions of a program involved in processing the data gathered with a Hartmann sensor appear in Appendix A. The program was coded this summer, and is entitled 'analyze.m'. Its main function is to construct phase screens using the pictures collected. The code was written in a basic text editor to be run in the MatLab mathematical software package. The inherent nature of MatLab is to work with matrices, and this makes it ideal for the task of working with arrays of pixels. Software that came with the CCD camera controls a video acquisition board placed in the PC, and images from the camera are stored on this board. These images are then read out to disk in raster binary format for storage and processing. A file contains one snapshot, or 256 x 256 ADU (analog to digital unit) values representing the intensity on the pixels at the time of the snapshot. The time between snapshots (frame rate) is expressed in snapshots per second. This value can range from 1 to 1000. The number of snapshots able to be taken at a time depends on the amount of memory on the video acquisition board. In this case 256 snapshots can be stored without recording over previous data.

Once the image files are on disk they are run through the phase construction program. A portion of this program was originally coded by Maj. Mike Roggemann and Cindy Hyde at Wright Patterson Air Force Base. This program first creates a vector known as the TLC (top left corner) locator vector. This vector contains the pixel locations, read from the top-left corner of the 256 x 256 array, corresponding to the top left corner of the sub-apertures. Because we are looking at 20 sub-aps. in a length of 256 pixels, each sub-ap. is set up to contain 11 x 11 active pixels with a border of unread pixels separating neighboring apertures. When the images are read into Matlab's memory, 121 pixels for each sub-aperture are picked out of the image array to be processed.

The first images read into Matlab are calibration images. Due to dark current in CCD's, a pixel is never quite at 0 adu's. This internal bias is measured with the lens cap on the camera, and is termed 'dark framing'. Also, slight variations in the voltages controlling the containment of the electrical signals in the pixels results in inherent differences between pixel adu values, even when

the pixels are illuminated with the same amount of light. This is measured by putting a 'flat field' (constant illumination) into the camera. To calibrate the camera, a number of dark frames and flat fields are taken and averaged. The averaged flat field data is then normalized. When the Hartmann sensor data is loaded into Matlab the dark frame intensity value of each pixel is subtracted from the image's corresponding pixel, and the result is divided by the normalized flat field pixel. In this way we avoid two major problems inherent in CCD cameras. A sample snapshot of the spots created by the lenslets is shown in Figure 2.

After calibration, the next step is to find the locations of the focused spots in the sub-apertures relative to the center of the sub-apertures. This is termed centroiding. The x position of the spot is given by the equation {1}:

$$x_c = \frac{\iint x f(x,y)\, dx\, dy}{\iint f(x,y)\, dx\, dy} = \frac{\sum\sum x_{ij} f(i,j)}{\sum\sum f(i,j)}$$

A similar equation tells the y position. Here i and j represent the number of pixels above/below and right/left of the sub-aperture center, f(i,j) is the intensity (adu's) in the i,j pixel, and x_{ij} is the distance in meters in the x direction between the center of the i,j pixel and the center pixel. These x_c and y_c locations are thus in meters, and are found for each sub-aperture and stored in two 20x20 arrays. We next arrive at the slope values of the phase from the following:

$$\text{Slope in x-direction} = s^x = \frac{2\pi l (\arctan(\frac{x_c}{fl}))}{\lambda}$$

with fl the focal length of a lenslet, l the width of a lenslet, and λ the wavelength of the light being used. Again a similar equation gives the y slopes.

The estimator for the phase $\Psi(\vec{x})$ of the wave front is given by the weighted sum of elementary functions, $e_i(\vec{x})$, according to

$$\Psi(\vec{x}) = \sum c_i e_i(\vec{x}).$$

We find the c_i weighting functions from

$$c_i = \sum M_{ij} s_j.$$

Here the slope values 's' have been reshaped into a vector of alternating x and y slopes. The matrix M is called the reconstruction matrix, and is established outside of the 'analyze' program. This matrix maps wave front sensor slope measurements to elementary function weights c_i, which in turn lead to phase values. The preceding method was found in the referenced book by Roggemann and Welsh {1}. Once we have these function weights, we use an interpolation

2-7

Figure 2: A snapshot of spots focused by the lenslet array.
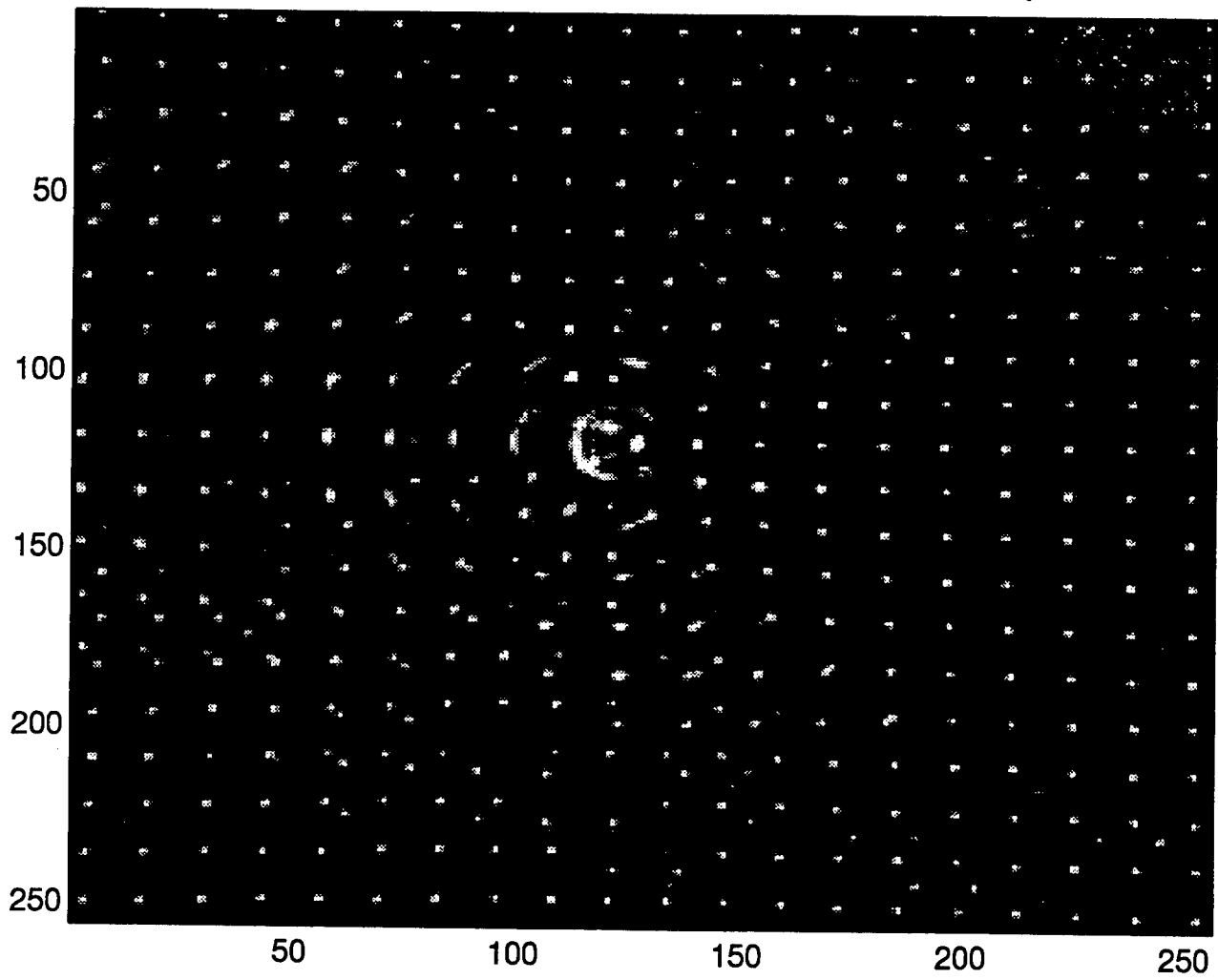
method known as a 'linear spline' to arrive at phase values. This employs the c_i values as weighted amplitudes of overlapping triangle functions. The phase value at a point is based on the size of all nearby weighted triangles. The built-in Matlab function 'interp2' utilizes this same method, and so is used to arrive at our final phase values. These values are in a square array, and are meshed to give a picture of the phase front (see Figure 3). Note that the units on the z-axis are in waves.

Results

Data was taken to study these turbulent effects. Two collimated plane waves were sent between two mountain peaks in the state of Hawaii, encountering turbulence in transit. To minimize the effects of extraneous light, a wavelength of 810 nm. was used and a line filter that passes only 810 nm light was placed between the collimating lens and the lenslet array of the receiving optics. A metal shroud covered the optical setup, which was contained on a portable optical breadboard. The entire setup was placed on a tripod that was aimed toward the light source on the opposite mountain. Data could then be taken. When the hard drive of the PC became full, all data was backed-up on tape. Log sheets were designed and used to record pertinent data about each run. This data is currently being processed at Wright Patterson Air Force Base in Dayton, Ohio by Wesley Bernard.

The program designed to create phase screens from Hartmann sensor data has so far worked well. This optical design and software creation encompassed most of the summer. The output of the software is a single data file consisting of all phase screens constructed in a given run. By creating a frame-by-frame movie of these phase screens one can see the evolution of the effects of turbulence on the beam. An example is shown in Figure 4, which contains phase screens for four consecutive snapshots. The frame rate the pictures were taken at was 1000 $\frac{frames}{\sec ond}$, and the units on the z-axis are waves.
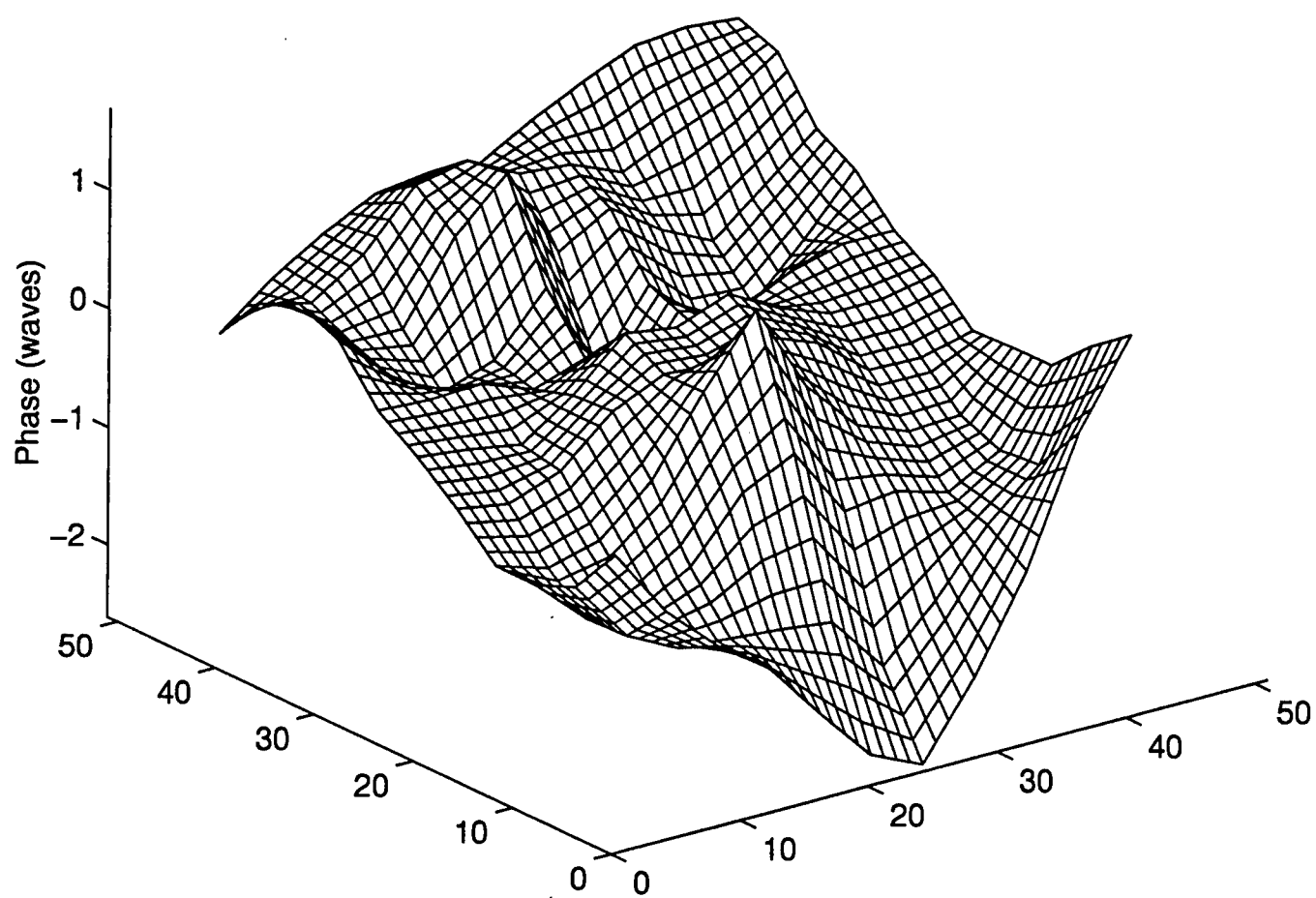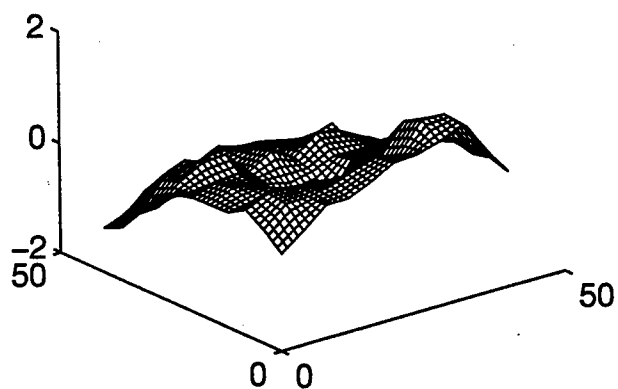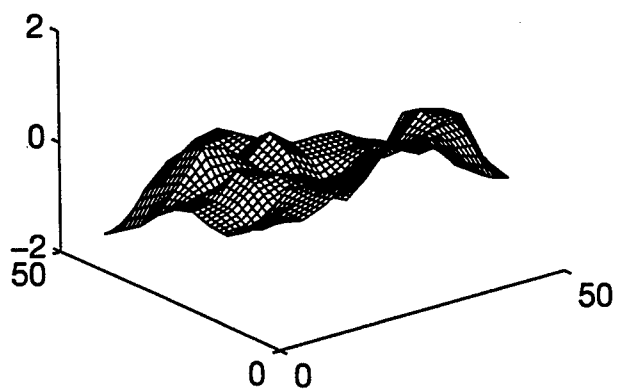
Figure 3: Phase Screen for an individual snapshot.
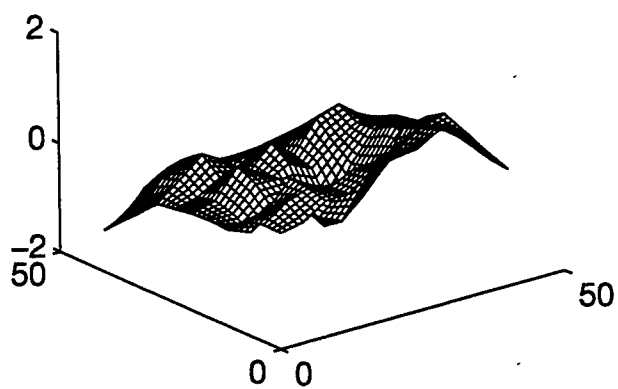
Figure 4: Variations of phase with time.

Phase screen for time t.

Phase screen for time t + 0.001 seconds.

Phase screen for time t+0.002 seconds.

Phase screen, time t+0.003 seconds.
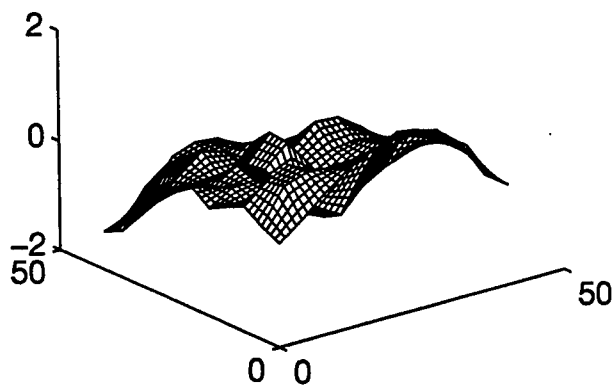
Conclusions

The method of adaptive optics is a relatively new area and is currently being studied for various applications. The use of these ideas to control optical beams carrying information requires first understanding the amount and nature of the effects of turbulence on this communications beam. A Hartmann sensor can be used for this purpose, as demonstrated above. Further processing of the data will include signal-to-noise studies and the correction for aberrations introduced by errors in the alignment of the optics .

References

[1] Michael C. Roggemann and Byron M. Welsh, Imaging Through Turbulence (CRC Press Inc.: To be published 1996) 1-11, 265-269.

[2] Laird Thompson, "Adaptive Optics in Astronomy," Physics Today December 1994: 24-31.

[3] Graham P. Collins, "Making Stars To See Stars: DOD Adaptive Optics Work is Declassified," Physics Today February 1992: 17-21.

Appendix A

Portions of phase reconstruction program 'analyze.m'

```
%  analyze.m to calculate phase screens for images from CCD camera
%  PC VERSION
        %  Coded by:  W. Bernard, G. Frensley, C. Hyde
        %  Last edited on:  17 August 95


%  create lookup-table vectors that convey pixel location in sub-aperture
ddx=.000016;                          % pixel separation
ddy=.000016;                          % (in meters)
icall=5:-1:-5;                        % Used to find which
icall=icall';                         % row of sub-ap we are in,
icall=icall*ddy;                      % and which column
jcall=-5:1:5;                         % of sub-ap we are in.
jcall=jcall*ddx;


%  create top-left-corner locator vector, accounting for drift.
%  This finds the top-left-corner pixel of each sub-aperture.
        tlc=2:13:256;
        for x=4:6
         tlc(x)=tlc(x)-1;
        end
        for x=7:9
         tlc(x)=tlc(x)-2;
        end
        for x=10:12
         tlc(x)=tlc(x)-3;
        end
        for x=13:15
         tlc(x)=tlc(x)-4;
        end
        for x=16:18
         tlc(x)=tlc(x)-5;
        end
        tlc(19)=tlc(19)-6;
        tlc(20)=tlc(20)-6;


%  Starting loop to open image files and find slopes
%=========================START==============================
for v = 1:nfiles
        vv=v-1;
```

2-14

```
if vv < 10
        fname=['d:\',fndata,'\',fndata,'-000',int2str(vv),'.img'];
end%if
if vv > 9 & vv < 100
        fname=['d:\',fndata,'\',fndata,'-00',int2str(vv),'.img'];
end%if
if vv > 99
        fname=['d:\',fndata,'\',fndata,'-0',int2str(vv),'.img'];
end%if
fid = fopen(fname);
array1=fread(fid,[256,256],'uchar');          % read in data.
fclose(fid);


% rotate and flip image array
array1=flipud(array1);                          % 256x256 pixel array
Image=rot90(array1,-1);                         % of a right-side-up image


disp(['File ',fname,' is loaded.'])


% Perform calibration if desired
if query~=1
  Image=(Image-darkf)./flatf;
  disp(['Calibration done.'])
end %if


% To find xc and yc, we need to
%  make the denominator and two numerators (one for each direction)
%  of the expression for centroids.
%-------------------------------------------------------------


% use look-up vectors and top-left-corner locator vectors to
% make D (Dsum) and Nx and Ny (Nsumx and Nsumy)


k=0;
for i=1:20
  k=k+1;
  m=0;
  for j=1:20
      m=m+1;
      f=Image(tlc(k):tlc(k)+10,tlc(m):tlc(m)+10);
          %creates an 11x11 array (representing the sub-aperture)
      fsum=sum(sum(f));
      Dsum(i,j)=fsum;
```

```
                    % makes 20x20 array of intensity sums in sub-ap.
            colmnsum=sum(f);
                    %makes sub-ap. array into a row vector
            colmnsum=colmnsum.*jcall;
                    %tells how far from center column
            sumx=sum(colmnsum);
                    %makes these columns into a #
            Nsumx(i,j)=sumx;
                    %makes 20x20 array of column intensities
            rowsum=sum(f)';
                    %makes sub-ap array into a column vector
            rowsum=rowsum.*icall;
                    %tells how far from center row
            sumy=sum(rowsum);
                    %makes these rows into a #
            Nsumy(i,j)=sumy;
                    %makes 20x20 array of row intensities
        end %for
    end %for


        %Find slopes
%----------------------------------------------------------------------


% x(c) and y(c) are the shifted spot-center locations
% with respect to sub-aperture centers.
% Use D (Dsum), Nx and Ny (Nsumx and Nsumy) to make x(c) and y(c)
% Then use x(c)and y(c) to make thetax and thetay.
% thetax, thetay are angles formed by spot-center wrt. sub-ap. center
% Then use thetax and thetay to make delphix and delphiy.
% delphix, delphiy are slopes, in the x and y directions,
%  of the entering wavefront
%  ***EACH STEP IS DONE FOR EACH SUBAPERTURE!!!***
% davgx and davgy are arrays containing sum of all previous
%  x and y slopes
% (used to find average slopes for each sub-apr. outside this loop)
disp(['Finding slopes.'])
        xc=Nsumx./Dsum;
        yc=Nsumy./Dsum;
        thetax=atan(xc/fl);
        thetay=atan(yc/fl);
        delphinx = 2*pi*l*thetax/wvl;          % 20x20 arrays of slopes
        delphiny = 2*pi*l*thetay/wvl;          %   in both directions
        eval(['delphix' int2str(v) '=delphinx;'])      % Naming slopes individually
```

2-16

```matlab
            eval(['delphiy' int2str(v) '=delphiny;'])           %  to be used later.
            davgx=davgx+delphinx;
            davgy=davgy+delphiny;

      disp(['Slopes found for file ',fname])
      disp([' ']);

end %for                      %End of Image-file loop (v-loop).


%=============================END=====================

% Load the reconstruction matrix
disp(['Loading reconstruction matrix.'])
pause(1);
eval(['load r',int2str(numac),'.mat;']);
rtemp=zeros(numac^2*800,1);
eval(['rtemp=r',int2str(numac),';']);

% convert reconstruction matrix data to a new array
  disp('Reshaping Reconstruction matrix.')
  pause(1);
  ee=reshape(rtemp,800,numac^2);
  rji=ee';

% Convert the two slopes arrays into an interleaved vector called delphi.
% Save this vector of slopes if desired (ie. to do structure functions),
%   Do estpup if desired, finding and saving phase screens.
%+*+*+*+*+*+*+*+*+*+*+*START+*+*+*+*+*+*+*+*+*+*+*+*+*+*+*+*+*+*+*
   disp('Reshaping slopes.')
   pause(1);
   for w=1:nfiles
        eval(['delphinx=delphix' int2str(w) ';'])
        eval(['delphiny=delphiy' int2str(w) ';'])

   % Prepare slopes to either be saved out or to find phases.
        delphinxx=delphinx';
        delphixvect=delphinxx(:);
        delphinyy=delphiny';
        delphiyvect=delphinyy(:);
      if doest==0
        delphi=zeros(800,1);
        delphi(1:2:799)=delphixvect;
```

```matlab
            delphi(2:2:800)=delphiyvect;
            eval(['clear delphix' int2str(w)])
            eval(['clear delphiy' int2str(w)])
        else
            % Save slopes to a file if not doing phase screens.  We save
            %   the slopes in sub-ap. in both x and y directions, and
            %   the sum of all intensities in sub-ap.
                Dsumm=Dsum';
                intgrint=Dsumm(:);
                fid=fopen(deltphisx,'a');
                 count=fwrite(fid,delphixvect,'float');
                fclose(fid);
                fid=fopen(deltphisy,'a');
                 count=fwrite(fid,delphiyvect,'float');
                fclose(fid);
                fid=fopen(deltphisi,'a');
                 count=fwrite(fid,intgrint,'float');
                fclose(fid);
        end %if


% Do estpup.m to find phase screens if desired (if doest=0).
%------------------------------------------------------------
if doest==0

            disp(['Finding phase screen for file # ', int2str(w)])
            pause(1);

%          Program: estpup.m
%--------- --------- --------- --------- --------- --------- --------- --
%          Translated FORTRAN estpup() code from sholozimg3's ao3.f file.
%           Originally coded by Mike Roggemann
%
%          Estpup() estimates the pupil phase for speckle holography processing
%
%          This code is meant to be used with the data acquired from the
%          Hartmann wavefront sensor equipment obtained in June 1995.
%
%          Translated by:  Cindy Hyde  9 May 1995
%          Last edited on: 27 June 1995
%
%          numac = actual # of actuators
%          rji = numac^2 by 2*numsa array of the reconstructor matrix
%          delphi = array of delta phis (slopes)
```

```
%        cj = 1-dim array of length madim containing actuator commands
%        xx, yy = original actuator spacing coordinates
%        xi, yi = new (more detailed) actuator spacing coordinates
%        estphs = 1-dim by 1-dim array holding corrected phase map
%-------- --------- --------- --------- --------- --------- --------- --

        cj = rji * delphi;              % leaving a numac^2 x 1 array
        cj=reshape(cj,numac,numac);     % convert cj to a square matrix
        cj=cj';                         % convert cj to correct orientation
        estphs = interp2(xx,yy,cj,xi,yi,'linear');      % Interpolate cj to convert to phase
        estphs = estphs/(2*pi);         % Convert from radians to waves

        % write current estphs to a file
        fid=fopen(phscrns,'a');
        count=fwrite(fid,estphs,'float');
        fclose(fid);

end %if

clear delphi            % clear slopes before going to next snapshot

end %for

%End of the nfiles loop (w loop)

%+*+*+*+*+*+*+*+*+*+*+*+*+*+*+*+*+*END+*+*+*+*+*+*+*+*+*+*+*+*+*+*+*+*+*

status=fclose('all')
end
```

A STUDY OF SUMMER ACTIVITIES TO INCLUDE PROCESS MODELING FOR VIRTUAL MANUFACTURING

David Liston Bias
Doctorial Candidate
School of Industrial Engineering & Management

Oklahoma State University
317F Engineering North
Stillwater, OK 74078

Table of Contents

Abstract:

Advances in Virtual Manufacturing (VM) are needed to help industry deal with the changing environment of lower production, higher variety, and decreasing budgets. These advances rely heavily on the integration of a number of technologies referred to as VM tools. One step toward full integration of these tools is to accurately and completely model the current, and proposed, processes involved in manufacturing which I have made some strides in accomplishing.

This paper attempts to summarize the activities performed by myself during the summer of 1995 while at Wright-Patterson Air Force Base. Although impossible to capture all I have learned, I have tried to capture some major points of interest and observation. Much of the work performed during the summer was done in conjunction with the modification of an F-15 part being redesigned at McDonnell Douglas Corporation using VM tools. Engineers and other personnel at McDonnell Douglas Corporation were very helpful in providing me with a better understanding of how things are manufacturing in their Company.

Introduction:

Current practices in manufacturing are quickly approaching extinction. With the reality of low volume production, demand for high variety, and reduced budgets, industry needs to continually develop methods to address these issues. What exactly does all this mean? Low volume requires increased emphasis on the reduction of one-time product development cost, including set-up. High Variety means that companies need to ability to changeover from one product line to another quickly and easily. Finally, reduced budgets demand that companies analyze alternatives quickly and accurately to estimate the cost and risks involved. Virtual Manufacturing is one philosophy that could prove quite successful at addressing all of these issues.

Although Virtual Manufacturing (VM) may just sound like another catchy buzz word, it is the word associated with a number of new technologies that attempt to reduce the total cost of producing and maintaining a product. These new technologies, also known as VM tools, are: 3D simulation, materials management, production process modeling, rapid prototyping, resource modeling, electronic information transfer, and CNC manufacturing. Although VM has been around for years (maybe not by said name), manufacturers have yet to experience a full VM system in use. A full VM system would enable manufacturers to analyze a wide range of issues involving a product long before production. These issues may include cost estimates, as well as make versus buy decisions. Progression toward creating a "full" VM system will require the full integration of a number of technologies already labeled as VM tools. One step toward this end is to accurate depict the processes involved in current, as well as proposed, manufacturing

systems. A problem statement for work in this area can best be described as: What steps need to followed in order to create a formal driver for all simulation tools involved with virtual manufacturing philosophy? As indicated above, in order to accomplish this task, a model needs to be developed that encapsulates all the processes involved.

This paper attempts to summarize much of the work performed during the summer of 1995 while working at Wright Laboratories in Dayton, Ohio. Although impossible to capture all I have learned, I have attempted to address the major points of interest & commitment (see index). The key task to be addressed are software evaluation, process modeling, and advantages of assembly simulation. All of these task centered around an effort to move in the direction of creating a full VM system, or formal driver for all simulation tools involved with virtual manufacturing. The initial hope of completing all task by summer's end did not occur, but some progress was made. The first task involved evaluating software for use in developing models of the current process. I examined two pieces of software in this effort, IKE & IDEF/DESIGN, and will discuss both later in this paper. My second task involved the creation of a complete process model for how McDonnell Douglas implemented its VM approach to redesigning a part of the F-15 fighter jet using VM tools. This task was later adjusted to include a more generic approach to design of assembly. My final task, a tangent of developing process model, was the analyzation of how assembly simulation (VM tool) would aid McDonnell Douglas Corporation compared to current practices. All three task were performed with much assistance from individual at WPAFB, McDonnell Douglas Corporation, and respective software vendors. In addition to above task, I will also discuss recommendation for future research and summer program.

3-5

Software Evaluation:

IKE Software:

The IKE (Integrated Knowledge Based) software has the potential to be a very powerful tool for process modeling. The manufactures of IKE, KBE (Knowledge Based Engineering), boast for its ability to process model in their user manual:

> To Summarize, an IKE-PDMS model is much more than just a simple drawing showing relations between activities of the process. An IKE-PDMS process model is a diagram with a supporting object-oriented database containing all the semantics of the model (activity sequencing relationship and junction logic) along with the object and rule definitions that make the model a full blown process controlled application.

All of this sounds good on paper, but implementing all the features with the current version (2.12) turned out to be quite a task. First of all, the program is based heavily on multi-media technology meaning that it basically requires 16-32 Meg of RAM and a Pentium processor to run at a bearable speed. Secondly, the steps involved in creating a single process (known as Unit of Behavior in IKE) with associated input, output, control, and mechanisms requires many, many steps. Finally, the visual output of the model was not very impressive to these eyes. Of course, the software was designed for much greater usage than just creating pretty models to look at. Making better use of the software would require the defining of classes and rules so that a process could be simulated by click on each box one at a time (another drawback).

Among the positive features of the software was the ability to create multiple views from one process box (Unit of Behavior). These views could be linked to an application program such as Microsoft Excel or just be another image depicting a difference between, for example, a marketing and engineering perspective. The most promising feature of this software is the

projected release of Version 3.0 by the end of August 1995. The new version promising to be much more user friendly. Adjustment that required 7-8 steps in version 2.12 are accomplished in just 3-4 with the new version. Also, the new version make better use of arranging icon on the screen so that they are always available and out of the way. For future investments in developing a formal driver for Virtual Manufacturing, I would STRONGLY suggest a good luck be taken at the new version. Sample Output from IKE can be found in Appendix C.

IDEF/DESIGN software:

The IDEF/DESIGN software by Metasoft proved to be a relatively simple tool for graphically depicting the processes involved. I used the software to model the process of creating a new assembly at McDonnell Douglas Corporation (see Appendix D for examples) using IDEF0 technology. Although a good start, IDEF0 is probably not the best tool for modeling processes. IDEF0 was designed for modeling activity flow with input, output, mechanism, and control.

I had a little trouble getting the arrows and boxes to adjust just the way I would like, but persistence usually paid off. The software also lacked the automatic ability to create dictionary of terms and link objects to activities/processes as have other IDEF modeling tools I have used. The visual product, however, did appear to look good with work. I would not recommend this software be used for process flow modeling in the future. It does not have the direct ability to manipulate flow for analyzation. It does, however, provide means for input the models into other software packages as a starting point to simulation. Since I was having so much trouble with IKE and timing prevented me from researching alternatives, this software proved very helpful.

3-7

Process Modeling:

The development of the Process model underwent many changes before arriving at the somewhat final product found in Appendix B (3-13). Initial discussion surrounding the process flow model focused around how McDonnell Douglas Corporation was implementing virtual manufacturing into their redesign of an F-15 part. Their current efforts at using VM were more or less piece mealed together. McDonnell Douglas Corporation has a number of VM tools (process flow simulation, 3D Models), but it lacked a coherent linking of these tools into one. Each tool acted independently of the others, except for the fact that 3-D models provided some input into the process flow simulation. Based on time constraints with project and desire to generalize the process flow model to a more broad base, it was decided that process flow models created would depict the general operations involved in created a new assembly or re-working an old. The method of depicting this flow would be IDEF0. This would allow for processes to be graphically depicted with input, output, control, and mechanisms included. To begin with, a text version of the process flow was developed via multiple conversations with experts at McDonnell Douglas Corporation (Appendix A). After the text version was complete, the model data was fed into IKE (Appendix C) and IDEF/DESIGN (Appendix D) software.

Creating accurate process flow diagrams requires a large of amount of discussion with frequent revisions to the current model. It was quickly discovered that there was no documented way of accomplishing things, only a number of task that needed to be completed. The keys to creating a New Assembly involve Detail Planning Parts, Assembly Tool Order, Assembly Planning, and Production as depicted in listing with decompositions.

Advantages of Assembly Simulation:

After developing the process model for with VM and without VM, there arose some concern about what true benefits VM does have in the design through production phases of development. Benefits could be found in the conceptual phase as cost analysis could be done to determine with continuing would be prudent. Benefits could also be found in the post production phases when the number of parts needing re-work should be reduced significantly. We (McDonnell Douglas engineers and self) were, however, concentrating of the steps between conceptualization and post production. What benefits could be found in this area? It was initially thought that the number of steps would be far less, but that was not the case. Initially attempts at creating process flow proved that to be quite false showing process flow with VM actually had more steps. The only real difference was that the computer was doing the work where humans had done it before. From this line of thinking, a discussion arose on how Assembly Simulation is better than the current process. It was thought that Assembly Planning would be the steps most benefiting of this advancement. A list of these benefits can be found in Appendix A (3-12). The list overlaps a little bit in to other phases of development, but get one thinking about how things are different. McDonnell Douglas appears to be big into using assembly simulation to analyze decisions.

Conclusion:

Progress in developing a Formal Driver for Virtual Manufacturing still has a long way to go. The contents of this paper provide some direction of how to get to this Formal Driver, although it does fall way short in reaching that point. The software programs analyzed can provide a starting point for software selection, but other programs should also be analyzed. To move the effort even further, the models developed in the Appendix can be expounded upon and others can be created. Other means for forging ahead can be found below listed under Future Research. The key to moving ahead with Virtual Manufacturing is to fully integrate the many tools capable of benefiting the effort.

Future Research:

* Invest in learning how to use a powerful process modeling tool such as IKE before attempting to model with extreme detail.

* Continue work on creating a complete process flow analysis for new assembly and rework.

* Highlight in some matter the differences between using VM tools vs. not using VM tools in regard to process flow models.

* Integrate the individual VM tools used into the actual model. Much of this can be done in IKE (or similar programs) by creating a view that launches an application.

* Gather input from multiple sources to insure that some commonalty is found on what is involved in a standard new assembly process model. If no consensus can be found, model related processes.

Summer Program Recommendation & Observation:

* Try to decide on applicants earlier, if possible. As previously mentioned to Alan Winn, I had already committed to working the summer as a lifeguard. I spend over $400 and dedicated 40 hours a week for the last three weeks of school to get certified. These classes made studying and packing very difficult. Knowing that it was all for null makes it very frustrating. Also, my wife had committed to job in Florida over summer that she could not back out of with good conscience meaning we spent much of the summer apart.

* Along the lines of number one, provide graduate students an opportunity to learn about program prior to arrival. I think a small investment in visiting Dayton prior to my actually arrival would have been money well spent... in fact, I would even pay if someone organized it. I spent the first few weeks gathering info on software vendors I had readily available prior to packing for summer. And I spent much of the summer researching VM when I had professors nearby that could have discussed it with me.

* Outline Expectation to summer research associate. I never really knew what my expectations were, although I sought clarification. I would have preferred to have the freedom to decide on course of study, but was unclear of my options. Fast Track program was a good choice.

* Explain to summer research associates on onset about the autonomy aspect of division. How can the summer research associate go about getting their questions answered? Perhaps scheduled personal meeting with focal point every other week to insure on track could prove quite helpful.

* Alan Winn was extremely helpful to me this summer (especially early on), however, we did have some problems communicating. Many of the problems stemmed from the fact that he was very busy. I could see his vision on where he wanted me to be, but I did not always know how he wanted me to get there. I hope my work was, at least, heading in the right direction.

* As mentioned previously in this paper, I learned a lot from this summer experience that can not be captured on paper. I was, and still am, in awe at how they make the F-15 fighter jet. My best lessons come from observing how people interact with colleagues and superiors. I believe it is this knowledge, in conjunction with technically background, that will prove most useful to me some day. Thank You!

* I would love to do something similar to this experience in the future, however, I would better prepare myself with knowledge background and I would definitely have my wife in town with me :-)

Use of Assembly Simulation:

Replace:
- Tool/Part Tryouts
- Tool Usage Instructions

Augment:
- LOAPS Books (Large Order Assembly Planning)
- Training
- Automated Planning
- First Article
- Automated Tooling Orders
- Visual Aids
- Rework Evaluation
- Tool Design Study

Improvements from current process:
- Allows up front analyzation of engineering and tooling, opportunity to check interference or access problems.
- Better individual shop cell layout.
- Better sequence planning, manipulation of assy simulation to properly sequence the installation of parts assemblies.
- Many different scenarios can be run, feasibility checked and modification made before commitment to build.
- Supply superior visual aids that accompany the large order planning books.
- Few errors in reducing non-reoccuring cost.
- Enhance communication between departments, ability to electronically pass designs between various team members.
- Schedule manufacturing resources for Just-In-Time inventory.
- Shorten manufacturing cycle times.
- Detect problems up front that may occur during assembly installation.
- Assist in rework evaluation.
- Improved precision and efficiency in building tools.
- Replace tool/part tryouts.
- Eliminate physical mock-ups.
- Better training activities
- Eliminate tool usage instructions.
- Concurrent engineering vs. sequential engineering.
- Seeing the product before it is built.
- 3-D models viewed and understood more easily than 2-D drawings.
- Better essential information available for decision making.

FAST TRACK Process/Activity Flow for New Assembly
8/10/95   1100 Bias

P-0
    P0: New Assembly
        P1:   Detail Planning of Parts (Non-Design Tooling for Parts)
        P2:   Assembly Tool Order (Design Tooling)
        P3:   Assembly Planning (Steps involved in assembling parts)
        P4:   Production (Does not change with introduction of VM tools)
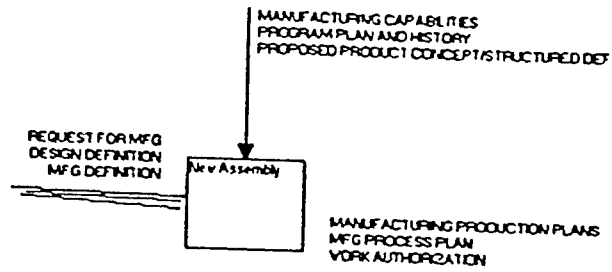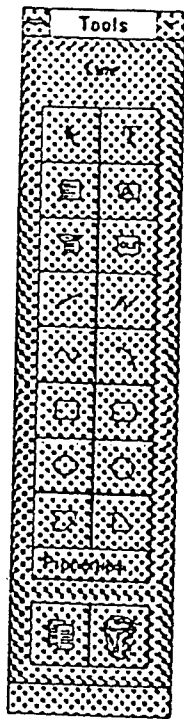
Without Virtual Manufacturing (VM)

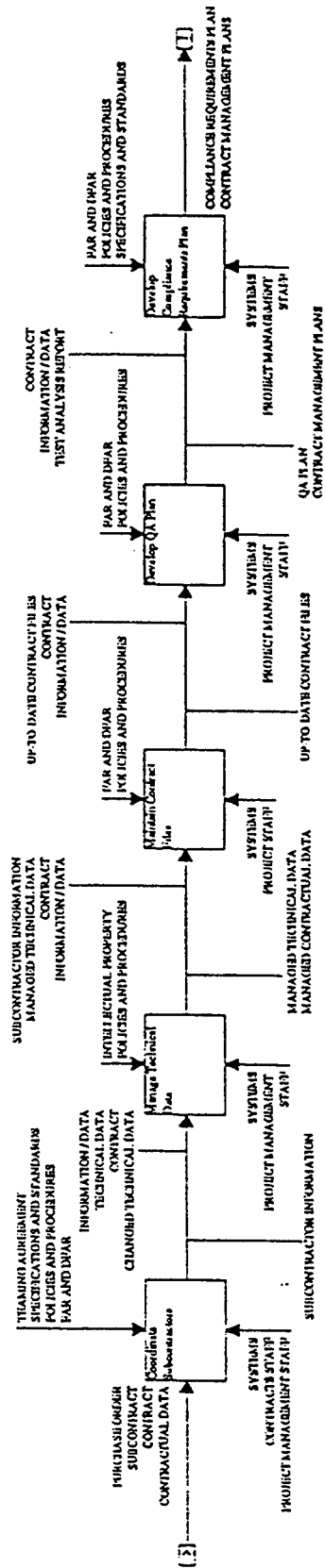Input: B/P, Parts List, Scheduling, and Related Info (Orders, Planning).

P11: Coordination with Detail Manufacturing Engineer
P12: Create "complete" Automated Planning Instruction (loop if incomplete)
    P121: Determine Parts that need Detail Planning
    P122: Quantity of Each Part
    P123: Effectively of Each Part
    P124: Material Requirements
    P125: Special Tool Requirements
P13: Buy part from Vendor
P14: Make Part
    P141: Create non-Design Tooling for Detail Part
    P142: Create Detail Sequence Planning for Shop Floor
    P143: Fabricate (make part and tools per detail planning)

P21: Confer with Tool Engineer for proper Tooling Technique
P22: Create Design & Fab instructions for Tool order
    P221: Determine Usage Effectively
    P222: Indicate any interchangeability
    P223: Determine Parts to be located by tool
    P224: Which parts to be jig located in tool.
    P225: Determine holes that need to be drilled by tool.
    P226: Sequence of loading and unloading by tool.
P23: Issue Tool Usage Instructions if needed
P24: Release completed tool order to scheduling
P25: Make Tool (Design and Fab)

P31: Coordinate tooling and shop personnel to Establish Assy Approach
P32: Determine Proper Sequence of parts and Assembly installation/LOAPS
    P321: Determine Tools needed for Assembly
    P322: Determine Parts/Assembly Needed for Assembly
    P323: Develop Needed Effectively
    P324: Issue Parts list change notice for production control
    P325: Sequence of Asssembly
        P3251: Assembly
        P3252: Inspection
        P3253: Packing and Shipping
        P3254: Interchangeability
        P3255: Provide Process Specs
        P3256: Develop Visual Aids for complex sequences
P33: Approval of LOAPS/ASSY Installation
    P331: Quality Assurance
    P332: Manufacturing Methods
    P333: Requirements and Inventory Management
    P334: Shop Foreman

P41: Analyze A.S. (Assembly Simulation
P42: Build Assembly

LOAPS - Large Order Assembly Planning

FAST TRACK - 08/10/95

With Virtual Manufacturing (VM)

Input: B/P, Parts List, Scheduling, and Related Info (Orders, Planning).
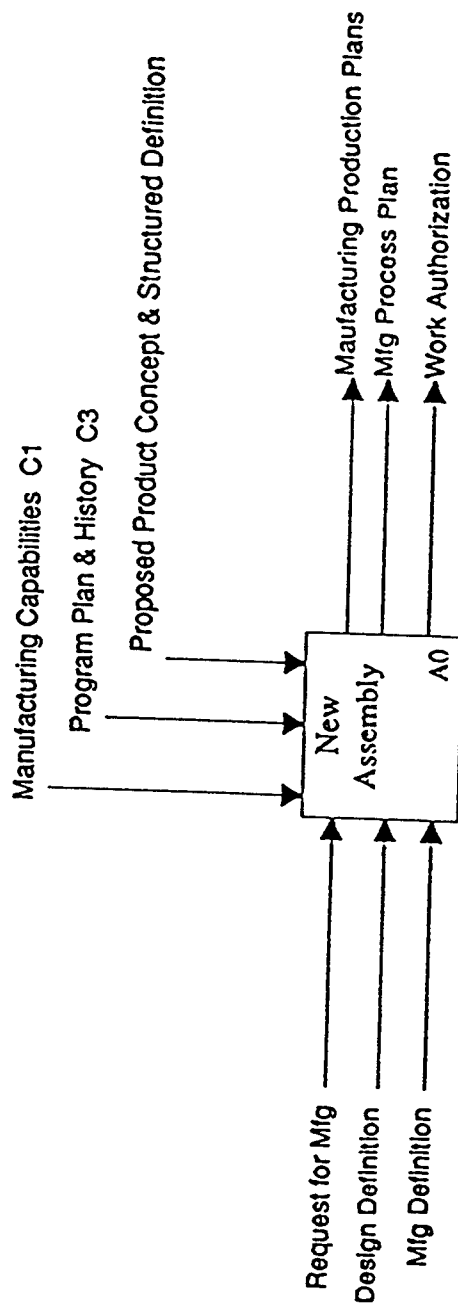
P11: Analyze A.S. (Assembly Simulation)
    P111: Determine Parts that need Detail Planning
    P112: Quantity of Each Part
    P113: Effectively of Each Part
    P114: Material Requirements
    P115: Special Tool Requirements
P12: Initiate A.S. to Create "complete" Automated Planning Instruction
P13: Buy part from Vendor
P14: Make Part
    P141: Create non-Design Tooling for Detail Part
    P142: Create Detail Sequence Planning for Shop Floor
    P143: Fabricate (make part and tools per detail planning)

P21: Analyze A.S. (Assembly Simulation)
    P211: Determine Usage Effectively
    P212: Indicate any interchangeability
    P213: Determine Parts to be located by tool
    P214: Which parts to be jig located in tool.
    P215: Determine holes that need to be drilled by tool.
    P216: Sequence of loading and unloading by tool.
P22: Initiate A.S. to Create Design & Fab instructions for Tool order
P23: Issue Tool Usage Instructions
P24: Release completed tool order to scheduling (pending approval)
P25: Make Tool (Design and Fab)

P31: Analyze A.S. (Assembly Simulation)
    P311: Determine Tools needed for Assembly
    P312: Determine Parts/Assembly Needed for Assembly
    P313: Develop Needed Effectively
    P314: Issue Parts list change notice for production control
    P315: Sequence of Asssembly
        P3151: Assembly
        P3152: Inspection
        P3153: Packing and Shipping
        P3154: Interchangeability
        P3155: Provide Process Specs
        P3156: Develop Visual Aids for complex sequences
P32: Initiate A.S. Determine Proper Sequence of parts and Assembly installation/LOAPS
P33: Approval of LOAPS/ASSY Installation electronic 'book'
    P331: Quality Assurance
    P332: Manufacturing Methods
    P333: Requirements and Inventory Management
    P334: Shop Foreman

P41: No Change!

LOAPS - Large Order Assembly Planning   FAST TRACK - 08/10/95

Tools

Cur

MANUFACTURING CAPABILITIES
PROGRAM PLAN AND HISTORY
PROPOSED PRODUCT CONCEPT/STRUCTURED DEF

REQUEST FOR MFG
DESIGN DEFINITION
MFG DEFINITION

New Assembly

MANUFACTURING PRODUCTION PLANS
MFG PROCESS PLAN
WORK AUTHORIZATION

MANUFACTURING CAPABILITIES
PROGRAM PLAN AND HISTORY
PROPOSED PRODUCT CONCEPT/STRUCTURED DEF

REQUEST FOR MFG
DESIGN DEFINITION
MFG DEFINITION

New Assembly

MANUFACTURING PRODUCTION PLANS
MFG PROCESS PLAN
WORK AUTHORIZATION

COMPLIANCE REQUIREMENTS PLAN AND CONTRACT MANAGEMENT PLANS

FAR AND DFAR
POLICIES AND PROCEDURES
SPECIFICATIONS AND STANDARDS

Develop Compliance Requirements Plan

SYSTEMS
PROJECT MANAGEMENT STAFF

CONTRACT
INFORMATION / DATA
TEST ANALYSIS REPORT

FAR AND DFAR
POLICIES AND PROCEDURES

Develop QA Plan

SYSTEMS
PROJECT MANAGEMENT STAFF

QA PLAN
CONTRACT MANAGEMENT PLAN

UP-TO-DATE CONTRACT FILES
CONTRACT
INFORMATION / DATA

FAR AND DFAR
POLICIES AND PROCEDURES

Maintain Contract Files

SYSTEMS
PROJECT STAFF

UP-TO-DATE CONTRACT FILES

SUBCONTRACTOR INFORMATION
MANAGED TECHNICAL DATA
CONTRACT
INFORMATION / DATA

INTELLECTUAL PROPERTY
POLICIES AND PROCEDURES

Manage Technical Data

SYSTEMS
PROJECT MANAGEMENT STAFF

MANAGED TECHNICAL DATA
MANAGED CONTRACTUAL DATA

TRAINING AGREEMENT
SPECIFICATIONS AND STANDARDS
POLICIES AND PROCEDURES
FAR AND DFAR

INFORMATION / DATA
TECHNICAL DATA
CONTRACT
CHANGED TECHNICAL DATA

Coordinate Subcontractors

SYSTEMS
CONTRACTS STAFF
PROJECT MANAGEMENT STAFF

PROJECT MANAGEMENT INFORMATION

SUBCONTRACTOR INFORMATION

PURCHASE ORDER
SUBCONTRACT
CONTRACT
CONTRACTUAL DATA

[2]

[1]

View: Manage Contract
Date: April 27, 1995
By: Knowledge Base Engineering, Inc.

3-17

APPENDIX D

USED AT:

AUTHOR: Liston Blas   DATE: 16 Aug 95
PROJECT: Process Modelling   REV:

NOTES: 1 2 3 4 5 6 7 8 9 10

WORKING	READER	DATE	CONTEXT:
X DRAFT			
RECOMMENDED			
PUBLICATION			

Manufacturing Capabilities C1

Program Plan & History C3

Proposed Product Concept & Structured Definition

New Assembly

A0

Maufacturing Production Plans

Mfg Process Plan

Work Authorization

Request for Mfg

Design Definition

Mfg Definition

NODE: TITLE: Process Model for New Assembly   NUMBER:

USED AT:	AUTHOR: Liston Bias	DATE: 16 Aug 95		READER	DATE	CONTEXT:
	PROJECT: Process Modelling	REV:				
			WORKING			
	NOTES: 1 2 3 4 5 6 7 8 9 10		X DRAFT			
			RECOMMENDED			
			PUBLICATION			

O1 Test Requirements

O2 Assy & Installation Plans

O3 Mfg Production Plans

O4 Planning Work Authorization

Planning Checklist C4

Process Specification C3

Standards & Procedures C2

Mfg Capabilities C1

Coordinate Tooling & Shop Personnel

A31

Determine Sequence of parts & Assy Installation

A32

Approval of LOAPS/ASSY Install

A33

Common Database M1

Req for Mfg I1

Mfg Process Improvement I2
Production Definition I3

Mfg Definition I4

Design Definition I5

TITLE: Process Model for New Assembly

NODE:

NUMBER:

3-19

USED AT:	AUTHOR: Liston Bias	DATE: 16 Aug 95	READER	DATE	CONTEXT:
	PROJECT: Process Modelling	REV:			⊠

NOTES: 1 2 3 4 5 6 7 8 9 10	WORKING	X	DRAFT		
			RECOMMENDED		
			PUBLICATION		

C1 Manufacturing Capabilities

C2 Standards & Procedures

C3 Program Plan & History

C4 Process Specifications

O1 Manufacturing Production

O2 Tooling Requirement

O3 Assy & Installation Plans

A1 Detail Planning of Parts

A2 Assembly Tool Order

A3 Assembly Planning

A4 Production

I1 Request for Mfg

I2 Design Definition

I3 Mfg Definition

I4 Production Definition Improvement

M1 3-D Modeler

TITLE: Process Model for New Assembly

NODE: NUMBER:

3-20

A STUDY OF PULSED LASER DEPOSITION
OF SILICON CARBIDE THIN FILMS

Ronald Birkhahn
Graduate Student Associate
Department of Materials Science

Andrew J. Steckl
Professor
Department of Electrical and Computer Engineering

University of Cincinnati
899 Rhodes Hall
P.O. Box 210030
Cincinnati, OH 45221-0030

A STUDY OF PULSED LASER DEPOSITION OF SILICON CARBIDE THIN FILMS

Ronald Birkhahn
Graduate Student Associate
Department of Materials Science

Andrew J. Steckl
Professor
Department of Electrical and Computer Engineering

ABSTRACT

We investigated the validity of using pulsed laser deposition (PLD) to deposit single crystal epitaxial SiC films during the Summer Research Program at Wright Patterson Air Force Base. After modification of the substrate stage for heating capability, SiC was pulsed-laser-deposited onto (001) Si, SiC on (111) Si, and SiC substrates. X-ray diffraction (XRD) showed that the crystallinity of the deposited SiC film improved with increasing substrate temperature and reduced laser repetition rate, but remained polycrystalline overall. However, discrepancies between temperature characterization techniques prevented us from accurately determining the substrate temperature.

TABLE OF CONTENTS

FIGURES AND TABLES

Figure 1: Schematic of PLD deposition system

Figure 2: Photo of high temperature stage with substrate

Figure 3: Stage temperature vs. input power

Figure 4: Organization of experiments

Figure 5: XRD of carbonized and low pressure CVD SiC grown on Si(111) substrate before and after SiC PLD

Figure 6: Combined XRD data for PLD runs #5-7 for comparison

Figure 7: XRD of PLD-SiC grown on SiC substrates

Figure 8: Large angular scan of PLD on Lely-grown 15R-SiC substrate

Table 1: Summary of SiC PLD growth conditions

A STUDY OF PULSED LASER DEPOSITION OF SILICON CARBIDE THIN FILMS

by
Ronald Birkhahn
Andrew J. Steckl

1. INTRODUCTION

Much work has been done with pulsed laser deposition (PLD) of SiC aiming for the ultimate goal of obtaining clean, epitaxial growth on substrates at low temperature. A list of references to the relevant literature is included with this report. To date, this has not been accomplished but several papers [Fenner(8), Rimai(17), Rimai(20)] have hinted at epitaxial growth. This "epitaxial" growth is primarily polycrystalline, sometimes including amorphous areas, with grain sizes on the order of tens of nanometers and exhibiting an oriented relationship with the substrate. The optimum growth temperatures associated with obtaining these polycrystalline "epitaxial" samples has been in the range of 800-1200°C. Most films have been grown on (001) or (111) Si substrates with one notable exception using 6H-SiC [Stan(23)]. Relatively few results have been published regarding the effect of the types of targets and laser energy. Many variables can affect the PLD growth of SiC: (a) laser parameters: energy, wavelength, pulse duration, repetition rate and deposition time; (b) substrate: type (Si, SiC), cleaning procedure, deposition temperature, and annealing. In this brief (2 month) project, we have attempted to explore a few of these parameters in our SiC PLD growth runs.

2. EXPERIMENTAL PROCEDURE

§2.1 PLD System Description

The PLD system is a high vacuum chamber designed for base pressures in the 10^{-7}-10^{-8} range. A backed turbo pump provides pressures to 10^{-6} at which time an ion getter pump takes over. The substrate and target are mounted along the long axis as seen in Fig. 1. Side ports are used for optical viewing, laser entry, sample exchange, and temperature measurement. The target is capable of rotation and the substrate stage contains the electrical feedthroughs for the molybdenum block heater capable of reaching a temperature of 1600°C. Fig. 2 shows a photograph of the high temperature stage with a Si substrate in place. We installed this high temperature stage to increase the capabilities of this PLD system, which was previously only able to run at room temperature. Fabrication of a new support cantilever was required as well as modification of the block heater to mount the small substrate samples. After installation, we

calibrated the stage temperature vs. input power from a high voltage power supply using an IRCON 2-color pyrometer (Fig.3). However, we experienced persistent problems in obtaining reliable temperature data for substrates mounted on the molybdenum block. Initial tests with the pyrometer and a chrome-alumel thermocouple attached to a piece of silicon on the heater yielded as much as a $300^{\circ}C$ discrepancy. Subsequent tests with the thermocouple attached to the Mo block showed ambiguous results after rotation of the substrate stage. During some PLD runs, the thermocouple was clipped to the substrate and yielded a consistent $300^{\circ}C$ difference compared to the pyrometer. This was probably due to three causes: 1) the substrate was not in full contact with the molybdenum block and presented a thermal transfer problem; 2) the pyrometer was limited by its field of focus and thus measured some of the glowing heater block; and 3) the thermocouple averaged temperature readings from the face of the substrate and the clip which acted as a heat sink. The temperature control itself, however, was consistent and reproducible.

§2.2 Sample Preparation and System Operation

Approximately 1x1 cm^2 samples used for deposition were first cleaned using standard RCA procedure for semiconductors using a base clean with NH_3OH and H_2O_2 and an acid dip of HCL and H_2O_2 at $70^{\circ}C$. The samples had a final HF dip before being clipped to the molybdenum heater and inserted in the chamber. The chamber was then pumped until a base pressure of low 10^{-7} or high 10^{-8} Torr is reached. Next, the sample is quickly ramped to deposition temperature and allowed to thermally equilibrate before deposition begins. A 248 nm Kr-Fl eximer laser provides the power to ablate the SiC target and to produce deposition onto the facing substrate. The laser pulses are introduced through a focusing and scanning mirror onto the target to simultaneously concentrate the power and provide a uniform deposition. The laser power was kept roughly constant for all experiments. The pulse has a 24 ns duration while the frequency is an adjustable parameter. The pulsed beam ablates the SiC target and the plume is ejected normal from surface, uniformly covering the substrate. The substrate temperature is monitored by the two-color IR pyrometer discussed above. The sample is allowed to cool after deposition and removed.

§2.3 Analysis and Characterization Equipment

After removal from the deposition chamber, the PLD layer thickness and morphology was determined by a Sloan Dektak profilometer and an optical microscope. The samples were also examined by a Philips x-ray diffractometer to determine the crystallinity of the layer and compared to previous θ-2θ rocking curves of the undeposited substrate.

3. EXPERIMENTAL RESULTS

§3.1 Experimental Conditions

Initially, we attempted PLD growth on (100) Si substrates. A second set of experiments utilized (111) Si substrates which had a single crystal 3C-SiC film grown on top. The (111) Si substrates were first carbonized at 1200°C and atmospheric pressure and then had 0.4 μm SiC film grown at 900°C and low pressure. These samples were grown in a CVD reactor at the University of Cincinnati. The other two types of samples used were 6H-SiC from Westinghouse (J23-#2) and Lely-grown 15R-SiC from Kiev, Ukraine. The organization of experiments is shown in Fig. 4.

As previously discussed in the introduction, there are many variables that could affect SiC PLD growth. The primary factors we investigated were substrate type, laser repetition rate, and temperature. During all runs the laser power was kept constant at around 230 mJ and the frequency of the laser was varied between 1 and 20 Hz. The duration of deposition was varied only to allow time for measurable SiC film to deposit. The temperature of the substrate during deposition was varied between 850 and 1200°C.

§3.2 Results and Discussion

The overall growth rate of the PLD samples varied according to the frequency of the laser. As shown in Table 1, the SiC growth rates per pulse were on the order of tenths of angstroms for the laser power utilized. This is extremely fast compared to CVD or MBE, corresponding to approximately 1mm per second of laser ablation time. A PLD study by Rimai et. al [17] reported growth rates on Si substrates using 300mJ per pulse and 800-1200°C temperatures to be still an order of magnitude larger at 2Å per pulse. The summation of all the data from the runs is listed in Table 1. The overall surface morphology determined by Dektak profilometry was fairly uniform with isolated peaks. Further examination of the PLD surface under an optical microscope revealed pits but an otherwise smooth surface layer.

The next step of analyzing the PLD films utilized the Philips x-ray diffractometer. Scans from initial PLD runs #1-3 on Si substrates had no x-ray peaks except for the substrate, indicating that the samples were amorphous in character. Figure 5 shows the results from the PLD runs on the 3C-SiC CVD growth on (111) Si. For comparison, the XRD scan in Fig. 5a was taken before PLD. All the graphs are drawn on the same scale and indicate the shifting and attenuation of the peak height with respect to the original. Run #5 (Fig. 5b) used a repetition rate of 10 Hz and substrate temperature around 850°C. Run #6 (Fig. 5c) decreased the rep rate to 5 Hz but kept the temperature of the substrate the same. The x-ray peak considerably flattened showing an amorphous character. This is a somewhat surprising result because it was expected that as you decrease the rep rate, the arriving Si and C atoms have sufficient time to rearrange on the surface to

form an oriented polycrystalline if not epitaxial film. This may have been an anomalous result considering that run #7 (Fig. 5d) had the same rep rate as #6 but a higher temperature and formed a considerably better film. A compilation of the x-ray scans of runs #5-7 are shown in Fig. 7. Note that these films are probably polycrystalline with an oriented relationship with the substrate. Another analytical technique such as transmission electron microscopy (TEM) would be necessary to confirm this.

Figure 7 displays for comparison all the PLD runs on SiC substrates along with x-ray diffraction on corresponding undeposited substrates. Run #9 exhibits a peak that is broader than the other scans for that type of substrate but the numerous amount of other peaks in the original and the scans after PLD do not allow us to draw many conclusions about the character of the films. It would appear that run #9 contained more polycrystallites. The results from the Lely-grown 15R-SiC were even more ambiguous. The original as well as the after growth sample had very sharp x-ray peaks (Fig.6d-e). A full x-ray scan of the sample (Fig. 7) revealed several peaks although the only conclusions we could draw were that there are peaks from a 15R-SiC substrate with possible evidence of 15R or 6H-SiC in a polycrystalline film. Since many of the peaks from the two different SiC polytypes overlap, it is necessary to use another analytical technique to determine the true character of the film. It is possible that an epitaxial single crystal film formed on the 15R substrate, but it is also possible that the PLD layer is completely amorphous. Both would present the same type of evidence by x-ray diffraction.

4. SUMMARY AND CONCLUSIONS

During our summer research program at Wright Patterson Air Force Base, we made progress investigating the validity of using pulsed layer deposition to deposit epitaxial films at reduced (or even room) temperatures. After installing the molybdenum heater stage to add the ability to heat the substrate during deposition, we proceeded with runs on different types of substrate under varying conditions and examined the results with x-ray diffraction. We were unable to make use of any other analytical techniques during the course of our brief stay to validate or reject the conclusions presented here. Results from those PLD runs are inconclusive at best and discouraging at worst. Gradually increasing the deposition temperature towards the 800-1200°C threshold for crystalline films found by others appeared to increase crystallinity. However, due to the discrepancy between our temperature measuring techniques for the substrate and block heater, we were unable to accurately and definitively determine true temperatures. The actual temperature might have been as much as 300°C lower that measured and would corroborate that it is not possible to attain epitaxial films below the threshold with these conditions. It is recommended that if research were to continue along this direction that the decisive answers be found for the inconclusive results (temperature, crystallinity) presented here before continuing.

REFERENCES

1.   Alunovic, M., *et al.*, *Description of transfer and depostition during PLD of thin ceramic films.* ISIJ International, 1994. **34**(6): p. 507-15.

2.   Balooch, M., *et al.*, *Deposition of SiC films by pulsed excimer laser ablation.* Applied physics letters, 1990. **57**(15): p. 1540-2.

3.   Blouin, M., *et al.*, *Atomic force microscopy study of the microroughness of SiC thin films.* Thin solid films, 1994. **249**: p. 38-43.

4.   Boily, S., *et al.*, *SiC membranes for x-ray masks produced by laser ablation deposition.* Journal of vacuum science & technology. b, 1991. **9**(6): p. 3254-7.

5.   Bourdelle, K.K., *et al.*, *Melting and damage production in silicon carbide under pulsed laser irradiation.* Phys. Stat. Sol., 1990. **121**: p. 399-406.

6.   Capano, M.A., *et al.*, *Pulsed laser deposition of silicon carbide at room temperature.* Applied physics letters, 1994. **64**(25): p. 3413-5.

7.   Chen, M.Y. and P.T. Murray, *Deposition and characterization of SiC and cordierite thin films grown by pulsed laser evaporation.* Journal of Materials Science, 1990. **25**: p. 4929-32.

8.   Fenner, D.B., *et al.*, *Pulsed laser deposition of cadmium telluride, mercury cadmium telluride and beta-silicon carbide thin films on silicon.* Mat. Res. Soc. Symp. Proc., 1992. **268(Materials Modification by Energetic Atoms and Ions)**: p. 235-40.

9.   Greenwood, P.F., G.D. Willett, and M.A. Wilson, *Mixed silicon carbide clusters studied by laser ablation Fourier transform ICR mass spectrometry.* Organic Mass Spectrometry, 1993. **28**: p. 831-40.

10.   Jean, A., *et al.*, *Biaxial Young's modulus of silicon carbide thin films.* Applied physics letters, 1993. **62**(18): p. 2200-2.

11.   Katayama, S., N. Fushiya, and A. Matsunawa, *Laser Physical Vapor Deposition of Si3N4 and SiC, and Film Formation Mechanism.* Transactions of JWRI, 1994. **23**(2): p. 181-9.

12.   Martin-Gago, J.A., *et al.*, *Electron loss spectroscopy study of the growth by laser ablation of ultra-thin diamond-like films on Si(100).* Surface Science Letters, 1992. **260**: p. L17-23.

13.   Mizunami, T., N. Toyama, and T. Uemura, *Optical emission spectroscopy of ArF-laser-irradiated disilane-acetylene mixtures for 3C-SiC epitaxial growth.* Journal of Applied Physics, 1993. **73**(4): p. 2024-6.

14.   Noda, T., *et al.*, *Formation of polycrystalline SiC film by excimer-laser chemical vapour deposition.* Journal of materials science letters, 1992. **11**: p. 477-8.

15.   Noda, T., *et al.*, *Microstructure and growth of SiC film by excimer laser chemical vapour deposition at low temperatures.* Journal of Materials Science, 1993. **28**: p. 2763-8.

16.   Pehrsson, P.E. and R. Kaplan, *Excimer laser cleaing, annealing, and ablation of Beta-SiC.* Journal of materials research, 1989. **4**(6): p. 1480-90.

17.   Rimai, L., *et al.*, *Preparation of Oriented Silicon Carbide Films by Laser Ablation of Ceramic Silicon Carbide Targets.* Applied physics letters, 1991. **59**(18): p. 2266-8.

18.   Rimai, L., *et al.*, *Pulsed layer deposition of SiC films on fused silica and sapphire substrates.* Journal of Applied Physics, 1993. **73**: p. 8242-9.

19.   Rimai, L., *et al.*, *Deposition of thin films of silicon carbide on fused quartz and on sapphire by laser ablation of ceramic silicon carbide targets.* Mat. Res. Soc. Symp. Proc., 1993. **285(Laser Ablation in Materials Processing)**: p. 495-500.

20.   Rimai, L., *et al.*, *Preparation of crystallographically aligned layers of silicon carbide by pulsed laser deposition of carbon onto Si wafers.* Applied physics letters, 1994. **65**(17): p. 2171-3.

21.   Rimai, L., *et al.*, *Deposition of epitaxially oriented films of cubic silicon carbide on silicon by laser ablation: Microstructure of the silicon-silicon- carbide interface.* Journal of Applied Physics, 1995. **77**(12): p. 6601-8.

22.   Scholz, M., W. FuBeta, and K.-L. Kompa, *Chemical vapor deposition of silicon carbide powders using pulsed CO2 lasers.* Advanced materials, 1993. **5**(1): p. 38-40.

23.   Stan, M.A., *et al.*, *Growth of 2H-SiC on 6H-SiC by pulsed laser ablation.* Applied physics letters, 1994. **64**(20): p. 2667-9.

24.   Suzuki, H., H. Araki, and T. Noda, *Effect of Incident Direction of ArF Laser to Graphite Substrates on the Formation of Photo-Chemical Vapor Deposition SiC Film.* Japanese journal of applied physics, Part 1, R, 1993. **32**(8): p. 3566-71.

25.   Suzuki, H., H. Araki, and T. Noda, *Microstructure of SiC thin films produced on graphite by excimer-laser chemical vapour deposition.* Journal of materials science letters, 1994. **13**: p. 49-52.

26.   Tench, R.J., *et al.*, *Clusters formed in laser-induced ablation of Si, SiC, Pt, UO2 and evaporation of UO2 observed by laser ionization time-of-flight mass spectrometry and scanning tunneling microscopy.* Journal of vacuum science & technology. b, 1991. **9**(9): p. 820-4.

27.   Zehnder, T., A. Blatter, and A. Bachli, *SiC thin films prepared by pulsed excimer laser deposition.* Thin solid films, 1994. **241**: p. 138-41.

28.   Zehnder, T., *et al.*, *Tribological properties of laser deposited   SiC coatings.* Mat. Res. Soc. Symp. Proc., 1994. **343(Polycrystalline Thin Films: Structure, Texture, Properties and Applications)**: p. 621-6.

Table 1: Summary of SiC PLD growth conditions.

Sample #	Run Date	Substrate Type	SUBSTRATE DEPOSITION				PLD CONDITIONS				SiC Thickness		Remarks
			Cleaning	Carboniz	SCB	SiC thick	Energy(mJ)	Rep-rate(Hz)	Time(min)	Temp(°C)	Total(μm)	Per Pulse(μm)	
1	8/7/95	Si (100)	RCA				240	10	30	938^1	0.5-1.0	4.2×10^{-5}	No XRD
2	8/8/95	Si (100)	RCA				210	20	60	938^1	1.0-3.0	2.8×10^{-5}	No XRD
3	8/9/95	Si (100)	RCA				---	10	60	850^2			Off-center
4	8/10/95	Si (100)	RCA				---	10	60	848^2	0.8-1.6	3.3×10^{-6}	
5	8/17/95	Si (111)	RCA	AP-1300	LP-900	0.4μm	200	10	60	850^2	0.7-0.8	2.0×10^{-5}	
6	8/22/95	Si (111)	RCA	AP-1300	LP-900	0.4μm	230	5	60	823^2	0.3-1.0	4.0×10^{-5}	
7	8/23/95	Si (111)	RCA	AP-1300	LP-900	0.4μm	230	5	60	938^2	0.5-0.9	4.0×10^{-5}	
8	8/25/95	Si (111)	RCA	AP-1300	LP-900	0.4μm	230	1	90	930^2	0.4-3.6	6.7×10^{-5}	
9	8/29/95	6H-SiC[3]	RCA				230	1	90	924^2	0.3-0.4	6.7×10^{-5}	
10	8/30/95	6H-SiC[3]	RCA				230	1	90	1191^2	0.2-0.3	3.3×10^{-5}	
11	8/31/95	15R-SiC[4]					230	1	90	1196^2	0.1-0.2	2.8×10^{-5}	

1 Measured with pyrometer aimed at block
2 Measured with pyrometer aimed at substrate
3 J23-#2 Westinghouse:WPAFB
4 Lely crystal grown in Kiev, Ukraine
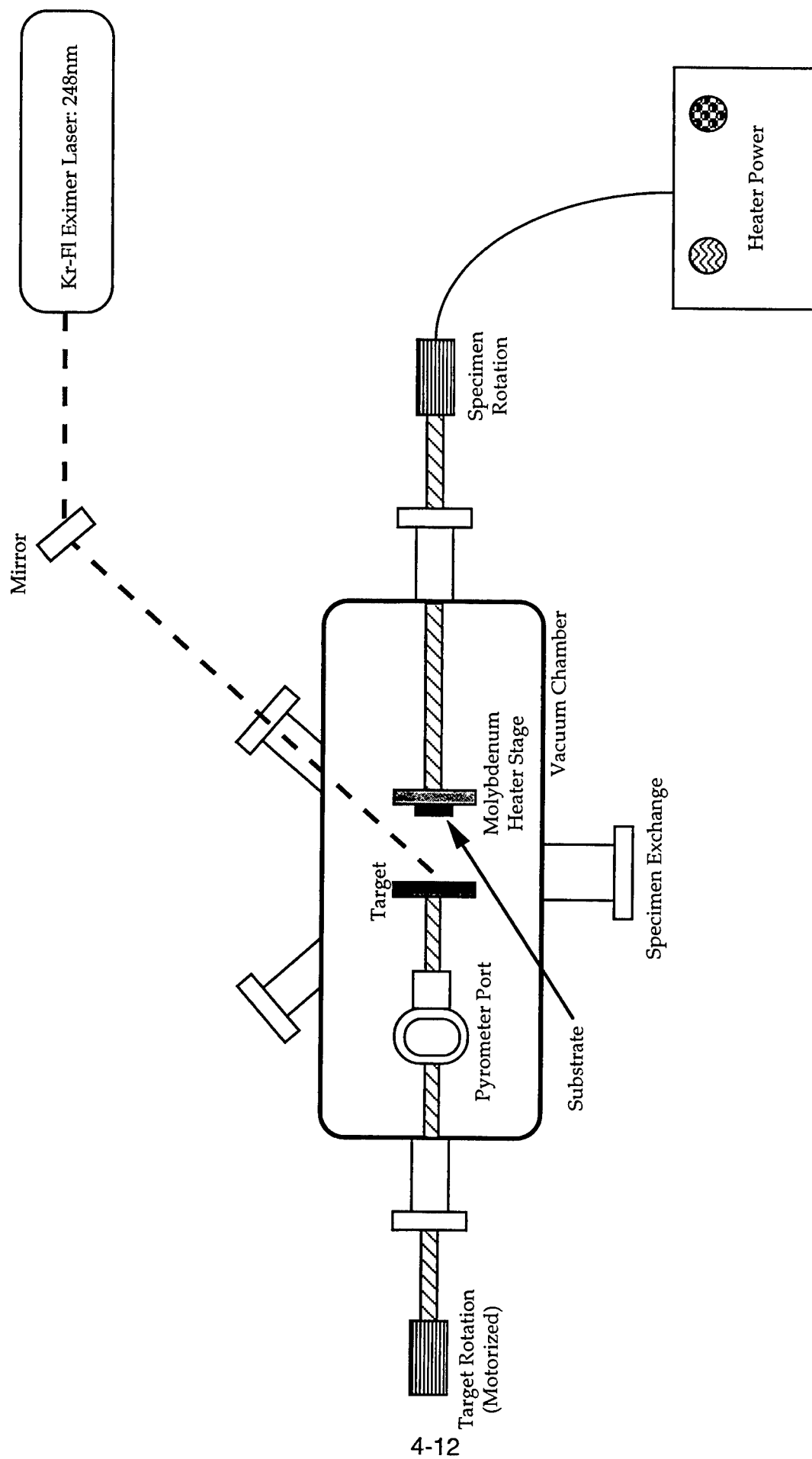
Figure 1: Pulsed Laser Deposition System

Kr-Fl Eximer Laser: 248nm

Mirror

Heater Power

Specimen Rotation

Molybdenum Heater Stage

Vacuum Chamber

Target

Specimen Exchange

Pyrometer Port

Substrate

Target Rotation (Motorized)

4-12
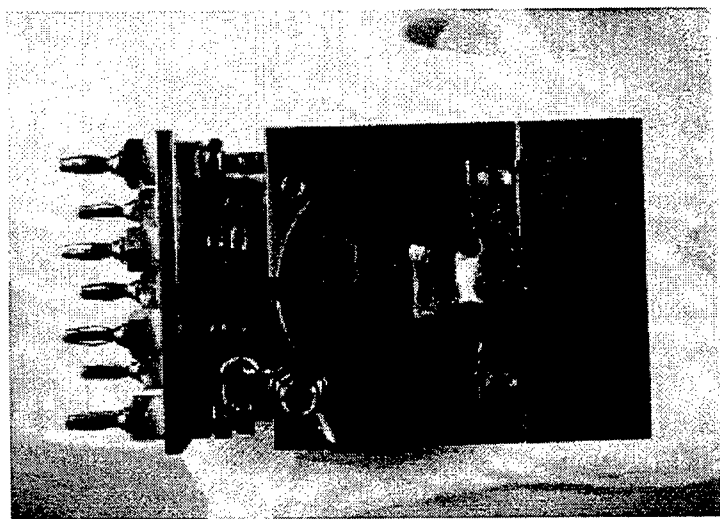
(a)
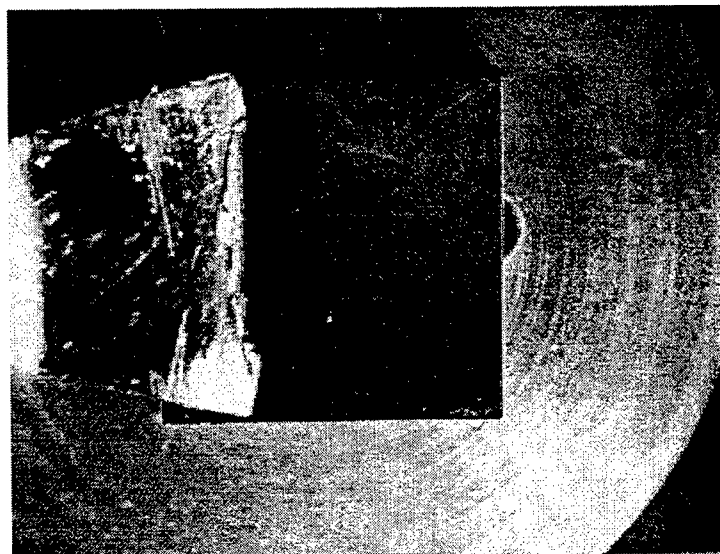
(b)

Figure 2: (a) Photo of high temperature heater stage with substrate and (b) close-up of substrate holder with sample.
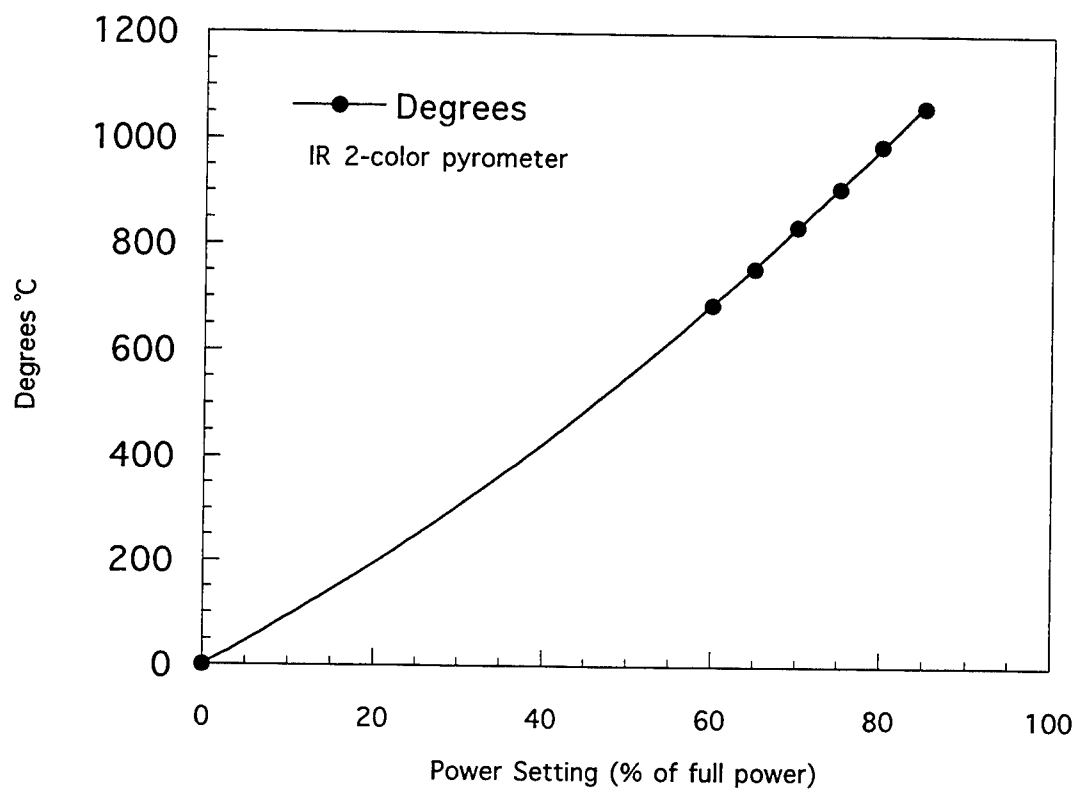
Figure 3: Molybdenum stage temperature vs. input power

Pulsed Laser Deposition
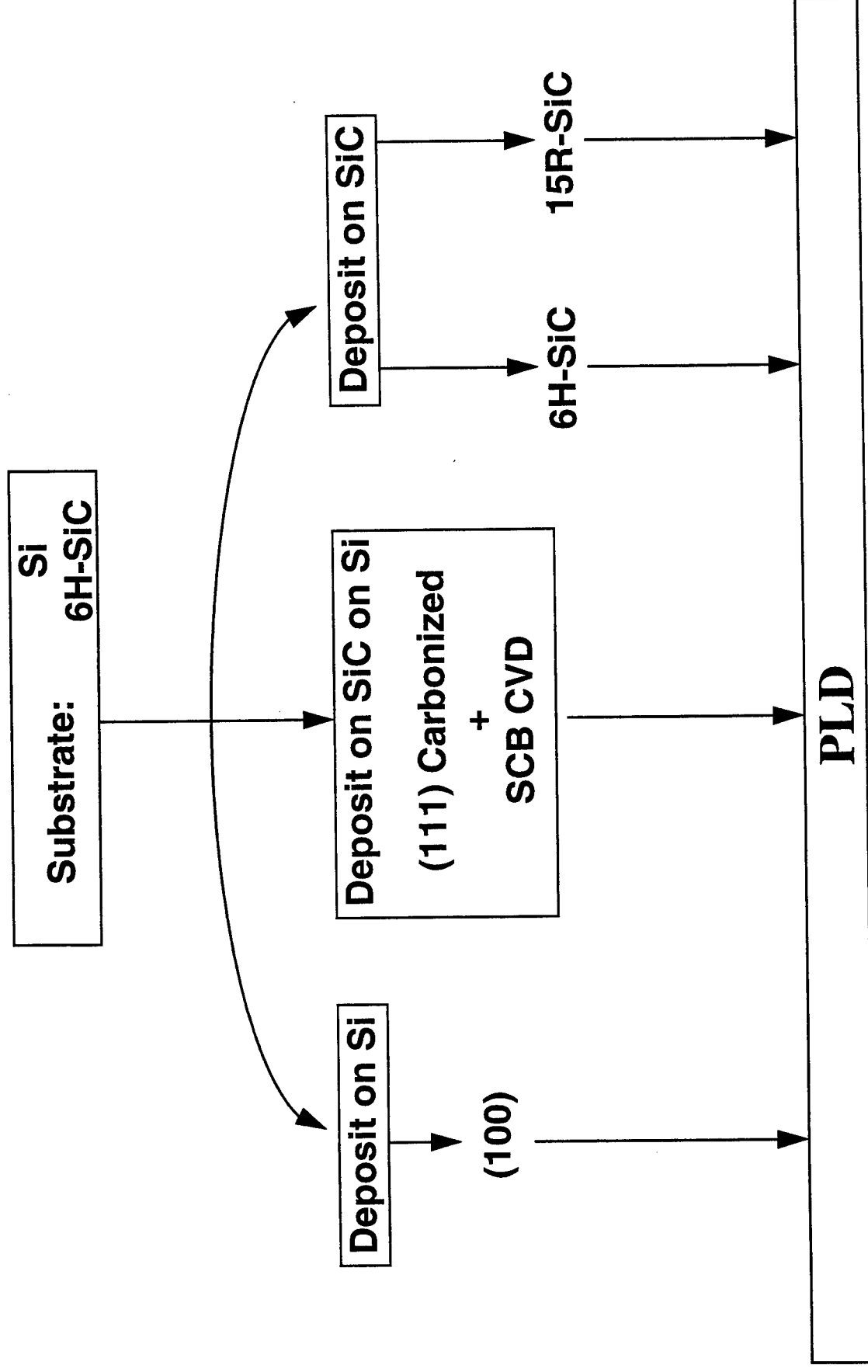
Figure 4: Organization of PLD experiments

4-15
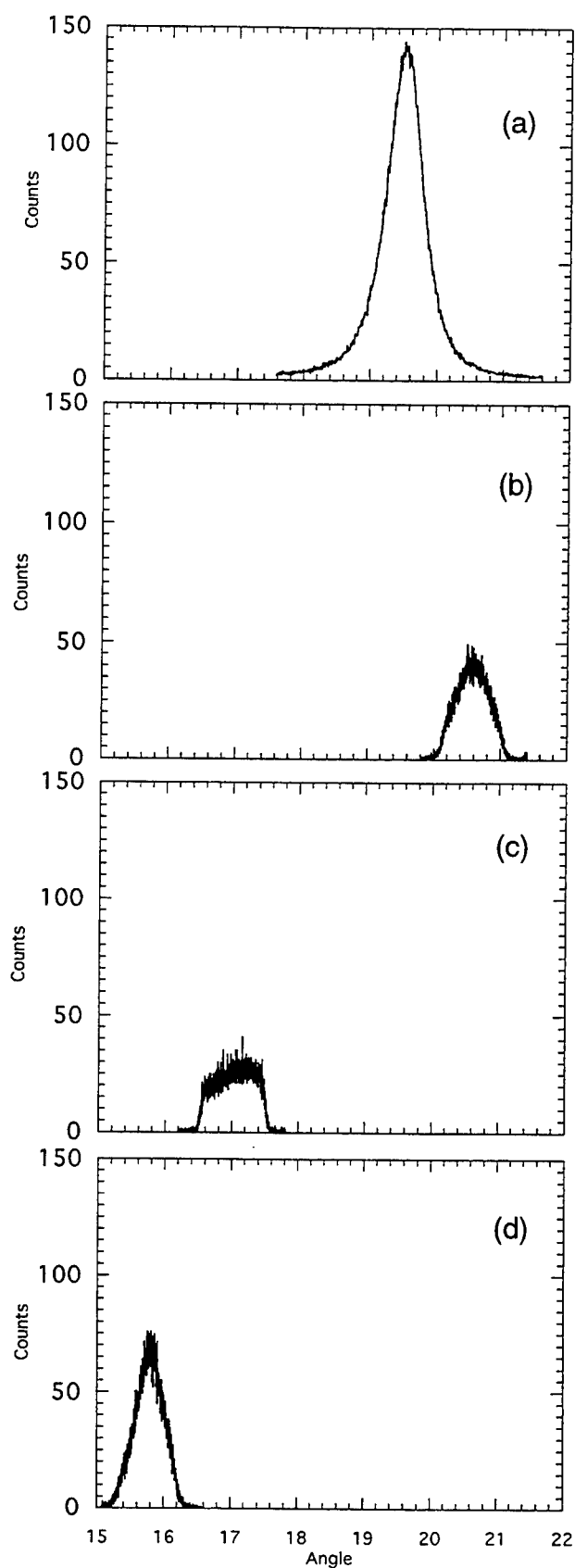
Figure 5: X-ray data from PLD runs on SiC on (111) Si:
(a) Substrate type A1 consisting of (111) carbonized with low pressure 3C-SiC growth before PLD deposition
(b) Run #5 on A1-(111) Si
(c) Run #6 on A1-(111) Si
(d) Run #7 on A1-(111) Si
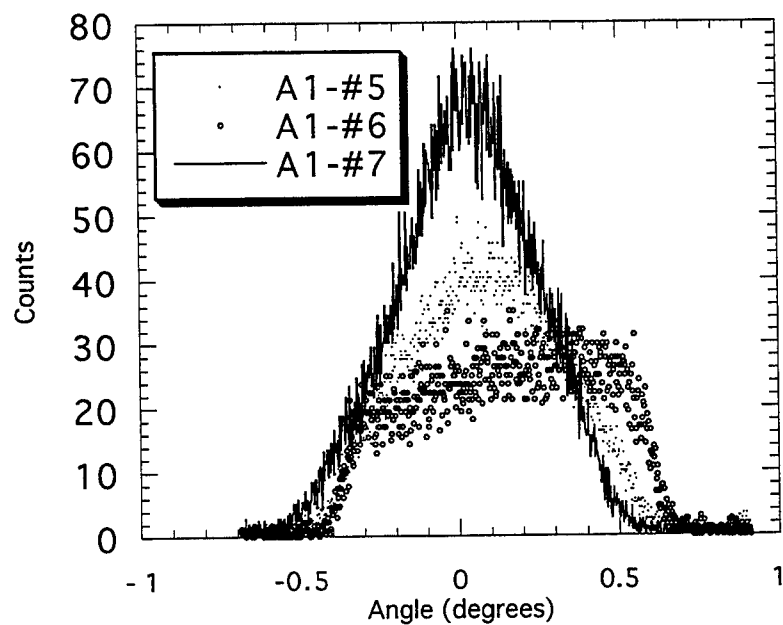
Figure 6: Runs 5-7 on (111) Si substrate
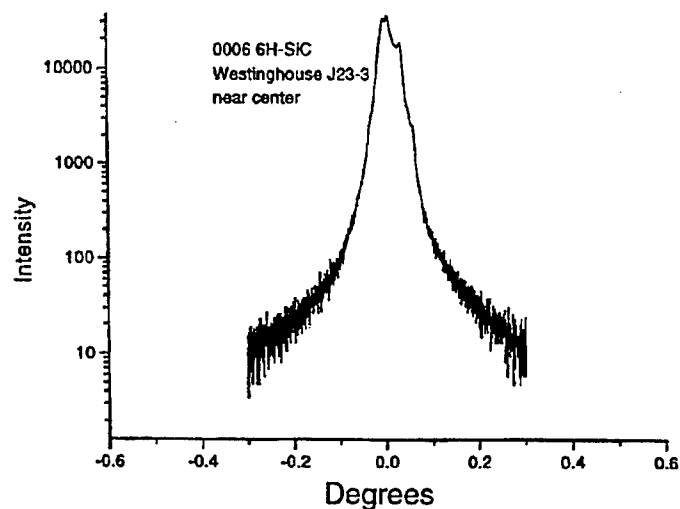
(a) XRD of 6H-SiC substrate grown by Westinghouse before PLD deposition runs #10 &11.
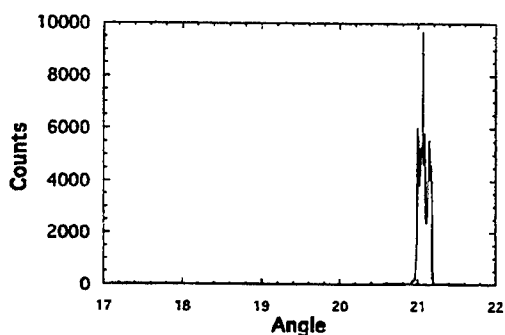
(b) Run #9 on 6H-SiC
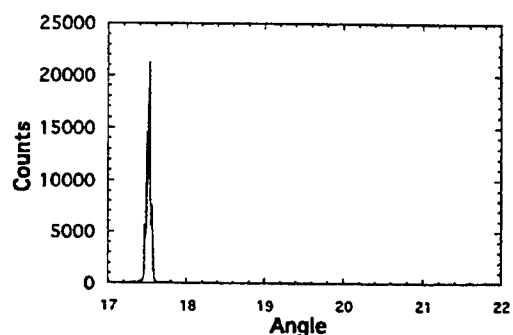
(c) Run #10 on 6H-SiC
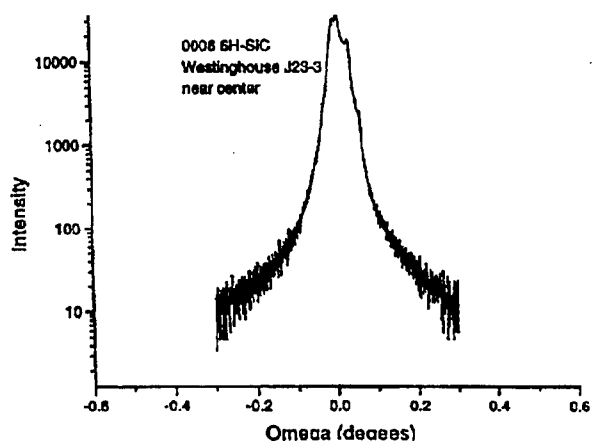
(d) Initial XRD of Lely-grown 15R-SiC
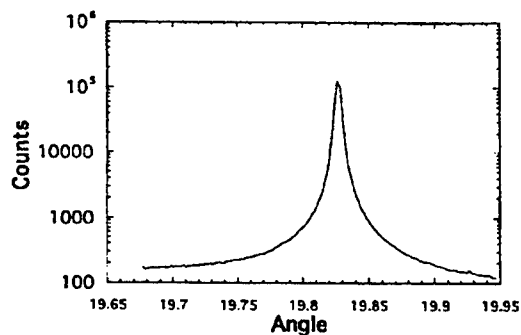
(e) Run #11 on 15R-SiC (Lely)

Figure 7: X-ray data from PLD growth runs on SiC substrates
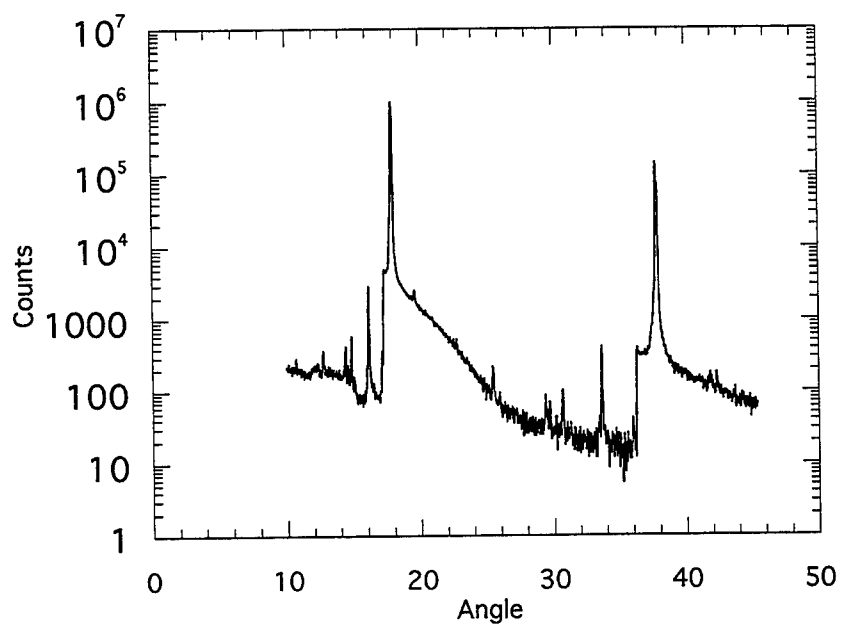
Figure 8: Large angular scan of PLD on
Lely-grown 15R-SiC substrate

FINITE ELEMENT MODELING OF JET ENGINE FAN BLADES

Jason Blair
Graduate Student
Department of Mechanical and Materials Engineering

Wright State University
Department of Mechanical and Materials Engineering
Dayton, OH 45435

August 1995

Finite Element Modeling of Jet Fan Engine Blades

Jason Blair
Graduate Student
Department of Mechanical and Materials Engineering
Wright State University

Abstract

Modeling of F100 jet engine third stage compressor fan blade was studied. A solid model of the fan blade was generated and its mode shapes and natural frequencies were determined. The model was processed using both MSC/PAL and MSC/NASTRAN for comparison. The results were in agreement to within 10%. A generic eight bladed hub assembly model was also constructed. It was created for use in the studying of component mode synthesis. This model was modified in three stages to fine tune the design.

Finite Element Modeling of Jet Engine Fan Blades

Jason Blair

Introduction

In the Spring of 1995, a problem due to high cycle fatigue in the fan blades of F100 jet engines caused the entire F-15 fleet to be grounded for several weeks. This event prompted the Air Force to initiate a study of high cycle fatigue failure and to determine what steps could be taken to elevate the problem. In modeling this phenomena, finite element analysis was used. Finite element analysis is a computer modeling procedure in which a model is discretized into small elements and dynamical analysis is performed on the individual elements. This procedure provides the natural frequencies and mode shapes of the model. This results are used in conjunction with experimental results to fine tune the model. This fine tuned model then can be exposed to different varying forces and their effects can accurately be predicted.

Pratt and Whitney Model

A geometry model of a Pratt and Whitney F100 third stage compressor blade was obtained. This model was imported into LAPCad, a finite element preprocessor, and elements were assigned to the 822 grid points of the geometry file. (fig. 1) The entire model was meshed and 368 HEX elements were used. Titanium Ti406 was assigned to all of the elements. The base of the blade was restricted in its movement, allowing no rotation or translation. This simulated clamping of the blade. This was done to model the experimental setup that was used to obtain the natural frequencies. In the experimental setup, the fan blade was clamped in a machinist's vise and excited with piezoceramics.
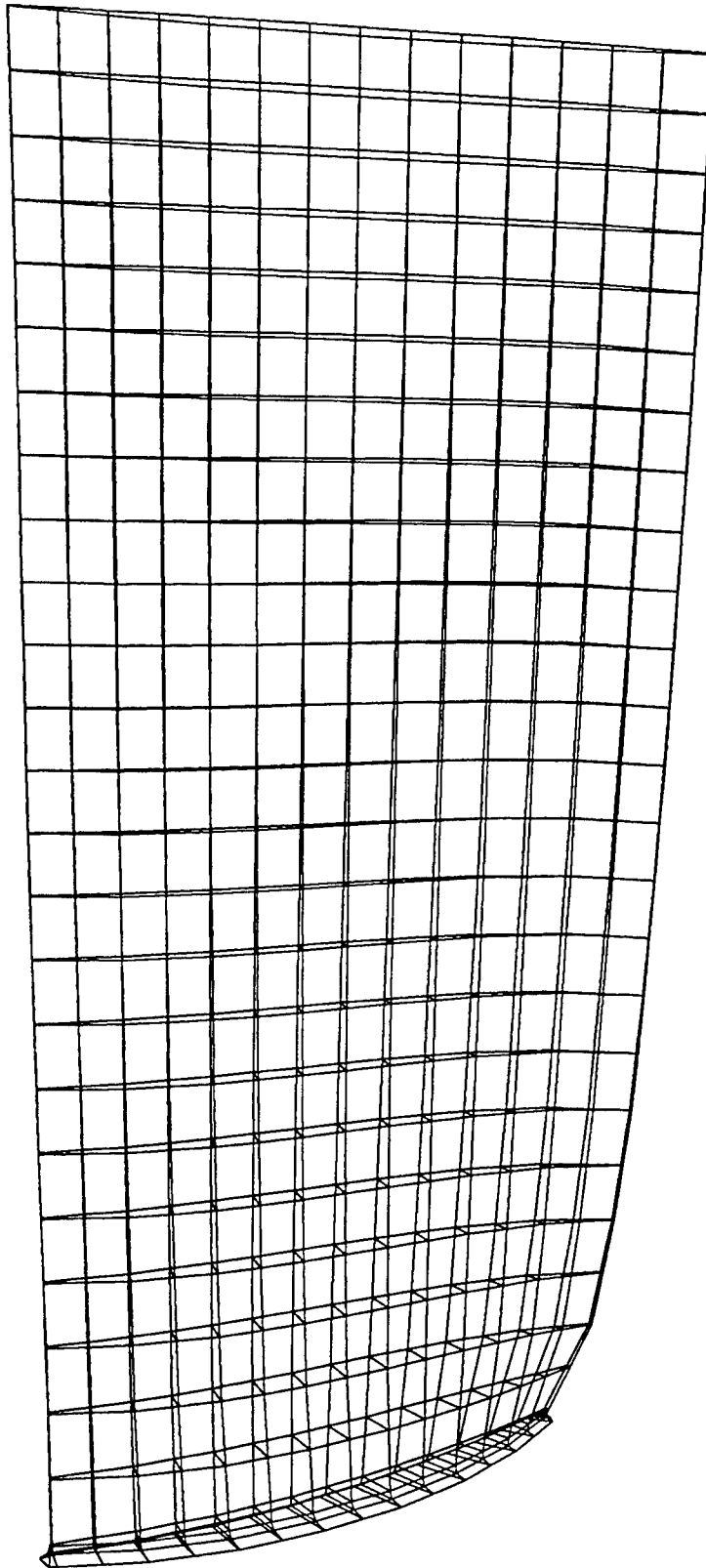
The following is a condensed version of the MSC/PAL model. The nodal geometry

definitions are first, followed by the connectivities and the boundary conditions.

```
TITLE Pratt2.mdl
C
C Geometry
C
NODAL POINT LOCATIONS 1
    1 -0.35260 -0.21132  5.99445
    2 -0.36268 -0.21149  5.99345
    3 -0.33694  0.18373  5.97375
    4 -0.39610  0.18261  5.96795
    5 -0.32488  0.57931  5.95265
    6 -0.41732  0.57800  5.94345
    7 -0.31819  0.97493  5.93095
    8 -0.42754  0.97396  5.92015
    9 -0.31790  1.37060  5.90866
   10 -0.42736  1.37004  5.89775 ...

C
C Connectivities
C
C lapcadlayer   1   1  unnamed1
MAT 1.650E+07  6.200E+06  4.170E-04  3.300E-01  0.000E+00  7.100E-06  7.000E+01 c Mtrl8
HEXA ELEMENT
CONNECT  213  215  216  214  193  195  196  194
HEXA ELEMENT
CONNECT  233  235  236  234  213  215  216  214
HEXA ELEMENT
CONNECT  249  251  252  250  229  231  232  230 ...

 ZEROS 1
ALL 255, 256, 257, 258 ...

END DEFINITION
```

The model had the following first ten natural frequencies:

Mode Number	Natural Frequency (Hz)
1	190
2	808
3	900
4	1675
5	2368
6	2726
7	4037
8	4377
9	4881
10	5971

The corresponding mode shapes are shown in figures 2,3,4. The color on the mode shapes represents relative displacement. To verify this results, a laser vibrometer was used to experimentally measure the mode shapes. A set of piezoceramics was used to excite and measure the natural frequencies. The finite element model results were found to be within 10% of the experimental results.

Generic Bladed Hub Assembly Model

During the course of studying the high cycle fatigue problem, it was noted that blade mistuning may have an impact on mode localization. The effects of mistuning were seldom modeled in current finite element models. A method of modeling that can account for mistuning is component mode synthesis. To verify mistuning a generic bladed hub
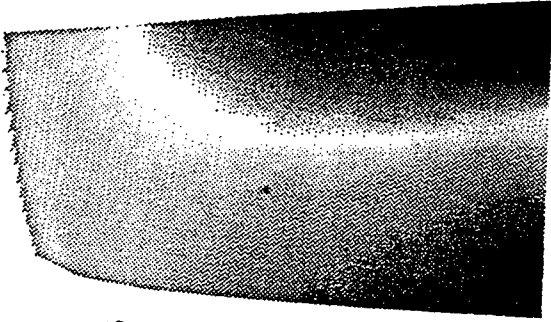
900 Hz
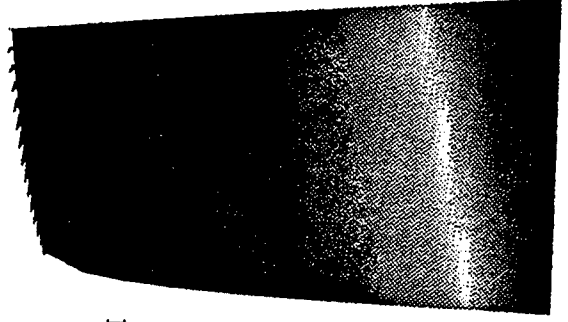
190 Hz
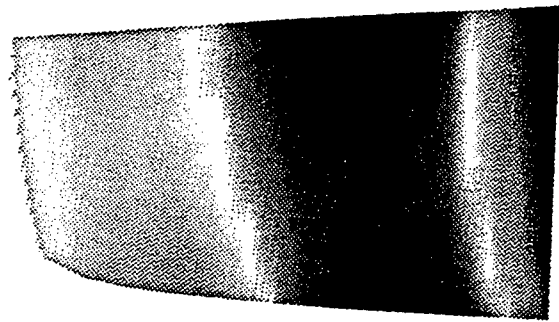
1675 Hz
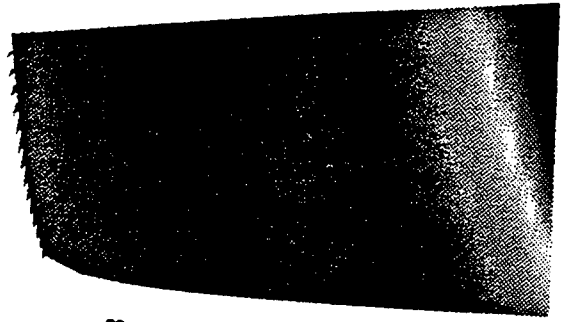
808 Hz
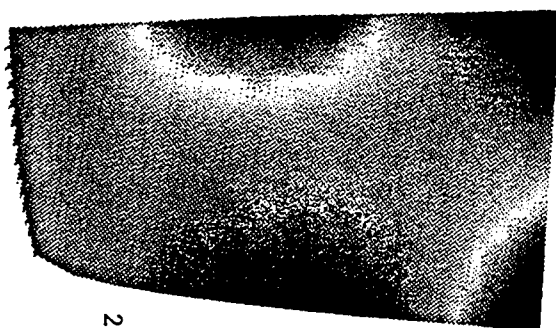
4037 Hz

2368 Hz
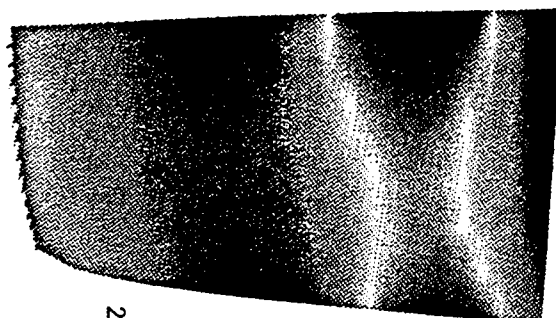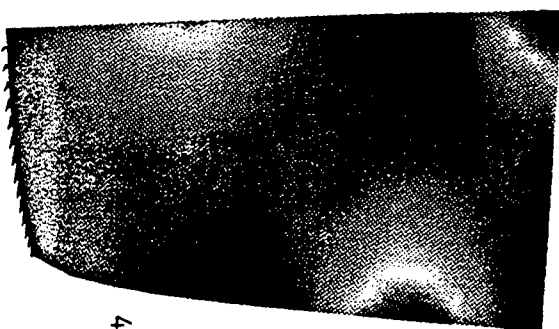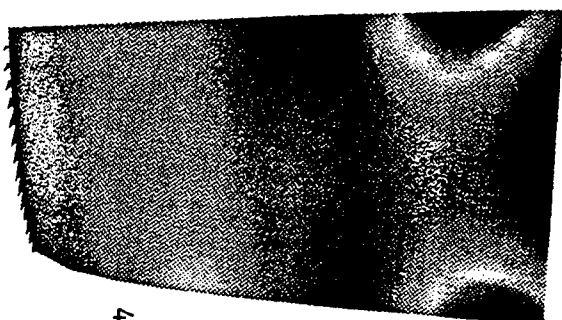
4377 Hz

2726 Hz
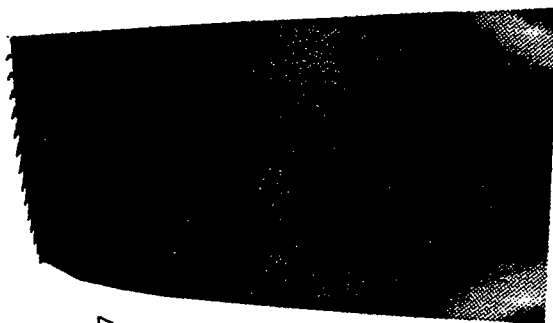
4881 Hz
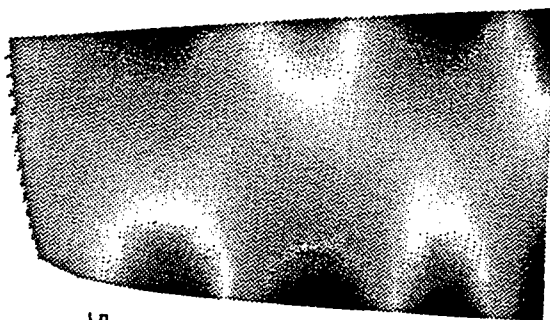
5971 Hz

assembly model was proposed. This model has a 12 inch blade tip to blade tip diameter. It is made up of eight symmetrically placed blades on a one inch thick central hub. (fig. 5) Each of the blades is one inch long and 0.5 inches thick. The blades taper from the root of the blade to a constant cross section that is 75% as wide and 50% as thick as the root element of the hub. This tapering occurs over the first element at the root of the blade.
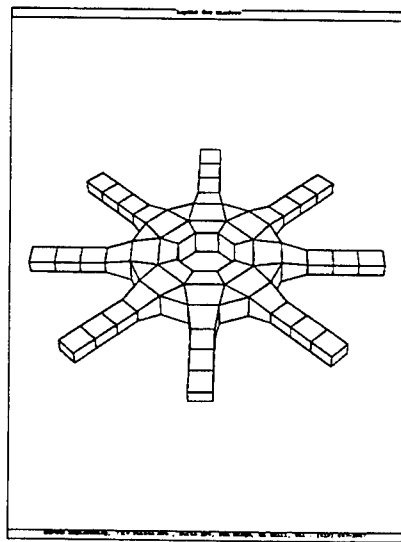
Fig. 5

This model has 192 nodes and is composed of 48 HEXA elements and 8 PENTA elements. Aluminum was used for the material and the boundary conditions were clamped at the inside of the hub for all rotations and translations. After examining the natural frequencies of this model, it was decided that the blades needed to be thinner. A new model was constructed in LAPCad. This model has a 0.5 inch thick blade. To keep the aspect ratio of the elements within two, the number of elements was increased to 160

HEXA and 16 PENTA. (Fig.6) This model tapers to a constant blade cross section over two rows of elements.
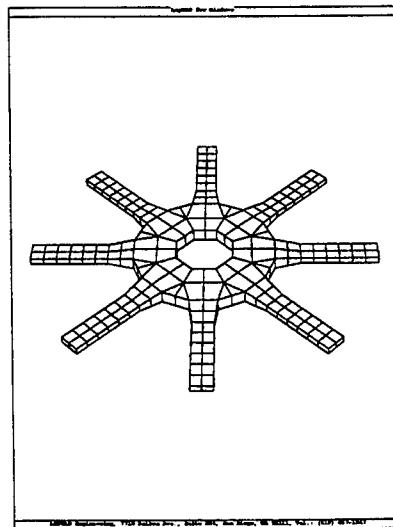
Fig. 6

This model also used aluminum for material and was clamped at the inside of the hub for all rotations and translations. This model had improved natural frequencies but, it was still not exhibiting the desired response. A third model was created to more accurately predict the response. A 45 degree twist was added to the root of the blade and the blade thickness was reduced to 0.25 inches. This was done to conform to a conventional bladed disk assembly. This twist gives the blade more stiffness at the root and increases the natural frequencies. This model also has a thinner hub and more elements. There are three layers of elements in the hub, each having a 0.25 inch thickness. (Fig. 7) This model was again constructed of aluminum and had the same boundary conditions as the previous models. The results of the dynamical analysis of this model were the best of the three models created thus far. To further improve the model, it was decided to lower the

modulus of elasticity and the density of the blades. This had the effect of decreasing the

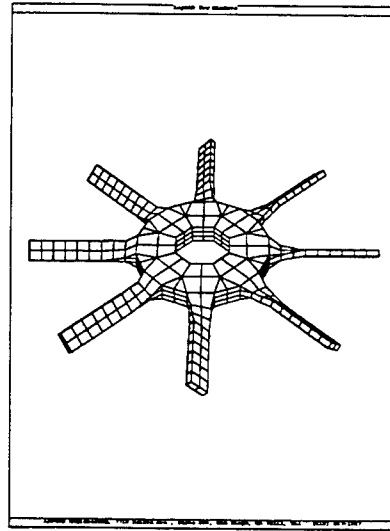stiffness of the blades compared to the hub.

Fig. 7

The decrease in properties was done in two cases to compare with the uniform property

case. The modulus of elasticity and density of aluminum were decreased by a factor of 0.1

and 0.31. The natural frequencies of the first ten modes are tabulated on the next page.

		Frequencies (Hz)	
Mode Number	Unmodified Properties	Modified by 0.1	Modified by 0.31
1	477.352	475.017	468.291
2	477.353	475.019	468.294
3	477.355	475.038	468.458
4	477.358	475.040	468.522
5	477.376	475.078	468.525

		Frequencies (Hz)	
Mode Number	Unmodified Properties	Modified by 0.1	Modified by 0.31
6	477.532	475.618	470.446
7	477.535	475.621	470.449
8	477.623	475.9	471.315
9	1260.6	1237.40	1175.74
10	1261.02	1240.09	1183.82

The above natural frequencies are grouped in eights. This is due to the fact that we have an eight bladed symmetrical hub assembly. The above chart demonstrates that the variation in each group of frequencies decreases as the blades become less stiff. This is the desired result. The MSC/PAL files are listed at the end of this report.

Conclusions

Several finite element models were generated and analyzed. A Pratt and Whitney F100 solid model was created and natural frequencies and mode shapes were created. These had an excellent agreement with available experimental data. Generic eight bladed hub assemblies were generated and analyzed. Modification of the geometry and material properties allowed the model to be fine tuned to a point where it could be used for component mode synthesis.

Acknowledgments

I would like to thank Dr. Joe Hollkamp, Bob Gordon and Doug Henderson for all of their help this summer.

```
TITLE c:\Slater.mdl
C
C Geometry
C
NODAL POINT LOCATIONS 1
    1 5.76537 6.84776 0.000E+00
    2 4.23463 6.84776 0.000E+00
    3 4.23463 6.84776 1.00000
    4 5.76537 6.84776 1.00000
    5 3.15224 5.76537 0.000E+00
    6 3.15224 5.76537 1.00000
    7 3.15224 4.23463 0.000E+00
    8 3.15224 4.23463 1.00000
    9 4.23463 3.15224 0.000E+00
   10 4.23463 3.15224 1.00000
    .
    .
    .

  190 5.45922 3.89135 1.00000
  191 6.10865 4.54078 0.000E+00
  192 6.10865 4.54078 1.00000

C
C Connectivities
C
C lapcadlayer    1    1 unnamed1
MAT 1.600E+07 5.970E+06 4.200E-04 3.400E-01 0.000E+00 7.100E-06 7.000E+01 c Titan
HEXA ELEMENT
CONNECT  137 133 136 140 138 134 135 139
HEXA ELEMENT
CONNECT  133 129 132 136 134 130 131 135
HEXA ELEMENT
CONNECT  129  66  65 132 130  68  67 131
    .
    .
    .

PENTA ELEMENT
CONNECT   38  10  40  37   9  39
PENTA ELEMENT
CONNECT   42  12  44  41  11  43

ZERO 1
ALL 177,178,179,180,181,182,183,184,185,186,187,188,189,190,191,192

END DEFINITION
```

SYNTHESIS OF NOVEL SECOND ORDER NONLINEAR OPTICAL MATERIALS

Lawrence L. Brott

Graduate Student

Department of Materials Science and Engineering

497 Rhodes Hall

University of Cincinnati

OH 45221-0012

Final Report for:

Graduate Student Research Program

WL/MLBP

Wright Patterson AFB

September 1995

SYNTHESIS OF NOVEL SECOND ORDER NONLINEAR OPTICAL MATERIALS

Lawrence L. Brott

Department of Materials Science and Engineering

University of Cincinnati

ABSTRACT

Synthesis of second order nonlinear optical (NLO) polymers represents an exciting field with the resulting chromophore containing materials being used in such devices as frequency doublers or electro-optical computers. In this research, a novel NLO chromophore is developed by incorporating a fluorene molecule in its backbone with thiophene and pyridine end groups that act as electron donating and withdrawing groups respectively. Long alkyl chains are attached to the C-9 carbon on the fluorene backbone to aid in the chromophore's solubility in the host polymer.

SYNTHESIS OF NOVEL SECOND ORDER NONLINEAR OPTICAL MATERIALS

Lawrence L. Brott

Department of Materials Science and Engineering

University of Cincinnati

INTRODUCTION

Interest in second order nonlinear optical (NLO) polymers has increased dramatically in the past few years as potential applications (for example, frequency doublers, optical switches, or electro-optical computers) begin to be realized [1,2]. Second order NLO compounds have multiple double bonds between electron donor and acceptor groups. Present polymers however still lack the nonlinearity and stability that are necessary for them to be used commercially. The objective of this research is to design a new fluorene-containing compound for a chromophore (**1**) for the use by the U.S. Air Force that will optimize nonlinearity while remaining thermally and structurally stable.
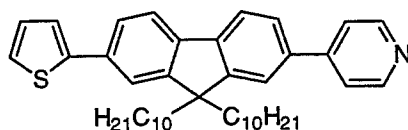
1   Fluorene-containing Chromophore

EXPERIMENTAL DETAILS

PREPARATION OF THE FLUORENE BACKBONE

The central building block of the chromophore (**1**) is the fluorene molecule. To make it more soluble and easier to handle, two long alkyl chains were added to the C-9 position of the fluorene. This approach allowed the C-2 and C-7 carbons to still be sterically unhindered and

reactive. As seen in Scheme I, fluorene was first treated with BuLi, complexed with TMEDA [3,4], and then treated with bromodecane to obtain monoalkylated fluorene. The monoalkylated fluorene, without isolation and purification, was further reacted with a second equivalent of BuLi and bromodecane to obtain dialkyl compound **3**. The product was purified by column chromatography followed by distillation under reduced pressure to remove any residual bromodecane.

SCHEME I
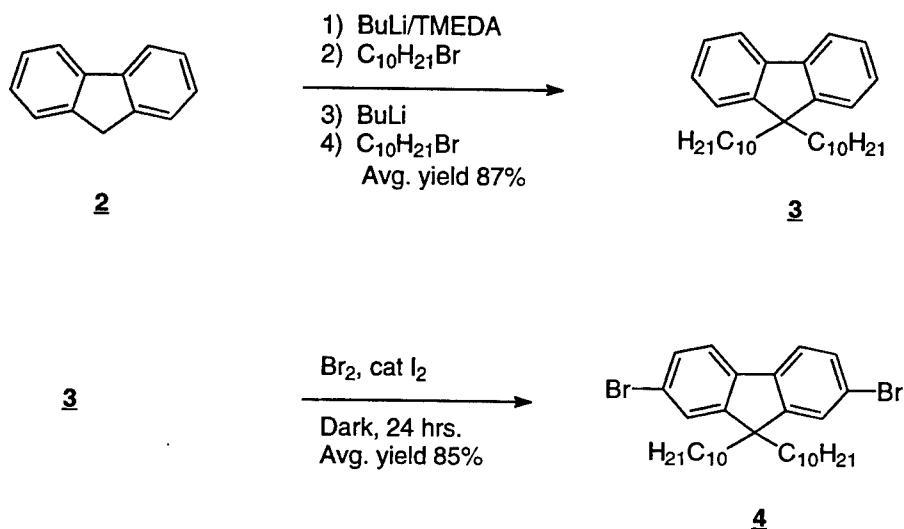
The next key step was to synthesize 2,7-dibromofluorene **4**. Compound **3** was reacted with bromine in the presence of a small amount of iodine and in the complete absence of light. The dibromofluorene **4** was then purified by column chromatography.

ARYL COUPLING

The thiophene and pyridine end groups are attached to the dibromofluorene **4** by a reaction as shown in Scheme II [5,6]. In this process, a (tributylstannyl)aryl **5** is reacted with the dibromofluorene **4** in the presence of a palladium catalyst to produce a coupled product.
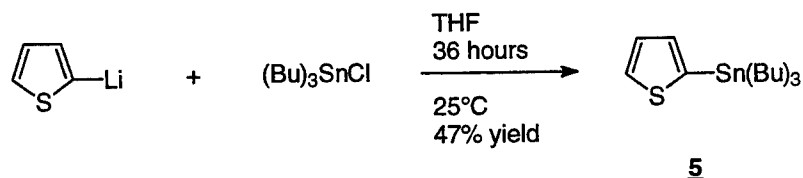
SCHEME II
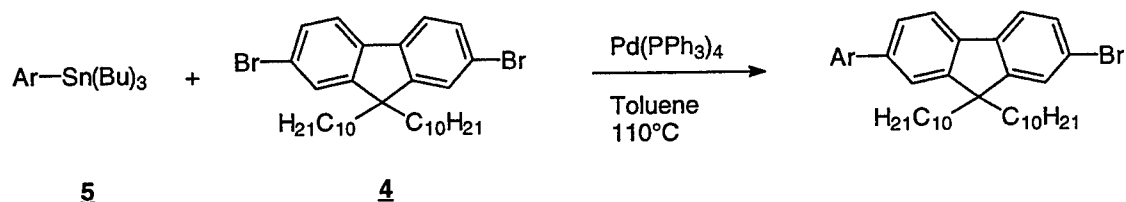
THIOPHENE STANNATION

The chromophore incorporates two different groups that act as electron donors and acceptors. In this research, a thiophene ring will act as the donor while the pyridine ring will be the acceptor. Consequently, two new products needed to be synthesized. Scheme III describes the preparation of the thiophene compound.

SCHEME III

In order to remove any unreacted tin compound, the THF was rotavaped off, and then hexanes added. An aqueous potassium fluoride solution was added to the flask and stirred vigorously for an hour. The layers were separated with the organic layer being dried with $MgSO_4$, filtered, and the product was then purified by column chromatography.

PYRIDINE STANNATION

The pyridine stannation is similar to the thiophene work-up, except that the 4-bromopyridine hydrochloride must be neutralized and lithiated before the tributyltin chloride

6-5

can be added. Both of these objectives can be achieved by adding two equivalents of butyl lithium as described in Scheme IV.

SCHEME IV

$$6$$
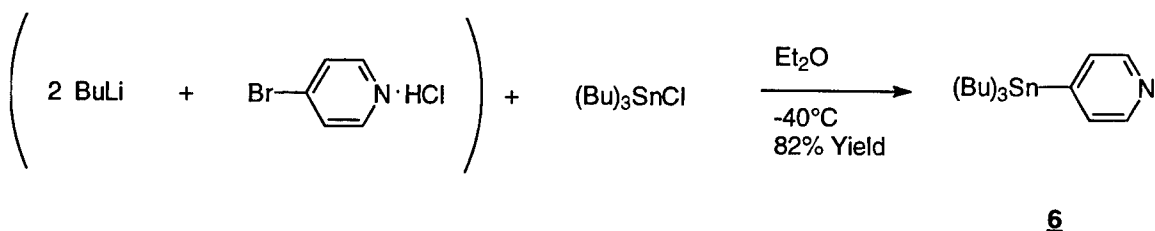
A slurry of the pyridine salt was vigorously stirred in dry diethyl ether which was cooled to -40°C. Butyl lithium was slowly dripped in so as to not raise the internal temperature. The solution was allowed to stir an additional twenty minutes before the tributyltin was added. The remaining work-up and purification was similar to the stannyl-thiophene **5**.

CHROMOPHORE SYNTHESIS

The chromophore **1** was completed by first coupling the stannyl-pyridine **6** with the dibromofluorene **4** as shown in Scheme V.

SCHEME V
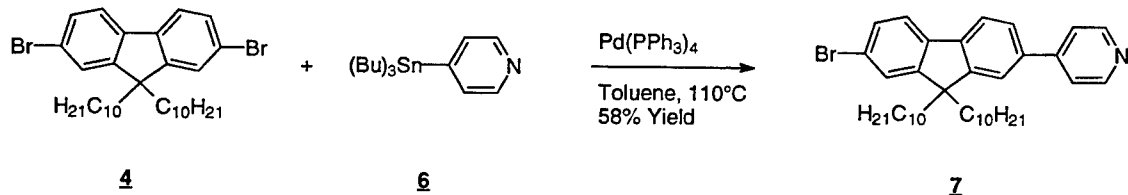
After adding compounds **4** and **6** together in toluene, palladium catalyst was added and the solution was refluxed for four hours. It was determined that the reaction was completed when the solution turns black. The work-up was the same as the stannyl-thiophene **5**, and the product was purified by column chromatography.

The final step was to react the stannyl-thiophene **5** with compound **7** as shown in Scheme VI.

SCHEME VI

| 5 | 7 | 1 |
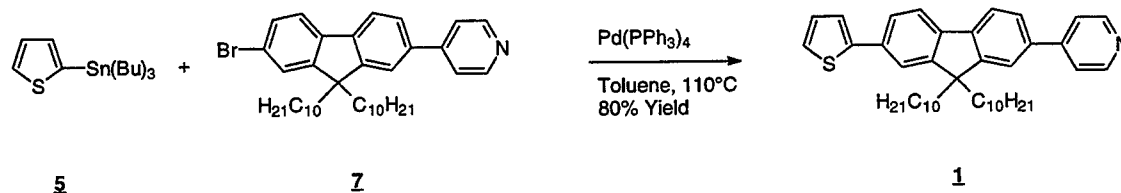
CONCLUDING REMARKS

The synthetic methods to yield a novel second order NLO material containing fluorene groups has been successfully developed. Under a University of Cincinnati / WL/WPAFB educational partnership agreement, the synthesis, purification and characterization of this compound will be carried out. The author will continue this successful investigation on NLO materials both at the University and WL/WPAFB under this joint agreement and second order NLO measurements of this material will be carried out in the coming months.

ACKNOWLEDGMENTS

BIBLIOGRAPHY

1.   Prasad, P.N. and Williams, D.J., *Introduction to Nonlinear Optical Effects in Molecules and Polymers*, Wiley-Interscience, New York, 1991.

2.   Allen, S., *New Scientist*, **1989**, 1, 59-63.

3.   Yasuda, H., Walczak, M., Rhine, W. and Stucky, G., *J. Organomett. Chem.*, **1975**, 90, 123-31.

4.   Zerger, R., Rhine, W. and Stucky, G., *J. Am. Chem. Soc.*, **1974**, 96, 5441-8.

5.   Takahashi, K. and Nihira, T., *Bull. Chem. Soc. Jpn.*, **1992**, 65, 1855-1859.

6.   Yamamoto, Y. and Yanagi, A., *Heterocycles*, **1981**, 16(7), 1161-1164.

AN INVESTIGATION OF STATISTICAL TECHNIQUES FOR FINDING RELATIONSHIPS BETWEEN PARAMETERS IN A SEMICONDUCTOR PROCESS DATA COLLECTION

Kember L. Brown
Graduate Student
Department of Electrical Engineering and Applied Science

Oregon Graduate University
20000 NW Walker Road
Beaverton, OR 97005

AN INVESTIGATION OF STATISTICAL TECHNIQUES FOR FINDING RELATIONSHIPS BETWEEN PARAMETERS IN A SEMICONDUCTOR PROCESS DATA COLLECTION

Kember L. Brown
Graduate Student
Department of Electrical Engineering and Applied Science
Oregon Graduate Institute

Abstract

The goal of this investigation is to study statistical techniques that can be used to find relationships among input and output data vectors from a semiconductor process data collection. Techniques explored include regression analysis, principle component analysis, and analysis of variance.

Introduction

At Wright Laboratory, neural network modeling of a GaAs semiconductor process is being investigated. The goal of this paper is to look into alternative statistical methods which can be used to find relationships between the input and output vectors associated with data collected at critical stages of a semiconductor process.

The stages of the process are named Substrate(S), Ohmic(C), Gate(G), and Final(F). Comparisons of how S relates to F, C relates to F, and G relates to F are to be investigated. F is the final result while S, C, and G are intermediate results from the sequential process. The S stage has ten parameters, the C stage has eight, the G stage has ten, and the F output stage has eight. Each parameter has 69 measurements. The first 50 are to be used in the analysis while the last 19 are to be used for comparison and testing.

The statistical analysis software package "DataDesk" for the Macintosh was used for all statistical computations. A complete report with all results included is available from Greg Creech, WL/ELMT, Wright-Patterson Air Force Base. Statistical techniques investigated included linear regression analysis, principle component analysis, and analysis of variance.

Linear Regression Analysis

A linear regression analysis was performed on each set of 50 measurements for each of the three process stage transitions: S->F, C->F, and G->F. The goal of a linear regression is to express the relationship between output and inputs in the form of a linear equation. See Appendix A - Linear Regression Results.

The coefficient vector b for the linear regression equation is obtained by solving the normal equations (page 74 in [1]):

$$XX'b=X'Y$$

Y is the output vector matrix and X is the input vector matrix. The coefficient vector b provides the least squares estimate of the resulting regression equation.

The standard error of estimate as well as the standard error of the regression coefficients can be computed (page 249, 257 in [2]). The standard error of the regression coefficients can then be used to find the t-ratio (page 257 in [2]) and using Student's t distribution one can test the hypothesis that the regression coefficient is zero. Datadesk performs this function and gives a probability that the coefficient is zero. This is very useful in deciding if the parameter in question is related to the output. If the probability of a regression coefficient being zero is high, then it is likely that the parameter associated with this coefficient has no effect on the output. The standard error of estimate is an indication of the accuracy of prediction when the input vectors are near their average values. For inputs further from average, the error of prediction will increase above that of the standard error of estimate(page 249 in [2].)

Another important measure of the usefulness of the linear regression is R squared. R squared is a measure of the proportion of variation of the output explained by the regression equation. R squared is calculated from the regression sum of squares and the total sum of squares as indicated below.

$$R^2=\text{RegresionSS/TotalSS}$$

$$\text{TotalSS}=\Sigma\,(Y_i-\overline{Y})^2 \quad \text{RegressionSS}=\Sigma\,(\,\widehat{Y}-\overline{Y})^2$$

Since R squared can always be made equal to 1 (100%) by adding more variables to a regression, another measure, the adjusted R squared can be used.

The adjusted R squared takes into account the degrees of freedom of which the regression is based on. Degrees of freedom basically indicates the number of independent pieces of information used to find the regression(page 145 in [2]).

An F-ratio (page 273 in [2]) can also be found for the regression. Using an F distribution one can test the hypothesis that all the regression coefficients are zero and hence the regression is not statistically significant(page 31 in [1].)

A linear regression was performed for each of the eight output parameters in stage F for all three process transitions: S->F, C->F, G->F. R squared results were 91%, 87%, 63%, 52%, 68%, 38%, 90%, and 61% for the S->F transition. The C->F transition gave 96%, 97%, 80%, 60%, 75%, 45%, 94%, and 59%. The G->F transition gave 99%, 98%, 97%, 98%, 97%, 95%, 98%, and 84%.

Parameter Trimmed Regression Analysis

As mentioned previously, we can determine the probability that a regression coefficient is zero. If the chance of a particular parameter having no effect on the output is high, we can remove it and repeat the regression analysis. The R squared value should be close to that obtained before removal of a variable if indeed the variable did not contribute much to the regression.

Each regression as stated previously was recalculated after removing variables with high probability of having zero coefficients. The resulting R squared values found were: S->F gave 91%, 87%, 63%, 49%, 68%, 36%, 90%, 60%. C->F gave 96%, 97%, 79%, 58%, 74%, 41%, 94%, and 57%. G->F gave 99%, 98%, 97%, 98%, 96%, 95%, 97%, and 84%. See Appendix B - Results of Trimmed Variable Regression.

Another measure, the mean squared error(MSE), is useful for estimating the accuracy of the regression(page 59 in [5]). The MSE for each individual output as well as the overall MSE for each regression was calculated and is given in Appendix F.

Beta Coefficients from a Standardized Regression

Beta Coefficients give an indication of which input parameters have more effect on an output. They are obtained by standardizing each variable and then performing a linear regression. Standardizing means normalizing each variable to have zero mean and a variance of one(page 260 in [2].) This is done by:

$$X_i = \frac{X_i - \overline{X}}{\sigma}$$

Beta coefficients were computed for each process transition and are shown in Appendix C - Beta Coefficients.

Correlation Matrix

A correlation matrix(page 223 in [2]) was computed for each process stage's variables. Each entry shows the Pearson Product-Moment correlation between each pair of variables. Most of the pair-wise correlation's in this data set were low, only a few being highly correlated. See Appendix D - Correlation Matrix.

Correlation among input pairs as well as multiple correlation's among several variables(multicollinearity) is of particular worry in linear regression analysis(page 181 in [3].) The goal of any regression is to assess the influence of an input parameter on the output. When the inputs are not independent but are instead related to each other, we cannot obtain a clear understating of which variables contribute since we cannot untangle the interrelationships among variables.

Principle Components Before Regression

Principle components or the more general term factor analysis can be used to uncorrelate input variables that contain multicollinearities(page 216 in [3].) Both methods offer a linear algebraic routine for decomposing a set of

variables into so called factors. These new factors are independent and can then be used in a regression analysis to determine which factors affect the output variable.

These new factors contain the same information that the original variables contained. However, in the case of principal components, each factor accounts for less and less of the variance in the data. For example if there were eight original variables, a principle components decomposition would result in eight new factors of which the first one would account for most of the variance while the eighth factor would account for very little of the variance in the data.

Since the information contained in the factors is the same, a regression using the factors will give an identical R squared. However it may be possible to drop factors that account for little variance and thus help remove multicollinearities. If exact multicollinearities existed, the factor matrix in a principle component matrix would show zero entries and we would be able to eliminate redundant factors. (See page 384 in [2] for a more complete discussion of Factor Analysis.) Since exact multicollinearities don't usually exist it is impossible to totally remove variable interdependencies without a loss of information. For example removing factors with small factor loadings will reduce the information contained in the data set.

See Appendix E - Principle Component Analysis.

The eigenvalues shown illustrate how much the first factor is worth in terms of the original variables. For example there were ten original variables. The first eigenvalue for the S stage shows that the first factor accounts for 6.1 times the amount of information in the original variables, while the tenth factor accounts for nearly none(precision past the third decimal is not shown but is still present.) Also it is seen that the first factor accounts for 61.2% of the variance in the data. The factor matrix shows the correlation between

7-7

each factor and the original variables. See [4] for a complete principle component discussion. If the input parameters were nearly independent, each eigenvalue would be close to one. In our case the first eigenvalue is 6.1, and the last is near zero which indicates a fair amount of multiple correlation. A regression would be improved if a more independant input parameter set was used(page 181 in [3]).

A principle components decomposition before regression was performed on the three process transitions. Since the amount of information does not change after decomposing the input variables into the new factors, the regression yielded the same R squared values. Dropping factors that accounted for a small proportion of variance and then redoing the regression yielded R squared numbers which were worse, as was expected.

Principle components or any factor decomposition can be useful in removing perfect multicollinearities, for example when a variable X1 is twice the variable X2 plus six times the variable X3. In this case factor analysis would indicate the existence of only two independent variables and the redundant information could then be removed. However when more nonlinear co-dependencies exist the relationships cannot be removed simply by deleting a factor since information will be lost. Thus a tradeoff exists when using a factor decomposition. Deleting a factor that still contains information (albeit a small proportion) before a regression can bias the regression and interfere with the interpretation of standard errors for the coefficients, etc. (See page 231 in [3] and [4] for a more complete discussion.)

Results from Predicting New Data

The linear regression equations obtained from the parameter trimmed regression analysis using the 50 measurements were used to predict the remaining 19 cases. The 19 parameter measurements from stages S, C, and G were used to estimate the F stage parameters and a Pearson product-moment correlation was computed between the predicted output parameters and the

actual known output parameters. A correlation of near one would indicate good predictive ability while zero would indicate little predictive ability. Also predicted versus actual scatter plots were created to illustrate graphically the accuracy of prediction. These are included in Appendix G - Graphical Results.

For the eight F stage parameters, the S->F predictions gave correlation's of .94, .94, .52, .71, .56, .46, .90, and .63. The C->F predictions gave .97, .98, .52, .71, .67, .70, .91, and .48. The G->F predictions gave .98, .99, .99, .98, .98, .99, .97, and .87.

Analysis of Variance

Analysis of variance is a statistical technique which can be used to determine if there exists a relationship between data. Analysis of variance (ANOVA) is used to determine whether variation in a data parameter is due purely to randomness or is instead related to an input parameter.

ANOVA is best illustrated by an example. Suppose there are two groups of an animal, one which lives in the dessert and one which lives in the tropics. The goal is to determine if the weight of the animal is effected by where it lives.

A within groups and between groups variance is found for the weight of the animals. The within groups variance is a measure of the random variability of the measurements and is basically the average of the variance of each group's weight. The between groups variance is the variance of each group's mean weight measured about the total combined mean weight (see page 278 in [2].)

Next, an F-ratio is calculated which is defined as the between groups variance divided by the within groups variance. Using an F-distribution one can then determine a probability that the weight differences between the two groups of animals was caused by location.

Of course, the same example could have been done with more than one "treatment" parameter. For instance instead of just location, weather and

terrain groups could have been added to determine if a causal relationship existed. The important thing to remember about ANOVA is that it determines whether a relationship exists due to treatments or due to randomness. ANOVA does not indicate the extent of the relationship as does regression. For example, if it was determined that variation in the animals' weights was more than just random variation, the cause (location, weather, terrain) could not be pinpointed by only ANOVA.

Non-Linear Regression

Non-linear regression is similar in concept to linear regression. In linear regression it is assumed that the output is a linear combination of the inputs. Due to the fact that the error surface is always a bowl for linear regression(page 478 in [3]), there is no need to perform complex minimization routines to find the regression coefficients. Instead we simply calculate them. In non-linear regression our assumption is that the output is some non-linear function of the inputs. For example the output Y is related to the input X by $Y=B1*e^{B2*X}$. Then in order to find the coefficients (B1 and B2 in this case) a complex computer routine such as the method of steepest descent, Gauss-Newton, Marquardt's method, etc. (page 473 in [3]) must be used to find the global minimum of the non-linear, non-bowl shaped error surface.

Solving for the coefficients can be accomplished easily using one of the listed routines implemented with a computer. The major drawback to non-linear regression is having to know which non-linear model to assume beforehand(page 465 in [3]). For this reason, a non-linear regression was not attempted for the semiconductor process data.

Although the basic assumption in linear regression that the output is a linear combination of the inputs is often violated over extended ranges of data(which gives a poor R squared), there usually is a range of input data where this assumption holds and the relationship can be considered linear.

Conclusion

Several statistical techniques were explored in this paper. Linear regression analysis is perhaps the most useful in quantifying the relationship among input and output parameters. The coefficients are computationally easy to calculate, and linear regression analysis provides many clues as to how well the regression predicts new output values. The major drawback to linear regression is that over an extended range of data the linear assumption may fail to hold true and thus the regression may not have significance. Linear regression provides many answers as to how good the regression is at explaining the variation in the data.

For our particular case of the semiconductor process data the linear regression results varied. Some regressions had very low R squared values showing little predictive capability, while many had good values. The plots showing the predicted (Y-axis) versus actual output values (X-axis) shows that over the range of values given the regression formula did predict outputs to a moderate degree. However, comparing these results to similar results from neural network models showed the network models superior. (Appendix H shows the output variable f21rfv plotted for all three process transitions against the predicted value by both linear regression and a neural network model.)

Using linear regression to determine variables of importance also allowed the "trimming" of the number of input variables used in the regression. This method showed that the trimmed regression yielded the same R squared values using fewer parameters. This also increases the degrees of freedom of the regression analysis which increases accuracy(reduces standard error). By standardizing all regression parameters, beta coefficients can be found which show the degree an input variable contributes to an output. This is quite useful for the semiconductor data since it indicates the variables which are most crucial in affecting the output parameter.

7-11

The principle components factor decomposition before linear regression technique was also investigated. It was found that decomposing data into principle components does not improve the regression. Principle components can be used to remove multicollinearities from data but pure multicollinearities rarely occur and a loss of data is the price paid for removing factors from a principle component analysis. Principle components or any factor decomposition can be extremely useful as an aid to understanding which parameters make up a factor(in other words which parameters share multiple correlation's and can be grouped together as one factor.) The factor matrix illustrates which parameters are associated with which factor. Principle components is also an excellent method for determining the extent of multiple correlation's or multicollinearity among parameters. A principle component analysis showed our data did have a fair amount of multiple dependencies.

Analysis of variance is a technique to determine if relationships exist among data. It is not useful as a predictor and does not quantify the extent of the relation. It is most useful in determining if slight variations among data groups are due to random sampling variations or are instead due to something different about the groups. Datadesk did claim to predict new values using ANOVA but a reference was never found which mentioned using ANOVA as a prediction tool.

Lastly, non-linear regression was mentioned. Non-linear regression seems best suited when a priori information is known about the data since a non-linear model must first be chosen.

<u>References</u>

[1] N.R.Draper, Applied Regression Analysis, New York: John Wiley & Sons, 1981.

[2] Kachigan, Statistical Analysis, New York: Radius Press, 1986

[3] S.A. Glantz, Primer of Applied Regression and Analysis of Variance, New York: Mcgraw-Hill, Inc., 1990.

[4]   E. Mansfield, Principle Component Approach to Handling Multicollinearity in Regression Analysis, Ann Arbor, Michigan: Xerox University Microfilms.

[5]   M. Smith, Neural Networks for Statistical Modeling, New York: Van Nostrand Reinhold, 1993.

TORSIONAL SPLIT-HOPKINSON BAR EXPERIMENTS ON OFHC COPPER, AL 2024 AND FILLER-E

Richard J. Caspar
Graduate Research Assistant
Department of Aerospace and Mechanical Engineering

University of Notre Dame
365 Fitzpatrick Hall
Notre Dame, IN 46556-5637

Final Report for:
Graduate Student Research Program
Wright Laboratories

August 1995

TORSIONAL SPLIT-HOPKINSON BAR EXPERIMENTS ON OFHC COPPER, AL 2024 AND FILLER-E

Richard J. Caspar
Graduate Research Assistant
Department of Aerospace and Mechanical Engineering
University of Notre Dame

Abstract

The solid explosive simulant, Filler-E, was successfully tested with a torsional split-Hopkinson bar. In order to achieve this result, modifications were made in the design of the torsional Hopkinson bar at Eglin Air Force Base, Florida, in the Advanced Warheads Evaluation Facility (AWEF) to make it operable. Tests were then performed on Oxygen-Free-High-Conductivity (OFHC) Copper and Aluminum 2024-T6 to validate the accuracy of the Hopkinson bar. The ultimate stress for OFHC Copper at a strain rate of 700 s^{-1} was found to be 220 MPa, which closely compares to Weerasooriya's results (1990), which give an ultimate stress of 190 MPa for a strain rate of 800 s^{-1}. The ultimate and yield stresses for Al 2024 at a strain rate of 1100 s^{-1} were found to be 200 MPa and 310 MPa, respectively, which are within reason when compared to the quasi-static values of 230 MPa and 290 MPa, respectively. A specimen was designed for Filler-E, which resulted in values of yield stress and ultimate stress, for a strain rate of 600 s^{-1}, to be 3 MPa and 3.5 MPa, respectively. Important information was gained as to the testing of explosive simulants with the torsional Hopkinson bar, which will prove to be instrumental in the design of a Hopkinson bar at the University of Notre Dame.

TORSIONAL SPLIT-HOPKINSON BAR EXPERIMENTS ON OFHC COPPER, AL 2024 AND FILLER-E

Richard J. Caspar

Introduction

The torsional split-Hopkinson bar is a well established apparatus used to determine material properties at medium to high strain rates (10^2 to 10^4 s^{-1}). This research ultimately intends to focus on the torsional Hopkinson bar to test explosives at such strain rates. Little is known about the shear stress and shear strain characteristics of solid explosives. Experiments on these materials with the torsional Hopkinson bar will provide detailed data on the shear stress and shear strain characteristics of solid explosives at the indicated strain rates. This information should prove to be helpful in numerical simulations of explosive mechanics and should reduce the need for costly full scale tests and experiments on solid explosives.

It is also hoped that initiation of combustion in these explosives due to large amounts of induced deformation will occur. With the assistance a ultra-high-speed photography (two million frames per second), it is hoped to observe hot spot formation and a transition to detonation in these solid explosives. There are several reasons why the torsional Hopkinson bar is desirable for these experiments. First of all, in torsional loading, the maximum stress in the specimen occurs on the exterior surface of the material. The greatest deformation will thus occur on the exterior surface, making the probability of hot spot formation greatest, where it can easily be observed. Also, the torsional Hopkinson bar can be designed to produce a pulse of almost any desired length, and hence, large amounts of deformation in the specimen is possible. The apparatus can easily be designed to produce more deformation than the specimen can withstand. In addition, the torsional Hopkinson bar produces a pulse of pure torsion, thus reducing the presence of frictional effects between the specimen and bar, which are often seen in compressive loading.

There are, however, some drawback to the torsional Hopkinson bar. First of all, tests may only be run on the limited range of strain rates listed above. Also, if fracture occurs in the explosive specimen too soon, localization, and hence initiation, will not occur.

In order to gain familiarity with the torsional Hopkinson bar, the author spent the summer working with this apparatus at Eglin AFB, Florida, in the AWEF, helping to make their apparatus functional. Once this was achieved, validation tests were run on materials of known properties, and then tests were run on explosive simulants, in order to determine the limitations of the torsional Hopkinson bar when dealing with explosives.

Apparatus

The torsional split-Hopkinson bar consists of two elastic cylindrical bars: an incident and transmission bar; a torsional pulley; a clamp; and a specimen (see Figure 1). The two bars are constructed of aluminum
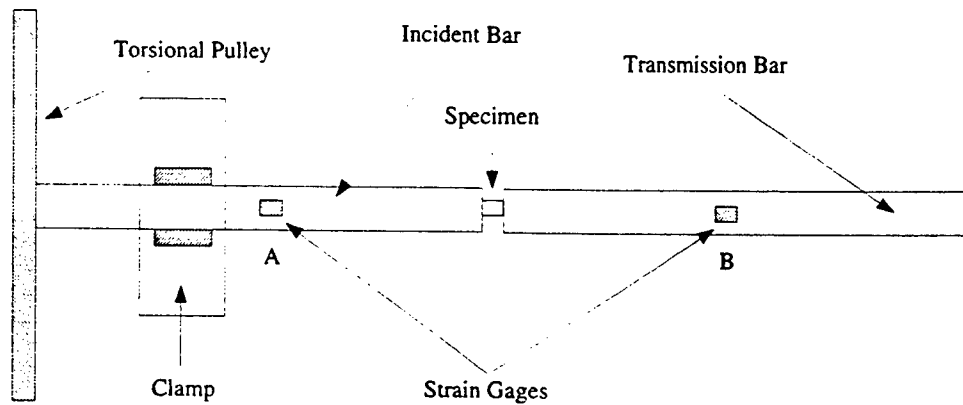
Figure 1: Schematic of the Torsional Hopkinson Bar

7075-T6 and are aligned along a common axis. Joining the two bars is a thin walled cylindrical specimen of known geometry, which may be either glued to the bar or inserted into a hexagonal slot that has been milled into the incident and transmission bars. The torsional pulley is attached to the end of the incident bar away from the specimen, and the clamp is placed at a variable distance from the pulley. The clamp is used to prevent rotation of the incident bar while the torsional pulley is rotated, thus storing a torsional pulse in the bar between the pulley and clamp. The sudden release of the clamp propagates an incident shear strain pulse down the length of the incident bar. The incident pulse reaches the specimen, transmitting some strain through the specimen to the transmission bar and reflecting some back into the incident bar.
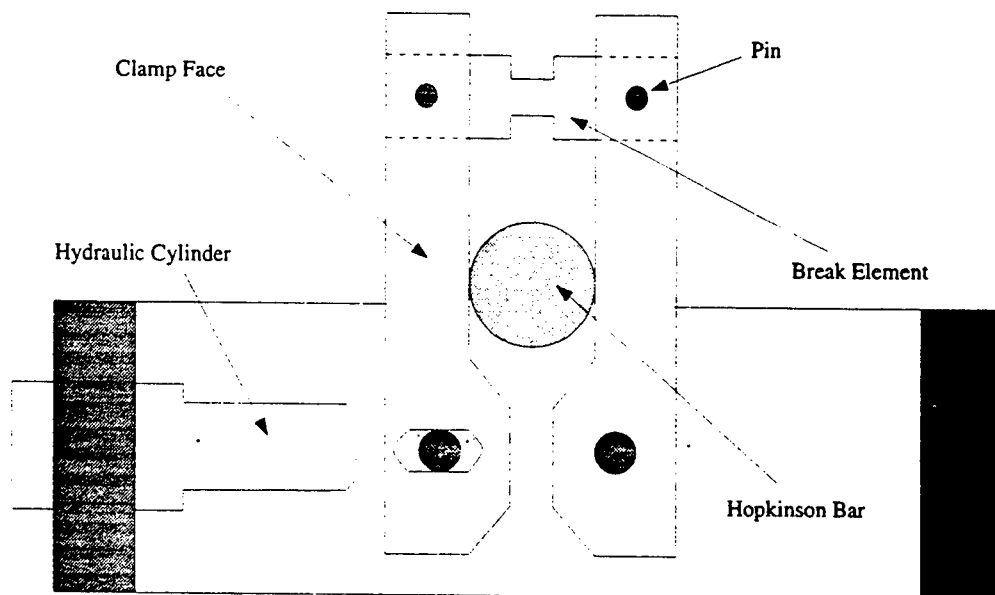

Figure 2: Original Schematic of the Clamp

<u>Modifications</u>

At the beginning of the summer, the torsional Hopkinson bar was not functional, partially due to an ineffective clamp design. A schematic of the clamp design that was in use is included in Figure 2. The clamp is engaged by pressurizing a hydraulic cylinder, which transmits pressure onto the Hopkinson bar. In order to release the clamp, the hydraulic pressure is increased until the break element fractures. In this clamp design, the break element was failing to fracture, and the pins holding it to the clamp face were shearing. Also, the clamp was unable to hold the desired torque in the bar without slipping. Finally, there was an asymmetry in the design of the clamp, in that the two clamp faces did not pivot about the same point upon fracture of the break element.
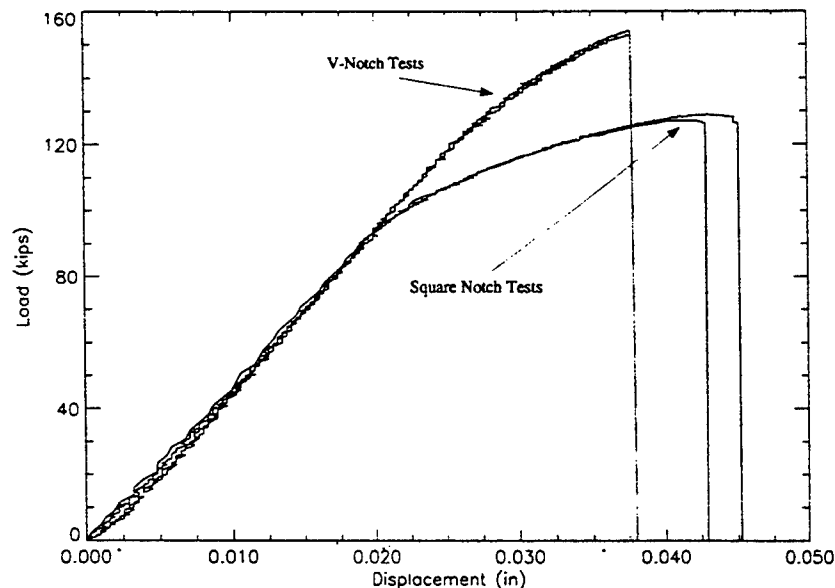

Figure 3: Break Element Notch Geometry Tension Test

In order to correct these problems, several modifications were made. As seen in Figure 2, the break element had a square notch machined into it. In order to determine if this was the most effective notch geometry, the author performed an experiment to test a square notch and a v-notch in a uniaxial tension machine. Figure 3 shows the results of these tests. From this figure, it is seen that the v-notched specimens exhibited a more elastic deformation, which is evident from the linear relationship seen in the graph; whereas the square notched specimens went through a significant amount of plastic deformation before failure. In the design of the break element, it is desired to store a large amount of elastic energy before failure, to allow for quick release of the clamp. This quick release will give an incident pulse with a short rise time and relatively constant magnitude, and hence a constant strain rate. The specimen will thus experience a relatively constant strain rate, as will be discussed in the analysis section. In plastic deformation, energy is being lost in unrecoverable deformation; elastic energy is thus more desirable since it is fully recoverable. In addition, Figure 3 shows that the square notched specimens displace a larger distance during deformation.
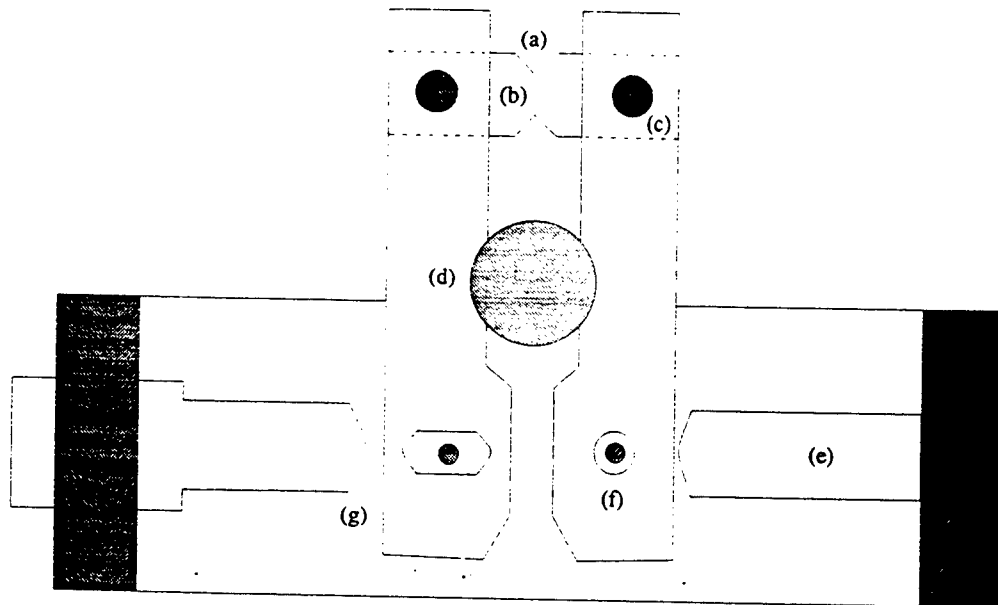
Figure 4: Schematic of Modifications to Clamp Design

This will result in more rotation of the clamp faces before release, thus providing a mechanism for the Hopkinson bar to slip in the clamp. Upon analysis of the failure surface of the break elements, it was noticed that the v-notch had a planar failure surface, while the square notch had a more tortuous failure surface. The v-notched break element tests were also very repeatable. As a result of these tests, a v-notch was implemented into the break element design, (see modification (a) on Figure 4).

In order to address the problem of the pin failure, the inner diameter of the notch was decreased to allow it to fail at a lower load (see b) and the pins were increased in diameter (see c). To prevent the Hopkinson bar from slipping in the clamp, cylindrical notches were cut into the clamp faces (see d) and the contact surfaces were sanded. Finally, the following modifications helped to make the design more symmetric: a cylindrical rod was added to the clamp to allow hydraulic pressure to be applied from both sides (see e); the diameter of the pins holding the clamp faces was decreased so that they would act merely as guides, not as fixed pins (see f); and the faces of the hydraulic ram and cylinder were rounded to provide a determined point of contact on the clamp face (see g). It is desired to have a symmetric design so that both clamp faces will release instantaneously.

With the previously mentioned modifications to the clamp, smooth incident pulses with fast rise times were observed. However, inaccurate results were being achieved from the analysis. The final problem proved to be elusive and was only discovered the day before departure from the AWEF. The right end of the transmission bar in Figure 1 had been fixed. It was noticed that when the torque was applied to the bar, a small amount of initial rotation in the clamping mechanism occurred. Since the far end of the transmission bar was fixed, this small torque was stored in the entire apparatus, causing the specimen to be pre-torqued. Upon removing the fixed end, results in accord with Weerasooriya's results (1990) were achieved.

Wave Motion

In order to understand the analysis for the torsional Hopkinson bar, it is first necessary to understand the motion of shear waves in a one dimensional solid cylinder of circular cross-section. The conservation of angular momentum tells us:

$$\frac{\partial T}{\partial x} = \rho J \ddot{\phi}, \tag{1}$$

where T is the torque; x is the distance along the length of a member; J is the polar moment of inertia; ϕ is the angle of rotation of the member, and the dots denote differentiation with respect to time, t. Torque is defined as the equivalent moment generated by the shear stresses over the cross-sectional area, which, for an elastic material and small strains, reduces to the relation:

$$T = JG\frac{\partial \phi}{\partial x}, \tag{2}$$

where G is the elastic modulus of the member. By plugging Equation (2) into Equation (1), one obtains the wave equation:

$$\frac{\partial^2 \phi}{\partial x^2} = \frac{1}{c^2}\ddot{\phi} \tag{3}$$

where c, which equals $\sqrt{\frac{G}{\rho}}$, is the wave speed in the member. The solution to this equation is known as D'Alembert's solution:

$$\phi = f(x + ct) + g(x - ct), \tag{4}$$

where f and g are any arbitrary functions. D'Alembert's solution states that for any induced disturbance, a right and left traveling wave may propagate through the member. If a torsional pulse were stored in a bar between two clamps, which were simultaneously released, Equation (4) shows that two pulses propagate (see Figure 5), with length equal to the stored pulse and of magnitude equal to half the stored pulse. For the torsional Hopkinson bar, the pulley acts as a rigid wall and immediately reflects the left traveling pulse without changing its sign, joining it with the right traveling pulse. The result is a right traveling pulse of length equal to twice the stored pulse and half the magnitude.
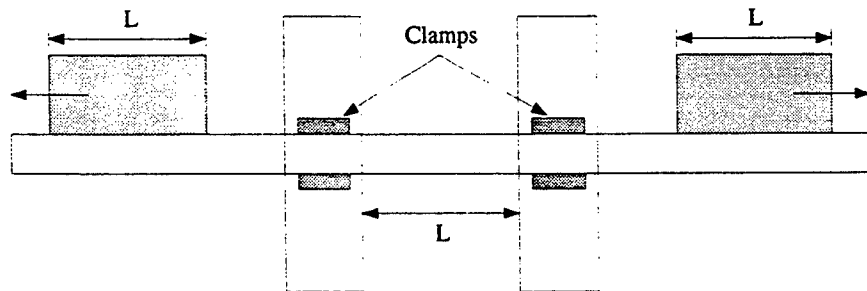

Figure 5: Wave Propagation in a Bar

Analysis

The values of the shear stress, shear strain and shear strain rate in the specimen are determined from the analysis of the strain in the incident and transmission bars. The shear strain rate in the specimen, $\dot{\gamma}_s(t)$, is determined from the reflected pulse. Integration of the shear strain rate then provides the shear strain, $\gamma_s(t)$. The shear strain on the surface of a right circular cylinder is defined as the change in circumferential displacement, L_c, divided by the longitudinal length, L:

$$\gamma = \frac{L_c}{L} = \frac{D_c \phi}{2L} = \frac{D_c}{2} \frac{\partial \phi}{\partial x},\tag{5}$$

where D_c is its diameter and x is the position along its length. Hence, the average shear strain in the specimen is given by:

$$\gamma_s = \frac{D_s(\phi_1 - \phi_2)}{2L_s},\tag{6}$$

where ϕ_1 is the angle of rotation of the specimen/incident bar interface and ϕ_2 is the angle of rotation of the specimen/transmission bar interface; D_s is the mean diameter of the specimen; and L_s is its length. From Equation (5), it is seen that the value of ϕ_2 can be determined from the shear strain on the surface of the transmission bar at the specimen interface, γ_T:

$$\gamma_T = \frac{D}{2} \frac{\partial \phi_2}{\partial x} = \frac{D}{2c} \frac{\partial \phi_2}{\partial t},\tag{7}$$

where D is the diameter of both bars and the spatial derivative is converted to a time derivative with the help of D'Alembert's solution for the right traveling transmitted pulse (see Equation 4). Equation (7) is then integrated to determine ϕ_2:

$$\phi_2 = \frac{2c}{D} \int_0^t \gamma_T(\tau)\ d\tau.\tag{8}$$

In a similar manner, ϕ_1 is determined from the shear strain at the surface of the incident bar at the specimen interface; composed of the right traveling incident strain pulse, $\gamma_I(t)$, and the left traveling reflected strain pulse, $\gamma_R(t)$. Hence,

$$\phi_1 = \frac{2c}{D} \int_0^t [\gamma_I(\tau) - \gamma_R(\tau)]\ d\tau.\tag{9}$$

Equations (8) and (9) are then plugged into Equation (6) to yield:

$$\gamma_s(t) = \frac{cD_s}{L_s D} \int_0^t [\gamma_T(\tau) - \{\gamma_I(\tau) - \gamma_R(\tau)\}]\ d\tau.\tag{10}$$

Now, for a homogeneous state of strain in the specimen, the torque at the specimen/incident bar interface, T_1, is approximately equal to the torque at the specimen/transmission bar interface, T_2. Since torque is proportional to shear strain during elastic deformation of the bar, γ_1 is approximately equal to γ_2 and since γ_T, γ_R, and γ_I are measured in the bar,

$$\gamma_T \approx \gamma_I + \gamma_R.\tag{11}$$

This relation is then plugged into Equation (10) to obtain the expression for the shear strain in the specimen:

$$\gamma_s(t) = \frac{2cD_s}{L_s D} \int_0^t \gamma_R(\tau)\ d\tau.\tag{12}$$

It can also be shown that the transmitted pulse provides a measure of the shear stress in the specimen, τ_s. For a right circular cylinder, the shear stress, τ_c, is defined as:

$$\tau_c = \frac{Tr}{J},\tag{13}$$

where T is the torque, r is the radius measured from the axis of the cylinder and J is the polar moment of inertia. After plugging in the expression for the polar moment of inertia for a thin-walled tube, we obtain the following expression for the shear stress in the specimen:

$$\tau_s = \frac{2T_s}{\pi D_s^2 t_s},\tag{14}$$

where T_s is the average torque in the specimen and t_s is the wall thickness of the specimen. The average torque in the specimen can be determined by the average of the torque at the two bar/specimen interfaces:

$$T_s = \frac{T_1 + T_2}{2},\tag{15}$$

where T_1 is the torque at the specimen/incident bar interface and T_2 is the torque at the specimen/transmission bar interface. Using Equation (13) and the fact that $\tau = G\gamma$ in the elastic region, these torques are determined to be:

$$T_1 = \frac{\tau_1 J}{r} = \frac{G\pi D^3}{16}(\gamma_I + \gamma_R)\tag{16}$$

and

$$T_2 = \frac{\tau_2 J}{r} = \frac{G\pi D^3}{16}\gamma_T.\tag{17}$$

From Equations (11), (14), (15), (16) and (17), one obtains the expression for the shear stress in the specimen:

$$\tau_s = \frac{GD^3}{8D_s^2 t_s}\gamma_T.\tag{18}$$

Data Reduction

The shear strain pulses in the incident and transmission bars are recorded by means of a strain gage Wheatstone bridge in full bridge configuration. In order to convert the output voltage, V_o, of the bridge into the shear strain, γ, of the bar, the following relationship is used:

$$\gamma = \frac{2V_o}{FEG},\tag{19}$$

where F is the gage factor of the gages, E is the excitation voltage supplied to the bridge and G is the gain of the amplifier through which the signal is conditioned. Figure 6 shows typical waveforms recorded from the oscilloscope at the two gage stations, A and B (see Figure 1).

Results

In order to verify the stress strain curves generated by the torsional Hopkinson bar, they were compared to curves obtained by Weerasooriya (May 1990) for Oxygen-Free-High-Conductivity (OFHC) Copper. Due to a lack of time and material, only one test on OFHC Copper was performed successfully. The results of
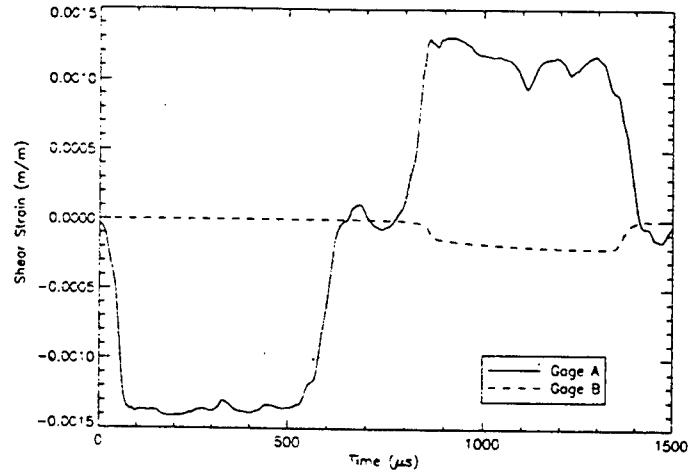
Figure 6: Typical Shear Stress Pulses for Al 2024

this test can be seen in Figure 7. This test was run at a strain rate of approximately 700 s^{-1} and achieved an ultimate stress of about 220 MPa. These results compare very closely to Weerasooriya's results, which show an ultimate stress of about 190 MPa for a strain rate of 800 s^{-1}. Although an uncertainty analysis of the torsional Hopkinson bar at the AWEF has not yet been performed, it is believed that these values will be within the uncertainty. The oscillatory behavior is thought to be due to slipping in the specimen mount. A few tests were then performed on Al 2024. Figure 8 show that for a strain rate of 1100 s^{-1}, the yield stress and ultimate stress are about 200 MPa and 310 MPa, respectively. Figure 9 show that for a strain rate of 1800 s^{-1}, the yield stress and ultimate stress are about 200 MPa and 295 MPa, respectively. These values do agree well with what one would expect: the quasi-static yield stress in torsion for Al 2024 is about 230 MPa and the ultimate stress is about 290 MPa. Since the summer was nearing completion, more extensive verification was not possible.
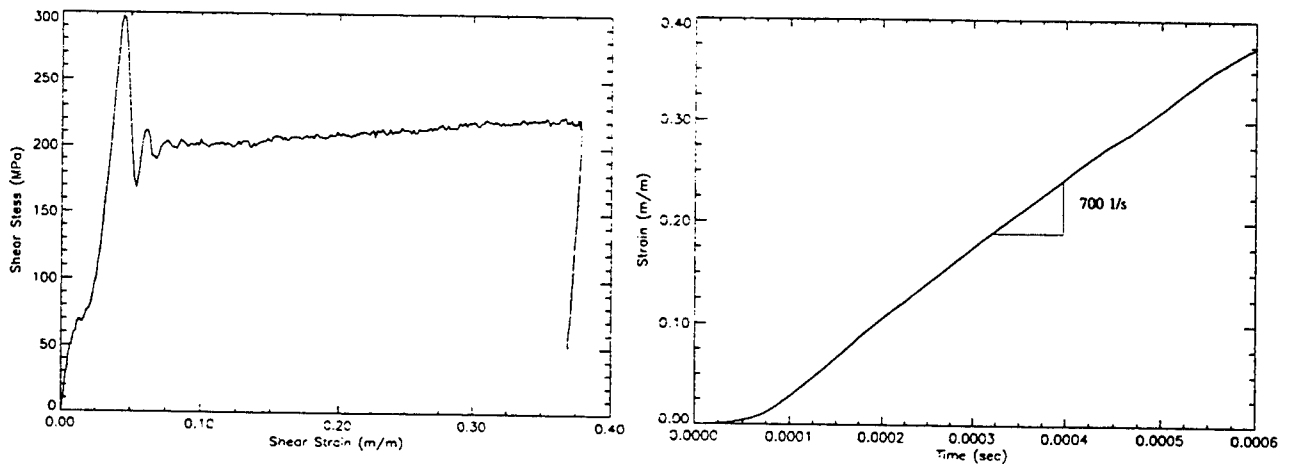

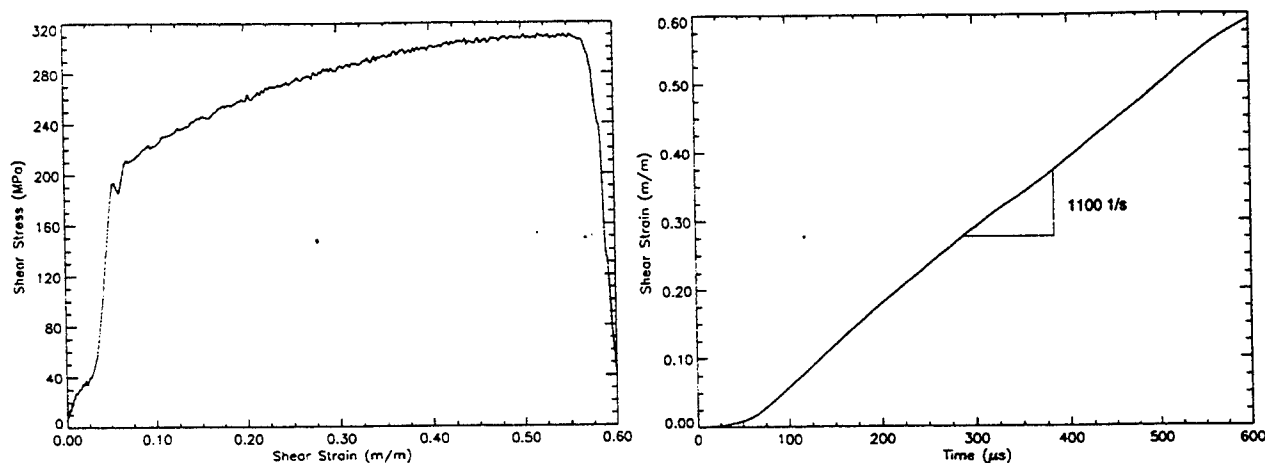Figure 7: Results of Torsional Hopkinson Bar Test on OFHC Copper, Test 12

Figure 8: Results of Torsional Hopkinson Bar Test on Al 2024, Test 13
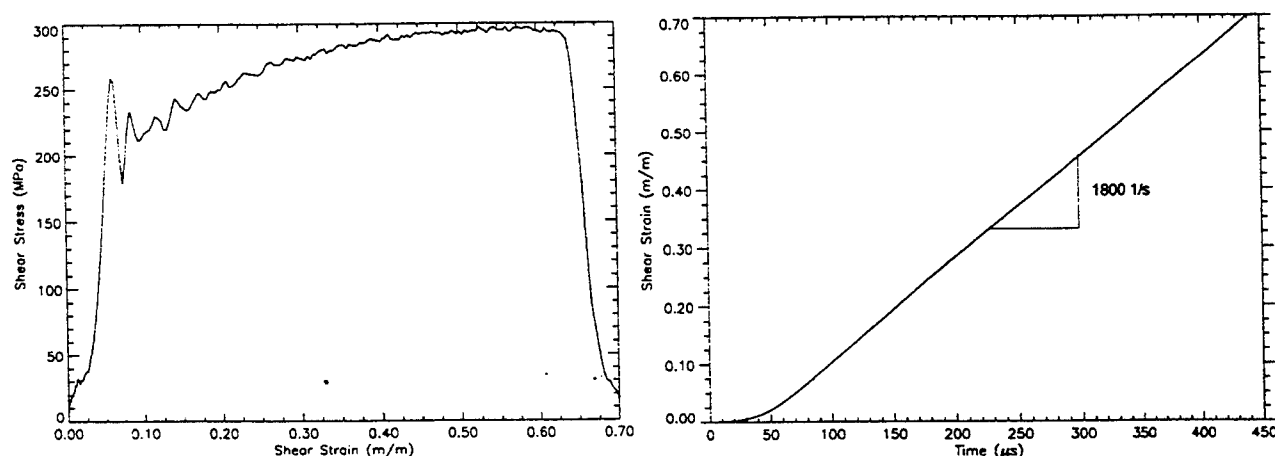

Figure 9: Results of Torsional Hopkinson Bar Test on Al 2024, Test 15

One of the objectives of this summer's research was to gain knowledge of the explosive simulants used by the Air Force. One of these simulants is Filler-E, which is used to approximate the material properties of tritonal, a commonly used solid explosive. Throughout the course of the summer, the author worked to finalize the design for a Filler-E specimen. Due to the difficulty of machining, it was decided to design a specimen that could be glued to the Hopkinson bar, instead of using the hexagonal notch which was being used to mount metal specimens. An adaptor was thus designed that would fit securely into the hexagonal mount and provide a surface to which the specimen could be glued. Figure 10 shows schematics of the adapter and specimen designs. Two tests were then performed of Filler-E. The tests were found to be repeatable, and the resulting plots can be seen in Figure 11. It was thus determined that for a strain rate of 600 s^{-1} the yield stress of Filler-E is 3 MPa and the ultimate stress is 3.5 MPa. However, the wall thickness of the specimen is large (0.1 inch), and the assumption of a thin wall may not be valid. The nature of the effects of this assumption should be more carefully examined. Also, the specimens fragmented and the details of

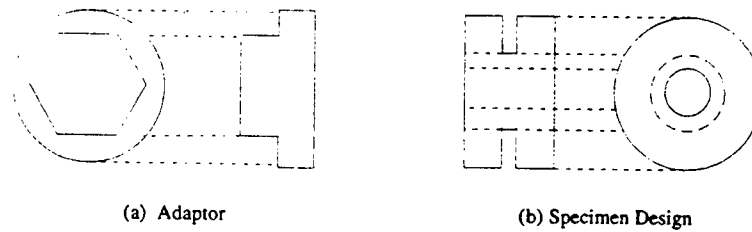(a) Adaptor   (b) Specimen Design

Figure 10: Schematics of Design Modifications for Filler-E

this failure can only be assumed. High speed photography would characterize the failure and its effects on the results in Figure 11.
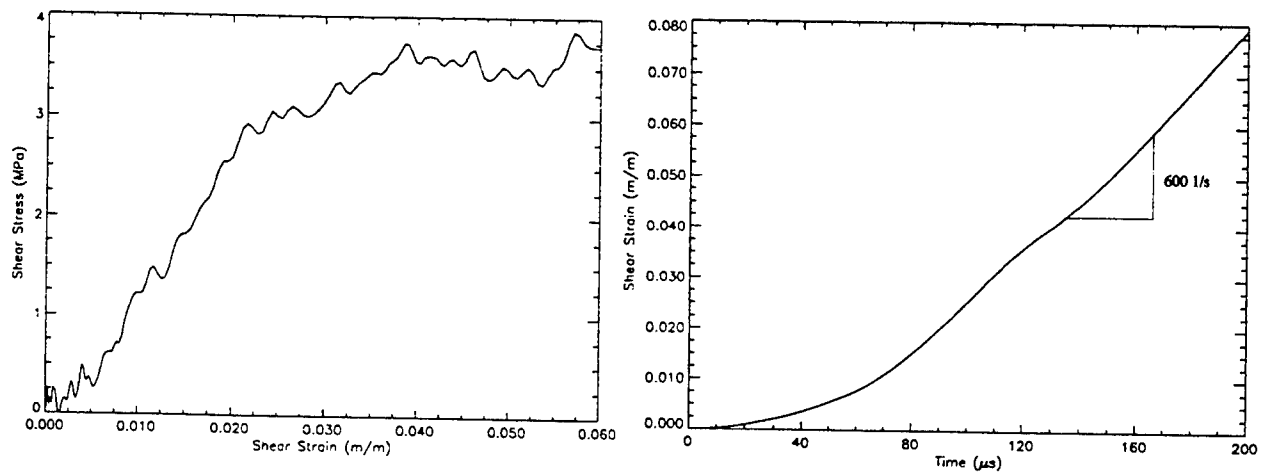

Figure 11: Results of Torsional Hopkinson Bar Test on Al 2024, Test 6

Summary

This summer was very productive. The author gained valuable experience and knowledge as to the design and operation of the torsional Hopkinson bar. This information should prove to be useful in the design of a torsional Hopkinson bar at the University of Notre Dame. After many modifications, the clamp was made operable, producing smooth pulses with short rise times. These pulses have been analyzed to give shear stress and shear strain curves for OFHC Copper, Al 2024 and Filler-E. In addition, it was discovered that tests of explosive simulants can be performed on the torsional Hopkinson bar, and hence, it is reasoned that tests on solid explosive will also be possible.

Recommendations

In performing the experiments at the AWEF, it was discovered that the current alignment procedure is unreliable. Analysis of the bending and axial strains in the bar showed magnitudes that are larger than desired. It is believed that more accurate alignment of the bar will reduce these strains. It is recommended

that a spotting laser be used to align the bar. It is also recommended that the current metal bearings used to support the torsional Hopkinson bar be replaced with teflon bearings to allow for smoother travel of the bar. Finally, the fixed end attachment on the transmission bar should be removed and a bearing should be installed to allow for its free rotation.

Future Work

Due to the successful results of this summer's experiments, the author will design and build a torsional Hopkinson bar at the University of Notre Dame for use in testing solid explosives. Designs for the solid explosive specimens will be finalized and tests will then be performed on them to determine their material properties and to hopefully observe shear localization and ignition. The author will also be working on writing a computer code to model and predict the specimen's behavior.

References

1. Duffy, J., Campbell, J. D., and Hawley, R. H., 1971, "On the Use of a Torsional Split Hopkinson Bar to Study Rate Effects in 1100-0 Aluminum," *Journal of Applied Mechanics*, Vol. 93, pp. 83-91.

2. Hartley, K. A., Duffy, J., and Hawley, R. H., "The Torsional Kolsky (Split-Hopkinson) Bar, High Strain Rate Testing," *Metal Hand Book*, American Society for Metals, Vol. 8, pp. 218-238.

3. Lewis, J.L., and Campbell, J. D., 1972, "The Development and Use of a Torsional Hopkinson Bar Apparatus," *Experimental Mechanics*, Vol. 12 (No. 11), pp. 520-524.

4. Weerasooriya, T., 1990, "The MTL Torsional Split-Hopkinson Bar," MTL TR 90-27, U.S. Army Materials Technology Laboratory, Watertown, MA.

THE DESIGN OF A PC-BASED DATA ACQUISITION AND CONTROL ENVIRONMENT
FOR USE IN A DSP-BASED ACTIVE DYNAMOMETER

James L. Cifarelli
Research Assistant
Department of Electrical and Computer Engineering

Clarkson University
Box 5720
Potsdam, NY 13699-5720

THE DESIGN OF A PC-BASED DATA ACQUISITION AND CONTROL ENVIRONMENT FOR USE IN A DSP-BASED ACTIVE DYNAMOMETER

James L. Cifarelli
Research Assistant
Department of Electrical and Computer Engineering
Clarkson University

Abstract

This paper describes the software environment designed for implementing a DSP-based (Digital Signal Processor) active dynamometer. Such a dynamometer can dynamically change the load projected onto machines under test. With today's thrust into electrically mobilized vehicles and devices, a computer based active system can project the same dynamic loads on machines as would be found in the field. Our goal is to design and build a window's based graphical user interface (GUI) and subsystem for the control and data acquisition of this active dynamometer.

Discussion of Problem

There are four main areas that stress the need for an environment which can operate at high speeds and maintain a responsiveness to user control during dynamometer testing. First, the full active dynamometer setup requires both machines to be DSP controlled during experimentation. Second, depending on the machines chosen for the dynamometer and machine under test, additional controllers for the power source of each machine may also be needed. Third, test result data needs to be stored for analysis. Lastly, control parameters may need user adjustment during testing.

Methodology

The solution to design problems in handling each problem area lies in a mixture or proper DSP equipment selection, DSP code written to adjust to the many different machine setups for both the dynamometer and test machine, and a software environment designed to handle data transfer from the DSP equipment to the PC and user control from the PC to the DSP equipment. It is important to note that the PC operating system plays a major role in aiding in the design of a software solution.

Centered on the use of Texas Instruments TMS320 series digital signal processors, there were two type of DSP equipment that the full environment was designed around. Spectrum Signal Processing Inc.'s TMS320C30 Processor board and accompanying I/O daughter boards were first used in the design of the dynamometer. These boards are housed internal to the PC. The main processor board provides for communications with the PC, and for data transfer of external I/O signals for use in the DSP control program. The four daughterboards provide Analog-to-Digital conversion (ADC), Digital-to-Analog conversion (DAC), Digital I/O (DIO), and motor encoder resolution. Integrated Motions' MX31 Modular Embedded System was then used for further dynamometer design. This external unit houses all DSP boards. Just as the internal system is connected, the MX31 main processor board,

9-3

utilizing Texas Instruments's TMS320C31, connects it's I/O daughterboards to a peripheral bus. This unit is programmed and user controlled through a serial line connection to the host PC. The PC environment is designed to connect and communicate with both the internal and external (embedded) DSP units. Different I/O connections are necessary for the two systems.

Control system timing is critical for a functional dynamometer. The control code was designed to keep regular timing of the control algorithms for both machines and regular data logging intervals to the PC. The DSP equipment contains two onboard timers for use in keeping system control intervals and for time-stamping logged data.

A software environment was designed for the creation, simulation, and active control of the dynamometer system. Windows 3.x, the present platform for the environment, was chosen because of it's wide distribution and ease of use. This environment consists of a GUI (Graphical User Interface), DSP API (Application Programming Interface), DSP-specific library, and a Window's VxD (Virtual Device Driver).
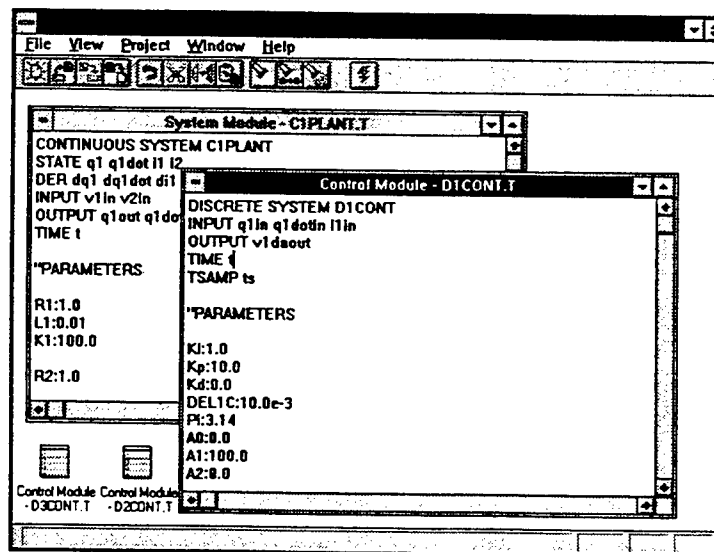

figure 1. PC Environment GUI

The GUI, as seen in figure 1, gives the user the ability to design the DSP code for dynamometer control and provide run-time adjustment to that control code. Both the machine under test and the dynamometer machine are controlled though separate modules entered in by the user. He or she has the power to define each controller though a simple system's language. This language, which is very similar to that contained in the widely used nonlinear simulations program Simnon, can make for rapid system development and implementation. The key to such time savings lies in using a systems approach in dynamometer design rather than lower level DSP source code written in C or Assembly language. The GUI also provides the user with a means to easily control system parameters during run-time. Such control gains or parameters appear as adjustable sliders under Windows 3.x. A means for graphing data is also provided for under the GUI. The user interface was written with Borland International's Object Windows Library (OWL). OWL provides the application programmer a full family of object-oriented classes that represent all Window's GUI objects. Through object-oriented programming, each object in the dynamometer GUI is instantiated. Once built, these objects take care of themselves. This enables a windows programmer to concentrate on the main program idea and operation without worrying about low level GUI programming. With the system written in OWL, cross-platform implementation of the PC environment into other operating systems is made much easier. The GUI is the top layer to the full environment. Just as people have skin, the GUI represents the shell we see and interact with.

The DSP API Library lies directly under the top layer. The full environment is designed for use with different types of digital signal processing equipment. This make for a flexible system where new libraries can be used in order to keep up with new and improved DSP equipment from many manufacturers. This layer provides a common DSP protocol for interacting with DSP-specific libraries and device drivers.

Some DSP equipment does not come with the appropriate libraries for use in a Window's application. While many manufacturers do provide a programming library for their equipment, some libraries need adjustment in order to achieve an optimum performance while running in a window's based operating system. This layer provides the adjustments necessary for Spectrum's C30 Processor board library. If necessary for specific DSP equipment, device driver interaction lies within the functions for this library level. With Integrated Motion's MX31 being connected through a PC serial port, this layer is nonexistent. The previous layer communicates directly with Microsoft's virtual communications driver.

A device driver provides for stable interaction with PC hardware during system operations. This is especially true for applications running on today's multitasking operating systems. These operating systems run software at ring levels of privilege. While there are five ring levels to system operations, only two are used. Ring 0, for kernel mode use is the highest privileged level. The virtual device drivers run at this level. These drivers then have the ability to interact best with on board system hardware such as Spectrum's C30 Processor board. This same ring level enables the virtual device drivers to accept hardware interrupts generated from the peripheral boards. This is one of the most important parts for the dynamometer environment. Without software running at this level, the GUI layer could miss these interrupts and thus miss logged data. Upon a full block of logged data, the Spectrum DSP equipment interrupts the PC. If the PC misses these interrupts, the data sets generated from system implementation would contain gaps. The second layer in use, Ring 3, is where the user applications run. The dynamometer GUI runs here. As long as the system critical code runs at Ring 0 in the virtual device driver, the GUI can catch up with data display and interaction. At worst case, a minimal delay may be introduced in the data display or when dynamometer parameters are adjusted at run-time. The goal is to make this delay as small as possible while maintaining full data acquisition of system data.

Results

From bottom to top, the first three layers of the PC environment for the dynamometer system have been designed, programmed, and successfully tested. The final layer, the GUI, is still under further design. Providing the appropriate dynamometer functionality while displaying interface objects in a way best suited for operation can become time consuming for the window's programmer. The key is in presenting the correct information in a correct way so as not to confuse or delay the dynamometer operator.

Apart from learning the details to specific Microsoft Windows 3.x operations such as building and using Dynamic Linked Libraries (DLLs), the understanding, design, and programming of a Windows 3.x Virtual Device Driver consumed many days. The VxD written for use with this system was designed to be general in the way we add DSP functionality and communications. From this groundwork, future VxD's can be written to accommodate new DSP equipment.

Future Work

A large part of the software environment designed for implementing an active dynamometer has been completed. Upon completion of the DSP code generation library, the first version of the PC environment will be ready for full testing. At that point, acquired test data, maximum control strategy rates, and maximum data logging rates for the complete system will be available.

Conclusion

The software environment to implement a DSP-based active dynamometer has been designed for controlling both the dynamometer and machine under test while providing data acquisition capabilities for machine analysis. This environment, divided into four layers, creates a flexible data acquisition and control system implemented through a simple systems definition language. It also provides the ability to interchange different types of DSP equipment and introduce future DSP equipment.

References

Hazzah, Karen. *Writing Windows VxDs and Device Drivers*, Lawrence, KS.: R&D Publications, 1995.

Thielen, David, and Woodruff, Bryan. *Writing Windows Virtual Device Drivers*. Addison-Wesley Publishing Company, 1995.

Holzner, Steven. Borland C++ Windows Programming. Indianapolis, IN.: Brady Publishing, 1994.

Borland International, Inc. *ObjectWindows Programmers Guide Version 2.5*. Scotts Valley, CA.: Borland Press, 1994.

Borland International, Inc. *ObjectWindows Reference Guide Version 2.5*. Scotts Valley, CA.: Borland Press, 1994.

Borland International, Inc. *Borland C++ Programmers Guide Version 4.5*. Scotts Valley, CA.: Borland Press, 1994.

Spectrum Signal Processing Inc. *TMS320C30 Processor Board User's Manual*. Burnaby, B.C.

Spectrum Signal Processing Inc. *32 Channel Digital I/O Board User's Manual*. Burnaby, B.C.

Spectrum Signal Processing Inc. *32 Channel Analog I/O Board User's Manual*. Burnaby, B.C.

Spectrum Signal Processing Inc. *16 Channel Analog Output Board User's Manual*. Burnaby, B.C.

Integrated Motions, Inc. *DS-2 Controller / Data Acquisition Module*. Berkeley, CA.

Integrated Motions, Inc. *MX31 Modular Embedded System*. Berkeley, CA.

A STUDY OF SUPER CAPACITOR APPLICATIONS

Robert C. Cravens, II
Department of Electrical Engineering

Ohio University
Athens, OH 45701

Final Report for:
Graduate Summer Research Program
Wright Laboratory

August 1995

A STUDY OF SUPER CAPACITOR APPLICATIONS

Robert C. Cravens, II
Department of Electrical Engineering
Ohio University
Athens, OH 45701

Abstract

The feasibility of the use of a super capacitor and DC/DC converter to improve the regulation of the bus voltage of an aircraft was studied. A boost DC/DC converter was used to transfer the energy from the capacitor to the dc bus voltage level. A buck DC/DC converter was used to transfer energy from the dc bus to the capacitor. Experimental results indicate that a super capacitor and DC/DC converter can be used to improve the regulation of the bus voltage of distributed power systems.

A STUDY OF SUPER CAPACITOR APPLICATIONS

Robert C. Cravens, II

I. INTRODUCTION

Recently, capacitors with large capacitances have been developed [1]–[4]. These capacitors are called *super capacitors*. The range of the capacitances is on the order of 1 to 500 F. However, The voltage ratings of the super capacitors is on the order of only 2.5 to 15 V.

The principal operation of super capacitors was first investigated by Helmholtz [5] in 1879. One electrode of a super capacitor is made of carbon and the other is made of a liquid electrolyte. When a positive voltage is applied to the carbon layer and the negative voltage applied to the liquid electrolyte, a thin dielectric layer is established. The plate area is extremely large, on the order of 1000 m^2/g, because of the porous surface of the carbon. The thickness of the dielectric layer is extremely small – on the order of 1 nm. As a result, a high volumetric efficiency is obtained. Capacitance densities on the order of 30 F/g of carbon and 1 F/cm^3 are achievable.

This high capacitance permits the storage of large amounts of energy which leads to a large number of new applications. A power electronics circuit can be used to condition the output voltage and current of a super capacitor. The combination of super capacitor and power electronic circuit can be called a *super battery*.

An electric aircraft contains a distributed power system. Its nominal dc line voltage is 270 V. This voltage can vary from 250 to 280 V for steady state. When actuators are activated, a larger load is added to the system. This causes an increased current to flow through the distributed line resistance and inductance thereby reducing the voltage seen at the load. Super capacitors can be used to improve the voltage regulation at the point of load in the aircraft distributed power systems.

The objective of this research was to investigate the feasibility of improving the voltage regulation of a distributed power system.

II. LIMITATIONS OF BATTERIES

1. Environmental hazard

2. Safety problems

3. Maintenance cost

4. Slow charging

5. Limited number of charge cycles and life

6. Memory problems in some batteries such as NiCd

7. Complicated charging circuits

8. Need for continuous replacement

III. FEATURES OF SUPER CAPACITORS

1. Very high energy density (20 times that of conventional capacitors)

2. Ultra long life. They can be fully charged and discharged more than 100,000 times with an expected operating lifetime longer than 25 years. Unlike batteries, super capacitors have no parasitic chemical reactions.

3. Some super capacitors are nonpolar.

4. Some super capacitors do not require current limiting resistors or over–voltage protection.

5. Maintenance free

6. Safer than batteries – super capacitors will not explode if short circuited.

7. Volume energy density 9 Wh/L

8. Weight energy density 4 Wh/kg

9. Volume power density 900 Wh/L

10. Weight power density 400 Wh/Kg

IV. APPLICATIONS OF CAPACITORS

1. Memory backup power supplies for computers, timers, and other electronic equipment such as security systems and programmable controllers

2. Power supplies for smoke detectors

3. Power supplies for emergency lights

4. Starters, ignitors, and actuators such as ignition systems for automobiles

5. Emergency power sources for aircraft

6. Voltage regulation in distributed systems such as aircraft power systems under variable load conditions

7. Source of large instantaneous power levels such as for aircraft actuators

8. Voltage regulation of systems with switched loads such as phase radars

9. Active power filters

V. EXPERIMENTAL RESULTS OF IMPROVED VOLTAGE REGULATION USING SUPER CAPACITORS

A. Switched Load

A circuit that simulates the variations of voltage in a switched load is needed. The voltage changes normally in a continuous manner. The worst case occurs when the change takes place instantaneously. Fig. 1(a) shows a switched load circuit. It consists of a regulated dc voltage V_I, load resistors R, and a power MOSFET. When the MOSFET is off, the output voltage is $V_I/2$. On the other hand, when the switch is on, the output voltage is $V_I/3$. If the MOSFET is switched periodically at 100 Hz, the load voltage V_O will jump from $V_I/3$ to $V_I/2$ and vice versa.

B. Test Circuit for Line Voltage Regulation Improvement

Fig. 1(b) shows a test circuit for line voltage regulation improvement. It consists of a super capacitor C, a step–up DC/DC converter, a switched load, and a dc bus voltage V. When the MOSFET is turned on, the effective load resistance is a parallel combination of R_2 and R_3. This causes the output voltage V_O to decrease. The DC/DC converter transfers the energy from the super capacitor to the switched load during this time interval. As a result, the load receives more current and the voltage is increased. Therefore, the load regulation of the bus voltage is improved. On the other hand, when the load resistance is too light, the bus voltage increases and the energy is transferred from the load to the super capacitor.

In the case of unidirectional step–up converter, the lower voltage level is increased close to the upper level. The super capacitor can improve voltage regulation for a limited length of time. When the super capacitor is discharged, its voltage decreases, and the voltage transfer function of the converter increases to its maximum value. At this time, the converter stops regulating the bus voltage.

Fig. 2 shows a bidirectional DC/DC converter, super capacitor C, and a load resistance R_L. During the discharging mode of the super capacitor, the circuit acts like a boost converter and transfers the energy from the super capacitor to the bus. Conversely, during the charging mode, the circuit acts like a buck converter and transfers the energy from the bus to the super capacitor.

C. Test Results

The super capacitor was built using four Panasonic 3.3 F/5.5 V super capacitors. Two pairs of capacitors were connected in series which in turn were connected in parallel to achieve a 3.3 F/11 V super capacitor bank.

A step–up boost circuit was built using an International Rectifier IRF530 power MOSFET, a Motorola MUR860 ultrafast recovery diode, an inductor $L = 183.8\ \mu H$, and a filter capacitor $C = 47\ \mu F$. The output voltage V_L was 20 V. The switching frequency of the converter was 100 kHz.

The switched load was built using $R_1 = R_2 = R_3 = 50\ \Omega$ and an IRF530 power MOSFET. The switching frequency of the switched load was 100 Hz.

Fig. 3 shows the waveforms of the line voltage in the circuit of Fig. 2(b) with the disturbance of the line voltage caused by a switched load and improvement due to the super capacitor and boost DC/DC converter at time $t = 0, 10, 25, 35, and 40\ s$. It can be seen that the peak–to–peak bus voltage is very low at $t = 0$. As t increases, the regulation improvement deteriorates. At $t = 40\ s$, the converter quit regulating the bus voltage and there was no longer any improvement in the line voltage.

Fig. 4 shows the peak–to–peak ripple of the line voltage in the super capacitor discharge mode with a switched load. Fig. 4(a) shows the output ripple voltage V_{opp} versus time t and Fig. 4(b) shows the output ripple voltage V_{opp} versus super capacitor voltage V_C.

D. Fixed Load

Fig. 5(a) shows the output voltage V_O of the super capacitor versus time t with a fixed load resistance $R_L = 100\ \Omega$. Fig. 5(b) shows the output voltage V_O versus super capacitor voltage V_C with a fixed load resistance $R_L = 100\ \Omega$.

VI. SUPER CAPACITOR CHARACTERISTICS

Fig. 6(a) shows the measured plots of capacitance C_S and equivalent series resistance R_S versus frequency f for Panasonic 3.3 F/5.5 V super capacitor. The capacitance decreases with frequency substantially as does the equivalent series resistance. The self resonant frequency occurs at approximately 290 kHz. The magnitude $|\ Z\ |$ and phase ϕ of the super capacitor versus frequency are shown in Fig. 6(b). The equipment used did not all the measurement of the capacitor below 100 Hz.

VIII. CONCLUSIONS

Experimental evidence has shown that super capacitors can be used to improve the line voltage regulation. In the demonstrated experiment, the line voltage regulation was improved for approximately 35 s. Super capacitors can be also used to provide emergency power at fix loads.

References

[1] The Evans Capattery Data Sheets.

[2] The Evans Capattery, The Next Generation in Double–Layer Capacitors, Technical Papers 1989–1994.

[3] Cesiwid Maxcap Double Layer Capacitors, Product Information and Application Data.

[4] The Fourth International Seminar on Double Layer Capacitors and Similar Energy Storage Devices, Boca Raton, FL, December 12–14, 1994.

[5] H. L. von Helmholtz, "Wied. Ann.," 7, 33, 1879.
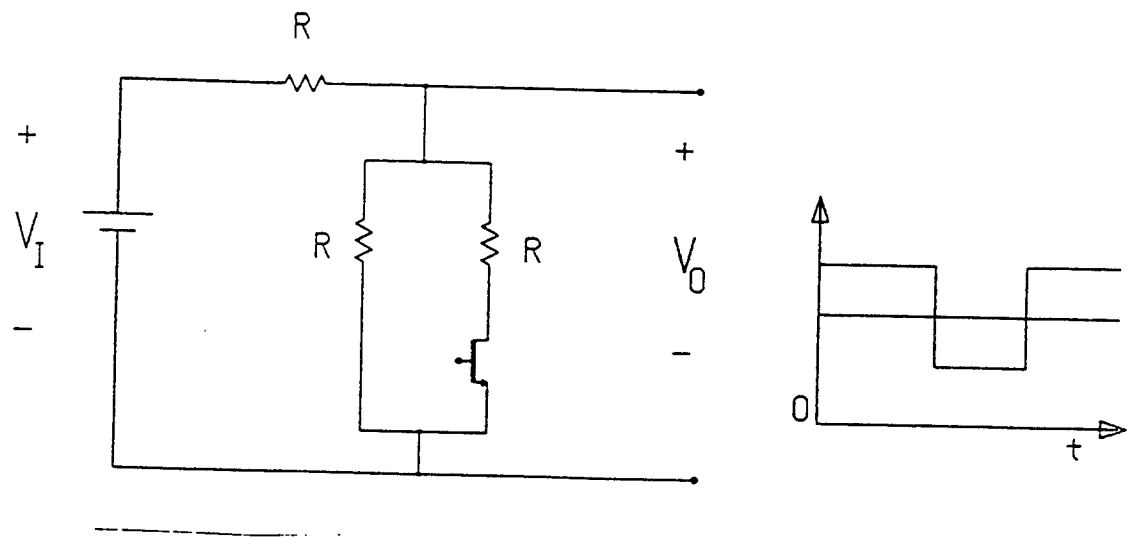
(a)
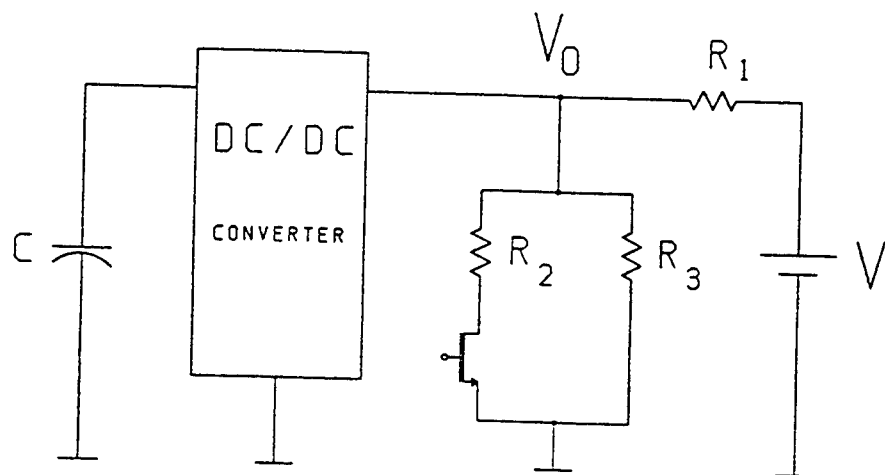
(b)

Figure 1: (a) Circuit diagram of switched load. (b) Line regulation improvement test circuit consisting of super capacitor C, DC/DC converter, switched load, and bus voltage V.
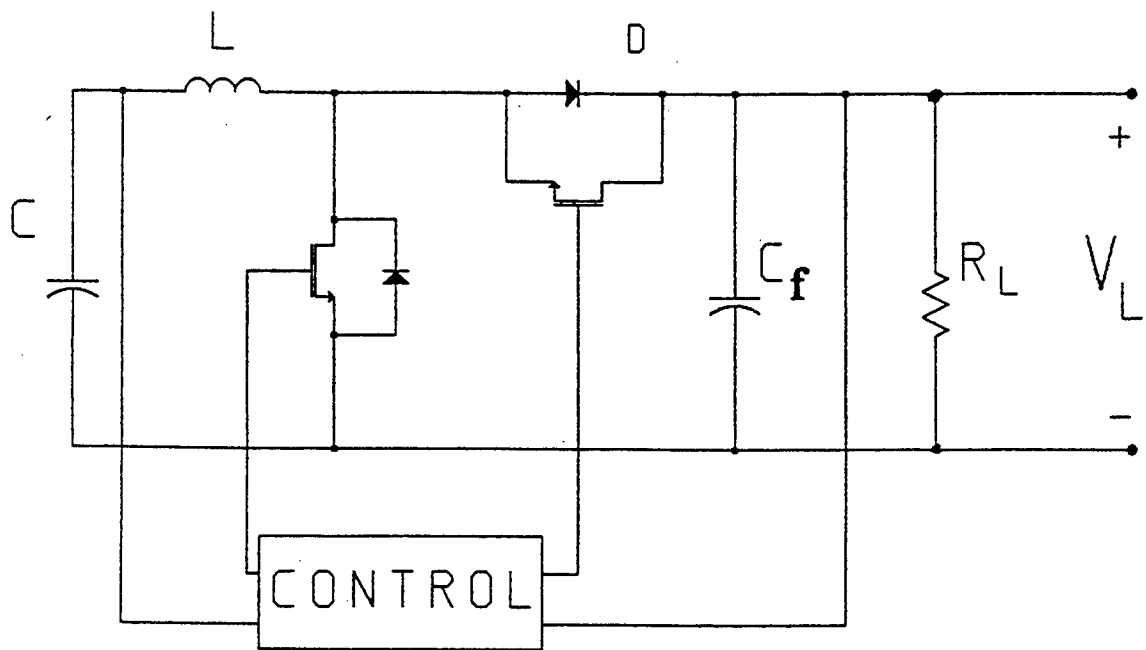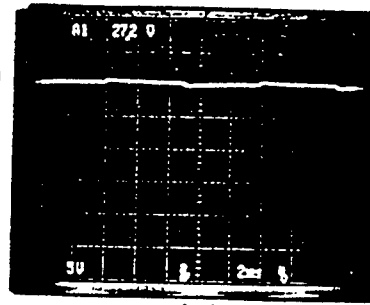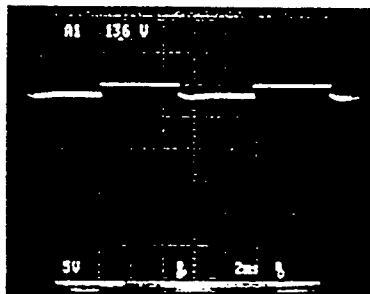
Figure 2: Circuit diagram of bidirectional DC/DC converter, super capacitor C, and load R_L.

$V_O(V)$

(a)   t = 0

(b)   t = 10 s

(c)   t = 25 s

(d)   t = 35 s

(e)   t = 40 s
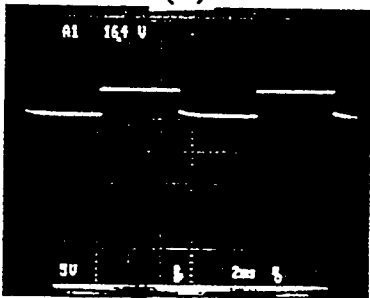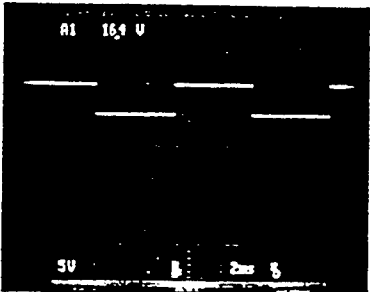
Figure 3: Waveforms of the line voltage in the circuit of Fig. 3(b) with the disturbance of the line caused by a switched load and improvement due to the super capacitor and bidirectional DC/DC converter. (a) At $t = 0$. (b) At $t = 10$ s. (c) At $t = 25$ s. (d) At $t = 35$ s. (e) At $t = 40$ s. Horizontal: 2 ms/div. Vertical: 5 V/div.

10-10
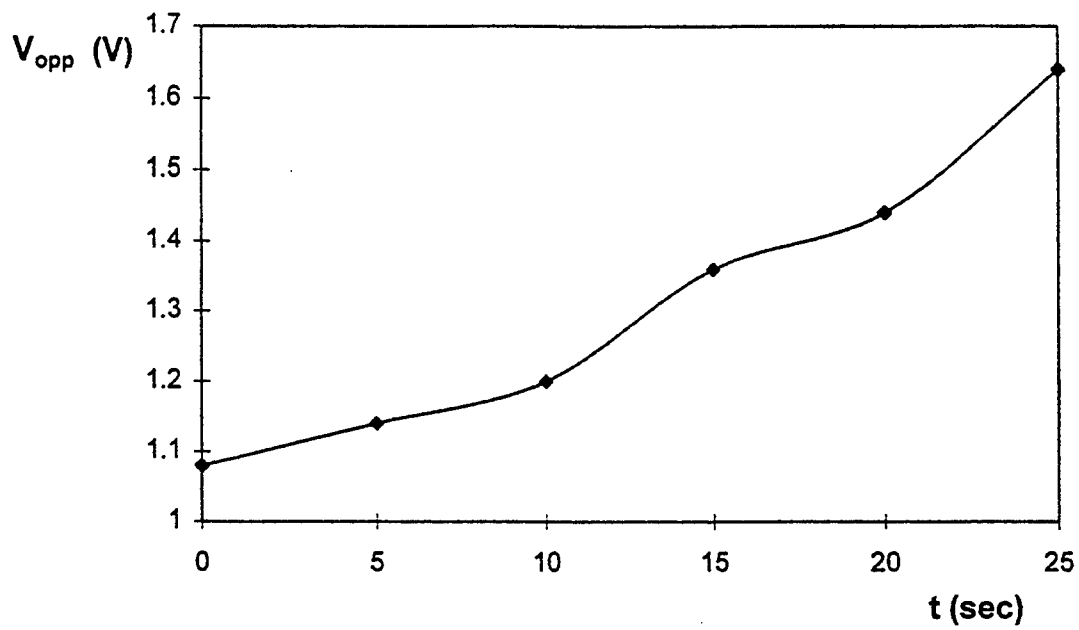
(a)
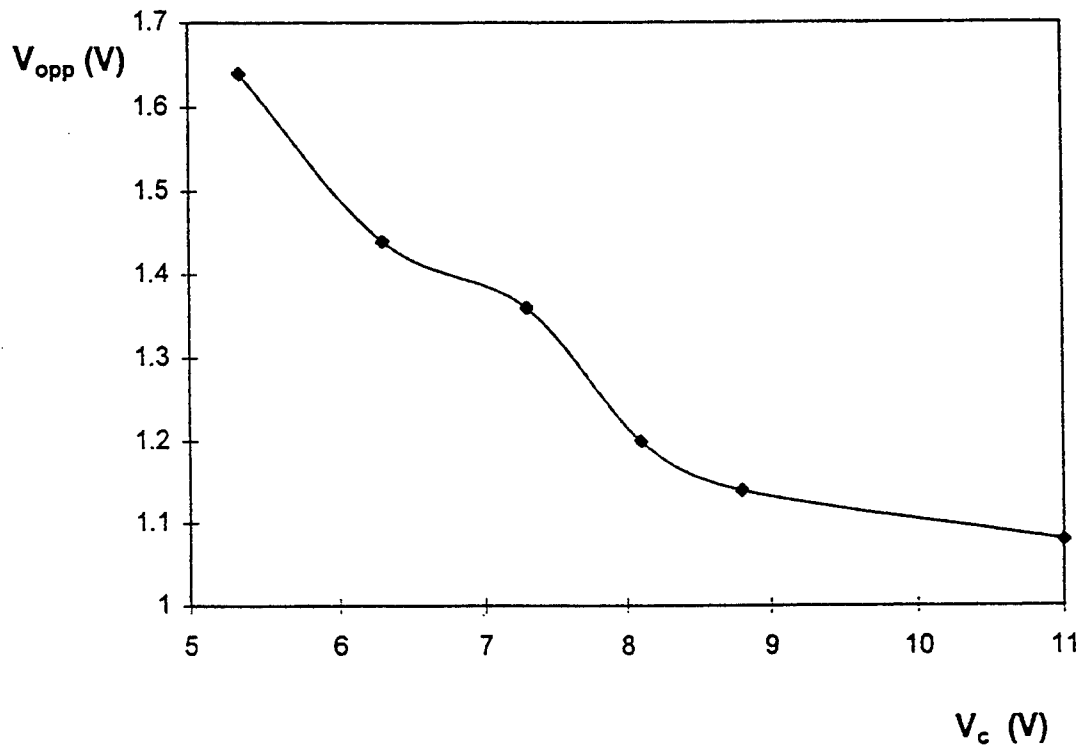
(b)

Figure 4: Peak–to–peak ripple of the line voltage in the super capacitor discharge mode with switched load. (a) Output ripple voltage V_{opp} versus time t. (b) Output ripple voltage V_{opp} versus super capacitor voltage V_C.
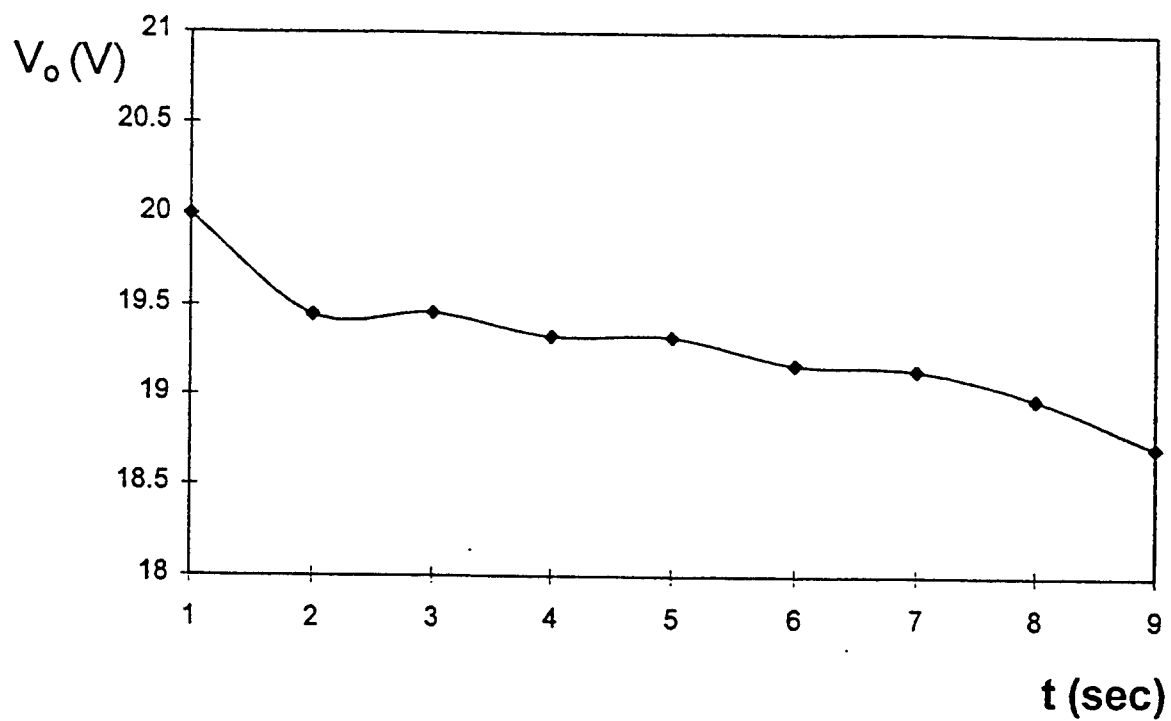
(a)
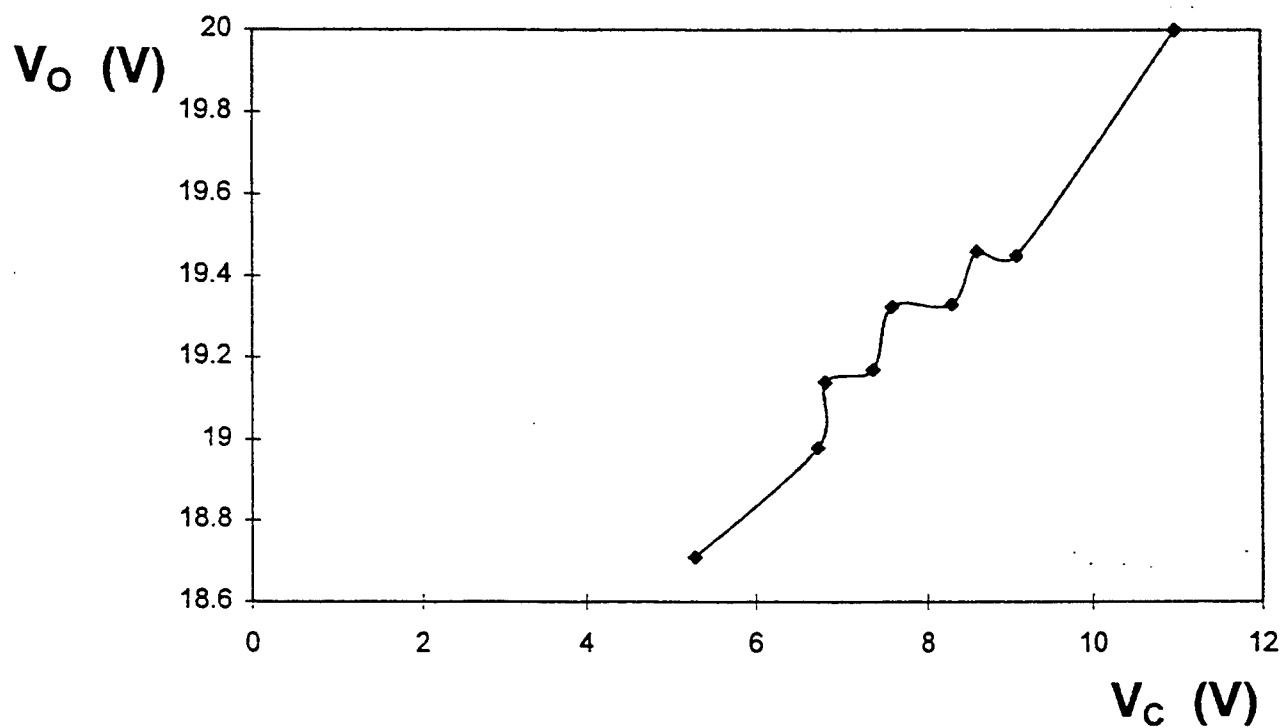
(b)

Figure 5: Output voltage in the super capacitor discharge mode with fixed load. (a) Output voltage V_O versus time t. (b) Output voltage V_O versus super capacitor voltage V_C.
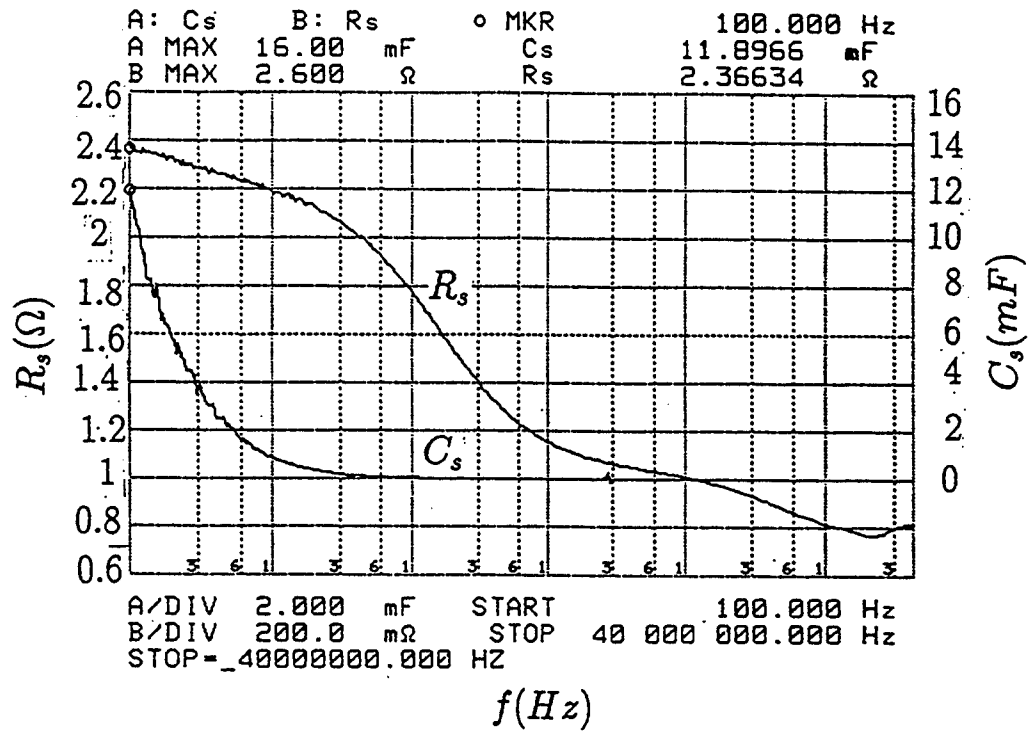
(a)
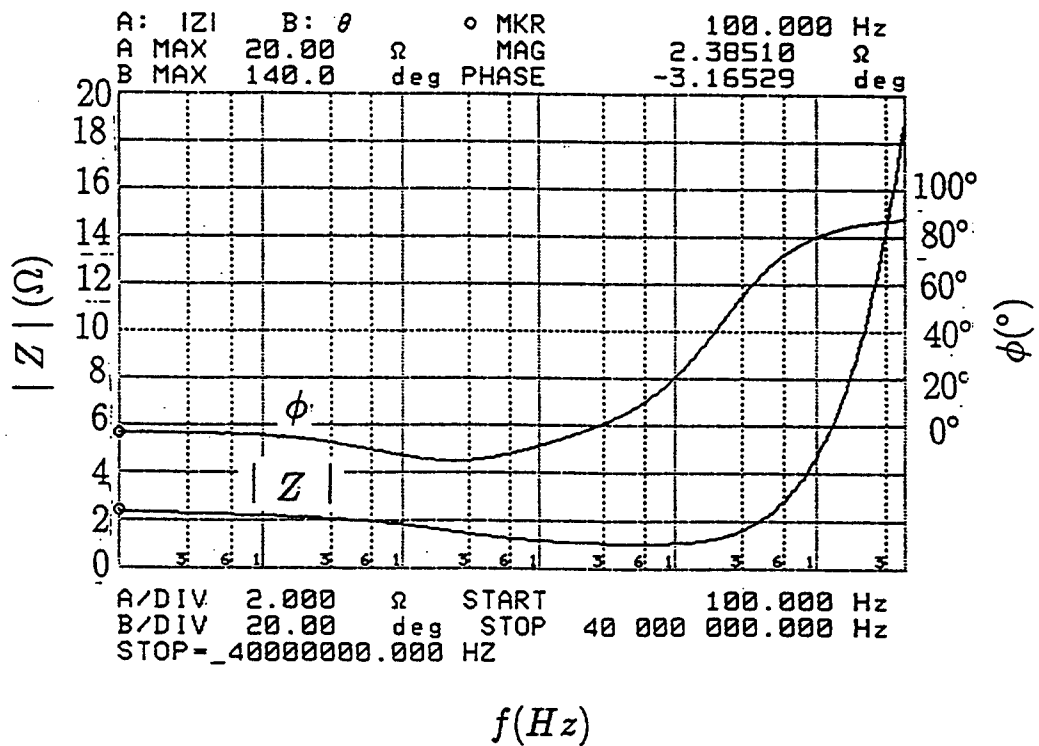
(b)

Figure 6: Super capacitor characteristics. (a) Capacitance C_S and equivalent series resistance R_S versus frequency f. (b) Magnitude $| Z |$ and phase ϕ of the super capacitor impedance versus frequency f.

Denisha Dawson Report not available at time of publication.

TECHNIQUES TO SUPPRESS A NEAR FIELD SCATTERER
IN DIRECTION FINDING

Edward Michael Friel
Graduate Student
Department of Electrical Engineering

University of Dayton
300 College Park
Dayton, Ohio 45469-0226

September 1995

TECHNIQUES TO SUPPRESS A NEAR FIELD SCATTERER
IN DIRECTION FINDING

Edward Michael Friel
Graduate Student
Department of Electrical Engineering
University of Dayton

Abstract

It is often necessary to estimate the angles of arrival of incident signals with a small angular separation. This estimate may be corrupted by an object in the near field of the antenna array that scatters energy toward the array. In this report, two techniques are presented to suppress the effects of a near field scatterer. The first technique suppresses the interference from the scatterer by modifying the array configuration such that a null is placed at the point of the scatterer. This technique successfully suppresses the scatterer and only reduces the number of effective antenna elements by one. The disadvantage of this technique is that it requires knowing the location of the scatterer. The second technique attempts to estimate the angles of arrival by first decorrelating the incident signals from the scattered signals by using spatial smoothing. It is shown in this report that standard spatial smoothing technique can be applied even for signals with non-planar wavefronts such as those from a near field scatterer. The angles of arrival can then be accurately estimated although a small spurious peak now occurs in the spatial spectrum. The advantage of this technique is that it does not require knowing the location of the scatterer. The disadvantage is that the number of elements in the antenna array must be twice the number of decorrelated signals or four times the number of uncorrelated incident plane waves.

Table of Contents

TECHNIQUES TO SUPPRESS A NEAR FIELD SCATTERER
IN DIRECTION FINDING

Edward Michael Friel

1.0 Introduction

It is often necessary to estimate the angles of arrival of incident signals. It is desirable to accomplish this with a high resolution direction finding algorithm such as the MUltiple SIgnal Classification (MUSIC) algorithm since only a small number of channels are available. This algorithm, along with other parametric "super-resolution" algorithms is very susceptible to errors in the signal model. In particular, it has been shown that ignoring the mutual coupling effects between the antenna elements prevents the MUSIC algorithm from resolving two signals with a small angular separation [1]. The resolution of the MUSIC algorithm can be restored by first pre-processing the signal with the terminal impedance matrix derived from the method of moments model of the antenna array [1]. The signals at the antenna array may also be corrupted by an object in the near field of the array [1]. This object scatters spherical waves that prevent the resolution of the incident signals as shown in figure 1. This object may be a nearby airplane wing or the inside of the antenna array's radome as shown in figure 2. This work examines two techniques for compensating for the effects of a near field scatterer.

The first technique attempts to suppress the interference from the scatterer [1]. This is accomplished by modifying the antenna array configuration. This produces a change in the search vector of the MUSIC algorithm. The result is that the resolution of the MUSIC algorithm is restored to that of the ideal case with no scatterer present. This technique, however, requires knowing the location of the scatterer. The new array configuration also decreases the number of effective antenna elements by one. This implies that the number of signals that can be estimated with the new configuration also decreases by one.

The second technique attempts to compensate for the interference by decorrelating the incident signals from the interference and searching for only the incident signals. This is accomplished by using a spatial smoothing technique before applying the MUSIC algorithm. This technique does not require knowing the location of the scatterer. The primary disadvantage of this technique is that it greatly reduces the number of effective channels and therefore the number of incident signals that can be estimated.
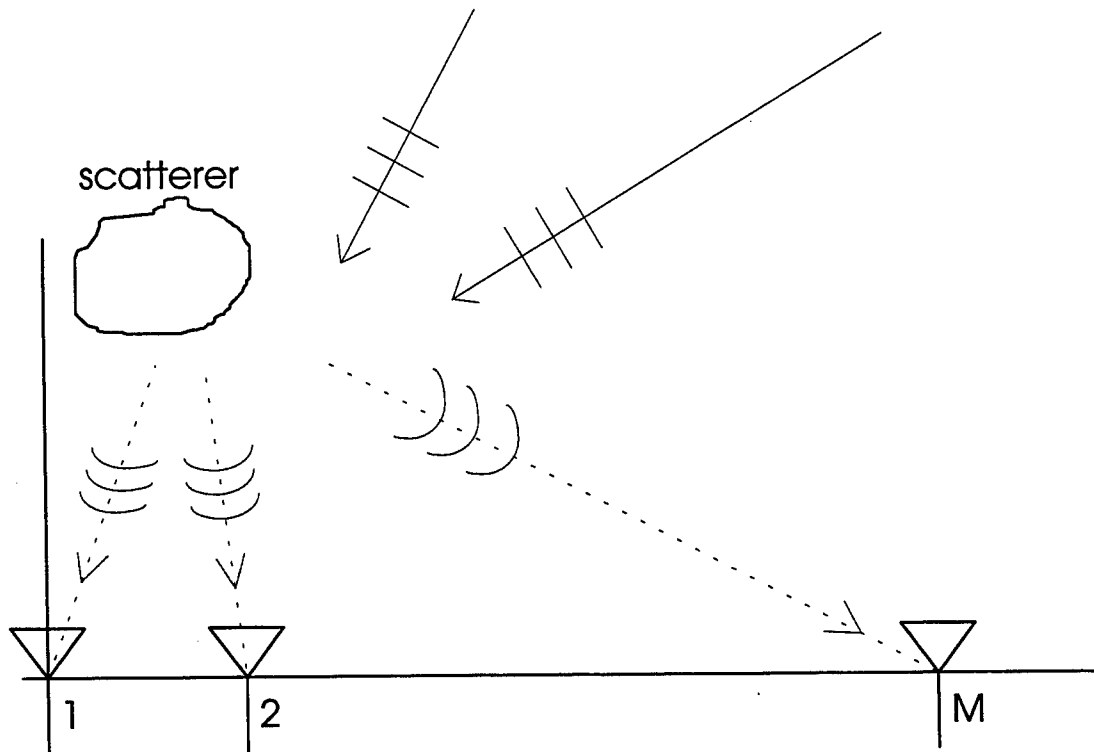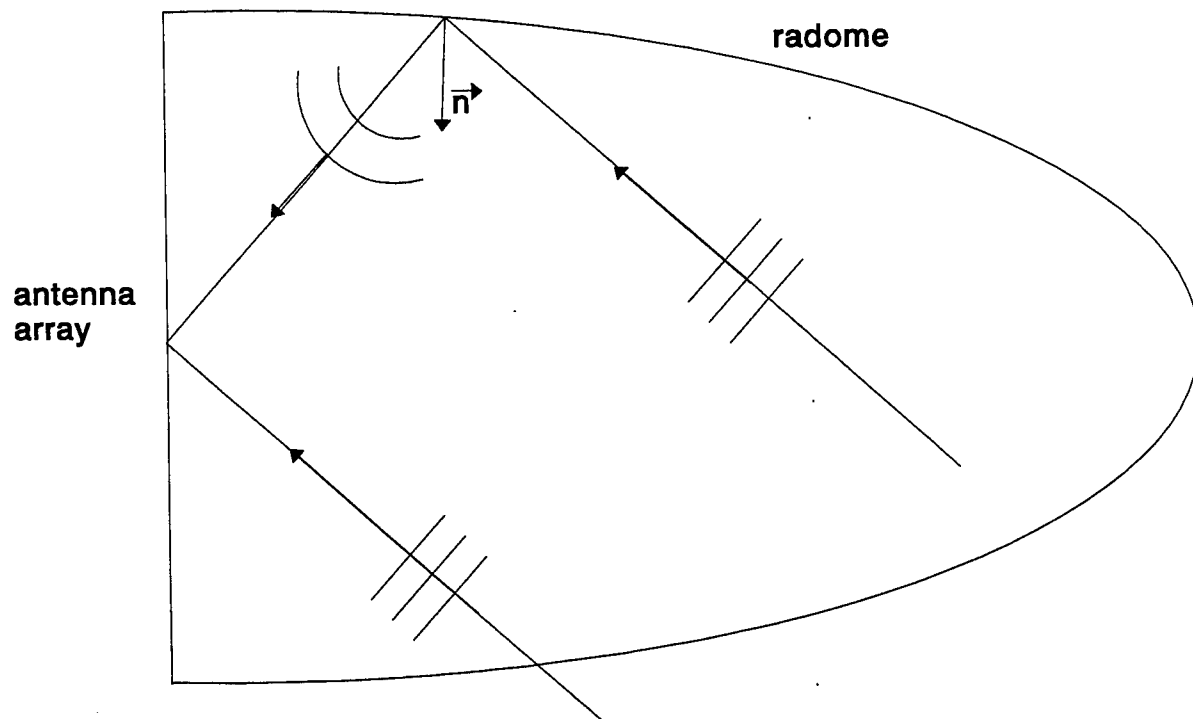
Figure 1: Geometry of Array, Sources, and Scatterer

Figure 2: Near Field Scattering by the Inside of a Radome

2.0 MUSIC Algorithm

The MUltiple SIgnal Classification (MUSIC) algorithm [4,5] is a very popular parametric method for estimating the angles of arrival of incident signals. This is primarily because its resolution capability is limited only by the signal to noise ratio. To apply the algorithm, the covariance matrix at the output of the antenna array is decomposed into its eigenvalues and eigenvectors. The eigenvectors associated with the noise can be separated from the eigenvectors associated with the signal by examining the eigenvalues. The noise eigenvectors are then used to form the noise subspace. The MUSIC spectrum is computed by searching for the plane waves with angles of arrival that are orthogonal to the noise subspace. Mathematically, the spectrum is computed with the equation

$$P(\phi) = \frac{1}{\displaystyle\sum_{i=K+1}^{M} \left| \vec{\beta}_i^{H} \vec{a}(\phi) \right|^2} \tag{1}$$

where K is the number of independent signals, M is the number of antenna elements, $\vec{\beta}_i$ is i^{th} noise eigenvector, and $\vec{a}(\phi)$ is the search vector given by the equation

$$\vec{a}(\phi) = [\ e^{-j\beta d_1 \cos\phi} \quad e^{-j\beta d_2 \cos\phi} \quad \cdots \quad e^{-j\beta d_M \cos\phi}\ ]^T \ . \tag{2}$$

Note that if $K \geq M$ then there will be no noise eigenvectors to form the noise subspace and the algorithm can not be used.

3.0 Effects of a Near Field Scatterer

The effects of a near field scatterer on the MUSIC algorithm are illustrated using the array and sources in figure 3. In this case, interference in the form of spherical waves are incident upon a nine element linear array designed to resolve narrowband signals over an one octave bandwidth. The design of this array is discussed in [1]. In this figure only the spherical waves are shown. The two plane waves are at 300 MHz and 305 MHz with angles of incidence at 45° and 55° relative to the x-axis. The spherical waves represent interference from a near field scatterer. These spherical waves are also at 300 MHz and 305 MHz since they simulate the scattering of the incident plane waves.

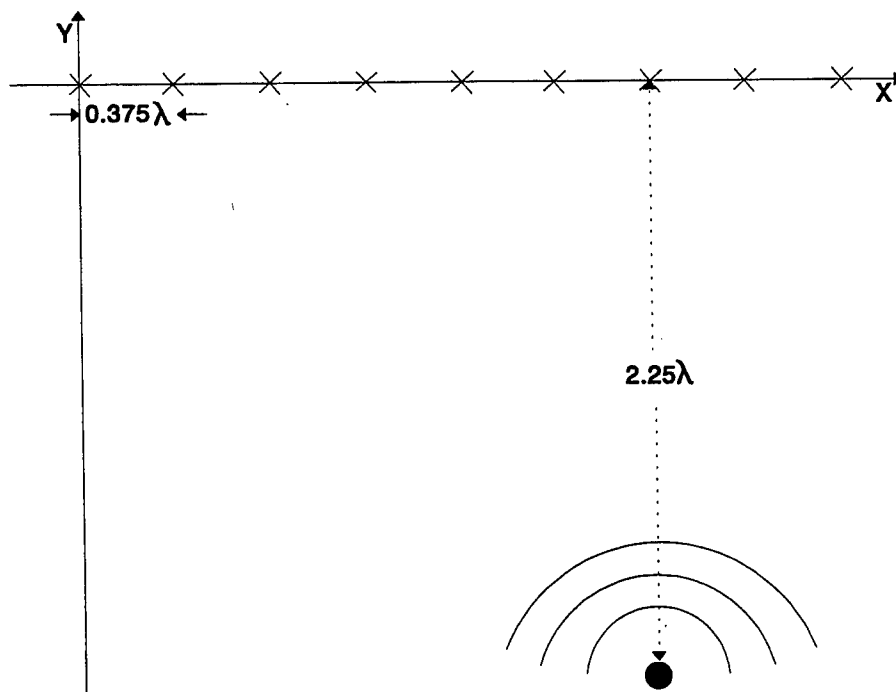Figure 4 shows the MUSIC spectrum for the problem in figure 3 for several different signal to interference

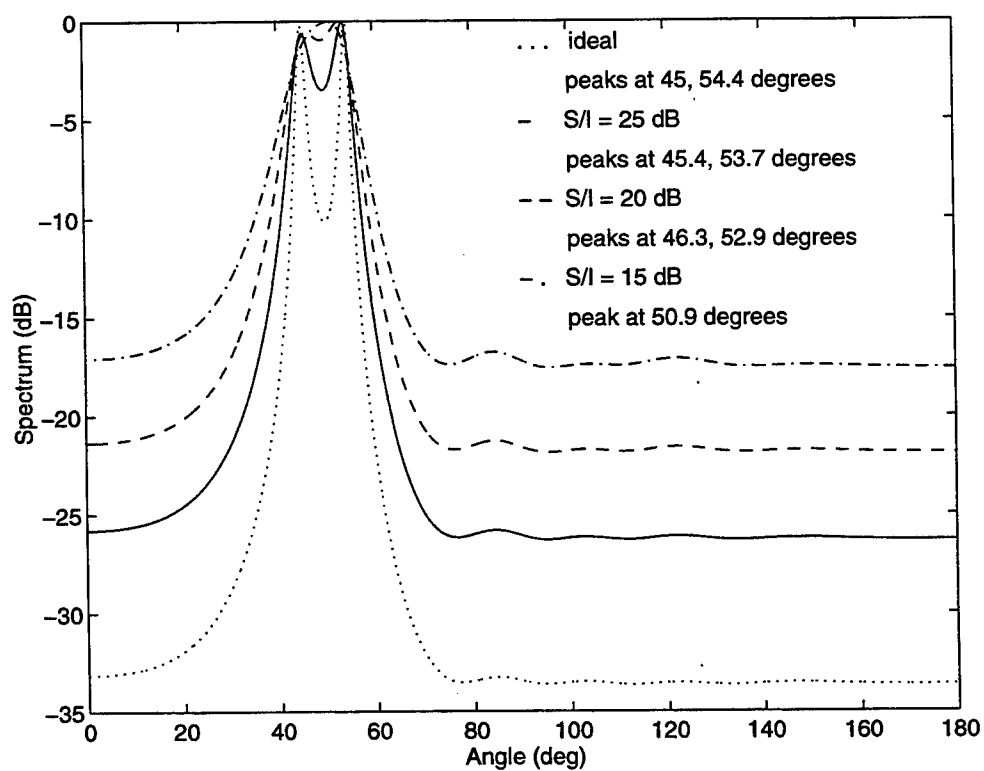**Figure 3: Plane and Spherical Waves Incident Upon an Array**

Figure 4: Effect of Spherical Waves on the MUSIC Spectrum

ratios (S/I). The plane waves are the desired signals and the spherical waves are the interference. The spectrum is a normalized average of twenty simulations. The ideal spectrum which shows the result of the MUSIC algorithm when no spherical waves are present is also included in figure 4. Notice that as the S/I ratio decreases, the two peaks began to merge. Notice also that when the S/I ratio is 15 dB the two signals can no longer be resolved. Figure 4 shows that even when the power in the plane waves is much greater than that in the interference, the resolution capability of the MUSIC algorithm is greatly affected.

4.0 Electromagnetic Model of the Array and Scatterer

The current on the antenna array due to the incident plane waves is calculated by solving the reaction integral equation. This equation is reduced to a system of linear equations using the method of moments [2]. Piecewise sinusoidal modes are used for both the weighting and testing functions in the method of moments to produce an accurate solution with only a few equations [2]. The piecewise sinusoidal expansion of the current on a dipole is shown in figure 5. In this case the current is shown composed of three piecewise sinusoids. The scatterer is incorporated into the system of equations by using a hybrid technique that combines the method of moments with the Uniform Theory of Diffraction [2,3]. This creates a system of equations that yields the current on all points of the antenna due to both the incident plane waves and the interference from the scatterer.

The system of equations which incorporates the scatterer is given in equation (3).

$$\sum_{n=1}^{N}(Z_{mn} + Z_{mn}^{g})I_{n} = (V_{m} + V_{m}^{g}) \qquad m = 1,2,...,N \qquad (3)$$

where Z_{mn} is the mutual coupling between piecewise sinusoidal modes m and n, Z_{mn}^{g} is the mutual coupling modes m and n through the scatterer, I_{n} is the piecewise sinusoidal current at mode n; V_{m} is the excitation at mode m due to the incident electric field, and V_{m}^{g} is the excitation at mode m due to the incident field scattered by the nearby object. The terms Z_{mn}, Z_{mn}^{g}, V_{m}, and V_{m}^{g} are calculated using the geometry of the array and scatterer as described in [1]. The current at all points on the antenna array is then found by solving equation (3).

5.0 Compensation for a Near Field Scatterer

To accurately suppress the effects of a near field scatterer, both the mutual coupling between the antenna elements and the scattered field from the nearby object must be compensated. The mutual coupling between two antenna elements with a scatterer present is composed of two terms. The first term is the direct mutual coupling
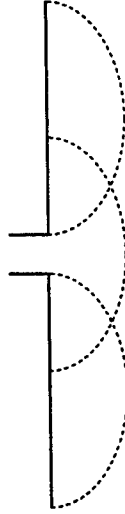
Figure 5: Piecewise Sinusoidal Current Expansion on a Dipole

between the antenna elements. The other term is the mutual coupling between the two elements through the scatterer. As shown in [1] all the mutual coupling between the antenna terminals with a scatterer present can be calculated using equation (4)

$$Z_{kl}^{Te} = \frac{1}{I_k^{Te} I_l^{Te}} \sum_{m=1+(k-1)N_m}^{kN_m} \sum_{p=1+(l-1)N_m}^{lN_m} \left[Z_{mp} + \sum_{q=1}^{N_s} Z_{mqp} \right] I_m I_p \tag{4}$$

where Z_{kl}^{Te} is the mutual coupling between antenna terminals k and l, I_k^{Te} is the current at terminal k, I_l^{Te} is the current at terminal l, N_m is the number of piecewise sinusoidal modes on one antenna element, and N_s is the number of segments comprising the scatterer. In general, since the scatterer is in the near field of the antenna array, it is decomposed into several segments so that each segment is in the far field of all the current modes on the antenna array.

Equation (4) accounts for all the mutual coupling present. In [1] it is shown that the mutual coupling directly between the antenna elements is much stronger than the mutual coupling between the elements through the scatterer. Mathematically, this can be stated as

$$Z_{mp} >> \sum_{q=1}^{N_s} Z_{mqp} \qquad \text{for every m and p.} \tag{5}$$

This reduces equation (4) to

12 - 9

$$Z_{kl}^{Te} = \frac{1}{I_k^{Te} I_l^{Te}} \sum_{m=1+(k-1)N_m}^{kN_m} \sum_{p=1+(l-1)N_m}^{lN_m} Z_{mp} I_m I_p \qquad (6)$$

Therefore, while Z_{mn}^g is still calculated and used to determine the currents on the array using equation (3), it is not necessarily to know it when compensating for the mutual coupling effects. Therefore, it is not necessary to know the location or even the type of scatterer to determine the terminal impedance matrix.

It is still necessary to compensate for the interference due to the plane waves scattered by the near field object. Mathematically the objective is to suppress V_m^g such that equation (3) becomes

$$\sum_{l=1}^{M} Z_{kl}^{Te} I_l = V_k \qquad k = 1,2,...,M \qquad (7)$$

where M is the number of antenna elements, Z_{kl}^{Te} is the terminal impedance matrix calculated using equation (6), I_l is the piecewise sinusoidal current at terminal l, and V_k is the voltage at the kth terminal of the array. Therefore, it only remains to suppress the field scattered by the nearby object to leave the voltage, V_k, due to the incident plane waves. Two techniques are now presented to suppress the interference from the scatterer.

5.1 Near Field Scatterer Nulling Technique

The first technique used to suppress the interference from the scatterer uses a modified antenna array configuration and search vector. The antenna elements are combined in pairs as shown in figure 6. The weights are chosen such that a null is formed by each pair of antenna elements in the direction of the scatterer as shown in figure 7. It is shown in [1] that the weights should be chosen to satisfy the equation

$$w_i = -\frac{r_{i+1}}{r_i} e^{-j\beta(r_i - r_{i+1})} \qquad (8)$$

where w_i is the weight at the ith antenna pair, r_i is the distance from the ith antenna element to the scatterer, and β is the phase propagation constant. Notice that each pair of elements shares at least one of its original elements with another pair of elements. Therefore, the uncorrelated noise sources at the original elements will be partially correlated with neighboring elements at the new antenna elements. Next, it is necessary to determine the effects of combining the elements in pairs on the MUSIC algorithm. This is accomplished by first developing a model for the signal at the outputs of the new antenna elements.

12 - 10
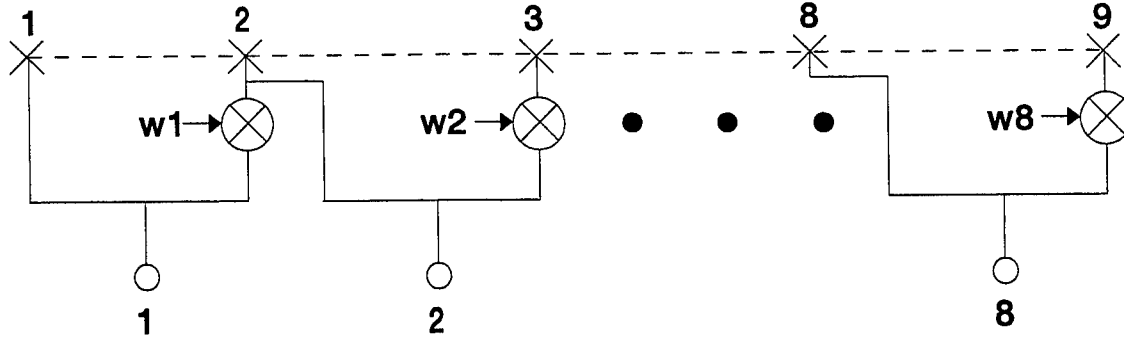
Figure 6: Configuration for Near Field Scatterer Nulling
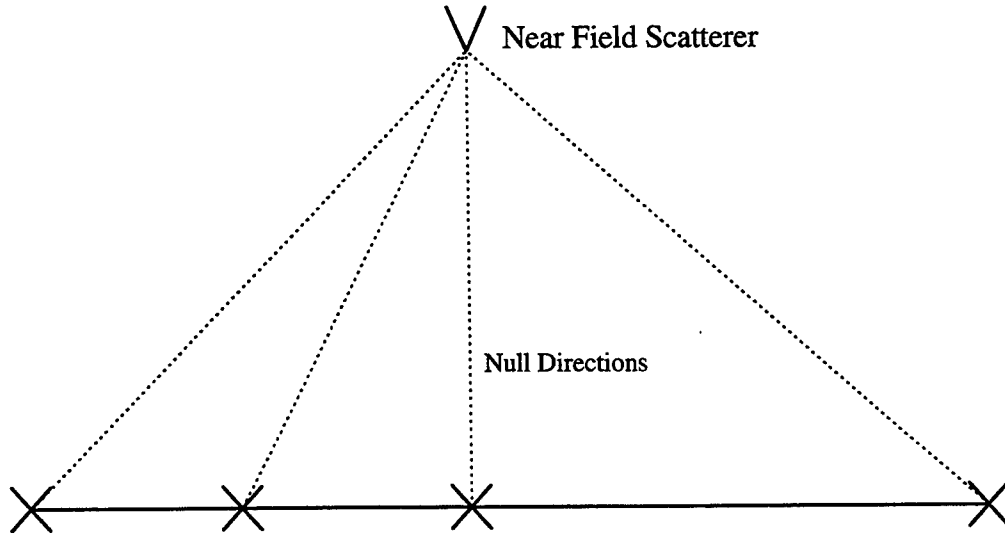
Figure 7: Equivalent Elements with Nulls in the Direction of the Scatterer

5.1.1 Signal Model

The signal at the output of the new array in figure 6 is given by the expression

$$x_i(t) = \sum_{k=1}^{K} u_k(t) [e^{+j\beta d_i \cos(\phi_k)} + w_i e^{+j\beta d_{i+1} \cos(\phi_k)}] + n_i(t) + w_i n_{i+1}(t) \qquad (9)$$

where $u_k(t)$ is the kth narrowband plane wave, β is the phase propagation constant, d_i is the distance from the origin to the ith antenna element, ϕ_k is the incident angle of the kth signal, $n_i(t)$ is the noise at the ith antenna element, w_i is the complex weight for the ith antenna pair, and K is the number of independent far field sources. For two signals equation (9) becomes

$$\vec{x} = A\vec{u} + \vec{n}_a + \vec{n}_b \qquad (10)$$

12 - 11

where

$$A = \begin{bmatrix} e^{+j\beta d_1 \cos\phi_1} + w_1 e^{+j\beta d_2 \cos\phi_1} & e^{+j\beta d_1 \cos\phi_2} + w_1 e^{+j\beta d_2 \cos\phi_2} \\ \vdots & \vdots \\ e^{+j\beta d_8 \cos\phi_1} + w_8 e^{+j\beta d_9 \cos\phi_1} & e^{+j\beta d_8 \cos\phi_2} + w_8 e^{+j\beta d_9 \cos\phi_2} \end{bmatrix} \tag{11}$$

$$\vec{u} = [\, u_1(t) \quad u_2(t) \,]^T \tag{12}$$

$$\vec{n}_a = [\, n_1(t) \quad n_2(t) \quad \cdots \quad n_8(t) \,]^T \tag{13}$$

$$\vec{n}_b = [\, w_1 n_2(t) \quad w_2 n_3(t) \quad \cdots \quad w_8 n_9(t) \,]^T \tag{14}$$

The covariance matrix is given by

$$R_x = E[\, \vec{x}\, \vec{x}^H \,] = E[(A\vec{u} + \vec{n}_a + \vec{n}_b)\,(A\vec{u} + \vec{n}_a + \vec{n}_b)^H] \tag{15}$$

where E [•] denotes mathematical expectation. As shown in [1], equation (15) reduces to

$$R_x = A R_u A^H + \sigma^2 \sum_\eta \tag{16}$$

where R_u is the covariance matrix of the incident signals given by the expression

$$R_u = E[\vec{u}\,\vec{u}^H] \tag{17}$$

and

$$\sum_\eta = \begin{bmatrix} 1+|w_1|^2 & w_1 & 0 & \cdots & 0 \\ w_1^* & 1+|w_2|^2 & w_2 & \cdots & 0 \\ 0 & w_2^* & 1+|w_3|^2 & \cdots & 0 \\ \vdots & \vdots & \vdots & \ddots & w_7 \\ 0 & 0 & 0 & w_7^* & 1+|w_8|^2 \end{bmatrix} \tag{18}$$

The matrix $\sum_\eta$ shows that the noises sources at the output of the new antenna elements are partially correlated with their neighboring elements. By applying the Mahalanobis transformation [6],

$$\vec{y} = \sum_\eta^{-1/2} \vec{x} \tag{19}$$

the covariance matrix becomes

$$R_y = \sum_\eta{}^{-1/2} A R_u A^H \sum_\eta{}^{-H/2} + \sigma^2 I \tag{20}$$

where I is the identity matrix. The noise sources are now uncorrelated. The MUSIC spectrum is calculated by first decomposing the matrix R_y into its eigenvalues and eigenvectors. The noise eigenvectors are then used with the search vector in equation (21) to compute the spectrum using equation (1).

$$a(\phi) = \sum_\eta{}^{-1/2} \begin{bmatrix} e^{+j\beta d_1 \cos\phi} & + & w_1 e^{+j\beta d_2 \cos\phi} \\ & \vdots & \\ e^{+j\beta d_8 \cos\phi} & + & w_8 e^{+j\beta d_9 \cos\phi} \end{bmatrix} \tag{21}$$

5.2 Decorrelation Technique

The second technique attempts to estimate the angles of arrival by first decorrelating the incident signals with those from the near field scatterer. Since the interference is from a scatterer, the scattered fields are coherent with the incident fields. This analysis shows that when the coherent signals have a non-planar wavefront, they can still be decorrelated from the incident signals using the data smoothing technique in [4]. The decorrelation of the signals is accomplished by dividing the original array into several smaller subarrays and averaging the covariance matrices from each of the arrays. To show that the averaging procedure decorrelates the signals even when they have a non-planar wavefront, it is first necessary to develop a model of the signal at the output of the linear antenna array. The output of the array is given by

$$\bar{x} = [x_1\ x_2 \cdots x_9]^T \tag{22}$$

where the elements of the vector are defined below

$$x_1 = u_1 e^{-j\beta d_1 \cos\phi_1} + \alpha_{11} u_1 e^{-j\beta d_1 \cos\psi} + u_2 e^{-j\beta d_1 \cos\phi_2} + \alpha_{21} u_2 e^{-j\beta d_1 \cos\psi} + n_1$$

$$x_2 = u_1 e^{-j\beta d_2 \cos\phi_1} + \alpha_{12} u_1 e^{-j\beta d_2 \cos\psi} + u_2 e^{-j\beta d_2 \cos\phi_2} + \alpha_{22} u_2 e^{-j\beta d_2 \cos\psi} + n_2 \tag{23}$$

$$\vdots \qquad\qquad \vdots \qquad\qquad \vdots \qquad\qquad \vdots$$

$$x_9 = u_1 e^{-j\beta d_9 \cos\phi_1} + \alpha_{19} u_1 e^{-j\beta d_9 \cos\psi} + u_2 e^{-j\beta d_9 \cos\phi_2} + \alpha_{29} u_2 e^{-j\beta d_9 \cos\psi} + n_9.$$

In equation (23) u_1 and u_2 are the incident signals, β is the phase propagation constant, d_i is the distance from the origin to the ith element, ϕ_1 is the angle of signal u_1, ϕ_2 is the angle of u_2, ψ is the angle or the scattered signal with

12 - 13

respect to the first element, and n_1, n_2, through n_9 are the independent Gaussian noise sources at elements 1 through 9 respectively. Note that if the scatterer is in the far field of the array, the scattered signals are plane waves and $\alpha_{11} = \alpha_{12} = ... = \alpha_{19}$, and $\alpha_{21} = \alpha_{22} = ... = \alpha_{29}$. Note also that $\alpha_{11} \neq \alpha_{21}$, $\alpha_{12} \neq \alpha_{22}$, ..., $\alpha_{19} \neq \alpha_{29}$ since these values are dependent upon the reflection coefficient which is a function of both the angle of incidence and the angle of reflection. For the general case of a near field scatterer the previous equations can be expressed in matrix form as

$$
\begin{bmatrix} x_1 \\ \vdots \\ x_9 \end{bmatrix} = \begin{bmatrix} e^{-j\beta\, d_1 \cos\phi_1} & \alpha_{11} e^{-j\beta\, d_1 \cos\psi} & e^{-j\beta\, d_1 \cos\phi_2} & \alpha_{21} e^{-j\beta\, d_1 \cos\psi} \\ \vdots & \vdots & \vdots & \vdots \\ e^{-j\beta\, d_9 \cos\phi_1} & \alpha_{19} e^{-j\beta\, d_9 \cos\psi} & e^{-j\beta\, d_9 \cos\phi_2} & \alpha_{29} e^{-j\beta\, d_9 \cos\psi} \end{bmatrix} \begin{bmatrix} u_1 \\ u_1 \\ u_2 \\ u_2 \end{bmatrix} + \begin{bmatrix} n_1 \\ n_2 \\ \vdots \\ n_9 \end{bmatrix}. \quad (24)
$$

since there are two incident signals and two correlated signals from the scatterer, there must be at least five elements in one subarray. This is necessary so that there will be at least one eigenvector to form the noise subspace. Since there are nine elements, five subarrays can be formed as shown below.
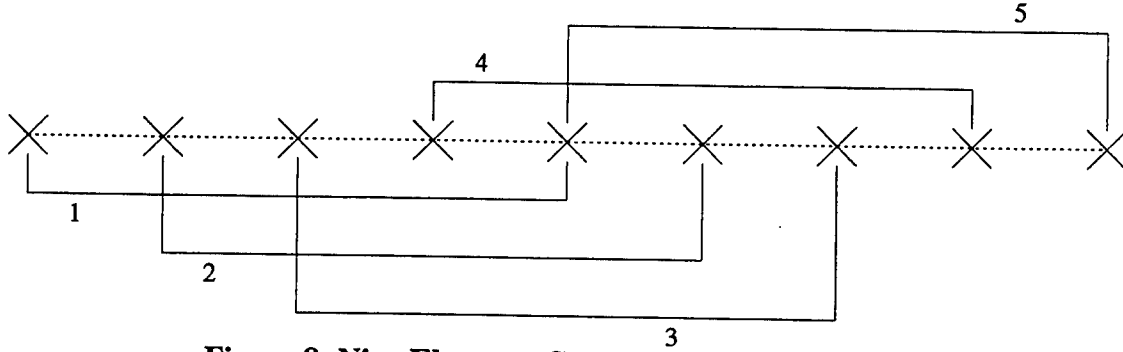
Figure 8: Nine Elements Grouped into Five Subarrays

In figure 8, the first five elements form subarray 1, elements 2 through 6 form subarray 2, etc. The output of the first subarray can be expressed as

$$
\vec{y}_1 = [\vec{B}_1 \quad k_{11}\vec{B}_2 \quad \vec{B}_3 \quad k_{21}\vec{B}_2]\vec{u} + \vec{n}_1 \quad (25)
$$

where

$$
\vec{y}_1 = \begin{bmatrix} x_1 \\ x_2 \\ \vdots \\ x_5 \end{bmatrix} \qquad \vec{B}_1 = \begin{bmatrix} e^{-j\beta\, d_1 \cos\phi_1} \\ \vdots \\ e^{-j\beta\, d_5 \cos\phi_1} \end{bmatrix} \qquad (26), (27)
$$

12 - 14

$$\vec{B}_2 = \begin{bmatrix} e^{-j\beta d_1 \cos\psi} \\ \vdots \\ e^{-j\beta d_5 \cos\psi} \end{bmatrix} \qquad \vec{B}_3 = \begin{bmatrix} e^{-j\beta d_1 \cos\phi_2} \\ \vdots \\ e^{-j\beta d_5 \cos\phi_2} \end{bmatrix} \qquad (28), (29)$$

$$k_{11} = \begin{bmatrix} \alpha_{11} & 0 & \cdots & 0 \\ 0 & \alpha_{12} & \cdots & 0 \\ \vdots & \vdots & \ddots & 0 \\ 0 & 0 & 0 & \alpha_{15} \end{bmatrix} \qquad k_{21} = \begin{bmatrix} \alpha_{21} & 0 & \cdots & 0 \\ 0 & \alpha_{22} & \cdots & 0 \\ \vdots & \vdots & \ddots & 0 \\ 0 & 0 & 0 & \alpha_{25} \end{bmatrix} \qquad (30), (31)$$

$$\vec{u} = \begin{bmatrix} u_1 \\ u_1 \\ u_2 \\ u_2 \end{bmatrix} \qquad \vec{n}_1' = \begin{bmatrix} n_1 \\ n_2 \\ \vdots \\ n_5 \end{bmatrix} \qquad (32), (33)$$

The output of the first subarray can be simplified to

$$\vec{y}_1 = [(\vec{B}_1 + k_{11}\vec{B}_2) \quad (\vec{B}_3 + k_{21}\vec{B}_2)] \begin{bmatrix} u_1 \\ u_2 \end{bmatrix} + \vec{n}_1' \qquad (34)$$

The covariance matrix of the first subarray can now be expressed as

$$R_{y1} = E\left[\vec{y}_1 \vec{y}_1^H\right] = E\left\{ [(\vec{B}_1 + k_{11}\vec{B}_2) \, (\vec{B}_3 + k_{21}\vec{B}_2)] \begin{bmatrix} u_1 \\ u_2 \end{bmatrix} [u_1^* \ u_2^*] \begin{bmatrix} (\vec{B}_1 + k_{11}\vec{B}_2)^H \\ (\vec{B}_3 + k_{21}\vec{B}_2)^H \end{bmatrix} \right\} + \sigma^2 I \quad (35)$$

where I is the identity matrix. Simplifying this yields

$$R_{y1} = E\left\{ [(\vec{B}_1 + k_{11}\vec{B}_2)u_1 + (\vec{B}_3 + k_{21}\vec{B}_2)u_2][u_1^*(\vec{B}_1 + k_{11}\vec{B}_2)^H + u_2^*(\vec{B}_3 + k_{21}\vec{B}_2)^H] \right\} + \sigma^2 I \quad (36)$$

Next, let

$$\vec{Z}_1 = [(\vec{B}_1 + k_{11}\vec{B}_2)u_1 + (\vec{B}_3 + k_{21}\vec{B}_2)u_2] \qquad (37)$$

The covariance matrix for the first subarray can now be expressed as

$$R_{y1} = E\{[\vec{Z}_1 \vec{Z}_1^H]\} + \sigma^2 I \qquad (38)$$

The matrix $E\{[\vec{Z}_1 \vec{Z}_1^H]\}$ has a rank of one since Z_1 is a column vector. For the second subarray

$$\vec{y}_2 = [B_4 \quad k_{12}B_5 \quad B_6 \quad k_{22}B_5] \vec{u} + \vec{n}_2' \qquad (39)$$

12 - 15

where

$$\vec{B}_4 = e^{-j\beta d_1 \cos\phi_1} \vec{B}_1 \qquad \vec{B}_5 = e^{-j\beta d_1 \cos\psi} \vec{B}_2 \qquad \vec{B}_6 = e^{-j\beta d_1 \cos\phi_2} \vec{B}_3 \qquad (40), (41), (42)$$

$$k_{12} = \begin{bmatrix} \alpha_{12} & 0 & \cdots & 0 \\ 0 & \alpha_{13} & \cdots & 0 \\ \vdots & \vdots & \ddots & 0 \\ 0 & 0 & 0 & \alpha_{16} \end{bmatrix} \qquad k_{22} = \begin{bmatrix} \alpha_{22} & 0 & \cdots & 0 \\ 0 & \alpha_{23} & \cdots & 0 \\ \vdots & \vdots & \ddots & 0 \\ 0 & 0 & 0 & \alpha_{26} \end{bmatrix} \qquad \vec{n}_2 = \begin{bmatrix} n_2 \\ n_3 \\ \vdots \\ n_6 \end{bmatrix} \qquad (43), (44), (45)$$

The output of the second subarray can now be expressed as

$$\vec{y}_2 = [(\vec{B}_4 + k_{12}\vec{B}_5) \quad (\vec{B}_6 + k_{22}\vec{B}_5)] \begin{bmatrix} u_1 \\ u_2 \end{bmatrix} + \vec{n}_2 \qquad (46)$$

The covariance matrix for the second subarray is

$$R_{y2} = E[\vec{y}_2 \vec{y}_2^H] + \sigma^2 I \qquad (47)$$

or

$$R_{y2} = E\{[(\vec{B}_4 + k_{12}\vec{B}_5)u_1 + (\vec{B}_6 + k_{22}\vec{B}_5)u_2][u_1^*(\vec{B}_4 + k_{12}\vec{B}_5)^H + u_2^*(\vec{B}_6 + k_{22}\vec{B}_5)^H]\} + \sigma^2 I \qquad (48)$$

Next let

$$\vec{Z}_2 = [(\vec{B}_4 + k_{12}\vec{B}_5)u_1 + (\vec{B}_6 + k_{22}\vec{B}_5)u_2] \qquad (49)$$

The covariance matrix now becomes

$$R_{y2} = E\{[\vec{Z}_2 \vec{Z}_2^H]\} + \sigma^2 I \qquad (50)$$

The matrix $E\{[\vec{Z}_2 \vec{Z}_2^H]\}$ is also of rank 1. Similarly

$$R_{y3} = E\{[\vec{Z}_3 \vec{Z}_3^H]\} + \sigma^2 I \qquad (51)$$

$$R_{y4} = E\{[\vec{Z}_4 \vec{Z}_4^H]\} + \sigma^2 I \qquad (52)$$

$$R_{y5} = E\{[\vec{Z}_5 \vec{Z}_5^H]\} + \sigma^2 I \qquad (53)$$

for the third, fourth, and fifth subarrays respectively. These covariance matrices $E\{[\vec{Z}_3 \vec{Z}_3^H]\}$, $E\{[\vec{Z}_4 \vec{Z}_4^H]\}$, and $E\{[\vec{Z}_5 \vec{Z}_5^H]\}$ each have a rank of 1. Averaging the subarrays yields

$$R_y = \frac{1}{5}(R_{y1} + R_{y2} + R_{y3} + R_{y4} + R_{y5}) \tag{54}$$

Substituting equations (38), (47), (51), (52), and (53) into equation (54) yields

$$R_y = \frac{1}{5}\{E[\,\vec{Z}_1\vec{Z}_1^H\,] + E[\,\vec{Z}_2\vec{Z}_2^H\,] + E[\,\vec{Z}_3\vec{Z}_3^H\,] + E[\,\vec{Z}_4\vec{Z}_4^H\,] + E[\,\vec{Z}_5\vec{Z}_5^H\,] + 5\sigma^2 I\} \tag{55}$$

This can be expressed as

$$R_y = R_s + \sigma^2 I \tag{56}$$

where

$$R_s = \frac{1}{5}E\left\{\begin{bmatrix} \vec{Z}_1 & \vec{Z}_2 & \vec{Z}_3 & \vec{Z}_4 & \vec{Z}_5 \end{bmatrix}\begin{bmatrix} \vec{Z}_1^H \\ \vec{Z}_2^H \\ \vec{Z}_3^H \\ \vec{Z}_4^H \\ \vec{Z}_5^H \end{bmatrix}\right\} \tag{57}$$

Next, recall that

$$\vec{Z}_1 = \vec{B}_1 u_1 + k_{11}\vec{B}_2 u_1 + \vec{B}_3 u_2 + k_{21}\vec{B}_2 u_2 \tag{58}$$

Substituting equations (40), (41), and (42) into equation (49) yields

$$\vec{Z}_2 = e^{-j\beta d_1 \cos\phi_1}\vec{B}_1 u_1 + k_{12}e^{-j\beta d_1 \cos\psi}\vec{B}_2 u_1 + e^{-j\beta d_1 \cos\phi_2}\vec{B}_3 u_2 + k_{22}e^{-j\beta d_1 \cos\psi}\vec{B}_2 u_2 \tag{59}$$

Similarly, it can be shown that

$$\vec{Z}_3 = e^{-j\beta d_2 \cos\phi_1}\vec{B}_1 u_1 + k_{13}e^{-j\beta d_2 \cos\psi}\vec{B}_2 u_1 + e^{-j\beta d_2 \cos\phi_2}\vec{B}_3 u_2 + k_{23}e^{-j\beta d_2 \cos\psi}\vec{B}_2 u_2 \tag{60}$$

$$\vec{Z}_4 = e^{-j\beta d_3 \cos\phi_1}\vec{B}_1 u_1 + k_{14}e^{-j\beta d_3 \cos\psi}\vec{B}_2 u_1 + e^{-j\beta d_3 \cos\phi_2}\vec{B}_3 u_2 + k_{24}e^{-j\beta d_3 \cos\psi}\vec{B}_2 u_2 \tag{61}$$

$$\vec{Z}_5 = e^{-j\beta d_4 \cos\phi_1}\vec{B}_1 u_1 + k_{15}e^{-j\beta d_4 \cos\psi}\vec{B}_2 u_1 + e^{-j\beta d_4 \cos\phi_2}\vec{B}_3 u_2 + k_{25}e^{-j\beta d_4 \cos\psi}\vec{B}_2 u_2 \tag{62}$$

The matrix R_s will have a rank of 4 since the vectors $\vec{Z}_1$ through $\vec{Z}_5$ are composed of 4 independent vectors. R_y, however, is of rank 5. Therefore, there will be 4 eigenvectors of R_y that are associated with the signals and 1 eigenvector associated with the noise. The direction of the incident plane waves lie in the signal subspace which is orthogonal to the noise subspace. Therefore, the angles of arrival of the plane waves can be estimated by searching

for the angles that are orthogonal to the noise subspace. This is accomplished using equations (1) and (2) where the eigenvectors are found from the eigendecomposition of R_y. Since equation (2) represents a plane wave incident upon the array, $P(\phi)$ in equation (1) will not produce a peak due to the spherical waves from the scatterer.

It is important to note that the rank of R_s must equal the number of sources present. This includes the coherent sources. Therefore, the number of subarrays must be equal to at least the number of sources. This can be expressed as $L \geq K$ where L is the number of subarrays and K is the number of sources. As discussed earlier the number of elements in each subarray must be at least one greater than the number of sources present. Mathematically, this means that $M \geq K + 1$ where M is the number of elements in each subarray. This requirement follows since there must be at least one eigenvector to represent the noise subspace. The total number of possible subarrays in an array with M_o elements is $L = M_o - M + 1$. Combining these criteria implies that the total number of elements needed to decorrelate K signals is 2K. This is the same result derived in [4] for the plane wave case. Therefore, for two incident signals with a near field scatterer present, the total number of elements in the array must be at least 8.

<u>6.0 Results</u>

The nulling and decorrelation techniques are each used with the terminal impedance matrix to suppress the effects of a near field scatterer. The simulations are performed on the linear array in figure 3. The antenna elements are dipoles modeled using the Method of Moments (MoM). A near field point scatterer replaces the point sources in figure 3. The scatterer has a Radar Cross Section (RCS) of 0 dBsm. The plane waves are incident at 45° and 55° relative to the array axis with frequencies of 300 MHz, and 305 MHz respectively. The Signal to Noise Ratio (SNR) is set at 10 dB. The final spectra are obtained by normalizing the average of 20 simulations. These parameters are used to compare the two techniques.

Figure 8 shows the results of the two techniques. The ideal curve shows the spectrum when no scatterer is present and the antenna elements are ideal implying that there is no mutual coupling between them. Notice that the angles of arrival are very accurately estimated using the MUSIC algorithm. The solid curve labeled "actual" shows the result of compensating for only the mutual coupling between the dipoles using equation (6) and not the near field scatterer. In this case the original nine element linear array is used and not the array configuration of figure 6.

Notice that the two signals can not be resolved. The third curve labeled "nulling technique" shows the result of correcting for the mutual coupling between the antenna elements using equation (6) and compensating for the near field scatterer using the new array configuration in figure 6 along with the corresponding new search vector in equation (21). Notice that the spectrum is almost identical to that of the ideal case. The estimated angles of arrival are also almost as accurate as the ideal case. The fourth spectra labeled "decorrelation technique" shows the spectrum using the second method of suppressing the interference from the scatterer. Notice that the actual angles of arrival are very accurately estimated. Notice also that a spurious peak occurs at 94°. This peak is due to the non-planar wavefront from the near field scatterer. Figure 8 shows that both techniques can suppress the effects of a near field scatterer.
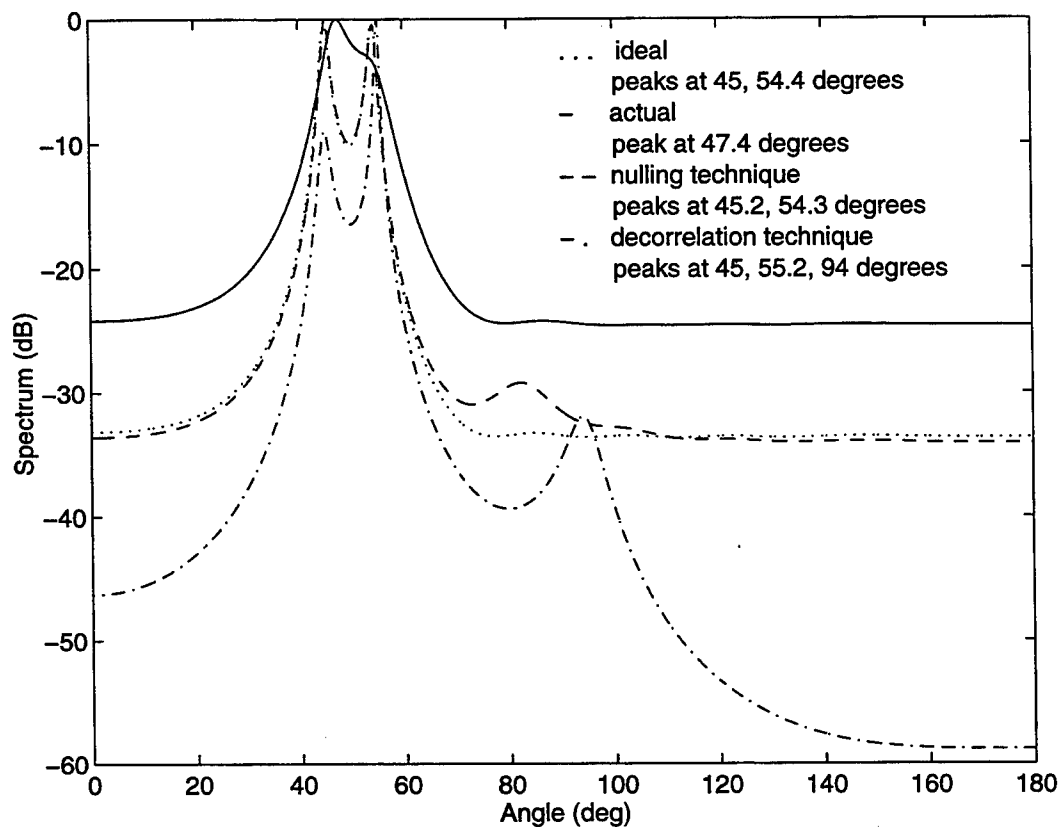

Figure 8: MUSIC Spectra Comparing the Two Techniques

7.0 Conclusions

In this report two techniques for suppressing the effects of a near field scatterer are investigated. The first technique modifies the antenna array configuration to place a null at the point of the near field scatterer. This

techniques alters the search vector of the MUSIC algorithm but restores the performance of the algorithm to practically the ideal case. The disadvantages of the technique are that it requires knowing the location of the scatterer and it decreases the effective number of antenna elements by one. This implies that one less signal can be estimated by the array.

The second technique attempts to estimate the angles of arrival of the incident signals by first decorrelating the incident signals from the scattered signals. This is accomplished by dividing the array into overlapping subarrays and averaging the covariance matrix from each array. The new covariance matrix is then decomposed into its eigenvalues and eigenvectors. The MUSIC spectrum is generated by searching for the angles of arrival of the plane waves that are orthogonal to the noise subspace. The signals from the scatterer will not dominate the spectrum since the search vector does not represent any spherical waves.

In this report, the spatial smoothing technique of [4] is extended to include non-planar wavefronts. Moreover, it has been shown that spatial smoothing can be applied regardless of the number of coherent signals and the wavefronts of the incident signals. It is also shown that the number of elements needed in the non-planar wavefront case is the same as that of the planar wavefront case.

8.0 References

1.   Friel, E. M., "Direction Finding with Compensation for Electromagnetic Effects", Ph.D. Dissertation, University of Dayton, Dayton, Ohio, 1995.

2.   Stutzman, W. L., Thiele, G. A., Antenna Theory and Design, New York, Wiley & Sons, 1981.

3.   Thiele, G. A., Newhouse, T. H., "A Hybrid Technique for Combining Moment Methods with the Geometric Theory of Diffraction," Proc. IEEE, Vol. 62, pp. 1438-1447, 1974.

4.   Pillai, S. U., Array Signal Processing New York, Springer-Verlag 1989.

5.   Schmidt, R. O., "Multiple Emitter Location and Signal Parameter Estimation" in Proc. RADC Spectral Estimation Workshop, Oct. 1979, pp. 243-258; reprinted in IEEE Transactions on Antennas and Propagation Vol. AP-34, pp. 276-280, March 1986.

6.   Therrien, C. W., Discrete Random Signals and Statistical Signal Processing, Prentice Hall, Englewood Cliffs NJ, 1992

A NUMERICAL INVESTIGATION OF TWO-PHASE DETONATION

Keith A. Gonthier
Ph.D. Candidate
Department of Aerospace and Mechanical Engineering

University of Notre Dame
365 Fitzpatrick Hall
Notre Dame, IN 46556-5637

A NUMERICAL INVESTIGATION OF TWO-PHASE DETONATION

Keith A. Gonthier
Ph.D. Candidate
Department of Aerospace and Mechanical Engineering
University of Notre Dame

Abstract

A two-phase model based upon principles of continuum mixture theory is numerically solved to predict the evolution of detonation in a granulated reactive material. Shock to detonation transition (SDT) is considered in which combustion is initiated by the motion of a piston. In particular, this study demonstrates the existence of an SDT path which gives rise to a steady two-phase Chapman-Jouguet (CJ) detonation structure consisting of a shocked gas and unshocked solid; this structure has previously been independently predicted by a strictly steady-state theory. The numerical algorithm used to solve the model equations is based upon Godunov's method and incorporates an approximate Riemann solver which is constructed to handle non-ideal equations of state. Comparisons are made between numerical predictions and known theoretical results for 1) an inert two-phase shock tube problem, 2) an inert compaction wave structure, and 3) a reactive two-phase detonation structure; in all cases, good agreement exists.

A NUMERICAL INVESTIGATION OF TWO-PHASE DETONATION

Keith A. Gonthier

Introduction

The detonation of high explosives is relevant in several aerospace applications. One such application is the Super*Zip separation joint which is regularly used on the Space Shuttle to release spacecraft from the Shuttle's cargo bay (Bement and Schimmel 1988). This device uses a detonating explosive cord as a severance mechanism to achieve separation. During experimental test firings, this device has been observed to malfunction; in order to better assess the causes of such malfunctions, it is necessary to understand the combustion dynamics occurring during device operation. Also, there are concerns associated with the detonability of solid propellants used in solid rocket motors. Situations may arise in which the cast solid propellant is inadvertently fractured, thus creating locally granulated regions. In such regions, it is possible for the combustion wave present during normal motor operation to accelerate and undergo transition to detonation (Bernecker and Price 1974a, 1974b). Other concerns are associated with the safe handling and storage of high explosives.

A schematic of a hypothetical two-phase (reactive solid and inert gas) detonation, in the context of the model of Powers et al. (1990a), is given in Fig. 1. Here, transition to detonation has already occurred in response to the impact of a piston which moves with a prescribed constant velocity of U_p; the steady detonation wave is propagating to the right with speed D. The detonation consists of a lead shock in the gas followed by a subsonic region in the gas in which combustion of the solid occurs; this region is referred to as the reaction zone. The end of the reaction zone is marked by the point at which the solid has been completely consumed due to combustion. The compression of the gas by the shock and the subsequent heat transfer to the solid provides sufficient stimulus to initiate combustion of the solid. Due to combustion, solid particle mass is converted into gaseous products within the reaction zone with the conversion of chemical energy into thermal and kinetic energy. The energy released by the reaction supports the propagation of the shock through the gas by acoustic transmission of energy from the point of local reaction to the shock. For a piston speed less than a minimum critical value, $U_{p_{CJ}}$ (which is dependent upon the properties of the explosive, the ambient state of the mixture, etc.), a Chapman-Jouguet (CJ) detonation wave results. A steady CJ wave propagates at a unique speed, D_{CJ}, defined as the wave speed for a self-supported detonation. For such a wave, the gas flow at the end of the reaction zone is locally sonic (with respect to the wave); consequently, energy transmitted to the gas from the moving piston cannot propagate through the sonic point to influence the detonation. However, for a piston speed greater than $U_{p_{CJ}}$, the gas flow at the end of the reaction zone is subsonic; consequently, in addition to the energy released by chemical reaction, energy transmitted to the gas from the moving piston can influence the detonation resulting in a piston-supported detonation, also
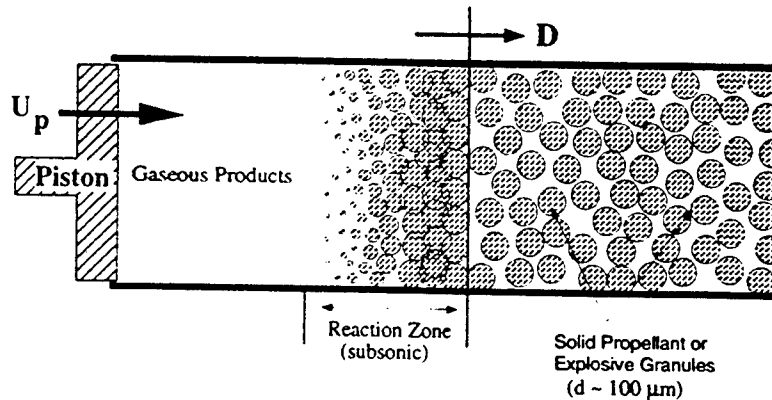
Figure 1: Schematic of a detonation wave propagating in a granulated mixture

known as an overdriven detonation.

In order to rationally address issues related to the detonation of granulated high explosives, it is necessary to develop models. To this end, a number of models have been formulated using principles of continuum mixture theory (e.g., Butler and Krier 1986; Baer and Nunziato 1986; Powers et al. 1990a). Most modeling efforts have focused on predicting the transient events associated with deflagration to detonation transition (DDT) and have placed little emphasis on the detailed analysis of the resulting steady detonation structure. The steady structure, however, is important because it reveals existence conditions and fine length scale structures which are often unresolved by coarsely gridded numerical simulations using the unsteady models. To address these issues, the fundamental problem of steady detonation structure was studied by Powers et al. (1988, 1990b) in which they classified and discussed steady two-phase detonations within the context of the well established theory for one phase detonations (Fickett and Davis 1979).

The goal of this study is to numerically predict the time-dependent development of a fully resolved CJ detonation in a granulated reactive material in response to a moving piston. The acceleration of the piston is specified as a function of time such that it attains a maximum constant velocity after a time interval which is short relative to the time required for the detonation to develop. The model used in this study was developed by Powers et al. (1990a). The specific form of the equations for various models used to predict two-phase detonation in granulated systems has historically been controversial; both the functional form of the constitutive models and the functional form of the evolution equations have been the focus of debate. Some relevant issues are discussed in detail by Powers et al. (1990a) and are not repeated here. Here, we follow the rationale of that study and adopt certain modeling choices in order to 1) maintain tractability and to 2) allow direct comparisons of numerical predictions with those given by the steady-state analysis of Powers et al. (1990b). It is not the emphasis of this study to accurately reproduce all experimentally observed features associated with the transition to detonation in granulated systems (i.e., transition time, transition length, etc.); rather, the emphasis is on demonstrating a technique to show the existence of a transition path which results in a detonation structure predicted by the steady-state analysis. Nevertheless,

the model does predict results commensurate with experiments for the CJ wave speed ($\sim 7500\ m/s$) and the peak detonation pressure ($\sim 20\ GPa$) in granulated HMX. Moreover, the techniques described herein are quite general and can be easily extended to other two-phase detonation models.

The numerical scheme used to solve the model equations is an upwind scheme which is based upon Godunov's method. The scheme has both second order accuracy in time and space in regions of smooth flow, but reduces to first order in space in regions of discontinuous flow. The numerical predictions for the resulting detonation structure are compared with predictions given by the steady state analysis. To the best of our knowledge, this work is the first to give detailed comparisons of unsteady predictions for two-phase detonation structure with steady state predictions. In addition to the SDT simulation, an inert two-phase shock tube problem is simulated and the evolution of a compaction wave in response to a moving piston is simulated; for each simulation, the numerically predicted results are compared with known solutions to demonstrate the validity of the numerical algorithm.

Included in this paper are 1) a discussion of the model including both the model assumptions and the equations, 2) a discussion of the mathematical structure of the model equations, 3) a discussion of the numerical method, 4) results for the inert two-phase shock tube simulation, the compaction wave simulation, and the SDT simulation, and 5) some conclusions.

Model Equations

The model assumes the existence of reactive solid particles and an inert gas, both having fixed composition. Mass exchange from the solid to the gas due to chemical reaction is modeled as an irreversible process, and all reaction is assumed to take place in an infinitely thin region along the particle surface. In addition to mass exchange between the phases, both momentum and energy exchange are also modeled. Each phase is assumed to be compressible, and all intraphase diffusive processes are neglected.

The dimensional model equations are given in divergence form by the following:

$$\frac{\partial}{\partial t}\left[\rho_1\phi_1\right] + \frac{\partial}{\partial x}\left[\rho_1\phi_1 u_1\right] = \left(\frac{3}{r}\right)\rho_2\phi_2 a P_1^m, \tag{1}$$

$$\frac{\partial}{\partial t}\left[\rho_2\phi_2\right] + \frac{\partial}{\partial x}\left[\rho_2\phi_2 u_2\right] = -\left(\frac{3}{r}\right)\rho_2\phi_2 a P_1^m, \tag{2}$$

$$\frac{\partial}{\partial t}\left[\rho_1\phi_1 u_1\right] + \frac{\partial}{\partial x}\left[\rho_1\phi_1 u_1^2 + P_1\phi_1\right] = u_2\left(\frac{3}{r}\right)\rho_2\phi_2 a P_1^m + \beta\frac{\phi_1\phi_2}{r}\left(u_2 - u_1\right), \tag{3}$$

$$\frac{\partial}{\partial t}\left[\rho_2\phi_2 u_2\right] + \frac{\partial}{\partial x}\left[\rho_2\phi_2 u_2^2 + P_2\phi_2\right] = -u_2\left(\frac{3}{r}\right)\rho_2\phi_2 a P_1^m - \beta\frac{\phi_1\phi_2}{r}\left(u_2 - u_1\right), \tag{4}$$

$$\frac{\partial}{\partial t}\left[\rho_1\phi_1\left(e_1 + \frac{u_1^2}{2}\right)\right] + \frac{\partial}{\partial x}\left[\rho_1\phi_1 u_1\left(e_1 + \frac{u_1^2}{2} + \frac{P_1}{\rho_1}\right)\right]$$
$$= \left(e_2 + \frac{u_2^2}{2}\right)\left(\frac{3}{r}\right)\rho_2\phi_2 a P_1^m + \beta\frac{\phi_1\phi_2}{r}u_2\left(u_2 - u_1\right) + h\frac{\phi_1\phi_2}{r^{1/3}}\left(T_2 - T_1\right), \tag{5}$$

$$\frac{\partial}{\partial t}\left[\rho_2\phi_2\left(e_2 + \frac{u_2^2}{2}\right)\right] + \frac{\partial}{\partial x}\left[\rho_2\phi_2 u_2\left(e_2 + \frac{u_2^2}{2} + \frac{P_2}{\rho_2}\right)\right]$$

$$= -\left(e_2 + \frac{u_2^2}{2}\right)\left(\frac{3}{r}\right)\rho_2\phi_2 a P_1^m - \beta\frac{\phi_1\phi_2}{r}u_2(u_2 - u_1) - h\frac{\phi_1\phi_2}{r^{1/3}}(T_2 - T_1), \tag{6}$$

$$\frac{\partial}{\partial t}\left[\rho_2\phi_2^2\right] + \frac{\partial}{\partial x}\left[\rho_2 u_2\phi_2^2\right] = -2\left(\frac{3}{r}\right)\rho_2\phi_2^2 a P_1^m + \frac{\rho_2\phi_1\phi_2^2}{\mu_c}\left[P_2 - P_1 - f(\phi_2)\right], \tag{7}$$

$$\frac{\partial n}{\partial t} + \frac{\partial}{\partial x}\left[u_2 n\right] = 0, \tag{8}$$

$$P_1 = P_1(\rho_1, e_1), \tag{9}$$

$$e_1 = e_1(\rho_1, T_1), \tag{10}$$

$$c_1^2 = \left.\frac{\partial P_1}{\partial \rho_1}\right|_{s_1} = \frac{P_1}{\rho_1^2}\left.\frac{\partial P_1}{\partial e_1}\right|_{\rho_1} + \left.\frac{\partial P_1}{\partial \rho_1}\right|_{e_1}, \tag{11}$$

$$P_2 = P_2(\rho_2, e_2), \tag{12}$$

$$e_2 = e_2(\rho_2, T_2), \tag{13}$$

$$c_2^2 = \left.\frac{\partial P_2}{\partial \rho_2}\right|_{s_2} = \frac{P_2}{\rho_2^2}\left.\frac{\partial P_2}{\partial e_2}\right|_{\rho_1} + \left.\frac{\partial P_2}{\partial \rho_2}\right|_{e_2}, \tag{14}$$

$$n = \frac{3\phi_2}{4\pi r^3}, \tag{15}$$

$$\phi_1 + \phi_2 = 1. \tag{16}$$

In these equations, the subscripts "1" and "2" denote quantities associated with the gas and solid, respectively. The independent variables are time t and position x. Dependent variables are as follows: the phase density ρ_i ($i = 1, 2$), defined as the mass of phase i per unit volume occupied by that phase; the phase pressure P_i; the phase temperature T_i; the particle velocity measured with respect to a stationary reference frame u_i; the specific internal energy e_i; the specific entropy s_i; the sound speed c_i; the volume fraction ϕ_i, defined as the ratio of the volume occupied by phase i to the total volume; the radius of the spherical solid particles r; and the number of particles per unit volume n.

Equations (1), (3), and (5) are evolution equations for the mass, momentum, and energy of the gas. Equations (2), (4), and (6) are evolution equations for the mass, momentum, and energy of the solid. The evolution equations are constructed such that when Eqs. (1) and (2), Eqs. (3) and (4), and Eqs. (5) and (6) are added, respectively, the forcing terms cancel yielding conservation equations for the mixture mass, momentum, and energy. Furthermore, it can be easily shown that these equations are frame-invariant under a Galilean transformation.

The forcing terms in Eqs. (1) and (2) account for the exchange of mass from the solid to the gas due to chemical reaction. The reaction rate is modeled by a gas phase pressure-dependent burn law; such an assumption is commonly made in solid propellant combustion modeling (Williams et al. 1969). Values for the reaction rate parameters a and m are assumed constant for this study.

The forcing terms in Eqs. (3) and (4) account for two forms of momentum exchange between the gas and solid: first, the gas is gaining that momentum associated with the solid which is being converted into gas due to reaction; second, there is an exchange of momentum due to solid particle-gas drag interaction. The

drag interaction is modeled by a drag law which states that the drag is proportional to the difference in velocity between the phases and inversely proportional to the particle radius. In the drag law, β is defined as a constant drag coefficient.

The forcing terms in Eqs. (5) and (6) account for the exchange of energy between the gas and solid. Energy exchange associated with combustion and particle-gas drag interaction are accounted for as well as the exchange of thermal energy between the gas and the solid. The thermal energy exchange rate is assumed to be proportional to the temperature difference between the gas and the solid and inversely proportional to the cube root of the particle radius; here, h is defined as a constant heat transfer coefficient.

Equation (7) is a dynamic compaction equation describing changes in solid volume fraction due to compaction of the granular bed and due to combustion. This equation predicts that, in the absence of combustion, the solid volume fraction, ϕ_2, will equilibrate to a value such that the solid phase pressure, P_2, equals the sum of the gas phase pressure, P_1, and an intragranular, or configurational, stress, f, which is assumed to vary with ϕ_2; the equilibration rate is governed by the constant parameter μ_c which is referred to as the compaction viscosity.

Equation (8) is is an evolution equation for the particle number density; this equation expresses that the total number of particles in the system is conserved.

Equations (9-11) and (12-14) are functional dependencies for the thermal and caloric equations of state and the definition of the sound speed for the gas and the solid, respectively. Equation (15) is the definition of the local particle number density expressed in terms of the solid volume fraction and the particle radius, and Eq. (16) is a saturation condition.

Using vector notation, the evolution equations [Eqs. (1-8)] can be written in the following divergence form:

$$\frac{\partial \mathbf{u}}{\partial t} + \frac{\partial \mathbf{f}(\mathbf{u})}{\partial x} = \mathbf{g}(\mathbf{u}), \tag{17}$$

where

$$\mathbf{u} = \left[\rho_1 \phi_1, \ \rho_1 \phi_1 u_1, \ \rho_1 \phi_1 (e_1 + u_1^2/2), \ \rho_2 \phi_2, \ \rho_2 \phi_2 u_2, \ \rho_2 \phi_2 (e_2 + u_2^2/2), \ \rho_2 \phi_2^2, \ n \right]^T,$$

$$\mathbf{f}(\mathbf{u}) = \left[\rho_1 \phi_1 u_1, \ \rho_1 \phi_1 u_1^2 + P_1 \phi_1, \ \rho_1 \phi_1 u_1 (e_1 + u_1^2/2 + P_1/\rho_1), \ \rho_2 \phi_2 u_2, \ \rho_2 \phi_2 u_2^2 + P_2 \phi_2, \right.$$
$$\left. \rho_2 \phi_2 u_2 (e_2 + u_2^2 + P_2/\rho_2), \ \rho_2 u_2 \phi_2^2, \ u_2 n \right]^T,$$

$$\mathbf{g}(\mathbf{u}) = \left[(3/r)\rho_2 \phi_2 a P_1^m, \ -(3/r)\rho_2 \phi_2 a P_1^m, \ u_2 (3/r)\rho_2 \phi_2 a P_1^m + \beta \phi_1 \phi_2 (u_2 - u_1)/r, \ -u_2 (3/r)\rho_2 \phi_2 a P_1^m \right.$$
$$-\beta \phi_1 \phi_2 (u_2 - u_1)/r, \ (e_2 + u_2^2)(3/r)\rho_2 \phi_2 a P_1^m + \beta \phi_1 \phi_2 u_2 (u_2 - u_1)/r + h \phi_1 \phi_2 (T_2 - T_1)/r^{1/3},$$
$$-(e_2 + u_2^2)(3/r)\rho_2 \phi_2 a P_1^m - \beta \phi_1 \phi_2 u_2 (u_2 - u_1)/r - h \phi_1 \phi_2 (T_2 - T_1)/r^{1/3}, \ -2(3/r)\rho_2 \phi_2^2 a P_1^m$$
$$\left. +\rho_2 \phi_1 \phi_2^2 (P_2 - P_1 - f)/\mu_c, \ 0 \right]^T.$$

Furthermore, it can be shown (Gonthier 1996) that the model equations constitute a non-strictly hyperbolic system of equations except at the singular points $\phi_2 = 0$ and $u_2 = u_1 \pm c_1$ in which the equations degenerate

into a parabolic system. Similar singularities have been identified in the two-phase model proposed by Baer and Nunziato (1986); a detailed discussion is given by Embid and Baer (1992).

Numerical Method

Since the model equations [Eqs. (1-16)] constitute a non-strictly hyperbolic system of equations (for $\phi_2 \neq 0$, $u_2 \neq u_1 \pm c_1$), discontinuous solutions are admitted. A requirement of any numerical algorithm used to solve these equations is the ability to accurately resolve such discontinuities. For strictly hyperbolic systems, a number of high resolution numerical methods have been developed (Roe 1981; Osher 1981; Osher and Solomon 1982). Many of these methods are based upon Godunov's method and require the exact or approximate solution of a Riemann problem at computational cell interfaces in order to advance the solution in time. The numerical method described herein applies ideas associated with these well developed methods in constructing an upwind numerical algorithm for solving Eqs. (1-16). A summary of the numerical approach is given below.

The spatial domain $x \in [0, L]$ is discretized into N uniformly spaced nodes located at the points $x_j = (j-1)\Delta x$ $(j = 1, \ldots, N)$, where $\Delta x = L/(N-1)$. Each node x_j is located at the center of a computational cell of width Δx; the location of the boundaries of the jth cell are denoted as $x_{j\pm 1/2}$.

The model equations are numerically solved on the computational grid using the method of fractional steps (Strang 1968):

$$\mathbf{U}^{n+2} = \mathcal{L}_c^{\Delta t} \mathcal{L}_s^{\Delta t} \mathcal{L}_s^{\Delta t} \mathcal{L}_c^{\Delta t} \mathbf{U}^n, \tag{18}$$

where $\mathbf{U}^{n+2}$ and $\mathbf{U}^n$ are numerical approximations for u at the times $t_n + 2\Delta t$ and t_n $(t_n = n\Delta t)$, respectively; the numerical operator $\mathcal{L}_c^{\Delta t}$ represents the algorithm used to solve the homogeneous model equations which govern non-linear convection [obtained by setting the forcing terms in Eq. (17) to zero]; and the numerical operator $\mathcal{L}_s^{\Delta t}$ represents the algorithm used to solve the coupled system of ordinary differential equations (ODEs) [obtained by setting the spatial derivatives in Eq. (17) to zero] which govern the phase interaction processes. Here, the splitting procedure requires that each successive numerical step be performed over the time interval Δt which is chosen based upon a local Courant-Friedrichs-Lewy (CFL) condition [$\Delta t = (CFL)\Delta x/|\lambda|_{max}$].

The numerical algorithm used in the convective step is an upwind scheme which is based upon Godunov's method. Since the Riemann problem for this two-phase system has not been analytically studied, an approximate solution is used in the numerical algorithm. This approximate Riemann solution is obtained by an approach similar to that used by Glaister (1988) in formulating an approximate Riemann solution for the Euler equations for a non-ideal gas. Implicit in the construction of the approximate solution for the two-phase system is the assumption that a physically relevant exact solution of the Riemann problem exists which consists of at most eight waves: a 1) shock wave, 2) rarefaction wave, and 3) contact discontinuity (entropy wave) in the gas; a 4) shock wave, 5) rarefaction wave, and 6) contact discontinuity in the solid; a 7) compaction wave; and a 8) particle number density wave. Higher order spatial and temporal accuracy is

obtained by the use of non-linear flux limiters and a predictor/corrector Runge-Kutta integration procedure, respectively. Specifically, the algorithm $\mathcal{L}_c^{\Delta t} \mathbf{U}^n$ is as follows:

$$\overline{\mathbf{U}}_j = \mathbf{U}_j^n - \frac{\Delta t}{2 \Delta x} \left(\mathbf{F}_{j+1/2}^{(H)} - \mathbf{F}_{j-1/2}^{(H)} \right), \tag{19}$$

$$\mathbf{U}_j^{n+1} = \mathbf{U}_j^n - \frac{\Delta t}{\Delta x} \left(\overline{\mathbf{F}}_{j+1/2}^{(H)} - \overline{\mathbf{F}}_{j-1/2}^{(H)} \right), \tag{20}$$

where

$$\mathbf{F}_{j+1/2}^{(H)} = \mathbf{F}_{j+1/2}^{(L)} + \mathbf{F}_{j+1/2}^{(C)}.$$

Here, $\mathbf{F}_{j+1/2}^{(H)}$ and $\overline{\mathbf{F}}_{j+1/2}^{(H)}$ are higher order numerical fluxes evaluated using the initial data $\mathbf{U}^n$ and the intermediate data $\overline{\mathbf{U}}$, respectively. The higher order numerical flux consists of a lower order numerical flux $\mathbf{F}_{j+1/2}^{(L)}$ and a corrective flux $\mathbf{F}_{j+1/2}^{(C)}$. The lower order flux, which introduces a significant amount of numerical diffusion into the algorithm, is determined from the approximate solution of the Riemann problem. The corrective flux is constructed following the method of Chakravarthy and Osher (1985) and is limited based upon the local solution behavior in order to achieve nominally second order spatial accuracy in smooth regions of the flow; near discontinuities, the corrective flux is suppressed allowing a sufficient amount of lower order flux to prevent the generation of spurious oscillations. The lower order and corrective fluxes are mathematically defined by Gonthier (1996).

The numerical algorithm used in the source step is a stiff ODE solver contained in the standard package LSODE. Given the initial data $\mathbf{U}^n$, the source step $\mathcal{L}_s^{\Delta t} \mathbf{U}^n$ requires the solution of a system of ODEs having the following form at each computational node x_j $(j = 1, \ldots, N)$ to obtain $\mathbf{U}^{n+1}$:

$$\frac{d}{dt} \begin{bmatrix} \rho_2 \\ u_2 \\ e_2 \\ \phi_2 \end{bmatrix} = \begin{bmatrix} h_1(\rho_2, u_2, e_2, \phi_2) \\ h_2(\rho_2, u_2, e_2, \phi_2) \\ h_3(\rho_2, u_2, e_2, \phi_2) \\ h_4(\rho_2, u_2, e_2, \phi_2) \end{bmatrix}, \tag{21}$$

where h_1, h_2, h_3, and h_4 are algebraic functions of the solid phase variables. This reduced system of equations is obtained by reducing the system of ODEs given by Eq. (17) with $\partial/\partial x = 0$. The reductions involve obtaining algebraic expressions for ρ_1, u_1, e_1, ϕ_1, and n in terms of the solid phase variables and the initial data $\mathbf{U}^n$; details are given in Gonthier (1996).

Difficulties are encountered in the numerical algorithm near the singular points $\phi_2 = 0$ and $u_2 = u_1 \pm c_1$. At these points, the model equations degenerate into a parabolic system and the numerical algorithm breaks down. To avoid the singularity $\phi_2 = 0$ $(r = 0)$, combustion was terminated when the local solid volume fraction was less than 1.0×10^{-4}; however, no special treatment was used for the $u_2 = u_1 \pm c_1$ singularities. It is further noted that the complete combustion singularity $(\phi_2 = 0)$ also exists in the steady-state model and, within the context of that model, can be shown to be inconsequential (Powers et al. 1990b). Though not implemented for this study, Colella and Trangenstein (1990) give a methodology for use with higher order Godunov methods to eliminate numerical difficulties encountered near such singularities.

Table 1: Parameters and initial conditions used in the two-phase shock tube simulation

Parameter	Value	Units
b	5.00×10^{-2}	m^3/kg
c_{v1}	7.18×10^2	$J/kg/K$
c_{v2}	7.18×10^2	$J/kg/K$
R_1	2.87×10^2	$J/kg/K$
R_2	2.87×10^2	$J/kg/K$
u_{1L}	0	m/s
u_{2L}	0	m/s
u_{1R}	0	m/s
u_{2R}	0	m/s
ρ_{1L}/ρ_{1R}	1.00×10^1	
ρ_{2L}/ρ_{2R}	1.00×10^1	
P_{1L}/P_{1R}	1.00×10^1	
P_{2L}/P_{2R}	1.00×10^1	
n_L/n_R	1.00×10^0	

Results

Results are presented for three different simulations: an inert two-phase shock tube problem; the evolution of a compaction wave in response to a moving piston; and the evolution of a detonation wave in response to a moving piston. Comparisons are made with exact solutions for the shock tube problem, with predictions given by a simplified steady state theory for the compaction wave structure, and with predictions given by a formal steady state theory for the detonation wave structure. In all three simulations, a CFL number of 0.4 was used. The computations were performed on an IBM RS6000 Model 350 workstation.

Two-phase shock tube simulation

The two-phase shock tube problem involves the breakup of a single initial discontinuity separating constant left (L) and right (R) states into self-similar waves consisting of a shock wave, a rarefaction wave, and a contact discontinuity in both the gas and the solid. This problem considers convection only; consequently, all phase interaction processes (i.e., drag, heat transfer, etc.) are suppressed. In this simulation, an ideal equation of state was used for the gas [$P_1 = \rho_1 R_1 T_1$; $e_1 = c_{v1} T_1$] and a constant covolume non-ideal equation of state was used for the solid [$P_2 = \rho_2 R_2 T_2/(1 - b\rho_2)$; $e_2 = c_{v2} T_2$]. These state equations were chosen solely to compare numerical predictions with existing closed-form analytical solutions (Toro 1989). Values chosen
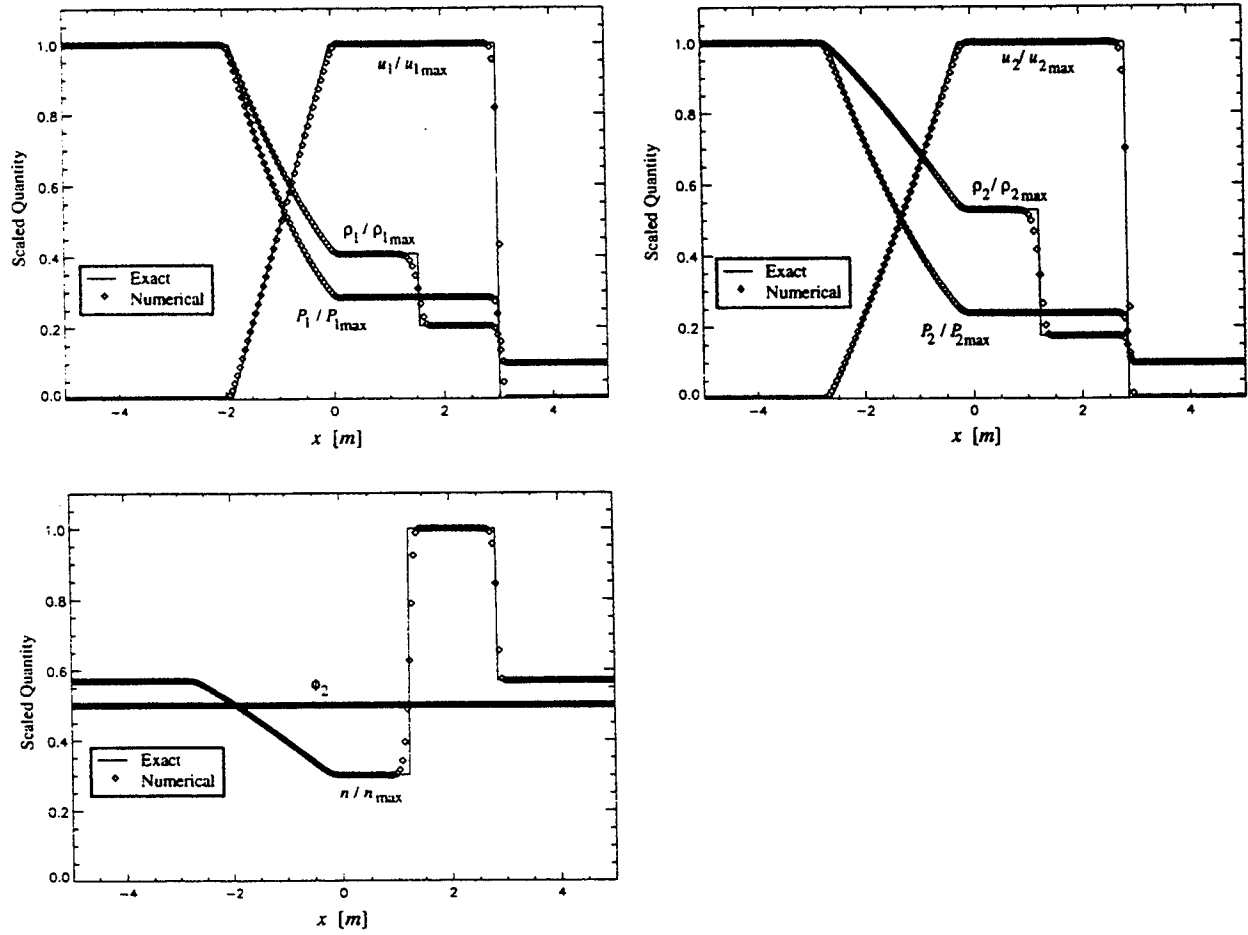
Figure 2: Comparison of the numerically predicted solution and the exact solution for the shock tube simulation ($t = 5\ ms$)

for the model parameters and the initial conditions are given in Table 1. The initial discontinuity was located at the position $x = 0\ m$. For this simulation, 200 computational nodes were used.

Shown in Fig. 2 are comparisons between the numerical and exact solutions at time $t = 5\ ms$. In these figures, all quantities have been scaled by the corresponding maximum exact values. For each phase, the solution consists of a right propagating shock wave, followed by a slower moving right propagating contact discontinuity, and a left propagating rarefaction wave. Also, a jump is predicted in the particle number density (n) across both the shock and the contact discontinuity in the solid; a continuous variation in n is predicted across the rarefaction wave. Good agreement exists between the numerically predicted solution and the exact solution.

Compaction wave simulation

This simulation considers the evolution of an inert compaction wave in response to the acceleration of a piston from zero initial velocity ($t = 0\ \mu s$) to a constant velocity of 100 m/s ($t \geq 2.0\ \mu s$). Here, a compaction wave

Table 2: Parameters used in the compaction wave and the detonation wave simulations

Parameter	Compaction (Numerical 1)	Compaction (Numerical 2)	Detonation	Units
b	1.10×10^{-3}	1.10×10^{-3}	1.10×10^{-3}	m^3/kg
R_1	8.50×10^2	8.50×10^2	8.50×10^2	$J/kg/K$
c_{v1}	2.40×10^3	2.40×10^3	2.40×10^3	$J/kg/K$
c_{v2}	1.50×10^3	1.50×10^3	1.50×10^3	$J/kg/K$
γ_2	5.00×10^0	5.00×10^0	5.00×10^0	
σ	8.98×10^6	8.98×10^6	8.98×10^6	$(m/s)^2$
q	0	0	5.84×10^6	J/kg
a	0	0	2.90×10^{-9}	$m/(sPa)$
m			1.00×10^0	
β	0	1.00×10^4	1.00×10^4	$kg/s/m^2$
h	0	1.00×10^7	1.00×10^7	$J/(sKm^{8/3})$
μ_c	1.00×10^3	1.00×10^3	1.00×10^6	$kg/m/s$
T_{ig}			3.10×10^2	K
r_o	1.00×10^{-4}	1.00×10^{-4}	1.00×10^{-4}	m
ϕ_{2o}	7.30×10^{-1}	7.30×10^{-1}	7.30×10^{-1}	
T_o	3.00×10^2	3.00×10^2	3.00×10^2	K
ρ_{1o}	1.00×10^1	1.00×10^1	1.00×10^1	kg/m^3
ρ_{2o}	1.90×10^3	1.90×10^3	1.90×10^3	kg/m^3

refers to the propagation of a disturbance in the porosity of the system due to mechanical stresses. In this simulation, a virial equation of state was used for the gas $[P_1 = \rho_1 R_1 T_1 (1 + b\rho_1); e_1 = c_{v1}T_1]$ and a Tait equation of state $[P_2 = (\gamma_2 - 1)c_{v2}\rho_2 T_2 - \rho_{2o}\sigma/\gamma_2; e_2 = c_{v2}T_2 + \rho_{2o}\sigma/\gamma_2\rho_2 + q]$ was used for the solid ; also, the configurational stress $f(\phi_2)$ given by Powers et al. (1989) was used:

$$f = (P_{2o} - P_{1o})\frac{\phi_2^2}{\phi_{2o}^2}\frac{(2 - \phi_{2o})^2}{(2 - \phi_2)^2}\frac{\ln(\frac{1}{1-\phi_2})}{\ln(\frac{1}{1-\phi_{2o}})}.$$

Here, the notation subscript "o" is used to denote ambient conditions. For this simulation, the model equations were transformed to the accelerating reference frame of the piston such that the transformed velocity at the piston surface was zero. Reflective boundary conditions were enforced at the piston surface (Thompson 1987); no boundary conditions needed to be enforced at the upstream boundary since time was restricted such that there was insufficient time for the wave to reach this boundary. The computational domain, which consisted of 600 nodes, was initialized with the ambient state given in Table 2. Values for the model parameters are also given in Table 2. The computational run time for this simulation was
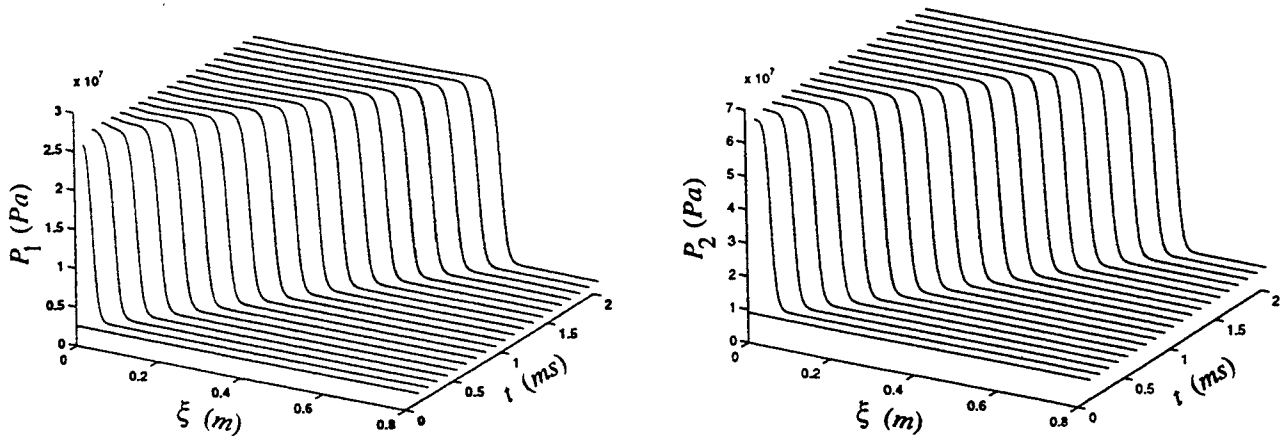
Figure 3: Gas and solid pressure histories for the compaction wave simulation
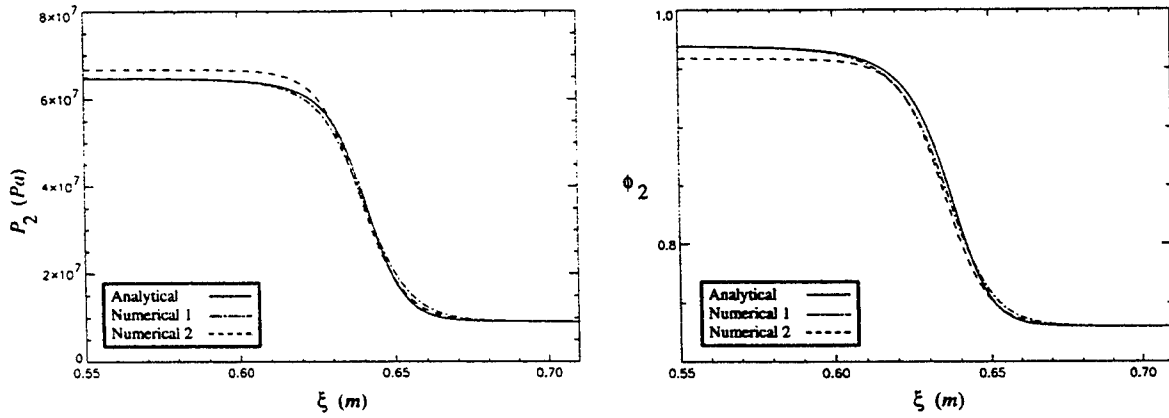

Figure 4: Solid pressure and solid volume fraction predictions in the steady compaction wave

approximately 45 minutes.

Figures 5 and 6 show the gas and solid pressure histories; here, ξ is the position measured in the piston-attached coordinate system (the piston surface is located at $\xi = 0\ m$). A smooth increase is initially predicted in both the gas and solid pressure in response to the moving piston. The gas pressure rises from its ambient value of 2.58 MPa to a maximum value of 28.26 MPa in 0.3 ms; the solid pressure rises from its ambient value of 9.12 MPa to a maximum value of 69.16 MPa in 0.2 ms. Subsequently, both pressures remain essentially constant as a steady compaction wave develops and propagates away from the piston. Though not shown here, there is also a smooth increase in the other state variables across the compaction wave. The predicted length and time for transition to a fully developed compaction wave are approximately 0.1 m (measured relative to the piston) and 0.6 ms, respectively. The predicted thickness of the resulting fully developed compaction wave is approximately 13 cm.

Figures 7 and 8 show the numerically predicted variation in solid pressure and solid volume fraction within

the compaction wave; also shown in these figures are predictions for the steady wave structure given by the simplified analysis of Powers et al. (1989). In their analysis, Powers et al. ignore gas phase effects and describe steady compaction wave structure in terms of the solid variables. In these figures, the flow located between the piston ($\xi = 0$) and the trailing edge of the compaction wave ($\xi = 0.55\ m$) is not shown. The curve labeled Numerical 1 corresponds to predictions obtained for a case in which the same assumptions were made as with the simplified analysis permitting a direct comparison between the numerical and theoretical predictions of the steady wave structure; the curve labeled Numerical 2 corresponds to the prediction presented in Fig. 5 at $t = 2\ ms$. As seen in these figures, the numerical and theoretical predictions agree well. It is noted that a continuous structure is predicted in both the gas and the solid throughout the compaction wave. The wave speed predicted by the steady analysis is 404 m/s which agrees well with the numerically predicted value of 407 m/s (for the simulation denoted as Numerical 1). The wave speed predicted for the simulation denoted as Numerical 2 is 430 m/s. Experimentally observed compaction wave speeds of 432 m/s in porous HMX ($\phi_{2o} = 0.73$) resulting from the impact of a 100 m/s piston have been reported by Sandusky and Liddiard (1985).

Detonation wave simulation

This simulation considers the evolution of a two-phase detonation wave in response to a moving piston. The results presented here were obtained for a piston having the same prescribed motion as for the compaction wave simulation presented in the previous section. The same state equations, boundary conditions, and initial conditions used in the compaction wave simulation were also used here; however, the following configurational stress $f(\phi_2)$ given by Powers et al. (1990b) was used:

$$ f = \frac{P_{2o} - P_{1o}}{\phi_{2o}} \phi_2. $$

Values for the model parameters are given in Table 2. For this simulation, the computational domain consisted of 1000 nodes and the computational run time was approximately 2 hours.

Figures 9 and 10 show the velocity histories for the gas and solid, respectively. Figures 11 and 12 show the pressure histories for the gas and solid, respectively. In these figures, each curve for the solid phase quantities are plotted up to the point of complete combustion (i.e., for $\phi_2 \geq 1.0 \times 10^{-4}$). Initially, a compaction wave having a continuous structure in both the gas and solid is predicted to propagate away from the piston with a speed of 2600 m/s. This speed is higher than those observed in experiments, which would be better modeled with the configurational stress used in the compaction wave simulation; the present model was used so that proper comparisons could be made with existing published steady predictions. Onset of combustion occurs near the piston surface when the gas temperature exceeds T_{ig}, the value of which was chosen ad hoc for this simulation. The combustion rate then accelerates due to the increasing gas pressure, the combustion wave strengthens and undergoes a transition to detonation near $\xi = 0.06\ m$ at $t = 36\ \mu s$. Here, it is noted that as the value of T_{ig} was chosen ad hoc, the values for the transition length and time should not be construed as representative of SDT experiments; however, these values do agree with the numerical predictions reported
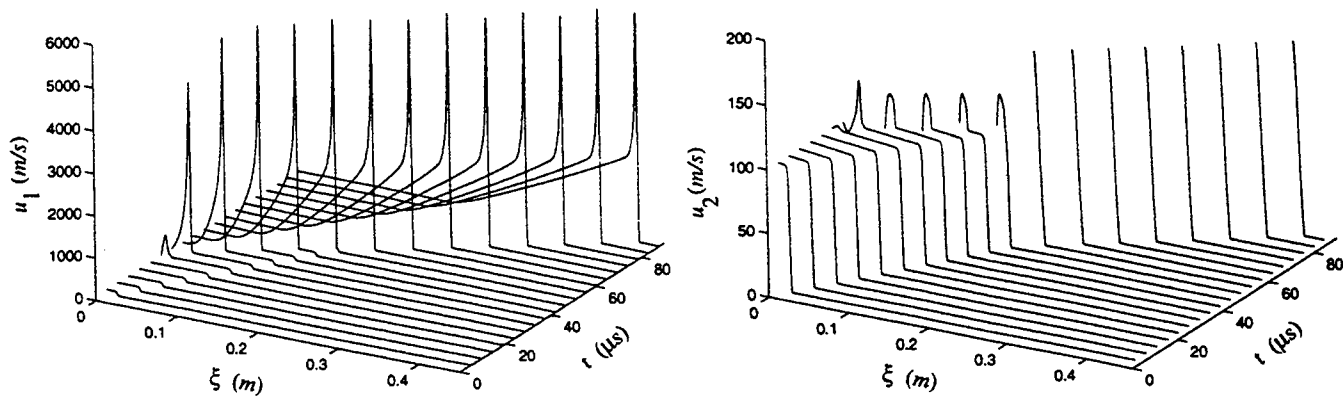
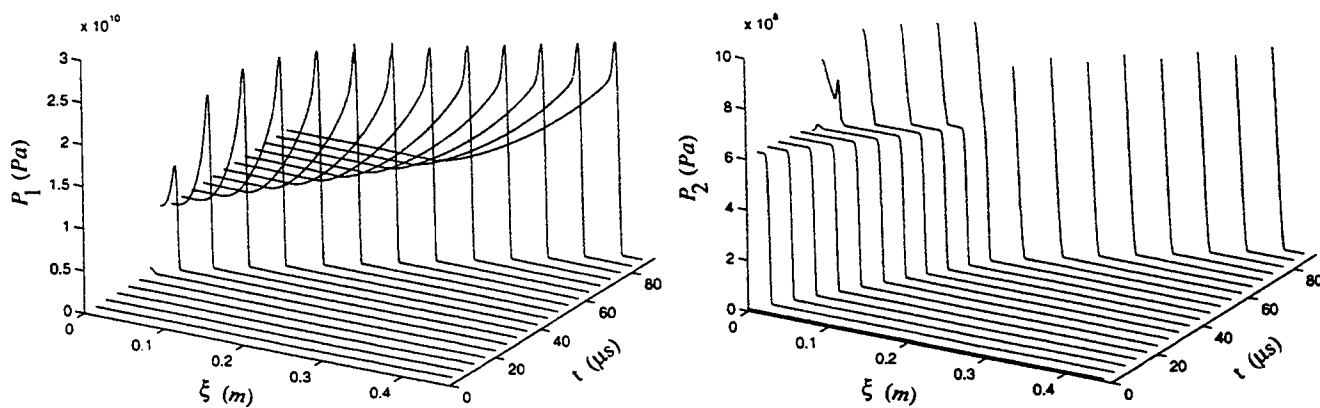Figure 5: Gas and solid velocity histories for the detonation wave simulation

Figure 6: Gas and solid pressure histories for the detonation wave simulation
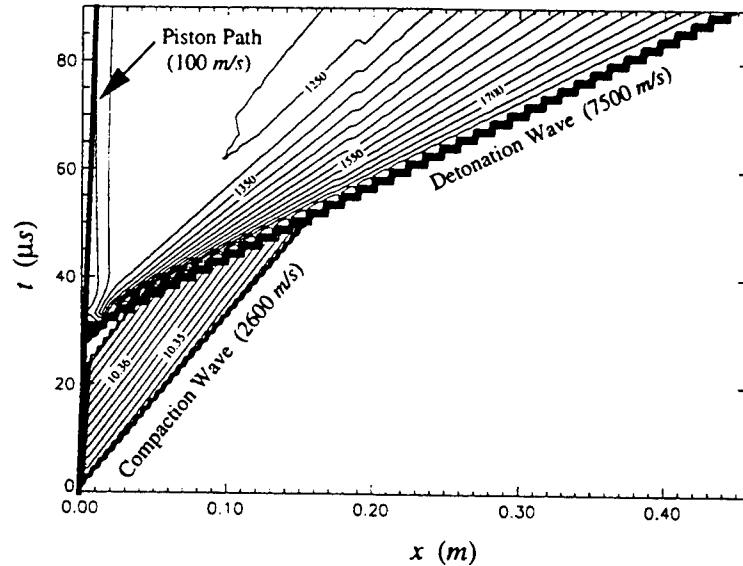
Figure 7: Gas density (kg/m^3) contours for the detonation wave simulation

by Baer and Nunziato (1986) for the length (0.06 m) and time (33 μs) associated with DDT in porous HMX ($\phi_{2o} = 0.73$). The detonation wave, traveling at a faster speed, overtakes the compaction front at $t = 51$ μs; subsequently, a fully developed detonation wave having a reaction zone length of approximately 11 mm is formed. The detonation wave is followed by an expansion wave in the gas which decreases the gas velocity from its value at the end of the reaction zone (2960 m/s) to that of the piston (100 m/s). The wave patterns can be more easily seen in the gas density contours (projected in the x-t plane) given in Fig. 13.

Figures 14-16 give numerical predictions for the variation in gas and solid pressure, gas and solid Mach number squared (relative to the wave), and solid volume fraction within the detonation wave at $t = 90$ μs; also plotted in these figures are the corresponding variations predicted by steady state theory (Powers et al. 1990b). Good agreement exists between the numerical predictions and the steady-state theory predictions. It is noted that the wave structure consists of a shocked gas and an unshocked solid. Also, since the Mach number of the gas relative to the detonation front is locally sonic at the end of the reaction zone, the wave requires no external energy input to sustain its propagation; therefore, the wave represents a two-phase equivalent of a single phase CJ detonation. The CJ wave speed predicted by the steady-state theory is 7498 m/s; the numerically predicted wave speed is approximately 7500 m/s. These values are representative of experimentally observed CJ wave speeds in porous HMX.

Conclusions

In conclusion, a two-phase continuum model was numerically solved to predict detonation in a granulated reactive material in response to a moving piston. The model equations were solved using an upwind numerical scheme which is based upon Godunov's method; the numerical scheme gave excellent results for a number of
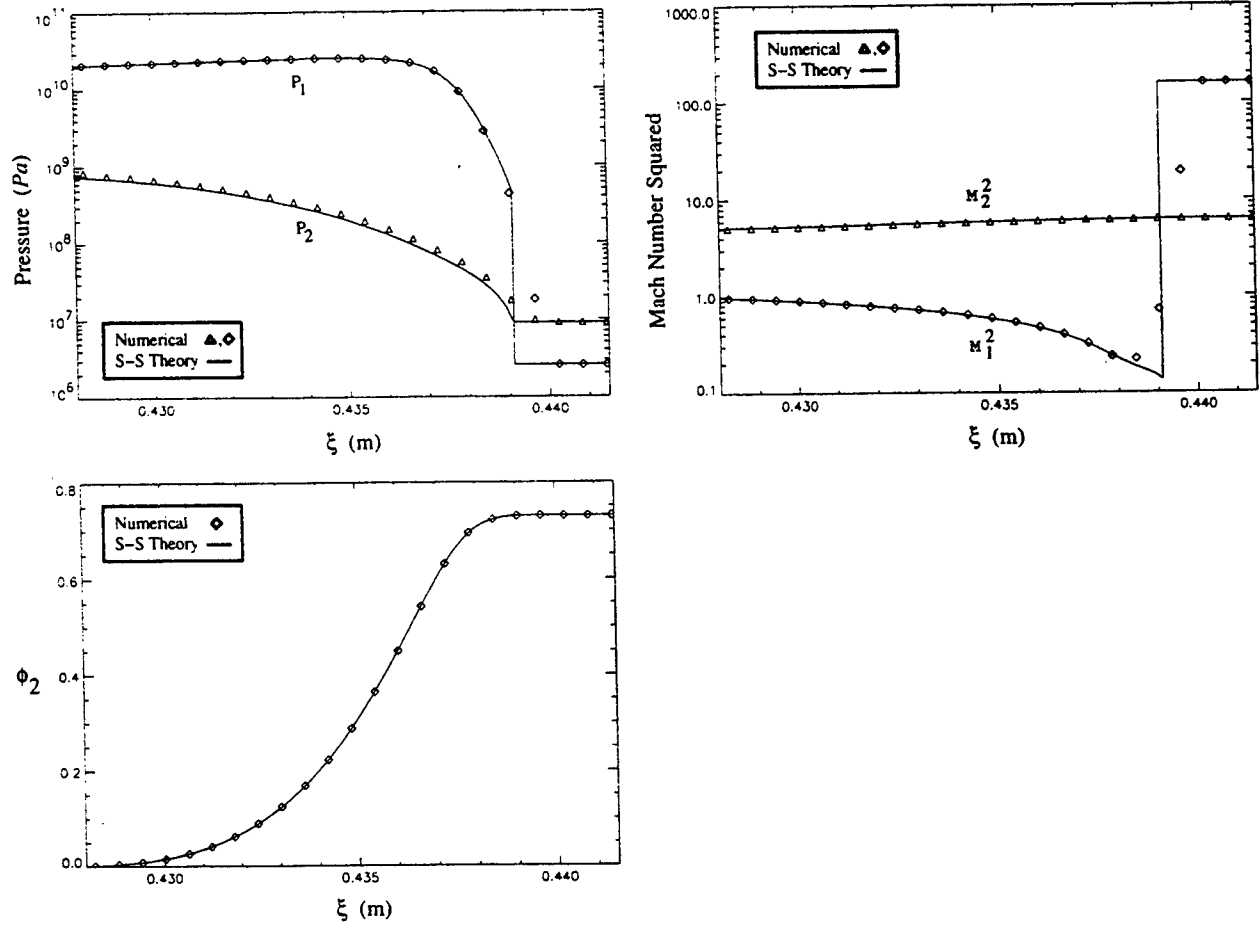
Figure 8: Comparisons of unsteady model predictions with steady-state theory (S-S) predictions for the variation in gas (P_1) and solid (P_2) pressure, gas (M_1^2) and solid (M_2^2) Mach number squared, and solid volume fraction (ϕ_2) within the reaction zone

test problems in which analytical results were available for comparison. The existence of a shock to detonation (SDT) path leading to a fully resolved two-phase Chapman-Jouguet (CJ) detonation was demonstrated. Detailed comparisons between the numerical predictions and predictions given by a formal steady-state analysis clearly show that the detonation structure consists of a shocked gas and an unshocked solid.

Since the focus of this study was on obtaining unsteady predictions which could be directly compared with previously published results for a steady two-phase CJ detonation, simple constitutive relations were used. Constitutive relations which are more representative of real physical systems can be easily incorporated into the model in order to obtain better predictive capabilities. Lastly, we note that additional work is needed to determine the influence of the singularities (associated with a parabolic degeneracy in the model equations) on both the analytical and computational solution behavior.

References

Baer MR, Nunziato JW (1986) A two-phase mixture theory for the deflagration to detonation transition (DDT) in reactive granular materials. Int J Multiphase Flow 12:861-889

Bement LJ, Schimmel ML (1988) Investigation of Super*Zip separation joint. NASA Technical Memorandum 4031

Bernecker RR, Price D (1974a) Studies in the transition from deflagration to detonation in granular explosives. I. Experimental arrangement and behavior of explosives which fail to exhibit detonation. Combust and Flame 22:111-118

Bernecker RR, Price D (1974b) Studies in the transition from deflagration to detonation in granular explosives. II. Transitional characteristics and mechanisms observed in 91/9 RDX wax. Combust and Flame 22:119-129

Butler PB, Krier H (1986) Analysis of deflagration to detonation transition in high-energy solid propellants. Combust and Flame 63:31-48

Chakravarthy SR, Osher S (1985) Computing with high-resolution upwind schemes for hyperbolic equations. In: Lectures in Applied Mathematics, American Mathematical Society (22), pp 57-86

Colella P, Trangenstein JA (1989) Higher order Godunov methods for general systems of hyperbolic conservation laws. J Comp Phys 82:362-397

Embid P, Baer M (1992) Mathematical analysis of a two-phase continuum mixture theory. Continuum Mech Thermodyn 4:279-312

Fickett W, Davis WC (1979) Detonation. University of California Press

Glaister P (1988) An approximate linearised Riemann solver for the Euler equations for real gases. J Comp Phys 74:382-408

Gonthier KA (1996) PhD dissertation (in progress). Dept of Aero and Mech Engr, University of Notre Dame, Notre Dame, IN

Osher S (1981) Numerical solution of singular perturbation problems and hyperbolic systems of conservation

laws. In: Mathematical Studies. North-Holland, New York, pp 47

Osher S, Solomon F (1982) Upwind difference schemes for hyperbolic systems of conservation laws. Math Comp 38:339-374

Powers JM, Stewart DS, Krier H (1988) Two-phase steady detonation analysis. Prog Astronaut Aeronaut 114:341-361

Powers JM, Stewart DS, Krier H (1989) Analysis of steady compaction waves in porous materials. J Appl Mech 56:15-24

Powers JM, Stewart DS, Krier H (1990a) Theory of two-phase detonation – part I: modeling. Combust and Flame 80:264-279

Powers JM, Stewart DS, Krier H (1990b) Theory of two-phase detonation – part II: structure. Combust and Flame 80:280-303

Roe PL (1981) Approximate Riemann solvers, parameter vectors, and difference schemes. J Comp Phys 43:357-372

Sandusky HW, Liddiard TP (1985) Dynamic compaction of porous beds. Naval Surface Weapons Center NSWC TR 83-246

Strang G (1968) On the construction and comparison of difference schemes. SIAM J Num Anal 5:506-517

Thompson KW (1987) Time dependent boundary conditions for hyperbolic systems. J Comp Phys 68:1-24

Toro EF (1989) A fast Riemann solver with constant covolume applied to the random choice method. Int J for Numer Methods Fluids 9:1145-1164

Williams FA, Barrere M, Huang NC (1969) Aspects of solid propellant rockets. NATO AGARDograph 116

INVESTIGATION OF
FRANZ-KELDYSH OSCILLATION AND
PHOTOLUMINESCENCE DECAY
IN SEMICONDUCTOR STRUCTURES

Jeremy A. Grata
Graduate Student
Department of Physics and Astronomy

Bowling Green State University
104 Overman Hall/Ridge Street
Bowling Green, OH 43403

INVESTIGATION OF
FRANZ-KELDYSH OSCILLATION AND
PHOTOLUMINESCENCE DECAY
IN SEMICONDUCTOR STRUCTURES

Jeremy A. Grata

Graduate Student

Department of Physics and Astronomy

Bowling Green State University

Abstract

We present a new technique that accurately extracts the bandgap from Franz-Keldysh oscillations (FKOs) by perturbing the internal electric field of a SIN structure or a laser PIN diode with a second, unmodulated laser pump. FKOs observed when the sample is illuminated by this perturbing pump shows small shifts in the peak energies relative to those in the unperturbed FKOs. These shifts are analyzed, using only linear least-square fitting, to provide both the phase and the critical point energy in the asymptotic expression for the FKOs. The technique works even when the near-bandgap spectrum is distorted. We have applied the perturbed photoreflectance technique to GaAs surface-intrinsic-n-doped (SIN) structures and to laser PIN diodes. In the SIN sample, we extract bandgaps within several meV of the expected values of the band-gaps. We have particularly tested our technique on the laser PIN diode. We extract the bandgap of the AlGaAs confinement barriers corresponding to an Al composition of 18% in good agreement with the nominal value.

We have measured the photoluminescence decay of various coupling structures of quantum wells. We have determined the carrier densities for band-filling effects.

INVESTIGATION OF
FRANZ-KELDYSH OSCILLATION AND
PHOTOLUMINESCENCE DECAY
IN SEMICONDUCTOR STRUCTURES

Jeremy A. Grata

1. Introduction

Photo-reflection (PR) modulation spectroscopy becomes essential to characterize semiconductor microstructures. Sharp oscillating features due to Franz-Keldysh oscillation (FKO) can be used to study the variation of the material properties on pressure, temperature, electric fields, etc. The basic principle of the PR modulation spectroscopy, rigorously formulated in Ref. [1], is based on evaluating the derivative with respect to some parameter, such as electric field. The derivative nature of the modulation spectra suppresses uninteresting background effects and emphasizes structure localized in the energy region of interband transitions at critical points in the mini-Brillouin zone. In addition, weak features that may not be have been seen in the absolute reflectance spectra are enhanced. Because of this derivative-like nature a large number of sharp spectral features can be observed even at room temperature. Furthermore, the spectrum also contains the information on the other modulation variables such as phase [2], modulation frequency [3], modulation amplitude, wavelength of the modulating pump beam [4], broadening, etc.

Recently, it has been shown that by interrupting sample growth at every interface, one can obtain multiple photoluminescence (PL) peaks with separate emission energies that correspond to the excitonic emissions at interface islands of different sizes [5-8]. Because of the formation of these interface islands, the well widths at these islands generally differ by one monolayer with respect to the designed width in high quality samples [9]. However, the area ratios among all these islands of different well widths are random, which cannot be controlled in growth process. Without the growth interruption, the recombination of the carriers in the wells with different widths results in the inhomogeneous broadening in the PL spectrum. At low temperatures, all the carriers generated by the pump will be eventually relaxed down to the lowest energy levels and localized in the islands, resulting in very large carrier densities. If the total area of the islands is small, it would be possible to completely fill exciton states in these islands at relatively low intensities that may manifest as the saturation of the PL peaks. By the same token, the carrier density can be sufficiently high to strongly renormalize the band-gap (BGR), which manifests as change of the PL linewidth of the exciton peak. It is worth noting that in growth-interrupted samples, BGR and band-filling effects

are spatially-localized effects, due to additional confinement along the interface, similar to situation in quantum dots (i.e. all the islands are spatially isolated).

2. Discussion of Problem

a. Franz-Keldysh oscillation

Previously, the ability to fit the lineshape [10] gives PR modulation spectroscopy an important advantage over other optical methods such as photoluminescence, photoluminescence excitation spectroscopy, photoconductivity, resonance Raman scattering, etc. It is possible to evaluate energy positions of spectral features to within several meV even at room temperature, to extract small and important features, to obtain accurate broadening parameters, etc. However, in some cases, the lineshape fitting is not accurate to determine parameters of the materials such as the band-gap. For example, near the band-edge, there are some features due to presence of trap sites that may distort the FKOs. Therefore, we have developed a modified PR modulation technique to extract the band-structure parameters based on all the oscillating cycles observable, rather than a few cycles near the band-edge.

b. Photoluminescence decay

The sample was grown by MBE on a semi-insulating GaAs substrate in collaboration with Naval Research Labs. The epitaxial layers consist of 10 periods, each of which is composed of three narrow asymmetric coupled GaAs quantum wells with the designed thicknesses of $45\,\text{Å}$, $30\,\text{Å}$ and $50\,\text{Å}$, coupled by $40\,\text{Å}$-$Al_{0.3}Ga_{0.7}As$ barriers, see Fig. 1. The thicknesses of the barriers between the adjacent periods are $40\,\text{Å}$. One sample is undoped while the other one is doped with silicon ($10^{17}\,\text{cm}^{-3}$) in the barrier layer between the 30-Å and 50-Å wells. During the sample growth there is an interruption for 60 seconds at every interface. Because of this growth interruption, interface islands with sizes larger than the average exciton radius are formed, allowing excitons being spatially-localized within these islands with separate optical transition energies from that of free-excitons [5]. As a result, in each designed well the absorption and/or emission peaks are separated from each other corresponding to one monolayer thickness ($2.8\,\text{Å}$) difference. In our low temperature photoluminescence excitation (PLE) spectra, we have clearly observed both the primary excitonic emission peaks (I) for the designed quantum well widths and the secondary excitonic emission peaks (II) that correspond to interface islands with the well widths one monolayer thicker than the designed ones. The emission peaks corresponding to interface islands are much narrower than those without growth-interruption. At 0.54 W/cm^2 for the e_1hh_1 (II) emission, the half width at the half maximum determined from the low energy side is $\sim 4.5\,\text{Å}$

(0.95 meV). This is the narrowest linewidth obtained so far. When we change the intensity from 0.54 W/cm^2 to 1.9 kW/cm^2 at 4 K, we can see that the linewidth of the PL peak increases dramatically. Indeed, it increases from 0.95 meV to 4.4 meV. However, the energy of the emission peak stays the same for all the intensities. Following the argument in Ref. [11], We attribute the large increase of the PL linewidth to the band-gap renormalization.

As mentioned above, a single PL peak breaks into two because of the formation of interface islands with the size larger than the exciton radius. At low temperatures, all the carriers generated by the pump laser will be eventually relaxed down to the lowest energy levels and localized in the islands, resulting in large carrier densities. If the total area of the islands is small, it would be possible to completely fill exciton states in these islands at relatively low intensities, which manifests as the saturation of the PL peaks. This type of the band-filling effect only occurs at the spatially-localized islands.

It is expected that the carrier density required to observe these effects should be subsequently lower than that outside the islands. We intend to measure the photoluminescence decay time to determine the carrier densities.

3. Methodology

a. Franz-Keldysh oscillation

In this new scheme for the PR modulation spectroscopy, we have used two laser beams as pump beams with their frequencies above the frequency of the band-gap of the GaAs or AlGaAs layer (forming the Surface-Intrinsic-N-doped, SIN, structure or a laser PIN diode). A chopped He-Ne laser beam is used to modulate the bias, and therefore, the reflectance of a probe beam. A second, unmodulated, Argon laser beam is used to change the total bias across the GaAs or AlGaAs layer or the internal electric field. We can measure the modulated, relative reflectivity of a probe beam obtained by sending the lamp light through a monochromator. One should observe strong dependence of the Frank-Keldysh oscillation (FKO) on the intensity of the Argon pump: the extrema in the spectrum should shift when the Argon beam intensity increases. In the PR modulation spectrum, we can determine the photon energies of the extrema for the FKO. Based on the changes of the energies between two different intensities of the Argon pump beam and the linear least-square fitting, we can obtain the phase for the FKO. We can determine the band-gaps of GaAs or AlGaAs layer by least-square-fitting the energies vs. the 2/3 power of the phase-shifted FKO index. Fig. 2(a) shows our schematic set-up.

b. Photoluminescence decay

For the measurement of the PL decay, we used a mode-locked Ar^+ laser as our excitation pulse with the pulse duration of 150 ps and output wavelength of 5145 Å. The temporal traces of the PL signal were taken via a streak camera with a time resolution of 20 ps. Fig. 2(b) shows our schematic set-up.

4. Results

a. Franz-Keldysh oscillation

We studied two pieces of SINs cut from two different wafers. The intrinsic layer of each SIN consists of a thin GaAs layer. Fig. 4(a) shows the PR modulation spectra for one of the samples at two different intensities of the Argon pump: zero and high intensity. We can clearly see the FKOs in the spectra. Furthermore, there are obvious shifts between the corresponding extrema of two spectra. The photon energies of the extrema can be determined from Fig. 4(a) for both spectra; we call them $E_m^{(0,h)}$ where m = 1 corresponds to the first clearly resolved extremum and 0,h - zero and high pump intensity. We have plotted $[E_m^{(0)} - E_m^{(h)}]^{3/2}$ vs. the FKO index, m, in Fig. 4(b). From the least-square fit, we have determined the phases for the FKO for these two samples: $\phi_1 \approx -1.648 \pi$ and $\phi_2 \approx 0.8343 \pi$. Following Ref. [1], we obtain

$$E_m - E_g = [(3/2)(m\pi - \phi)]^{2/3} \hbar\Omega \tag{1}$$

where E_g is the band-gap, ϕ is the phase for the FKO, and $\hbar\Omega$ is the electro-optic energy, which is related to the electric field F through

$$(\hbar\Omega)^3 = e^2 \hbar^2 F^2 / 2\mu \tag{2}$$

where μ is the reduced interband mass of the electron-hole pair along $\vec{F}$. In Eq. (1) we can replace E_m by $E_m^{(0)}$ and ϕ by two different phases determined from our experiments. We have plotted $E_m^{(0)}$ vs. $[(3/2)(m\pi - \phi_1)]^{2/3}$ for one sample in Fig. 4(c). By least-square fitting the data in Fig. 4(c), we can determine the band-gap to be $E_{g,1} \approx 1.425 \, eV$. Similarly, for the second sample, $E_{g,2} \approx 1.447 \, eV$. The value of the band-gap for the second sample is larger than the accepted value for bulk GaAs (1.424 eV). We believe this is probably due to the presence of some intentionally incorporated AlAs layer during growth.

Our third sample is a laser pin diode structure. It consists of an InGaAs layer sandwiched by two GaAs layers. Next to each of the GaAs layers, there is an AlGaAs confinement barrier with the nominal value of the aluminum concentration of 20%. Next to each of these AlGaAs layers, there is a AlGaAs layer with much higher aluminum

concentration. Fig. 5(a) shows the PR modulation spectra for two different pump intensities. We can clearly see the shifts of the corresponding extrema between two spectra. We can follow exactly the same procedure for determining the band-gap of GaAs as shown above. (It is difficult for us to use the lineshape fit for determining the band-gap of the AlGaAs layer because of the presence of an additional set of the FKOs in the GaAs layers.) The phase of the FKO is 0.8191 π from Fig. 5(b). We can then determine the band-gap of AlGaAs to be 1.687 eV from Fig. 5(c). This translates into 18.1% of aluminum in the AlGaAs layers in good agreement with the nominal value (20%).

b. Photoluminescence decay

We have made the time-resolved PL measurements in both types of our samples. Fig. 6 shows the typical temporal PL traces detected at the center wavelengths of $e_1 hh_1$ (II) emission peaks (the excitonic emission peaks) as a result of the carrier recombination at the interface islands in the 18 ML well. After the excitation, the PL signals at the $e_1 hh_1$ (II) emission peak maximize at about 700 ps and 650 ps in the undoped [Fig. 6(a)] and the modulation doped [Fig. 6(b)] samples, respectively. This is due to the competition between the carrier intersubband relaxation and the carrier recombination. As indicated in Fig. 6, by fitting the decay portions of these traces to the exponential functions, we have obtained the PL decay time constants of 357 ps and 438 ps for the undoped [Fig. 6(a)] and the modulation doped [Fig. 6(b)] sample, respectively.

The life time of the excitons is determined by [12]

$$\tau = \frac{2\pi\varepsilon_0 m_0 c^3}{n_b e^2 \omega^2 f}$$ (3)

where ε_0 is the dielectric constant, m_0 is the electron free mass, c is the speed of light, n_b is the background refractive index, ω is the frequency of the radiative optical transition, and f is the corresponding transition strength. We therefore obtain the oscillator strengths for the $e_1 hh_1$ (II) excitons to be 6.13 for the undoped sample and 5 for the doped sample. This explains why the islands related emission peaks in our PLE spectra is weaker in the modulation doped sample than that in the undoped sample.

In the quasi-CW regime, the density of excitons can be determined as

$$N_{ex} = \tau \frac{I_{laser} \alpha}{\hbar\omega_{laser}}$$ (4)

where I_{laser} is the laser intensity, α is the absorption coefficient, and $\hbar\omega_{laser}$ is the energy of a single photon. The saturation intensity to completely fill the $e_1 hh_1$ (II) excitons states in the

modulation doped sample is about $1.2\,\mathrm{kW/cm^2}$. Assuming $\alpha \approx 10000\,\mathrm{cm^{-1}}$ at the pumping wavelength in our experiments, the exciton density is then estimated to be $2.03 \times 10^{16}\,\mathrm{cm^{-3}}$. The corresponding area density is $1.04 \times 10^{10}\,\mathrm{cm^{-2}}$. Assuming that for $I_{laser} \sim 1.2\,\mathrm{kW/cm^2}$, all the quantum states have been almost occupied, we can estimate the exciton density at the interface islands using the two dimensional density of states and the estimates of the island area ratio above. The carrier density in the first electron energy level with the energy position ε_1 and the linewidth $\Delta\varepsilon$ can be determined by

$$N(e_1) = \int_{\varepsilon_1 + \Delta\varepsilon/2}^{\varepsilon_1 - \Delta\varepsilon/2} \rho_{2D}(\varepsilon)f(\varepsilon)d\varepsilon \qquad (5)$$

where the two dimensional density of states, $\rho_{2D} = m^*/\pi\hbar^2$, is a constant, with m^* the effective mass, $f(\varepsilon) = 1/[1 + \exp(\varepsilon - \varepsilon_F)/kT]$ is the Fermi-Dirac distribution function, with ε_F the Fermi energy and k the Boltzmann constant. In the case of almost complete band filling at low temperatures, we may treat the electrons at the energy level ε_1 as degenerate electron gas. In this case, $f(\varepsilon) \approx 1$. Eq. (5) then reduces to

$$N(e_1) = \rho_{2D}\Delta\varepsilon(e_1) \qquad (6)$$

From the PLE spectrum, we estimated that the linewidth $\Delta\varepsilon(e_1)$ is about 5 meV in our samples. Based on the area ratio determined above, the carrier density to completely fill the interface islands regarding $e_1 hh_1$ (II) transition is estimated to be $\sim 1.12 \times 10^{10}\,\mathrm{cm^{-2}}$. This is in good agreement with the estimate obtained based on Eq. (4) above. This carrier density is an order of magnitude smaller than that outside the islands.

We have also measured PL decay of several other coupling structures with and without the presence of a dc magnetic field. We are in the process of analyzing our results.

5. Conclusion

We have developed a modified photo-reflectance modulation technique that can be used to characterize semiconductor structures, especially to determine the bandgaps and aluminum concentration. We have measured time-resolved photoluminescence decay in growth-interrupted multiple asymmetric three narrow quantum wells. We have subsequently determined decay times and characteristic carrier densities for observing pronounced band-filling effects. The spatially-localized band-filling effect in our sample is more pronounced than the conventional one for the same irradiance.

Some of our results have already been submitted for publication [13,14].

6. Acknowledgement

We are indebted to Dr. R. Sherriff, Mr. J. Hoelscher, and Dr. D. C. Reynolds for their expertise in the areas above, that had made it possible for us to complete four different projects during twelve-week period.

7. References

[1] D. E. Aspnes and A. A. Studna, Phys. Rev. B7, 4605 (1973).

[2] H. Shen, S. H. Pan, F. H. Pollak, M. Dutta, and T. R. AuCoin, Phys. Rev. B 36, 9384 (1987).

[3] H. Shen, Z. Hang, S. H. Pan, F. H. Pollak, and J. M. Woodall, Appl. Phys. Lett. 52, 2058 (1988).

[4] H. Shen, X. C. Shen, F. H. Pollak, and R. N. Sacks, Phys. Rev. B36, 3487 (1987).

[5] D. Bimberg, D. Mars, J. N. Miller, R. Bauer, O. Oertel, and J. Christen, Supperlatt. Microstruc. 3, 79 (1987).

[6] M. Kohl, D. Heitmann, S. Tarucha, K. Leo, and K. Ploog, Phys. Rev. B39, 7736 (1989).

[7] D. C. Reynolds, K. K. Bajaj, C. W. Litton, P. W. Yu, J. Singh, W. T. Masselink, R. Fischer, and H. Morkoc, Appl. Phys. Lett. 46, 51 (1985).

[8] K. Fujiwara, K. Kanamoto, and N. Tsukada, Phys. Rev. B40, 9698 (1989).

[9] B. Devcaud, A. Chomctte, N. Roy, B. Scrmagc, and D. S. Katzer, Sur. Sci. 267, 199 (1992); D. Gammon, B. V. Shanabrook, and D. S. Katzer, Appl. Phys. Lett. 57, 2710 (1990).

[10] C. Van Hoof, K. Deneffe, J. De Boeck, D. J. Arent, and G. Borghs, Appl. Phys. Lett. 54, 608 (1989).

[11] S. Schmitt-Rink, D. S. Chemla, and D. A. B. Miller, Adv. Phys. 38, 89 (1989).

[12] J. Feldmann, G. Peter, E. O. Göbel, P. Dawson, K. Moore, C. Foxon, and R. J. Elliott, Phys. Rev. Lett. 59, 2337 (1987).

[13] A. G. Cui, Y. J. Ding, S. J. Lee, J. V. D. Veliadis, J. B. Khurgin, S. Li, D. S. Katzer, D. C. Reynolds, J. Grata, and R. E. Sherriff, submitted to J. Opt. Soc. Am. B.

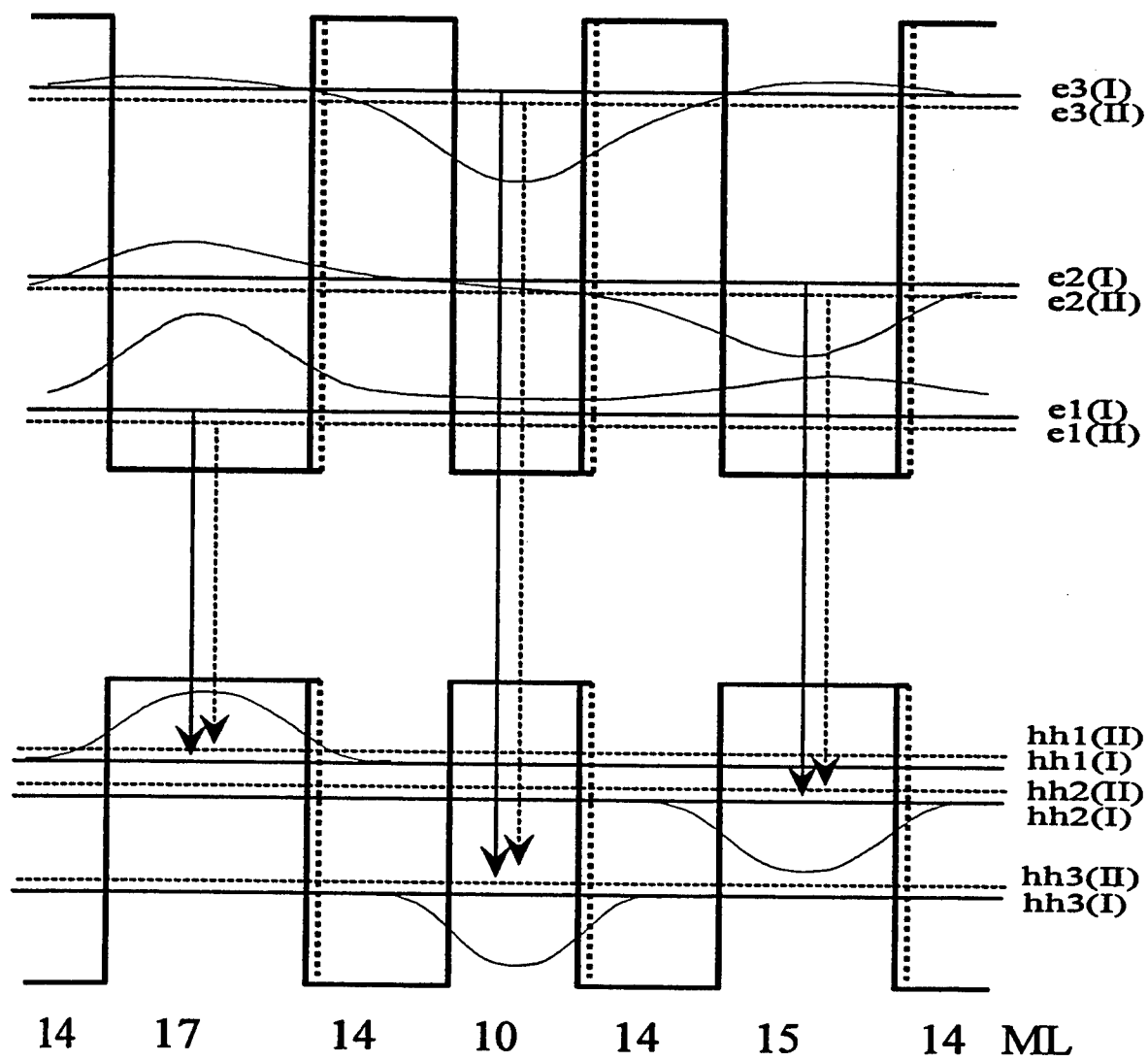[14] Y. J. Ding, J. Grata, J. Hoelscher, and R. E. Sherriff, submitted to 1995 Amer. Phys. Soc. Ohio Section Meeting.
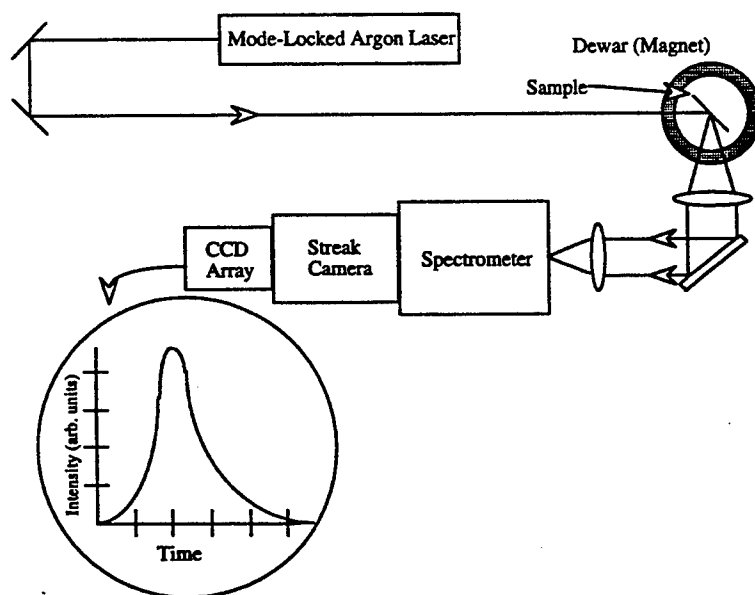
Figure 1
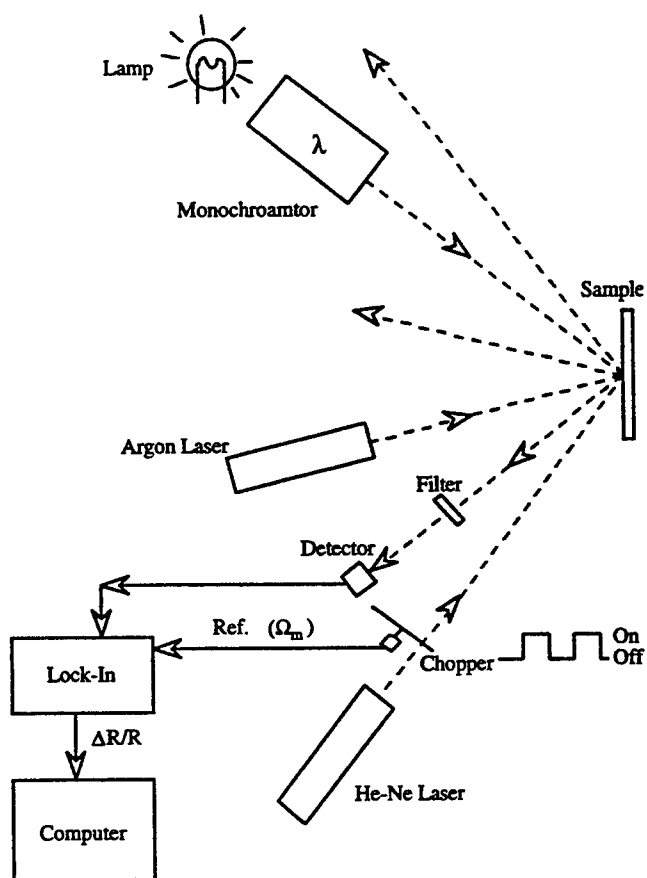
14−10

Figure 2

Figure 3

(a)

$\Delta R/R$

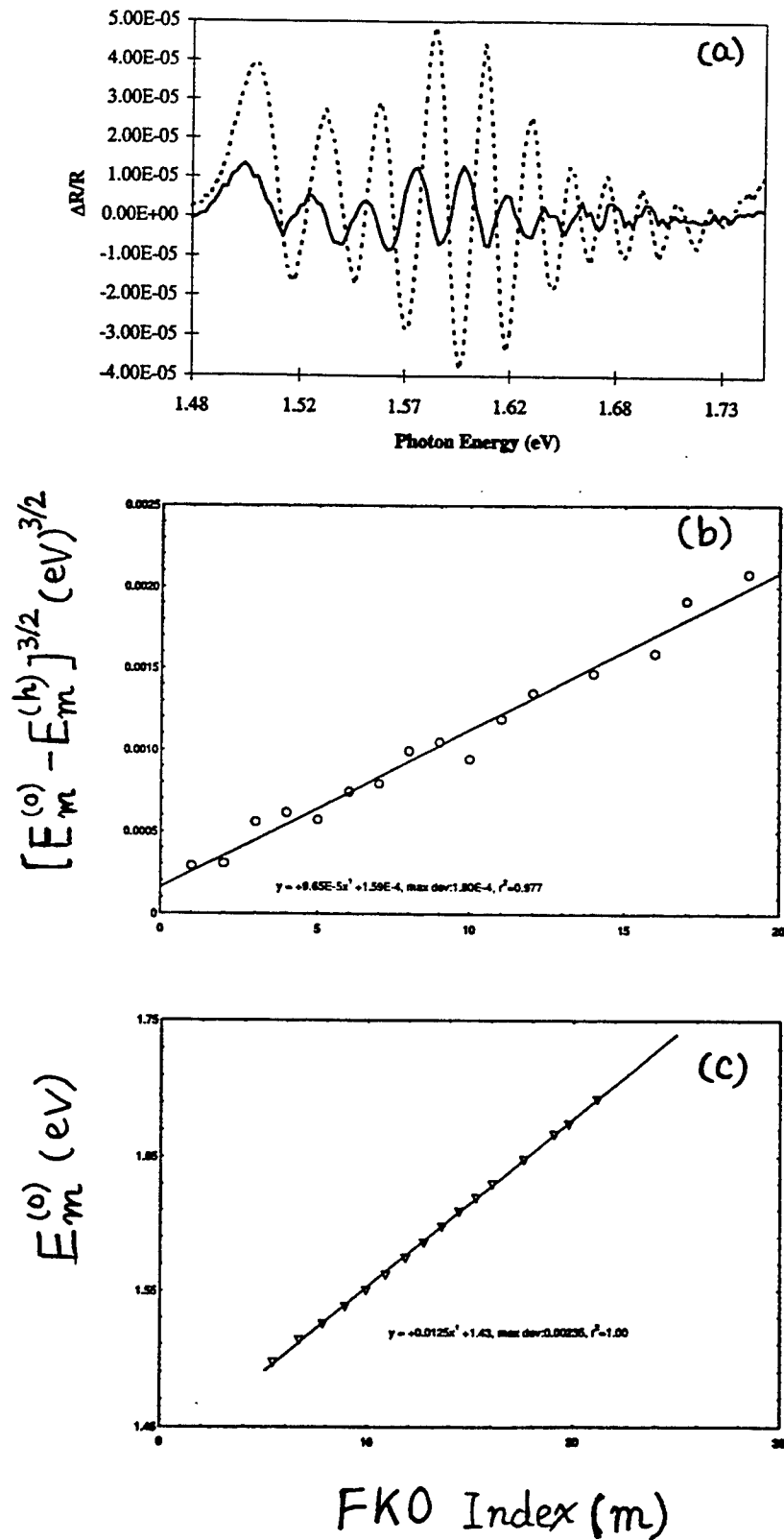Energy (eV)

852-plh
852-plc

(b)

$[E_m^{(0)} - E_m^{(h)}]^{3/2}$ $(eV)^{3/2}$

y = +3.21E-5x¹ -2.59E-5, max dev:1.08E-4, r²=0.907

(c)

$E_m^{(0)}$ (eV)

y = +0.0156x¹ +1.69, max dev:0.0178, r²=0.990

FKO Index (m)

Figure 4

14-13

Figure 5

14-14

CHARACTERIZATION OF POLED POLYMER THIN FILMS AND DEVELOPMENT OF AN OPTICAL FIBER ELECTRIC FIELD PROBE

Karen E. Hiser
Graduate Student
Department of Electro-Optics

Center for Electro-Optics
University of Dayton
300 College Park
Dayton, OH 45469-0245

Final Report for:
Summer Graduate Research Program
Wright Laboratory

August 1995
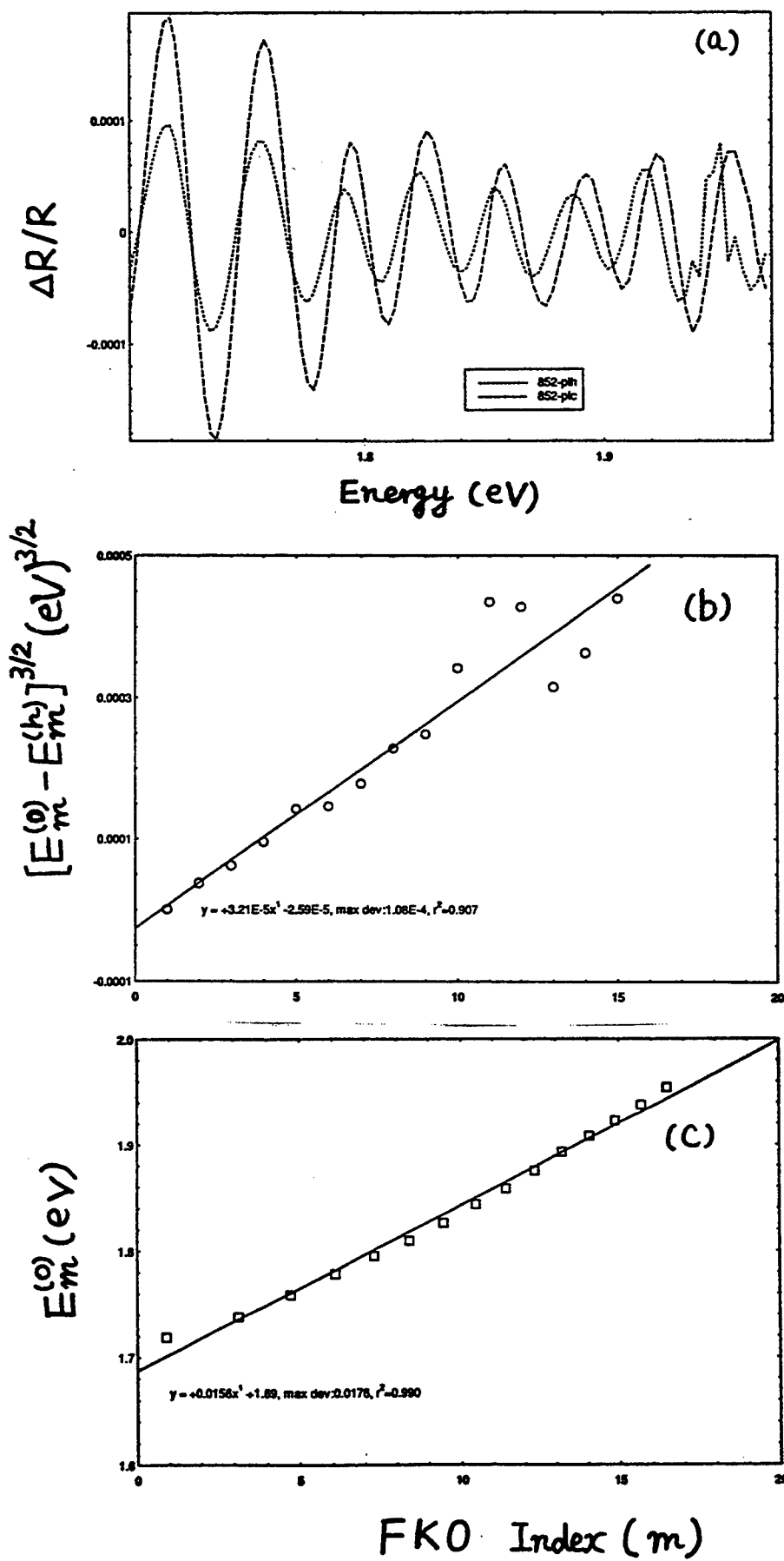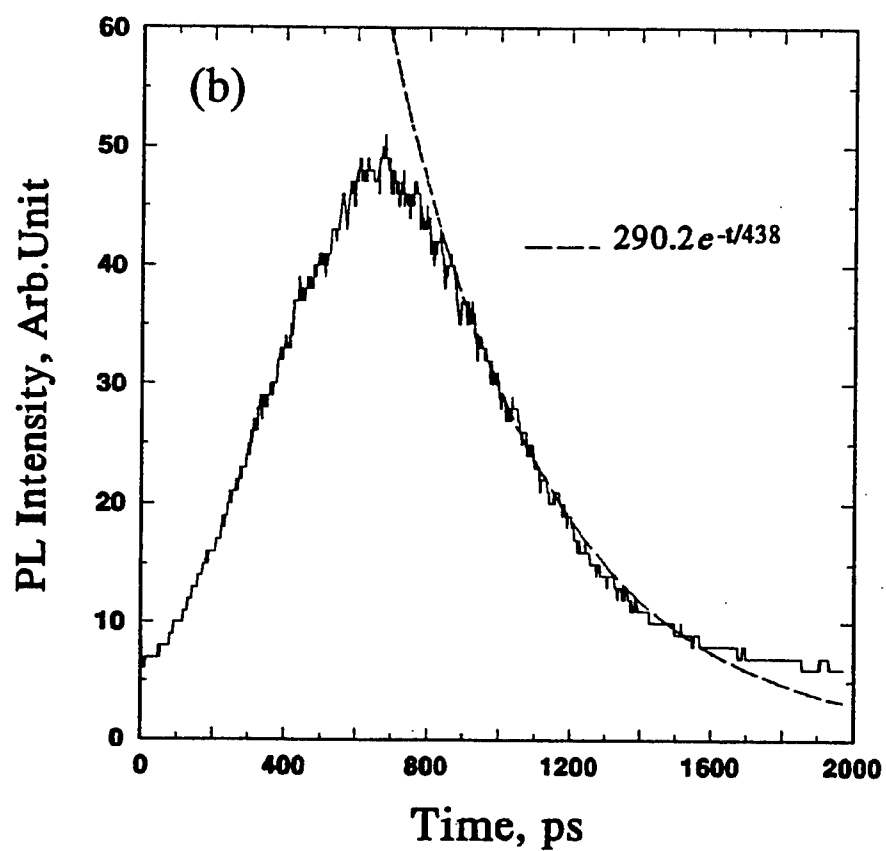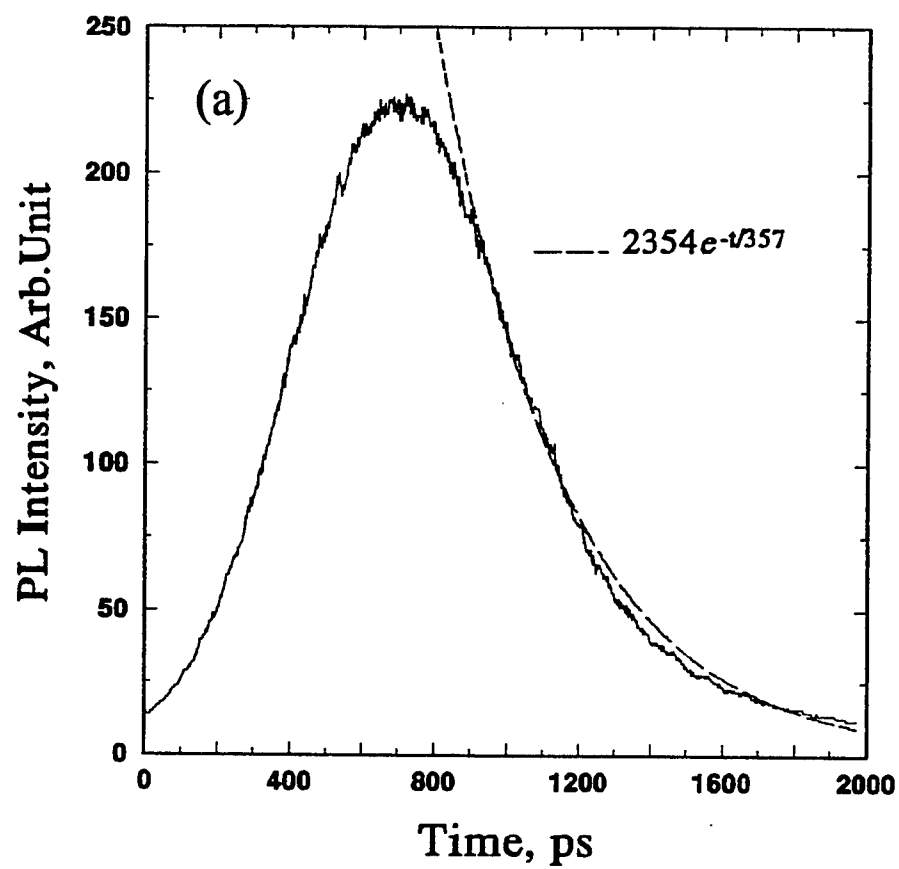
CHARACTERIZATION OF POLED POLYMER THIN FILMS AND DEVELOPMENT OF AN OPTICAL FIBER ELECTRIC FIELD PROBE

Karen E. Hiser
Graduate Student
Department of Electro-Optics

Abstract

We prepared and poled polymer samples for electro-optic measurements using various weight percents of Disperse Red 1 as a guest in a PMMA host. The capacitance and conductance were monitored versus temperature, ac frequency, and weight percent of DR1. We poled the samples using an apparatus that allows *in situ* monitoring of the electro-optic coefficient. The electro-optic coefficient was found to vary linearly versus DR1 weight percent and applied dc poling field. We also began development of a fiber probe that utilizes poled polymers attached to the tip of a fiber and an in-plane poling geometry to detect circuit board electric fields.

CHARACTERIZATION OF POLED POLYMER THIN FILMS AND DEVELOPMENT OF AN OPTICAL FIBER ELECTRIC FIELD PROBE

Karen E. Hiser

Introduction

Organic polymers for thin film optical devices (switches and modulators) are a promising recent development in the field of nonlinear optics. Certain organic polymers exhibit large optical nonlinearities when placed in strong electric fields at high temperature. The electro-optic coefficient of the polymers, a measure of the nonlinear activity exhibited by a material, is theoretically predicted to be larger than that of the common nonlinear crystals currently in use. For instance, poled-polymer electro-optic (EO) coefficients exceeding that of lithium niobate, ($\approx$30 pm/V) have recently been reported and EO coefficients approaching 100 pm/V are hypothesized for polymer systems.

Optical polymers can be made into thin films and waveguides much more readily than nonlinear crystals.[1] Since spin-coating of electro-optic polymers is readily adapted to current opto-electronic technology, optical polymer devices will be both inexpensive and easy to construct. Applications of nonlinear optical polymers include high capacity optical communication networks, optical data storage, and opto-electronic integrated circuits. Polymers may soon replace nonlinear crystals in optical switches and filters, frequency converters, and linear electro-optic modulators. In addition, we can place a thin film of poled polymer on the end of a fiber to detect the presence and strength of electric fields near circuit boards or other equipment. Such a poled polymer/fiber field probe will be much less invasive than current technology.

Theory

Nonlinear optical polymers consist of large organic molecules doped with chromophores. The chromophore is dipolar with one end that attracts and one end that repels electrons. The chromophores are usually attached to the polymer as a side-chain to increase the thermal stability of the alignment state. Our studies focused on the simpler to prepare guest/host mixture of chromophore/polymer. Raising the temperature of the system to the critical temperature, called the glass transition temperature T_g, allows the molecules to rotate ≈freely.[1] At elevated temperature, application of a strong electric field $\vec{E}_{poling}$ exerts a torque $\vec{\tau}$ on the molecular dipole $\vec{p}$ which aligns the molecules with the field: $\vec{\tau} = \vec{p} \times \vec{E}_{poling}$. Typically ≈15% chromophore alignment is achieved with this poling method.[2] In contact poling the polymer is placed between two electrodes, usually indium tin oxide (ITO - a transparent electrical conductor) and gold. The applied voltage aligns the molecules with the polar axis normal to the plate surface.[3] The molecules remain aligned after cooling the sample to room temperature with the electric field still applied.

Poling a polymer/chromophore system aligns the dipoles and removes the inversion symmetry causing the system to exhibit the linear electro-optic (Pockel's) effect. The electro-optic effect is a field-induced change in the optical dielectric properties and is often written:[4]

$$\Delta\{\overleftrightarrow{\varepsilon}_R^{-1}(\omega)\} = \overleftrightarrow{r} \cdot \vec{E}_{applied} \tag{1}$$

where $\overleftrightarrow{\varepsilon}_R^{-1}(\omega)$ is the inverse of the relative dielectric tensor evaluated at the optical frequency ω, $\overleftrightarrow{r}$ is the third-rank electro-optic tensor, and $\vec{E}_{applied}$ is the applied field. Since the complete tensor notation is intimidating, this expression is usually written under the limiting assumption of a $\hat{z}$-polarized probe beam and $\vec{E}_{applied} = E_{applied} \hat{z}$ ($\hat{z}$ is the polar axis of the poled polymer):

$$\Delta n_e = -\frac{1}{2} n_e^3 \, r_{33} \, E_{applied} \tag{2}$$

where n_e is the extra-ordinary refractive index of the polymer, r_{33} is the largest electro-optic coefficient, and $E_{applied}$ is the applied electric field. If the incident beam is not either purely extraordinary polarization (polarized parallel to $\hat{z}$)

or ordinary polarization (polarized in the xy plane) then the electro-optic effect will change the polarization state of the beam.[5]

The parameter of interest in nonlinear optical materials is $\chi^{(2)}$, the second-order electric susceptibility. The susceptibility of any order relates polarization density to the electric field. The second-order susceptibility is proportional to the electro-optic coefficient via:

$$\chi^{(2)}(-\omega;\omega,0) = -\frac{1}{2}n^4 r \qquad (3)$$

using the consistent notation of Butcher and Cotter.[6] Generally, the r_{33} value of a material is reported rather than $\chi^{(2)}$. The r_{33} value is quite often found by monitoring the change in polarization state of a probing optical beam. In the *in situ* poling apparatus the applied dc field $\vec{E}_{poling}$ can cause spurious effects that we wish to eliminate. The dc poling field operates through the $\chi^{(3)}$ of the material to give an *effective* $\chi^{(2)}$ (which according to Eqn. 3 above is equivalent to an electro-optic coefficient). In the following we distinguish between the dc poling field $\vec{E}_{poling}$ and the ac field $\vec{E}_{\Omega}$ which is applied to the sample to periodically modulate the polarization state via the electro-optic effect. We expand the field-induced change in the material polarization density in the frequency domain according to:

$$\Delta P(\omega + \Omega) = P^{(2)}(\omega + \Omega) + P^{(3)}(\omega + \Omega) + \dots \qquad (4)$$

where:

$$P^{(2)}(\omega + \Omega) = \varepsilon_o \chi^{(2)}(-\omega - \Omega;\omega,\Omega) E_\omega E_\Omega \qquad (5)$$

and:

$$P^{(3)}(\omega + \Omega) = \varepsilon_o \chi^{(3)}(-\omega - \Omega;\omega,\Omega,0) E_\omega E_\Omega E_{poling} \qquad (6)$$

where E_ω is the optical field. The optical beam leaving the electro-optic material (radiated by the total material polarization density) will contain sidelobe frequencies at $\omega \pm \Omega$. A lockin amplifier connected to a photodiode will detect a signal modulating at the frequency Ω that contains contributions from both terms above (Eqn. 5 & 6). We wish to find a method for removing the $\chi^{(3)}$ contribution from the measured signal and thus isolate the pure $\chi^{(2)}$

contribution. We attempt to do this by simultaneously measuring the lockin signal at Ω and the signal at 2Ω that is due to the term:

$$P^{(3)}(\omega + 2\Omega) = \varepsilon_o \, \chi^{(3)}(-\omega - 2\Omega; \omega, \Omega, \Omega) \, E_\omega \, E_\Omega \, E_\Omega. \qquad (7)$$

Since we know the relative strength of the ac field E_Ω and the dc poling field E_{poling}, we can determine the $\chi^{(3)}$ contribution to our signal and remove it.

Another important parameter for poled-polymer systems is the glass transition temperature, T_g. The glass transition occurs when the polymer main chain is free to move. During poling, the chromophore molecules align more readily to the applied field as the temperature approaches T_g because the molecules are then more free to move. As the chromophore molecules align the polymer becomes more polarizable and is then able to store more charge causing the relative dielectric permitivity $\varepsilon_R = \varepsilon'_R + i\varepsilon''_R$ to increase.[7] The polymer is assumed to be a parallel-plate capacitor with known area and thickness.[8] The sample capacitance measures the real part of the relative permitivity $\varepsilon'_R(\Omega)$ (at the ac frequency Ω) according to:

$$C = \frac{\varepsilon_o \, \varepsilon'_R(\Omega) \, A}{T} \qquad (8)$$

where A is the electrode area and T is the thickness of the polymer layer. Therefore, monitoring the capacitance of the polymer is equivalent to measuring the real part of the dielectric constant at the ac frequency: $\varepsilon'_R(\Omega)$. The capacitance and ε'_R are expected to increase and then level off as the temperature is raised to T_g.[7]

Let's consider the temperature dependence of ε_R. Increasing the temperature of the polymer in a dc field causes the molecules to begin moving. As T_g is approached, the high viscosity of the system requires electrical energy dissipation for molecular motion. This results in an increase in the dielectric loss represented by the imaginary part of the relative permitivity ε''_R. Above T_g the molecules are free to move (viscosity is low) and can readily respond to the applied field causing the dielectric loss to decrease back towards zero.[7] The dielectric loss is related to energy dissipation and its characteristics can be found by monitoring the conductance of the polymer.

Now consider the frequency dependence of the dielectric permitivity. The dipoles in the polymer are able to respond to low frequency ac fields. As the frequency increases they are eventually unable to respond because of their inertia thus reducing the ability of the polymer system to store charge and reducing ε_R'. At these higher frequencies, some of the energy needed to overcome the potential barrier to dipolar motion is supplied by electrical energy producing an increased dielectric loss. Thus, as the frequency increases there are more dipole/polymer interactions (viscous drag on the dipolar motion) causing an increase in ε_R''.[7]

Since poled polymers change the polarization of a beam in the presence of an electric field they are ideal for probing such fields. We designed an electric field probe utilizing a thin film of poled polymer placed on the end of a polarization preserving fiber. The output of a semi-conductor laser is coupled into the fiber such that the input polarization is at 45° to the polarization axes of the fiber. The beam exits the fiber through the poled polymer. When the fiber is placed near a metallic surface (*e.g.* from a circuit board) the beam will be partially reflected back into the fiber. The beam travels back through the fiber and the resultant polarization state is detected. If the tip of the fiber is immersed in an electric field the output polarization is altered because of the electro-optic effect in the poled polymer.

The polar axis of the polymer must lie in the plane of the electric field to maximize the polarization change. This is because the largest polarization change occurs when the field-induced change in the birefringence of the system is the largest. The largest change in birefringence occurs when the electric field is along the $\hat{z}$ axis and one polarization axis of the fiber is also $\hat{z}$ while the other axis is either $\hat{x}$ or $\hat{y}$. Under these conditions the field induced birefringence change is:

$$\Delta\Gamma = -\frac{\pi}{\lambda}\left\{n_e^3\, r_{33} - n_o^3\, r_{13}\right\} V_{applied} \approx -\frac{2\pi}{3\lambda} n^3\, r_{33}\, V_{applied} \qquad (9)$$

where n_e and n_o are the extraordinary and ordinary refractive indices of the poled polymer. We assumed that $n_e \approx n_o \approx n$ and $r_{33} = 3\, r_{13}$ (ref. 2) in the approximation. Achieving the highest sensitivity (largest $\Delta\Gamma$ vs. $V_{applied}$ slope) requires in-plane poling of the polymer as shown in Fig. 1.
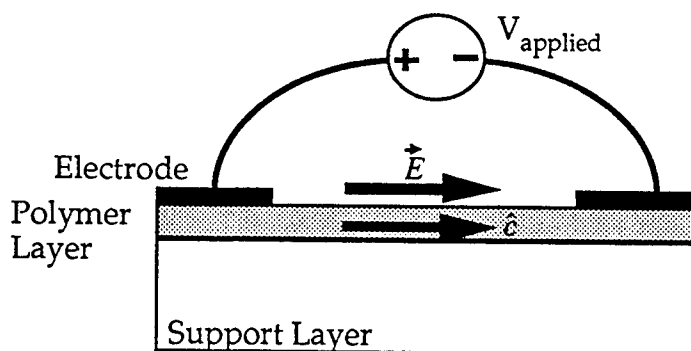
Figure 1)   In-plane poling of a polymer layer. The electrodes and support layer are removed before placing the polymer on the tip of a polarization preserving fiber. Note that this poling configuration will give the best sensitivity (using polarization interferometry) when the detected field is parallel (or anti-parallel) to the poling field.

Sample preparation

The polymer-chromophore group that we studied was Disperse Red 1 (DR1) in poly(methyl methacrylate) (PMMA). This system has been extensively studied.[1,5,8] The DR1 and PMMA were mixed in a solution with chloroform as the solvent. Weight percentages of .5, 1, 2, 5, and 10% DR1 (molecular weight 306) in PMMA (molecular weight ≈68000) were prepared for electro-optic measurements. The DR1 and PMMA came in powder form and chloroform was used as the solvent. The solutions were placed in a sonic bath to help dissolve the powders. The solutions were then filtered with a .2 μm filter before spinning them onto etched ITO-coated slides with a spin-coater in a cleanroom. After drying the slides overnight in an oven at 70°C to remove the remaining solvent, we evaporated gold electrodes/mirrors onto the polymer film. A Dektak profilometer was used to determine the thickness of the polymer films. The sample geometry is shown in Fig. 2.
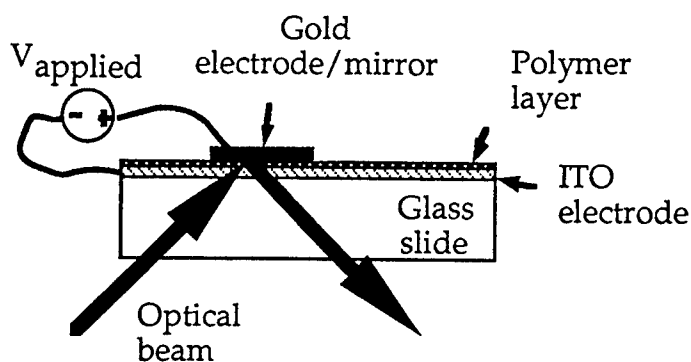

Figure 2a)   Side view of sample showing the ITO/polymer/gold layered stack.
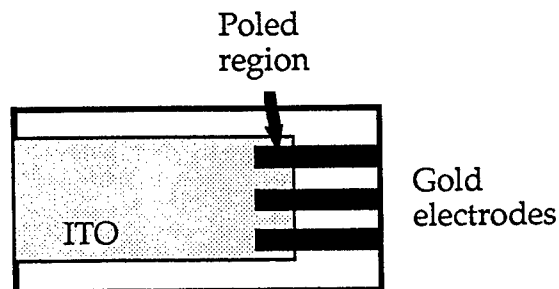
Figure 2b) Top view of sample shown above.

Cover slips were used for the in-plane poling samples. DR1/PMMA 10 wt. % in chloroform was spun onto the cover slips and then gold evaporated on top. Photolithography was used to place metallic electrodes with gaps from 10 to 25 microns wide on top of the polymer layer. The sample was then covered with an overcoat to prevent arcing during poling.
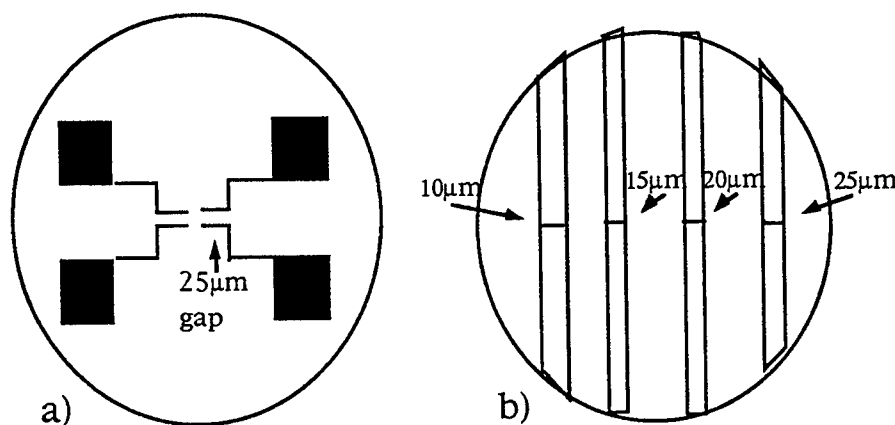

Figure 3) Top view of mask used on 18mm cover slips for gold electrodes. Figure a) shows the mask we used initially. One problem with this structure is arcing (in air) between the microprobes contacting the pads (black boxes above) during poling. Part b) shows the simple mask we designed to overcome this problem. The electrodes are easier to contact with the probes far enough apart to limit shorting between them.

Methodology

The capacitance, conductance, and glass-transition temperature of the DR1/PMMA samples were studied using a Hewlett-Packard 4274A LCR meter. Each weight percent sample was mounted on a heating element and connected to the LCR meter. The capacitance and conductance were monitored as the temperature of the sample was altered; the frequency of the

meter was held at 1kHz as each sample was probed. Then, a 10 wt. % sample was used to find the dependence of the capacitance and conductance on ac frequency and temperature. The T_g was found from the peak in the conductance versus temperature.

The set-up described by Teng and Man[9] was used to pole the samples and to study the electro-optic coefficient. The beam from a diode laser at 787 nm, polarized at +45° from vertical is incident upon the sample. The sample is mounted so that the beam is incident at 45° from the slide normal. The beam travels through the sample, is reflected off the gold electrode, and re-traverses the sample. The reflected light, polarized at +45° plus any change due to the electro-optic effect, then goes through a Babinet-Soleil retarder which changes the beam polarization to circular (in the absence of an electro-optic effect). An analyzer oriented at −45° is placed in front of a photodiode detector. Small changes in the polarization due to application of an electric field changes the intensity of the light passing through the analyzer. The sample is mounted on a heating element and connected to a signal generator/amplifier that produces both ac and dc voltages. Pieces of aluminum foil and alligator clips allow application of the voltage signal to the sample. A Stanford Research SR530 lock-in detects the output signal. The samples were poled by applying a one volt ac signal and 77 V/μm dc signal to the sample as it was heated up to 120°C $\approx T_g$ and then cooled back down to room temperature. The signal was monitored during poling and the electro-optic coefficient determined.
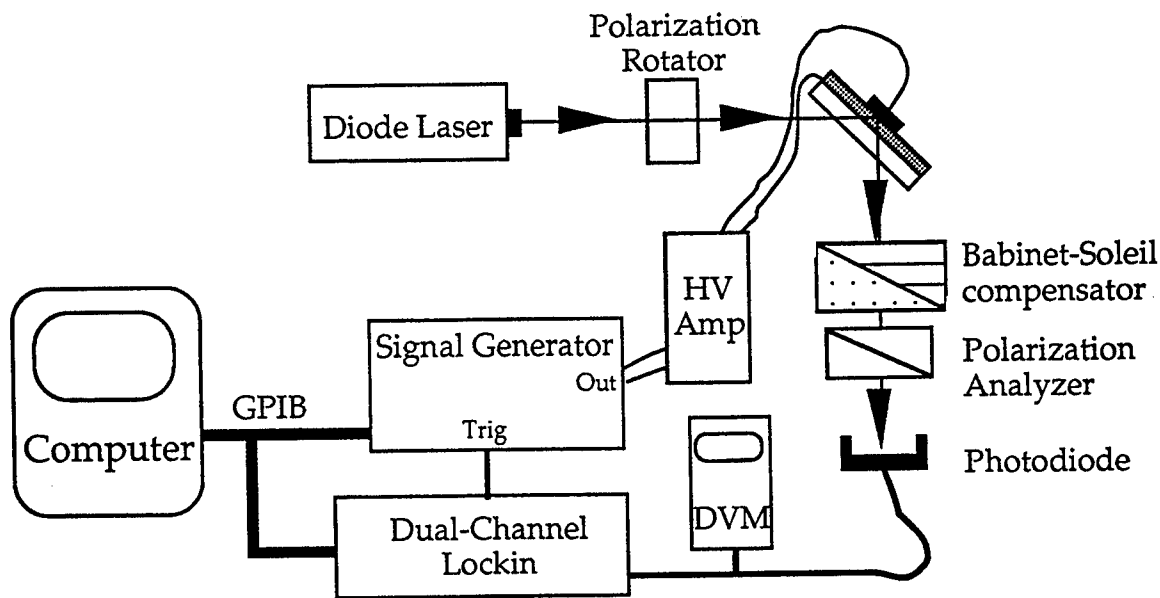
Figure 4)   Experimental set-up for poling and electro-optic measurements. The incident beam travels through the polymer and is reflected off the gold. The Babinet-Soleil makes the reflected light circularly polarized (in the absence of an electro-optic effect). Applying an electric field to the polymer induces small changes in the polarization and the intensity of the light passing through the analyzer is modulated.

The effect of changing the dc applied field on the electro-optic coefficient was evaluated for the different weight percent unpoled samples. The temperature was held constant at 30°C while the dc applied field was increased from 50 V to 200 V in 50 V increments. The *effective* electro-optic coefficient was found at each voltage. This spurious EO coefficient is due to the third-order effect (Eqn. 7) rather than from poling since the experiment was conducted so far below the poling temperature.

We utilized a two lockin method to further study the effect of the applied field on the EO coefficient during poling. A 10 wt. % sample was poled as described above while one lockin monitored the signal produced at the frequency of the applied ac field (Ω) and a second lockin monitored the signal produced at 2Ω. If both lockins have identical calibrations and the detector response is flat between Ω and 2Ω then according to Eqns. 5-8 the spurious signal measured at Ω can be removed by subtracting the quantity:

$$\frac{V_{poling}}{V_{\Omega}} \cdot \left\{ \text{signal measured at } 2\Omega \right\} \tag{10}$$

from the signal measured at Ω.

The electric field probe uses D-shaped Andrews Corporation polarization preserving fiber. The thin film polymer is attached to the end of the fiber with the poling axis aligned with the major axis of the elliptical fiber core.
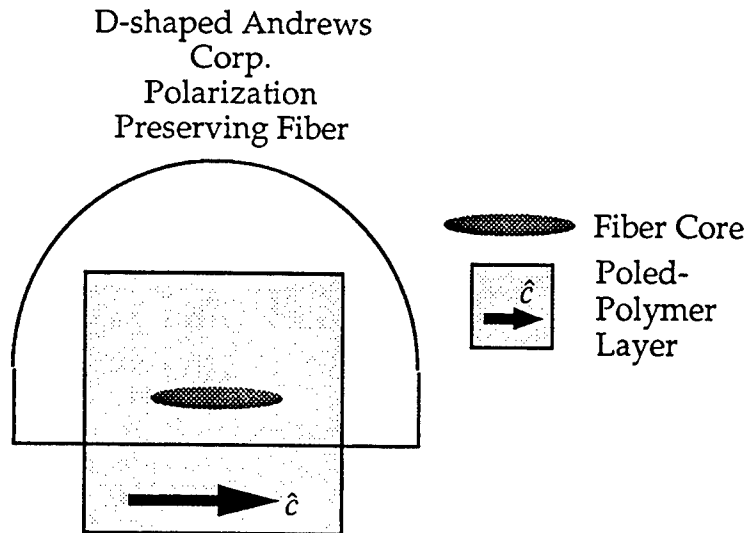
Figure 5) Alignment of the polar axis of the polymer with the polarization axis of the fiber at the fiber tip. The ellipticity of the fiber core is exaggerated.

The experimental set-up for the electric-field probe is shown in Fig. 6. A 676 nm semiconductor laser was used as the source. The reflected beam is made circularly polarized by a Babinet-Soleil compensator and is then split by a Wollaston prism into two orthogonally polarized beams that are detected by PIN photodiodes. If the polarization of the beam had been altered by an electrical field the two photodiodes will return different powers. The difference indicates the strength of the field.

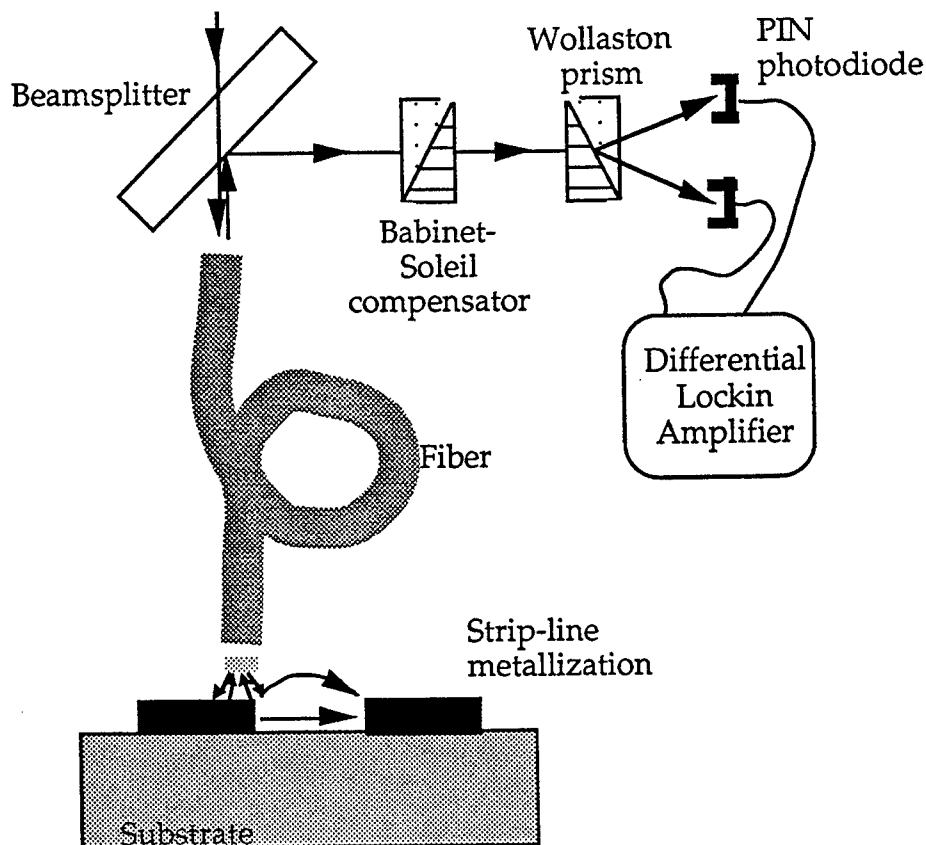Figure 6)   Experimental set-up for the electric-field probe. Light is sent into the fiber such that both polarization modes are excited. Light exiting the fiber is reflected from the metal back into the fiber. The returned light travels through a compensator and Wollaston prism. The photodiodes detect different intensities if there is a difference in the polarization state of the beam. The lockin amplifier measures the difference.

Results

Figure 7 shows the capacitance and conductance versus temperature for samples of 1-10 wt. % DR1. The T_g of DR1/PMMA is found from the peak in the conductance versus temperature curve. As the number of dopants increases the polymer will be more easily influenced by the applied field and the molecules will begin to move at a lower temperature. It has been shown that T_g decreases with increasing concentration of DR1.[8] Our data shows a slight downward shift in the temperature of the conductance peak. The shift should become larger at higher concentrations.
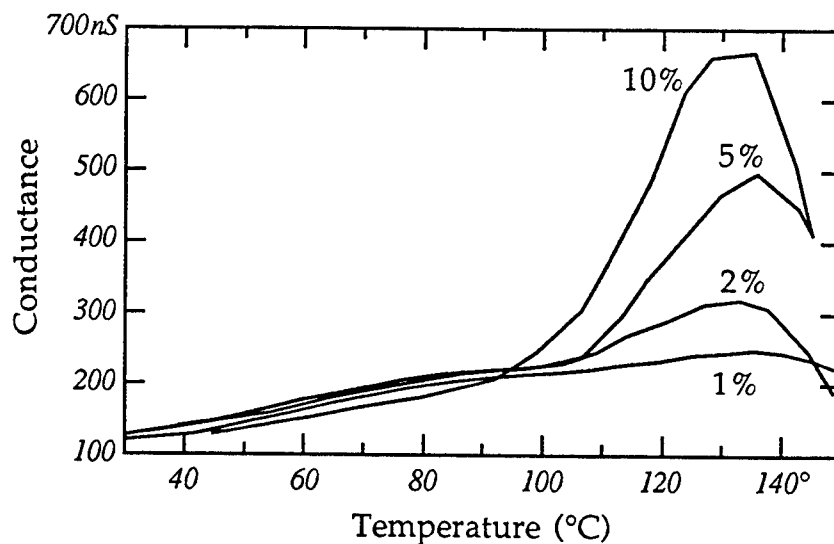
Figure 7) Graph of conductance versus temperature for four different weight percents of DR1. The peak in the conductance curve occurs at T_g and is shifted to lower temperature with increasing weight percent.

A 10 wt. % DR1/PMMA sample was used to find the temperature and frequency trends in the capacitance and conductance of the polymer. The results are shown in Fig. 8. The capacitance decreases with increasing frequency and increases with increasing temperature. These trends are due to the inability of the dipoles to align to the higher frequency ac fields and the increased polarizability of the polymer as the dipoles align near T_g. The conductance, on the other hand, increases with both frequency and temperature. These trends are due to the loss of energy from the applied field to overcome the viscous damping and align the molecules. Above T_g the energy loss decreases again and the conductance decreases. The temperature and frequency trends for capacitance and conductance agree with those seen by other researchers.[8,10]
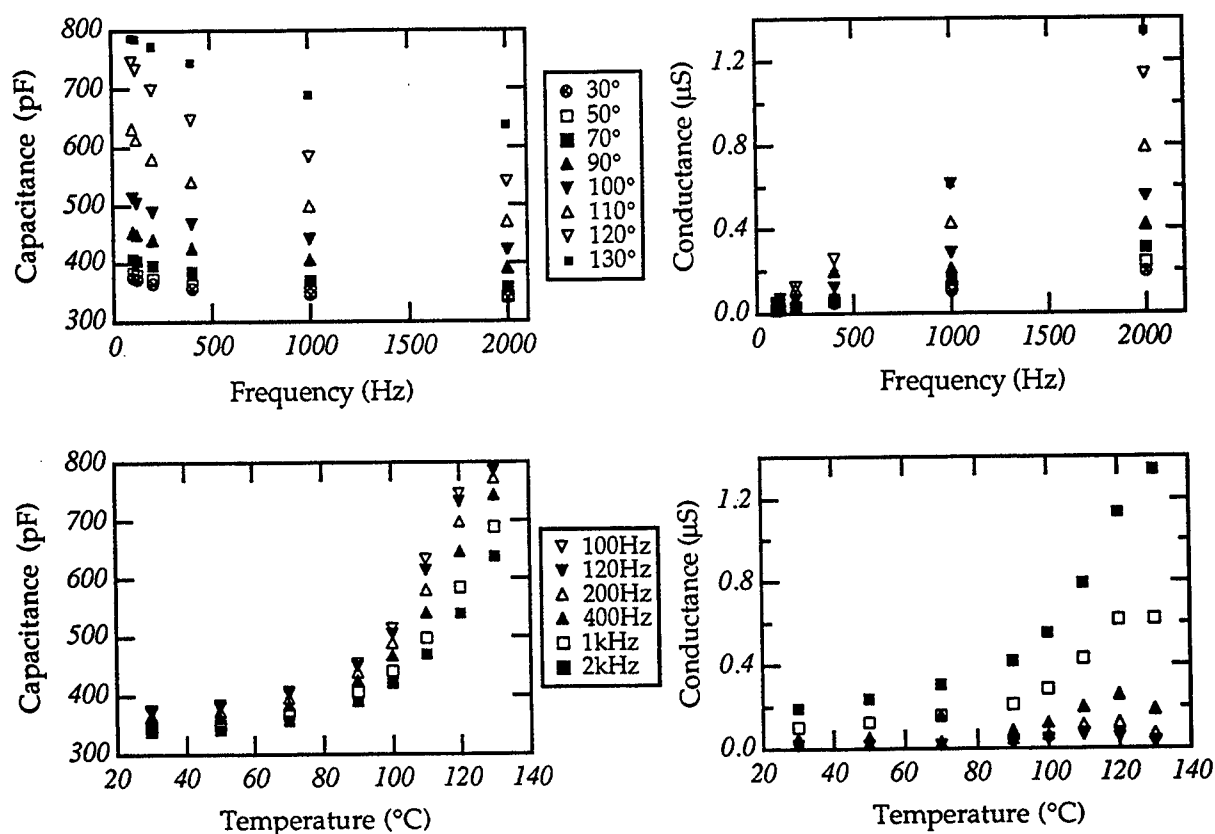
Figure 8)   Measured dependence of both the capacitance and conductance on ac probe field frequency and temperature. The sample was 10 wt. % DR1 in PMMA.

Samples of .5-10 weight percent DR1/PMMA were poled at 77 V/μm and 105°C. The electro-optic coefficient was measured after the samples were cooled back down to room temperature and the poling field was removed. The electro-optic coefficient increases linearly with weight percent of chromophore dopant as shown in Fig. 9. This is predicted since the electro-optic coefficient varies linearly with the chromophore number density.[2]
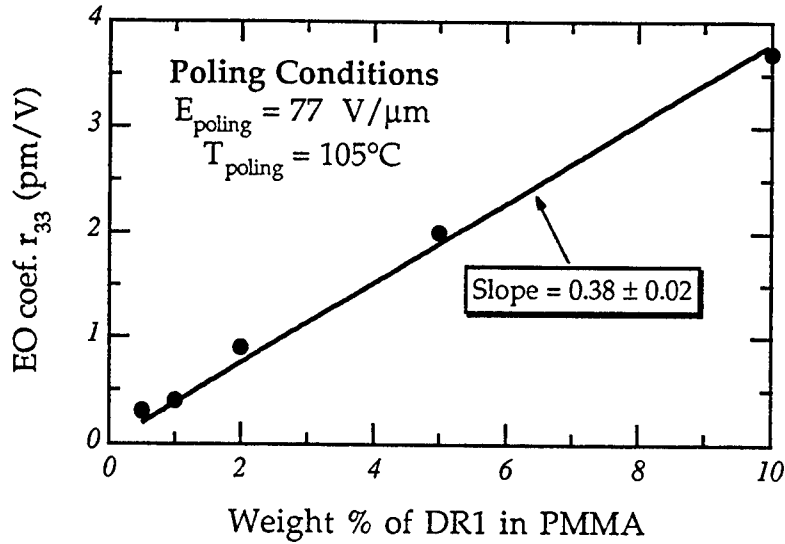
Figure 9) DR1/PMMA samples of .5, 1, 2, 5, and 10 weight percent with thicknesses of 2.3μm were poled with a 200V dc field at 105°C. The electro-optic coefficient was calculated using the corrected relationship for the Teng & Man experimental technique (see ref. 3).

The double lockin method was used to eliminate the spurious effect demonstrated in Eqn. 7. The *effective* $\chi^{(2)}$ arising from the dc poling field acting through $\chi^{(3)}$ shouldn't depend on temperature because $\chi^{(3)}$ isn't very sensitive to dipolar orientation during poling. Thus we can also check for temperature dependent changes in the EO coefficient during poling. We observed that the EO coefficient decreases with temperature after poling even though the dc field remained applied. The signal at twice the ac frequency (2Ω) monitored by the second lockin, was modified according to Eqn. 10 and then subtracted from the signal at Ω. The resulting signal should be due only to poling. Our results (Fig. 10) show that even after subtracting out the spurious dc field effect, the EO coefficient still has a temperature dependence that our model cannot explain.

Figure 10) Two lockin experiment data from poling of 10 wt. % sample of DR1/PMMA. The signals at the ac frequency Ω and a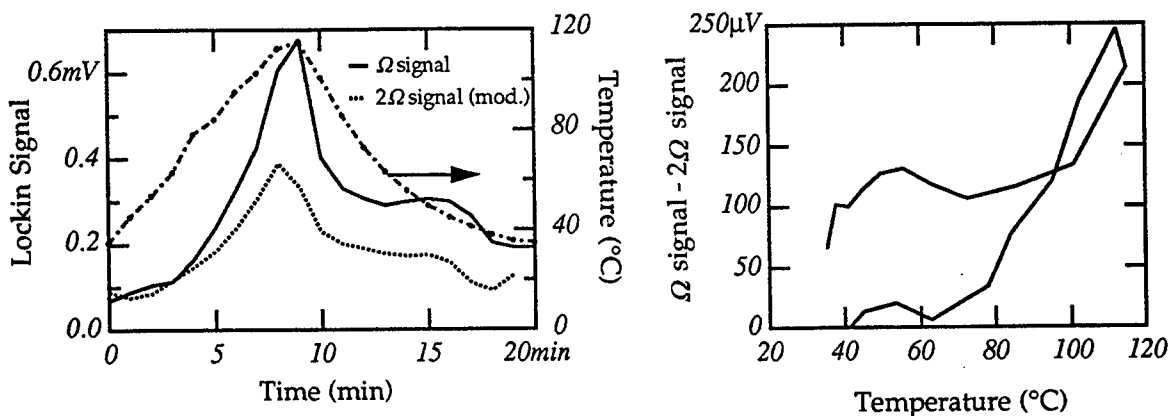t twice the ac frequency 2Ω as well as the temperature variation during the poling run are shown. The signal at twice the ac frequency was modified by the ratio of the dc to the ac field strength. The modified 2Ω signal was subtracted from the Ω frequency signal. The resulting signal should be due only to the poling process. The plot on the right shows that the adjusted signal still has a dependence on temperature.

We began construction of the electric-field probe. We first used a mask with a 25 μm gap and then we made a mask that contains gaps of 10, 15, 20, and 25 μm. Both masks were used to create gold electrodes on cover slips coated with a thin film of polymer. A probing station was used to contact the electrode pads and apply voltage across the gap. A high voltage supply created poling voltages up to 100 V/μm.

At high voltage, an overcoat is needed over the gap to prevent arcing and catastrophic damage to the polymer sample. We tried overcoats of EpoTech epoxy, five-minute epoxy, PMMA in chloroform, photoresist, and combinations of the above. All of the overcoats except the epoxies dissolved the silver paint that we used to attach gold wires to the electrode pads. Using PMMA as an overcladding caused the gap to become distorted and the metallizations to lift off the sample. Neither epoxy had sufficient resistivity and shorted during poling attempts. We successfully poled a sample coated with 10 wt. % PMMA in chloroform at 50 V/μm and a sample coated with a layer of spun photoresist covered with the 10 wt. % PMMA solution at 100 V/μm. Unfortunately, we haven't succeeded in reproducing these results.

We are currently testing overcoats with electrodes made from the new mask. The new mask does not need gold wires attached to it in order to apply

the voltage and the electrodes are far enough apart to prevent shorting between the connections to the electrodes. The overcoats we tried on the first mask will be tested using the second mask. Once an overcoat is found that will not short during poling, the samples will be poled at 100 V/μm. The electro-optic coefficient of the poled samples will be found using a transmission method similar to the Teng & Man[9] method described above. The sample can then be placed on the end of a fiber and made into an electric field probe.

Conclusion

Thin film samples of .5 - 10 weight percent Disperse Red 1/PMMA were prepared and analyzed. The capacitance and conductance of the polymer were measured as a function of weight percent, ac frequency, and temperature. Our results agree with published results although the plasticization shift in T_g is not evident in our data as we analyzed only low weight percent samples.

Each weight percent sample was poled and the electro-optic coefficient was monitored using the ellipsometric reflection method.[3,9] The EO coefficient varied linearly with weight percent of DR1 and with applied dc poling voltage. A double lockin experiment was performed to examine the spurious dc field effect on the observed EO coefficient. We attempted to remove the spurious signal and so isolate the temperature dependence during poling of the pure electro-optic effect. The modified electro-optic coefficient still decreases as the sample is cooled in the presence of the poling field. Our current model is not sufficient to explain the temperature dependence.

An electric-field probe utilizing poled polymer thin films was designed and construction started. The probe will detect electric fields through a change in polarization of a laser beam. In the presence of an electric field the polymer will alter the polarization of the beam as a result of Pockel's effect. We are currently perfecting the in-plane poling method required for this probe.

Acknowledgments

References

1. K. D. Singer, J. E. Sohn, and S. J. Lalama. "Second harmonic generation in poled polymer films," Appl. Phys. Lett. **49** (5), 248-250 (1986).

2. K. D. Singer, M. Kuzyk, and J. E. Sohn. "Second-order nonlinear-optical processes in orientationally ordered materials: relationship between molecular and macroscopic properties," J. Opt. Soc. Am. B **4** (6), 968-976 (1987).

3. J. Binford III, "Thermal stability apparatus design and error analysis for measurements of electro-optic poled polymers," AFOSR GSRP Final Report (1994).

4. A. Yariv, and P. Yeh, *Optical Waves in Crystals* (John Wiley & Sons, New York, 1984), pp. 220-270.

5. R. Page, *et al.* "Electrochromic and optical waveguide studies of corona-poled electro-optic polymer films" J. Opt. Soc. Am. B **7** (7) 1239-1250 (1990).

6. P. N. Butcher and D. Cotter, *The Elements of Nonlinear Optics* (Cambridge University Press, Cambridge, 1990).

7. J. M. Pochan and D. M. Pai, "Dielectric and Photoconductive Properties" in *Plastics Polymer Science and Technology* , M. D. Baijal ed. (John Wiley & Sons, New York, 1982).

8. D. Lei, J. Runt, A. Safari, and R. E. Newnham, "Dielectric Properties of Azo Dye-Poly(methyl-methacrylate Mixtures," Macromolecules **20**, 1797-1801 (1987).

9. C. C. Teng and H. I. Man. "Simple Reflection Technique for Measuring the Electro-Optic Coefficient of Poled Polymers," Appl. Phys. Lett. **56** (18), 1734-1736 (1990).

10. H. Lackritz, "Nonlinear Optical and Charge Distribution Studies Probing Electric Field Effects in Polymer Thin Films for Second Order Nonlinear Optics." AFOSR End of Year Report (1995).

LIGHT GAS GUN INTERNAL BALLISTICS CODE VALIDATION FOR WAVE GUN

Jason J. Hugenroth
Graduate Student
Department of Mechanical Engineering

Louisiana State University
Baton Rouge, LA 70803

LIGHT GAS GUN INTERNAL BALLISTICS CODE VALIDATION FOR WAVE GUN

Jason J. Hugenroth
Graduate Student
Department of Mechanical Engineering
Louisiana State University

Abstract

A specialized light gas gun firing cycle called Wave Gun, developed by Thomas Dahm of Astron Research and Engineering is being investigated as an improved model launcher for free flight aeroballistic tests. In partial fulfillment of this goal a limited experimental program has been instituted for the purpose of validating the internal ballistics code to be used in the study. Four of the seven shots fired to date have yielded sufficient data to be useful in code validation. The measured parameters include pressure histories in the propellant chamber, nozzle entrance, nozzle exit and three axial launch tube locations. In addition the time and speed of first piston compression, and muzzle velocity are recorded. The simulation has been validated to the point that it accurately predicts cycle timing and projectile arrival times. Muzzle velocities are predicted to within 8%. Some suggestions are made as to how the simulation code should be modified to improve accuracy.

Acknowledgments

The author would like to thank Mr. Gerald Winchenbach for selecting me to participate in this summer research program. I would also like to thank Dr. Robert W. Courter for providing guidance and insight to the author throughout this summer. Additionally, I am indebted to Mr. Charles McClenahan (Ballistics Experimentation Facility Chief), MSgt. Jon Aus, TSgt. Tim Coomes and Mrs. Karen Hinton (Range Technicians) for many hours of work under the hot Florida sun. Finally, I would like to thank the Air Force Office of Scientific Research for making this program possible.

LIGHT GAS GUN INTERNAL BALLISTICS CODE VALIDATION FOR WAVE GUN

Jason J. Hugenroth

Introduction

Aeroballistic range facilities consist in essence of a gun for launching aerodynamic models at high velocity and an instrumented range for recording aerodynamic data from the model in free flight. Conventional guns are frequently used for this purpose however, they lack the ability to accelerate projectiles to high velocities. This performance limit is due in part to the energy that must be expended uselessly accelerating the heavy propellant gasses. The problem is circumvented by inserting a second stage between the propellant chamber and the barrel. The second stage or pump tube is filled with a light gas, (usually hydrogen or helium) and is sealed upstream by a movable piston and downstream by a frangible diaphragm. Here a conventional propellant charge accelerates the piston which compresses the light gas causing the diaphragm to rupture. The ruptured diaphragm allows the light gas to expand, accelerating the projectile. Current light gas gun launchers typically operate on what has come to be known as the "isentropic compression" cycle. This cycle employs a heavy piston and a high volume pump tube with a low pressure gas charge. In this mode of operation the heavy and slow moving piston nearly isentropically compresses the light gas eventually rupturing the diaphragm and accelerating the model.

In 1981 in an effort to weaponize the light gas gun, Thomas Dahm[1] of Astron Research and Engineering invented a unique firing cycle. This cycle employed a light piston in a low volume pump tube with a high gas charge pressure. In this mode of operation the light piston would not immediately cause the diaphragm to rupture. Rather, it would rebound downstream due to the high pressure in the pump tube and the subsequent low pressure in the propellant chamber. The continued burning of the propellant would again accelerate the piston downstream this time rupturing the diaphragm. At this point a second rebound occurs followed by a third compression stroke which reaches the projectile before it leaves the barrel[i]. This gun type with its light piston and small pump tube volume made it an attractive candidate for weaponization. An unexpected offspring was the possibility that this design could be tailored to operate as an improved model launcher in aeroballistic ranges.

---

[i] This cycle termed a 2-3 cycle represents one firing mode that Wave Gun operates on. Other cycles such as a 1-2 or a 3-4 cycle are possible.

Motivation of the Present Research

Current aeroballistic range facilities performance limits are dictated not by a launcher's maximum attainable muzzle velocity, but rather by the maximum loading that the sometimes fragile models can withstand while being accelerated down the launch tube (barrel). Considerable effort has been put into designing a launcher that can attain higher muzzle velocities while maintaining or decreasing model loading. Some efforts such as electromagnetic rail guns and two-stage hybrid launchers[2] have had limited success and application for various reasons. The standard isentropic compression cycle produces a peak acceleration on the model which decays as the model moves down stream. This acceleration cannot exceed the model loading limits and is therefore what limits launcher performance. Limited by the same maximum model loading Wave Gun has the potential of producing multiple acceleration peaks (see Figure 1), with correspondingly higher muzzle velocities.

Due to the complexity of the various physical phenomenon occurring in Wave Gun (or any light gas gun) it is difficult to use solely analytical methods to study it. An entirely experimental research program would prove costly and inefficient. It is therefore desirable to employ a numerical internal ballistics simulation to investigate Wave Gun's potential. However, the difficulty of predicting accurately all of the variables needed to model Wave Gun necessitates the execution of a limited experimental program for the purpose of validating the numerical simulation. The acquisition of experimental data and the validation of the simulation code is the present thrust of the research effort.

Firing Cycle Simulation

Arnold Engineering Development Center's (AEDC) current light gas gun code has been obtained for the purpose of investigating Wave Gun's capabilities. The code was originally developed by Piacesi, Gates and Seigel[3], and has been extensively modified by DeWitt[4]. The code utilizes the "q" method of Von Neumann and Richtmyer[5] to solve quasi-one-dimensional hydrodynamic problems, including the treatment of shocks. The code

includes de Saint Robert's power law equation for propellant burning, virial-type real gas model for the light gas (helium for the present case), dissipative influences such as gas friction and heat transfer as well as sliding friction and piston deformation models. In addition Dr. Robert W. Courter and the present author have tailored the code to meet the requirements of the present program, including the handling of projectile friction and a piston release pressure.

Experimental Facility Description

The present experimental facility utilizes the Astron 30 mm Wave Gun originally designed to investigate light gas gun weaponization. It was recommishioned in may 1994 at Eglin Air Force Base in support of the present research program. In order to achieve the flexibility needed in the original research program Wave Gun uses a massive steel pressure vessel to house the guns internal parts. This design allows the internal geometry of the launcher to be modified by inserting sleeves of various size into the pressure vessel. A schematic is shown in Figure 2. Starting upstream the internal parts consist of the outer breech plug, spacer, inner breech and igniter assembly, propellant chamber, piston, pump tube, nozzle, projectile, barrel nut and barrel. Although the facility originally had three sets of internal parts only one configuration is available at present.

The outer pressure vessel contains nine instrumentation ports, (hereafter referred to as gun ports 1-9) with an additional four instrumentation ports located in the eight foot launch tube. Gun ports (GP) 2,8,9 and launch tube ports (LT) 1,2,3 contained quartz type piezoelectric pressure transducers which measured pressure histories in the propellant chamber, nozzle entrance, nozzle exit, and three axial launch tube locations respectively. The transducer signals were sent to charge amplifiers before being recorded by a High Techniques (HT) 600 digital oscilloscope. GP 5 and GP 6 contained breakwires which consisted of a wooden dowel with a thin loop of insulated wire glued axially along the dowel and a 3/8 in. bolt to which the dowel was epoxied. The breakwire assembly was screwed into the pumptube to measure the time of the first piston compression. The dowel acted as a stiffener for the wire so that it would shear cleanly upon piston passage. The breakwire signals were also recorded by the HT600 and all signals were on the same time base. The remaining instrumentation ports were inactive.

Muzzle velocity was recorded by either two infrared sky screens or Doppler radar. The sky screens were placed a known distance apart and were used to trigger counters as the projectile passes. Using this time and distance an average velocity was obtained. The radar unit, used when available, also has the ability to measure inbore velocity and acceleration. Neither the sky screens nor the radar were on the same time base as the other instrumentation. Figure 3 shows the locations of the instrumentation ports.

Loading and firing of the gun consists of inserting the nozzle and pump tube sleeves into the outer tube. Then a projectile is inserted into the upstream end of the launch tube and the barrel nut is screwed onto the pressure vessel. The model itself is an aluminum cylinder with an integral flange which serves as the diaphragm. The flange thickness can be any size up to a half inch, with a steel washer used to insure an adequate gas seal with the nozzle if the flange is less than a half inch thick. Next, the inner breech and igniter assembly is threaded onto the upstream end of the propellant chamber. The propellant charge is bagged and inserted around the spit tube. The polypropylux piston is threaded on one end so that it can be screwed onto the downstream section of the propellant chamber. This makes it possible to vary the piston start pressure by varying the number of threads engaged. The propellant chamber assembly is then inserted. The pump tube, nozzle and propellant chamber must all be carefully aligned both axially and radially so that the instrumentation ports in the sleeves align with the gun ports. Final assembly consists of inserting the spacer and outer breech plug and simultaneously torqueing the breech plug and barrel nut without disturbing the sleeves' alignment. The helium can then be added through a fill port located in the pump tube (not shown). The gun is then fired using a 20 mm electric primer.

Experimental Results

Since being commissioned at Eglin AFB in May of 1994, nine Wave Gun shots have been fired. The first two shots occurred during the 1994 Summer Research Program and are discussed in reference 6. Of the remaining seven shots three yielded little or no data. These three shots are considered useless for the purpose of code validation and are omitted from the following discussion. The four "good" shots (those yielding useful data) consisted of two pairs of nearly identical shots. All shots used M30/19 MP as the main propellant with a 16-17 gm

FFFG black powder primer charge in the spit tube. The instrumentation was triggered from LT 1. This was done to alleviate triggering problems that might occur in the gun ports if the alignment of the internal parts was off. The HT600 has the ability to record events that occur before and after the trigger which is crucial since the trigger occurs after a sizable portion of the ballistic event has occurred. The HT600 was set to sample at 500 kHz for 32 ms, which gave over three times the sweep time needed, with the actual ballistic event taking less than 10 ms. The parameters for the four shots used in the present experimental program are shown in Table 1 with the corresponding results in Table 2.

Shot number	Shot date	Propellant weight (gm)	Model weight (gm)	Distance piston screwed in (in)	Flange/ Diaphragm thickness (in)	Helium charge pressure (psi)
1	4/14/95	1280	111.6	1.88	1/4	2300
2	6/21/95	1280	111.6	1.88	1/4	2700
3	6/26/95	800	111.6	1.88	1/8	2200
4	7/06/95	800	111.6	1.88	1/8	2200

Table 1: Shot parameters

Shot number	Propellant chamber pressure at piston start (psi)	Model start pressure (psi)	Cycle type	Muzzle velocity (fps)
1	12000	40000	3-4	5626
2	12000	44000	3-4	6113
3	7500	25000	2-3	4143
4	8000	30000	1-2	3733

Table 2: Shot results

The shot parameters for shots 1 and 2 differ only in the helium charge pressure for reasons discussed later in this section. For shot 1 full sweeps were recorded at all pressure port locations. This shot was however, performed before the HT600 oscilloscope was equipped to handle all eight channels. The result was that LT 2 and LT 3 were not on the same time base as the rest of the traces and therefore proved somewhat useless in code validation. In addition the breakwires did not perform properly and no data was recovered from them. It should be noted that the breakwire assembly discussed in the previous section was actually a modification in response to the results of Shot 1 (the former assembly lacked the dowel stiffener). The muzzle velocity (see Table 2) was recorded using the infrared sky screens placed ten feet apart, with the first one approximately 10 feet from the muzzle. This

setup is necessary to prevent muzzle blast from triggering the sky screens. The polypropylux piston was completely extruded and shot down range. For Shot 2 all eight channels were recorded successfully on the HT600 oscilloscope. The muzzle velocity was successfully recorded using the radar and the piston was found to have wedged in the nozzle. Shot 3 was a success with the exception that GP 5 and GP 9 did not return data. It was discovered after the shot that rain water had leaked onto the electrical contact of the GP 9 transducer due to improper sealing of the transducer port between shots. The breakwire bolt in GP 5 fractured and subsequently blew out before piston passage occurred. The muzzle velocity was determined from radar. On Shot 4 LT 3 failed to return data for reasons never determined. It was decided for this shot however, to attempt to obtain inbore velocities using the radar. Although this capability was known to exist from the beginning of the experimental program difficulties with the rest of the instrumentation belated its use. This setup consisted quite simply of using an ordinary mirror to give the radar head a line of sight down the launch tube. It was also necessary to apply a correction factor to the data based upon the barrel bore and radar frequency to account for the barrel acting as a wave guide. The results were pleasing with a continuous track starting from approximately 250 fps to the muzzle velocity being recorded. The inability to monitor the initial model movement is a limitation of the radar head that was used and was expected. The data recovered also indicated two clear acceleration peaks of 34000 and 70000 G's respectively, confirming the Wave Gun cycle concept. As Tables 1 and 2 indicate the last two shots intended to be identical in fact executed different cycle types. This may be the result of a severe helium leak occurring through one or both of the breakwire ports. It was noted that after charging the pump tube to approximately 2600 psi a severe leak developed which was said by the range technician to have "stabilized" at 2200 psi. There is needless to say some ambiguity in how "stable" the leak became and what the actual pressure was at shot time, noting that several minutes elapse between final loading and shooting. However, the piston speed data (Table 3) does not support this hypothesis. A low charge pressure would in turn produce a high piston speed, but the experimental value is nearly half the predicted value. For both Shot 3 and Shot 4 the piston was found wedged in the nozzle.

The wear of the gun components is most evident at the meeting face of the pump tube and nozzle where erosion occurs, and a multitude of hairline cracks on the outside surface of the nozzle. This wear has not affected

gun performance nor has it compromised safety, in addition the wear seems to be increasing at a decreasing rate. The most dominant problem that has plagued the experimental program to date has been the inability to obtain high pressure helium. The small pump tube volume requires the helium charge pressure to be exceedingly high, 2500-4000 psi, compared to about 200 psi for standard light gas guns. The only suitable helium source found was from the Navy Dive School in Panama City, Florida, where two standard scuba tanks (80 ft³ standard air at 3000 psi) were obtained for the tests. Staging from standard helium bottles this allowed for a maximum pressure of 2700 psi in the pump tube. The helium deficiency was also related to other difficulties. Leaks frequently occurred in the gun when the helium pressure was much greater than 2000 psi. When this occurred a judgment call had to be made on how severe the leak was and whether to dump the helium and secure the leak or continue the test. Dumping the helium and securing the leak meant that the shot would have to be made at a lower pressure or completely aborted until the scuba bottles could be refilled.

Simulation Results

Most of the initial inputs to the simulation code were based upon first principles or documented empirical values. The two most notable exceptions to this were the piston and model start pressures, which were derived from the experimental pressure histories. In regard to these values a large degree of variability was noted for the piston start pressures. This may be attributed to the fact that both the piston and model shot start pressures are modeled as instantaneous events in the simulation code. Table 3 provides a summary of the simulation results and the respective experimental values.

Shot number		Piston start pressure (psi)	Model start pressure (psi)	Average piston speed between GP 5 & GP 6 (fps)	Maximum pressure (psi)	Muzzle velocity (fps)
1	Numerical	7975	47850	1112	96400	6068
	Experimental	9700	40000	------	76000	5626
2	Numerical	7975	47850	1063	95300	6108
	Experimental	9700	44000	1089	82000	6113
3	Numerical	5800	23200	848	37200	3874
	Experimental	5300	25000	------	25000	4143
4	Numerical	7250	23200	1156	86800	3874
	Experimental	7010	30000	617	30000	3684

Table 3: Experimental and numerical results

The predicted timing of the pressure waves at the gun port locations and the arrival of the projectile at the launch tube locations compares favorably with experiment (see Figures 5-8). There are however significant differences in the magnitudes of these pressure waves for certain cases. In the interest of brevity a detailed discussion of the pressure histories of each individual shot is not possible at this time. Instead the focus will be on the overall trends in the simulation output, as well as the major differences in the individual shots.

For the high performance shots (Shots 1 and 2) the later stages of the of the propellant chamber pressure histories are significantly underpredicted. Dahm and Randall[1] experienced this as well and attributed it to erosive burning. Although the conditions for erosive burning are very favorable in this type of cycle (see Ref. 1), it is usually considered insignificant in propellants with large grain structures, such as the present case. At any rate propellant gases appear to be evolving more quickly than predicted. Attempts to adjust the documented burn rate coefficient and exponent accordingly have not had the desired effect. This underprediction is also reflected at the nozzle entrance and exit where the pressures during piston rebound are predicted lower than observed. The model arrival times to the launch tube locations are based upon the first pressure rise at the respective launch tube ports. As was mentioned earlier the model arrival times are fairly well predicted. Qualitatively however, the pressure curves look very different, LT 3 of Shot 2 being the notable exception. For Shot 2 the piston speed is predicted within 3% of the measured speed. For Shot 1 the experimental piston speed data was lost. The predicted value was slightly higher than for Shot 2, owing to the lower helium charge pressure, and seems very reasonable. The velocity was also very closely predicted for Shot 2, within 1%. The Shot 1 velocity differs by slightly less than 8%, some of this variance can easily be attributed to the fact that sky screens were used to estimate the muzzle velocity.

The magnitudes of the pressures seem for the most part to be better predicted for the third and fourth shots. The deficiency in propellant gas evolution noted for the first two shots is also not evident. This may be due in part to the fact that these shots execute fewer cycles preventing inadequacies of the numerical model from compounding. The pressure histories at the launch tube locations seem better predicted for these lower performance shots in that they are qualitatively more similar. The magnitudes for the same are over predicted with a corresponding overprediction of the muzzle velocities of five to seven percent. The peak accelerations on the

model, which were measured for Shot 4, are overpredicted by significantly more than 100% by the simulation (see Figure 9). This is clearly inadequate especially in light of the fact that the present research is specifically interested in model accelerations.

Future Research

There are several physical phenomena that are known or are suspected to be occurring in the Wave Gun's ballistic cycle, which are not addressed by the simulation code. Some of these include, flow of and subsequent cooling of gasses in the annular regions between the sleeves and the outer pressure vessel. This occurrence was verified using closed bomb test detailed in Reference 7, and it was suggested that this effect could be modeled as a virtual leak. The modeling of the piston and model shot starts as instantaneous events were found to be insufficient based on experimental observances by Dahm and Randall[1]. A linearly decaying retarding force acting on the model and piston over the distance required for them to move clear of restraint is used in AIBAL (Astron Internal Ballistics Code) and should be added to the AEDC code. Nevertheless, significant progress has been made in the validation of the simulation code and though there is still room for improvement the results compare favorably with results obtained in other numerical studies (see Ref. 1 and 8).

Pending completion of the validation, parametric studies will be initiated in an effort to define gun loading parameters that provide for high muzzle velocities and low model loading. The principle parameters under consideration are pump tube volume, helium charge pressure, propellant type and loading, and piston and model start pressures. These parametric studies will be performed on the light gas gun currently being used at Eglin AFB's Aeroballistic Research Facility (ARF). The direction of the program will be based on the most recent analysis.

References

1. Dahm, T. J. and D. S. Randall, "The Wave Gun Concept for a Rapid Fire Hypervelocity Weapon," Presented at the 1984 JANNAF Propulsion Meeting, New Orleans, LA, 8 February 1984.

2. Dahm T. J. and J. D. Watson, "Analysis and Design of a Two-Stage Hybrid Launcher," Defense Nuclear Agency, DNA 4334F, 30 July 1977.

3. Piacesi, R., D. F. Gates and A. E. Seigel, "Computer Analysis of Two-Stage Hypervelocity Model Launchers," Navel Ordinance Laboratory, NOLTR 62-87, February 1963

4. Cable, A. J. and J. R. DeWitt, "Optimizing and Scaling of Hypervelocity Launchers and Comparisons with Measured Data," Arnold Engineering Development Center, AEDC-TR-67-82, April 1967.

5. Von Neumann, I. and Richtmyer, R. D., "A Method for the Numerical Calculation of Hydrodynamic Shocks," Journal of Applied Physics, Vol. 21, p. 232, 1932.

6. Courter, R. W. and J. J. Hugenroth, "A Research Plan for Evaluating Wave Gun as a Low -Loading Model Launcher for High Speed Aeroballistic Tests," Final Report, Summer Faculty Research Program, Eglin AFB, FL, August 1994.

7. Randall, D. S., "Wavegun Development During the Past Year," Presented at the 37th Meeting of the Aeroballistic Range Association, Quebec, Canada, September 1986.

8. Groth C. P. T. and J. J. Gottlieb, "Numerical Study of Two-Stage Light-Gas Hypervelocity Projectile Launchers," University of Toronto, Institute for Aerospace Studies, UTIAS Report No. 327, October 1988.

Conventional Light Gas Gun

Wave Gun

Piston
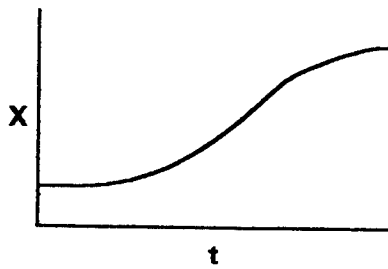
Piston
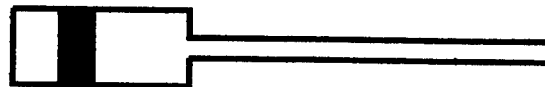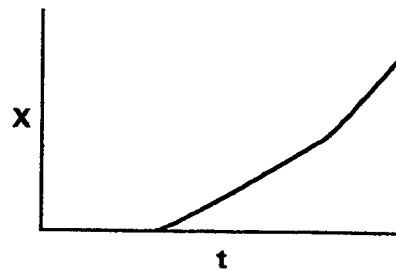

Projectile
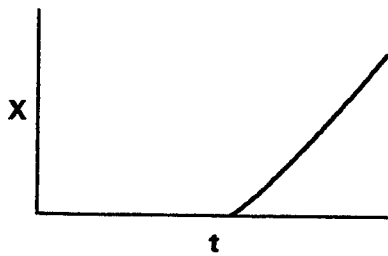
Projectile

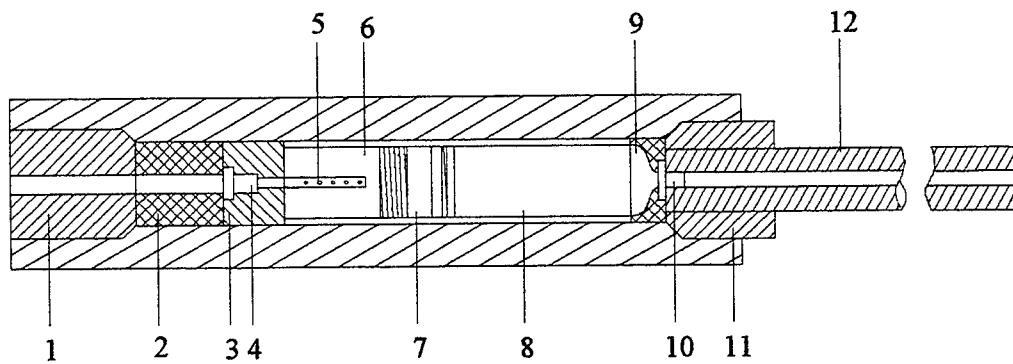

Heavy piston.

Low charge pressure.

Large pump tube volume.
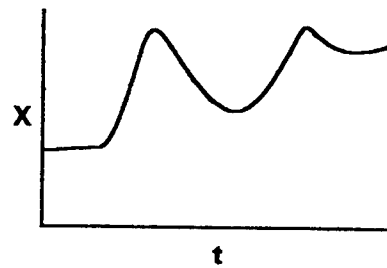
Light piston.

High charge pressure.

Small pump tube volume.

Figure 1: Comparison of Wave Gun and Conventional Light Gas Gun firing cycles

Figure 2: Wave Gun test apparatus

No.	Part	Length (cm)	Diameter (cm)	No.	Part	Length (cm)	Diameter (cm)
1	Breech plug (outer)	-	-	7	Piston	10.29	11.43
2	Spacer	16.04	13.29	8	Pump tube	41.81	11.43*
3	Breech plug (inner)	12.07	13.29	9	Nozzle	15.24	11.43*
4	Igniter	-	-	10	Model	5.72	3.00
5	Spit tube	-	-	11	Barrel nut	-	-
6	Propellant chamber	28.19	11.43*	12	Launch tube	243.84	3.00
					* Inside diameters		
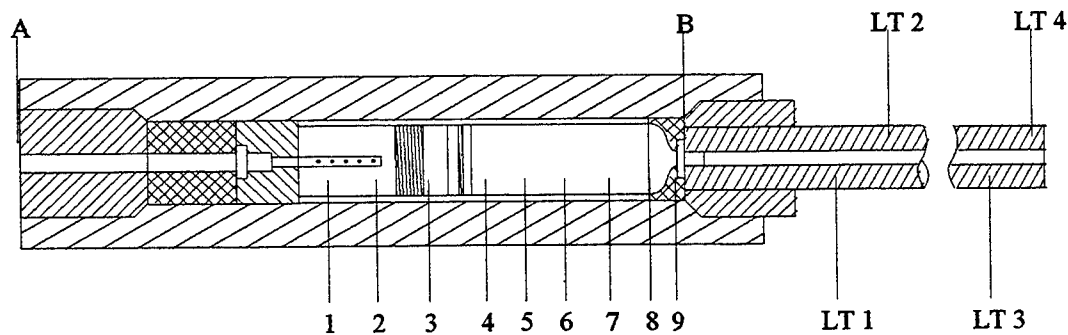
No.	Location (cm)*	Use	No.	Location (cm)**	Use
1	45.72	Not active	LT 1	45.72	Pressure transducer
2	60.96	Pressure transducer	LT 2	76.20	Pressure transducer
3	71.12	Not active	LT 3	137.16	Pressure transducer
4	81.28	Not active	LT 4	198.12	Not active
5	91.44	Break wire			
6	101.60	Break wire			
7	111.76	Not active			
8	121.92	Pressure transducer	* Measured from A		
9	128.11	Pressure transducer	** Measured from B		

Figure 3: Wave Gun instrumentation ports
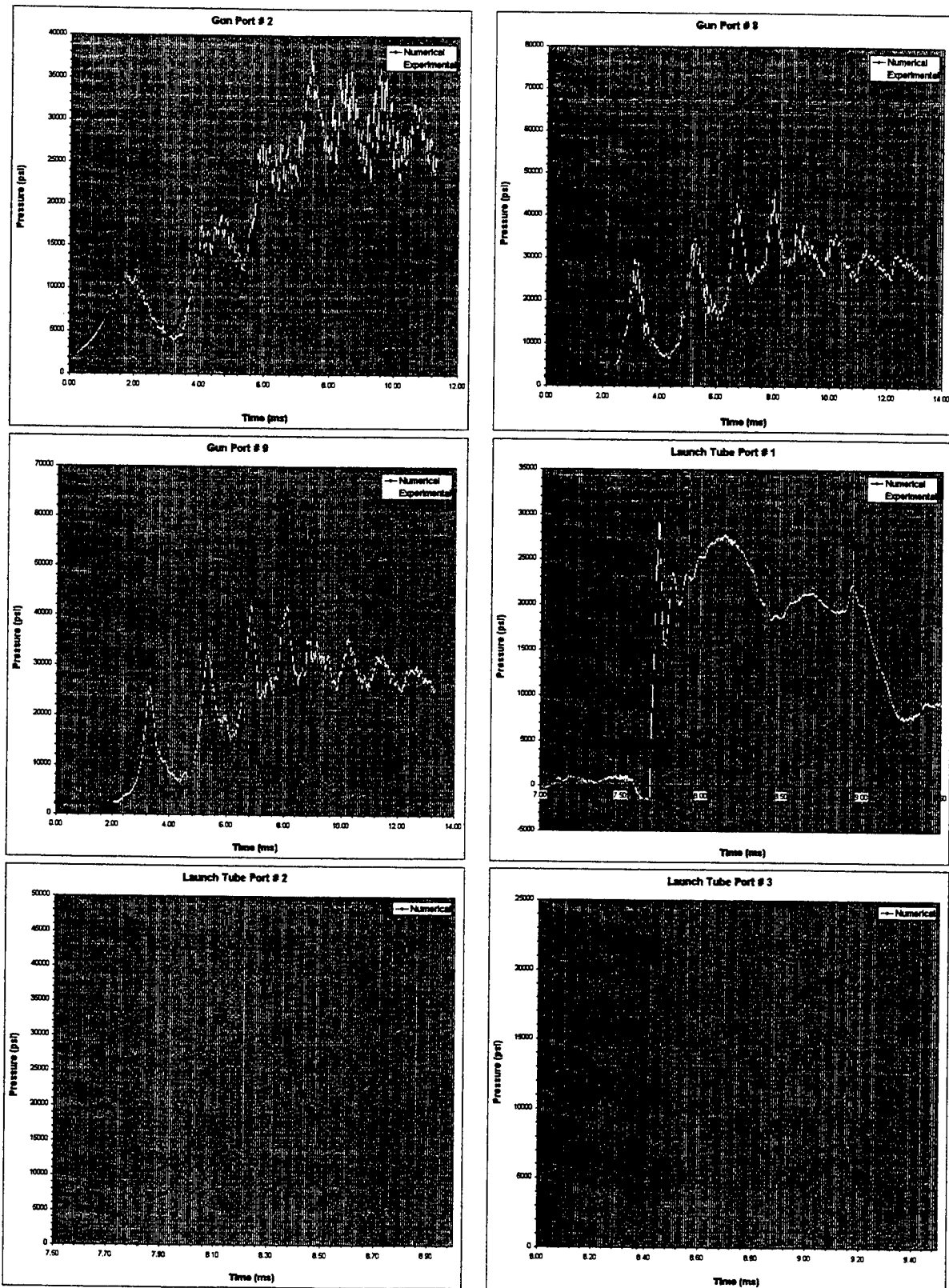
Figure 4: Shot 1 results

16-16
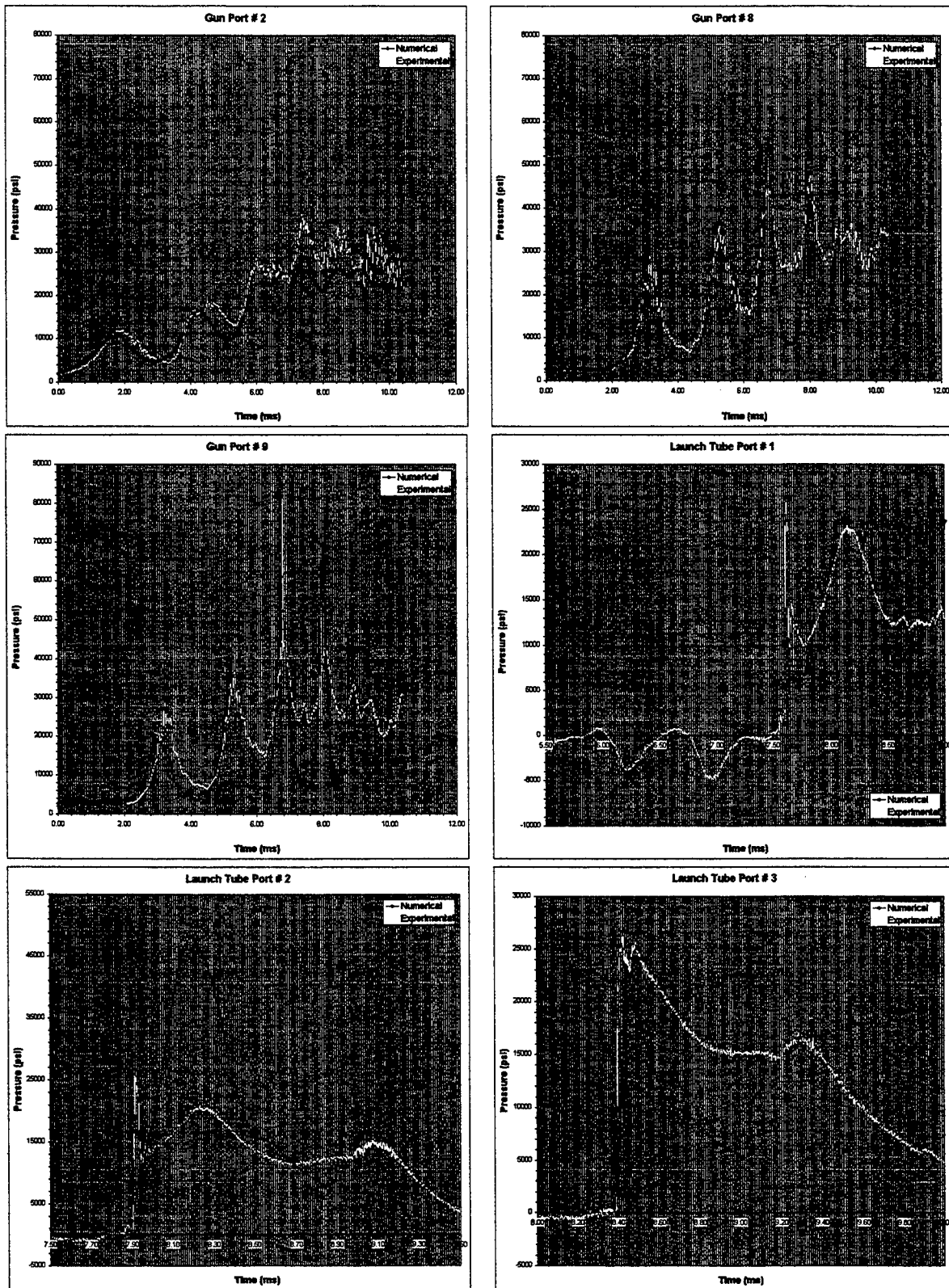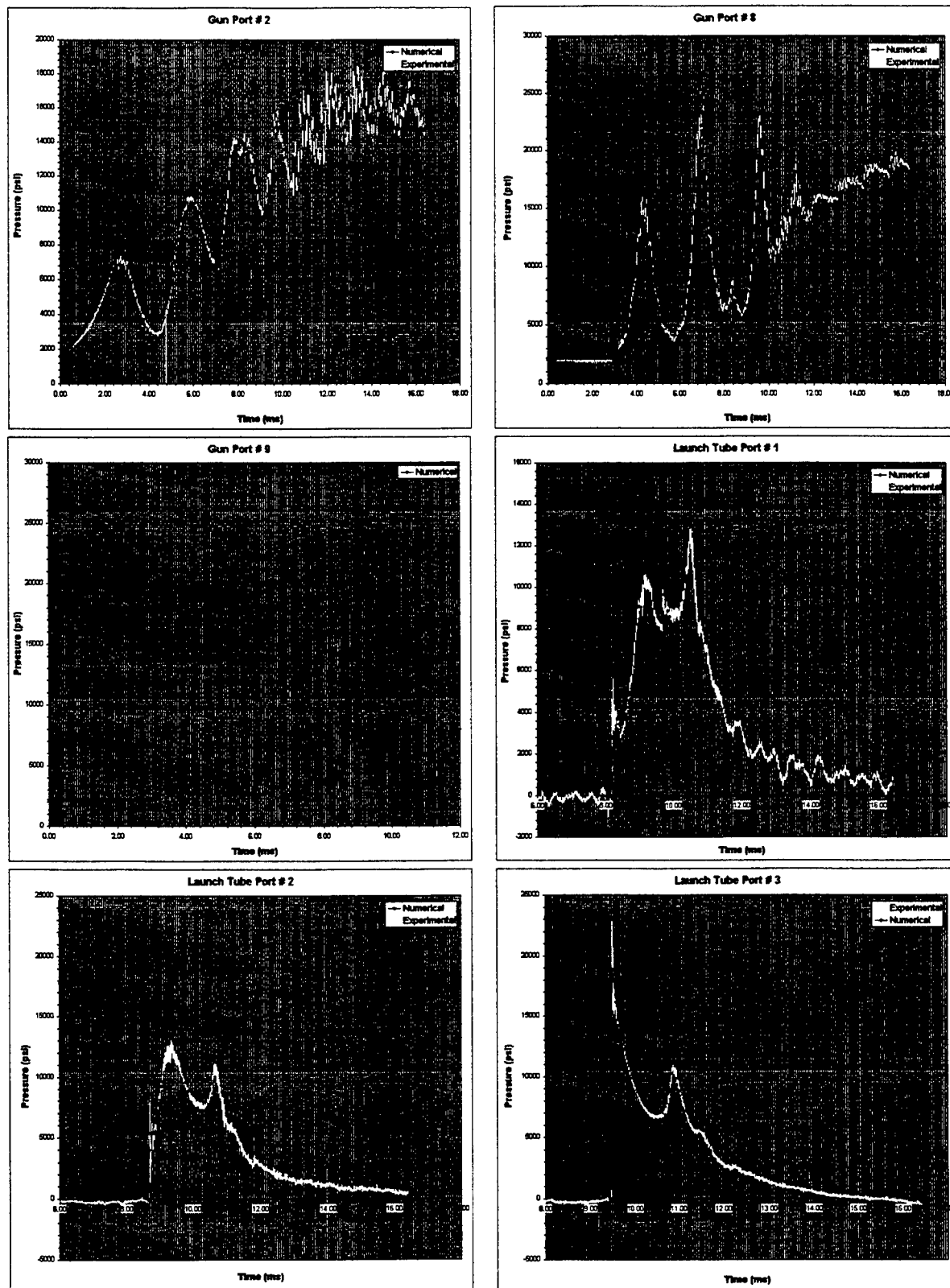
Figure 5: Shot 2 results
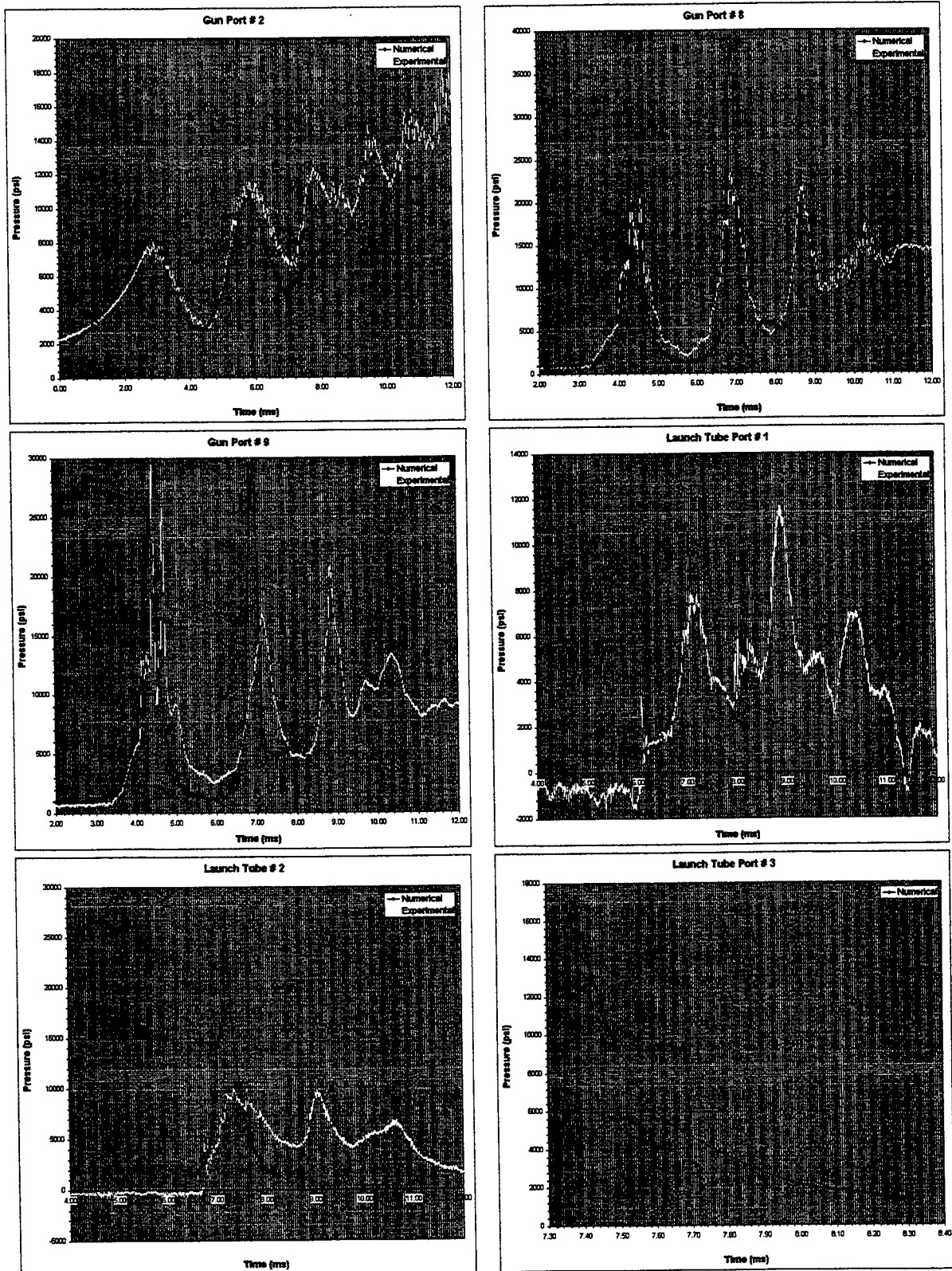
16-17

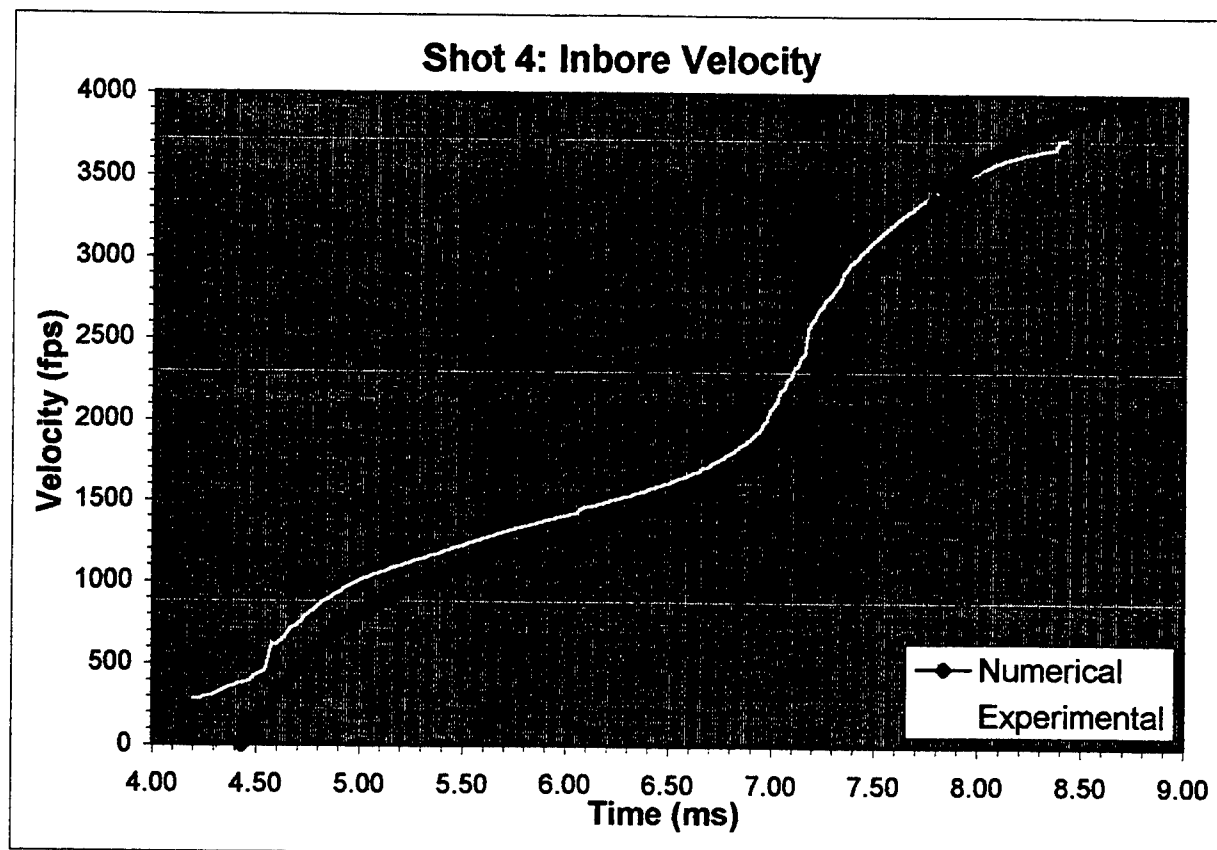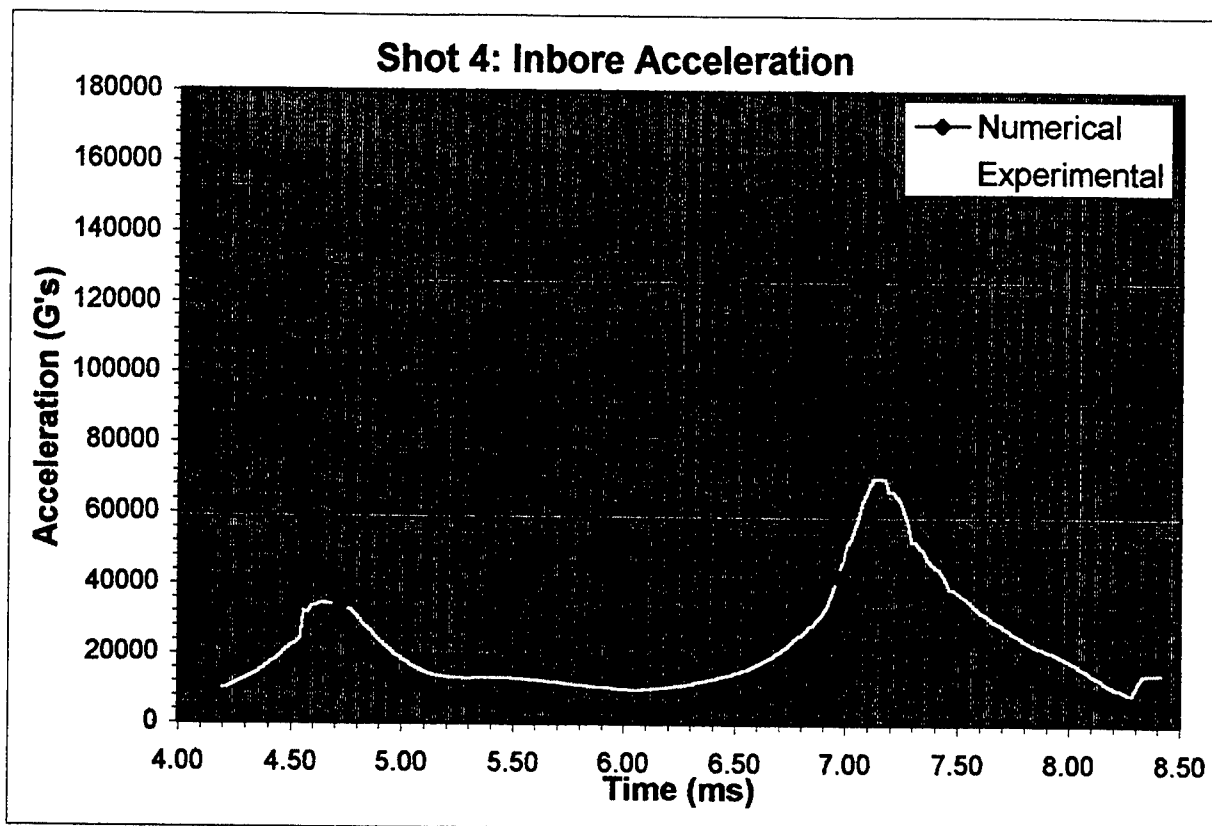Figure 6: Shot 3 results

16-18

Figure 7: Shot 4 results

Figure 8: Shot 4 inbore data

DEVELOPMENT OF A
LIQUID MERCURY OPTICAL SCINTILLATOR
(LMOS)

Roger T. Lindquist
Electro-Optics Engineer

University of Dayton
Center for Electro-Optics, KL 441
300 College Park
Dayton, OH 45469

DEVELOPMENT OF A
LIQUID MERCURY OPTICAL SCINTILLATOR
(LMOS)

Roger T. Lindquist
Electro-Optics Engineer
University of Dayton

ABSTRACT

Laboratory simulation of atmospheric laser scintillation is accomplished through a Liquid Mercury Optical Scintillator (LMOS). Spatial irradiance variations in the reflected beam exhibit probability distributions matching atmospheric ln-normal statistics. A large range of variance levels has been observed, indicating LMOS can simulate a wide range of turbulent atmospheric conditions. LMOS uses a vibrating liquid mercury design that is virtually wavelength independent and statistically controllable in real time. The invention has immediate applications in the laboratory evaluation of optical receivers and their performance under specific scintillation conditions.

LMOS uses the high reflectivity of the mercury surface to spatially modulate laser light. This modulated light mimics the effects observed when a laser beam propagates over a long path of turbulent atmosphere. Energy is coupled into the liquid mercury through an electro-magnetic solenoid and a magnet floating on the mercury's surface. This excites turbulent vibrations in the partially bounded mercury, creating angular distortion areas that redistribute energy in the reflected beam. The statistics of the energy redistribution depend on the applied energy spectrum, light beam angle of incidence, equivalent pathlength working distance, as well as the shape and texture of the containment vessel boundaries. Significant progress has been made in the examining these and other parameters of LMOS. Computer control of LMOS has been accomplished through Analog to Digital, Digital to Analog boards, and RS232 communications controlled by specialized software. LMOS prototype #3, has already been used in the developmental testing of an actual Laser Warning Receiver.

DEVELOPMENT OF A
LIQUID MERCURY OPTICAL SCINTILLATOR
(LMOS)

Roger T. Lindquist

INTRODUCTION

Atmospheric turbulence affects the propagation of electromagnetic waves. The atmosphere is a turbulent medium which creates a randomly varying index of refraction. When optical waves propagate through the earth's atmosphere, they experience phase distortions due to small temperature variations, constantly moved by winds and convection, which cause the air's index of refraction to randomly change. Optical waves propagating through such turbulent atmosphere are constantly and randomly refracted, causing perturbations in wavefront and propagation angle.

These perturbations in the propagating beam can affect the ability to accurately detect the optical wave. Characterizing the effects of turbulence on detection ability is important in communications and laser warning receiver design. To properly evaluate the performance of optical receivers requires testing of the receiver under realistic deployment conditions. Typically, extensive testing of optical receivers must be performed in both the laboratory and in the field. Field testing exposes the receiver to atmospheric scintillation effects that may affect the receiver's performance. However, during a field test it is not possible to control the atmospheric turbulence. Lack of predictability combined with the logistics and expense of field deployment presents a formidable obstacle to proper evaluation of receiver detection schemes. A laboratory instrument that can spatially modulate collimated light in a controlled fashion would be the logical choice to overcome this obstacle.

The Liquid Mercury Optical Scintillator (LMOS) provides a realistic laboratory simulation of the end effects that turbulent atmosphere have on a propagating laser beam. LMOS offers near wavelength independent spatial intensity modulation of light sources used for laboratory analysis of optical receivers. Simulation of atmospheric scintillation effects on laser and nonlaser sources can minimize extensive field testing of optical receivers, which often must operate in a variety of atmospheric turbulence levels. Currently during field testing of optical receivers, atmospheric turbulence levels may not span the receiver's entire dynamic range. With LMOS we can simulate all turbulence levels in which the receiver will be used. LMOS promises to be a major asset to receiver development and testing throughout industry and the Department of Defense.

BACKGROUND

The Liquid Mercury Optical Scintillator (LMOS); USAF invention # 21403 (patent pending, DeLong et al.), provides a laboratory controlled realistic simulation of optical atmospheric turbulence effects on laser beam propagation. Specifically, spatial irradiance variations in the reflected beam exhibit probability distributions matching atmospheric ln-normal statistics. This summer we characterized the parametric behavior of the third LMOS prototype.

LMOS represents a significantly different approach to scintillation simulation compared to its direct predecessor, the Reflective Membrane Optical Scintillator (RMOS), U.S. Patent #4,930,352, awarded June 5, 1990 to Parker et al. Both LMOS and RMOS simulate atmospheric turbulence effects using a vibrating reflective surface. However, LMOS depends on the chaotic behavior of a loosely bound, high surface tension fluid, whereas RMOS relies on the superimposed vibrational modes of a tightly stretched membrane [1].

Until the advent of LMOS or RMOS, proper evaluation of optical receivers required testing of hardware both in the laboratory and in the field. The objectives of field testing were to expose the receivers to atmospheric scintillation effects, which spatially modulates laser threat sources in ways that may influence receiver performance. Performance degradations exposed in field testing have been responsible for receiver design changes. Because of the continued need to enhance receiver performance, the statistical behavior of atmospheric scintillation has been an area of intense study. These studies have been carried out in analytical and empirical fashion. The result is a substantial data base relevant to the probability distributions and power spectrums of the spatial and temporal distribution patterns of laser and nonlaser sources. These statistics encompass a variety of sources, atmospheric conditions and regional locale. Analysis of optical receivers considering these atmospheric statistical effects often reveals the need to test certain detection mechanisms under specific scintillation conditions. This poses a disadvantage in field testing, because statistical control over atmospheric turbulence is not possible. This lack of predictability combined with the logistics and expense of field deployment presents a formidable obstacle in the proper evaluation of receiver detection schemes. A laboratory instrument that can spatially modulate collimated light is a logical choice to overcome this obstacle.

Alternate approaches to laboratory scintillation include thermal heat gradients [2],[3] and fluid tank simulations [4]. Air heating techniques, for example, provide strong modulation of the air's refractive index. However, this method offers poor statistical control and questionable reproducibility. Another method uses fluid tanks to simulate turbulence fluid mechanics. Fluid tanks use a liquid filled container with optical windows at each end, and heat exchangers to induce a temperature gradient across the medium orthogonal to the optical path direction. Statistical manipulation is achieved by temperature selection and by fluid viscosity. The main disadvantage to this technique is that both turbulence statistical behavior and optical transmission are heavily dependent on the wavelength of light propagating through the tank. Fluid tanks also require optical windows to accommodate the full spectral range of operation. In addition, fluid tanks are typically difficult to characterize because a fluid tank's response to changes in temperature gradients is slow, scintillation effects occur on a slower

time scale compared to atmospheric modulation. The advantage of both these techniques is they preserve all natural scintillation physics to create the irradiance fluctuations. No simulation is involved.

While the original RMOS device performs the purpose of this invention, it has to date not yet fulfilled our original expectations. With RMOS an acoustically excited, tightly stretched thin membrane spatially modulates the intensity of collimated light reflected off its surface. The membrane, which can be silvered to cause wavelength independent reflection, is stretched and secured over a frame having a clear opening, providing the mechanical boundaries for the acoustical excitation. Acoustic energy is coupled into the membrane through an electro-mechanical transducer similar to a loudspeaker driver mechanism. The transducer is attached to the membrane via a rigid "push rod" or piston. Audio signals presented to the transducer set up nodal vibrational modes in the bounded membrane, creating angular distortion areas along the surface. These distortion areas redirect rays of incident light, changing the spatial irradiance distribution of the overall light beam. The statistics of the energy redistribution depends on the applied acoustical spectrum and the shape and impedance of the boundary conditions imposed on the membrane. With random frequency excitation, non-stationary irradiance fluctuations simulate naturally scintillated laser light. Unfortunately, there are some significant performance limitations in the RMOS device that have not yet been resolved.

ATMOSPHERIC OPTICAL SCINTILLATION

The index of refraction of the atmosphere depends on the temperature, humidity, and wind velocity. If we look at one of these parameters, such as wind velocity, we find at any particular point in space the wind velocity fluctuates irregularly. Each of the other parameters exhibits this random behavior as well. The combined effects of these random fluctuations in temperature, humidity, and wind velocity describe atmospheric turbulence. Since the parameters which determine the index of refraction in the atmosphere randomly change so does the index of refraction. From electromagnetic wave theory we know a change in the index of refraction changes the direction of propagation of the electromagnetic wave. In the turbulent atmosphere a continuously changing refractive index constantly redirects light waves.

A uniform intensity monochromatic plane wave, such as that created by a collimated laser beam, does not remain uniform as it propagates through atmospheric turbulence. The atmosphere's randomly changing index of refraction both focuses and defocuses the beam, and therefore breaks up the uniform intensity, as shown in **Figure 1**.

Figure 1: Beam propagation through turbulent atmosphere

The focusing and expansion of the laser beam causes fluctuations in the intensity, known as scintillation. Anyone can observe scintillation by peering into the night sky and observing the twinkling appearance of stars. A star is a point source of constant light. When light from a star passes through the earth's atmosphere it is randomly refracted from the turbulence, perturbing the intensity and makes the star appear to twinkle. If we took an instantaneous picture of the uniform laser beam after propagating through turbulence we would observe something like **Figure 2** below. Notice the beam is no longer uniform in intensity, but appears to break into bright and dark portions. These bright and dark portions are constantly changing in both size and shape.
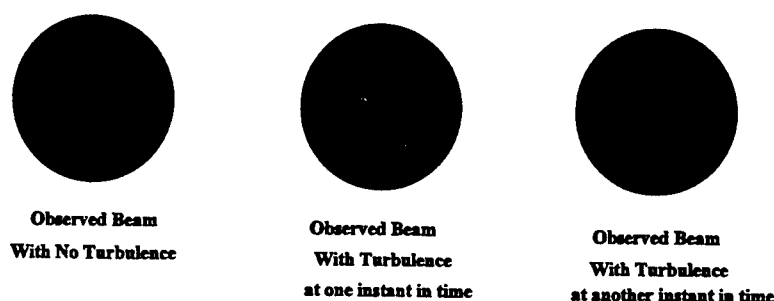

Observed Beam
With No Turbulence

Observed Beam
With Turbulence
at one instant in time

Observed Beam
With Turbulence
at another instant in time

Figure 2: Observation of propagating laser beam

This modification of the original beam may limit an optical laser warning receiver's ability to accurately detect a laser beam. If a receiver cannot accurately detect the propagating beam the quality of optical communications will be degraded. Imaging through the atmosphere is also degraded by atmospheric turbulence, as one can observe by looking at an object across a parking lot on a sunny day. However, We are more interested in the communications aspect, which involves laser beam propagation through the atmosphere. If a laser beam used for communications does not retain its intensity, because of atmospheric turbulence in its propagation path, its chance of accurate detection are reduced.

The randomness of turbulence effects requires statistical evaluation methods. Statistics work well for analyzing experimental data, however deriving a theoretical model that accurately predicts scintillation statistics is quite difficult to do without making many approximations. Even with many approximations, theorists find it difficult to obtain complete analytic solutions.

Early experiments with propagating laser beams in turbulent atmosphere show the detected beam irradiance fluctuations have a ln-normal distribution [5]. The ln-normal distribution indicates the logarithm of the irradiance is normally, or Gaussian, distributed. The Rytov method, which theoretically develops the ln-normal model, works very well for weak scintillation but does not predict the experimentally observed results if the scintillation becomes large. It was determined that the Rytov method is only valid for irradiance variance less than 0.3 [5]. Failure of Rytov's method results from not accounting for multiple scattering effects in a consistent manner. Many scientists propose new theories in an attempt to model this discrepancy; however, they use a large amount of approximations

and are very difficult to compute. We are interested in producing the same effects from LMOS as the turbulent atmosphere exhibits. Therefore, we will leave the debate over the theory to the atmospheric modelers.

Since we begin by simulating low levels of turbulence, we assume ln-normal distribution leading to the amplitude equation.

$$P_A(A, \bar{x}, \sigma_x) = \frac{1}{\sqrt{2\pi}\, \sigma_x A}\, e^{-\frac{(\ln(\frac{A}{A_o}) - \bar{x})^2}{2\sigma_x^2}} \tag{1}$$

Since optical detectors measure optical intensity we modify the ln-normal amplitude equation (1) using the probability transformation (2)

$$P_I(I) = P_x[x = \frac{1}{2}\ln(\frac{I}{I_o})]\, |\frac{dx}{dI}| \tag{2}$$

to form the ln-normal intensity equation (3) [6].

$$P_I(I, \bar{x}, \sigma_x) = \frac{1}{\sqrt{2\pi}\, \sigma_x 2 I}\, e^{-\frac{(\frac{1}{2}\ln(\frac{I}{I_o}) - \bar{x})^2}{2\sigma_x^2}} \tag{3}$$

If we plot the ln-normal intensity distribution vs intensity we obtain curves such as those in **Figure 3**.
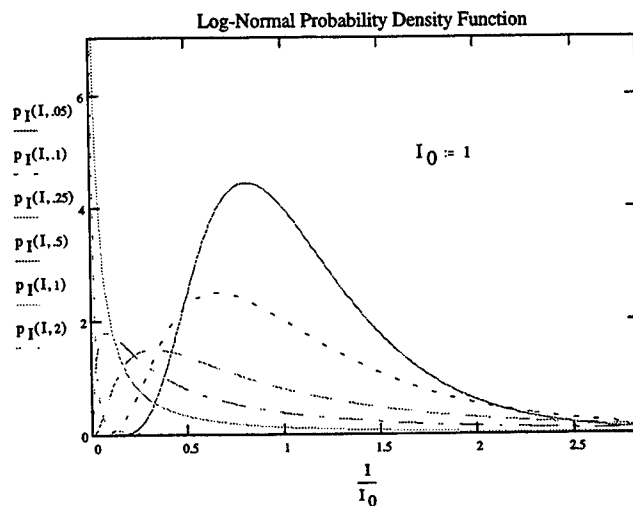

Figure 3: Log-normal probability density function for intensity

EXPERIMENTATION

The Liquid Mercury Optical Scintillator (LMOS) is designed to recreate the effects of atmospheric turbulence on laser beam propagation. The main components of LMOS are: the liquid mercury, to provide the reflective surface; a magnetic stirrer, to couple the signal into the Mercury; an electromagnetic solenoid, to couple electrical signal into the magnetic stirrer; and a vacuum sealed containment vessel. Mercury was originally chosen because it is the only room temperature fluid that offers high reflectivity over a broad spectrum of wavelengths. Later we discovered mercury's high surface tension and low viscosity nature significantly increase the mechanical coupling efficiency. This results in small scale structure of the fluid vibrations and allows for compact packaging of the critical components. Since mercury vapor is highly toxic and violently reactive with a variety of common compounds, a hermetically sealed containment vessel is essential for safety. Therefore, complete wavelength independence is compromised by the transmission characteristics of the containment vessel. However, wavelength dependence is minimized by choosing an optical material with a wide spectral bandwidth such as quartz.

In prototype # 3, a uniform intensity, collimated laser beam enters a "beam ladder" arrangement, passes through the vacuum sealed glass containment vessel, and strikes the vibrating mercury surface, see **Figure 4**. Outside the containment vessel, band-filtered white electrical noise drives an electro-mechanical solenoid that couples energy into the liquid mercury surface through the magnetic stirrer and produces surface vibrations on the surface of the mercury. The reflected beam is spatially modulated by the surface vibrations of the liquid mercury.
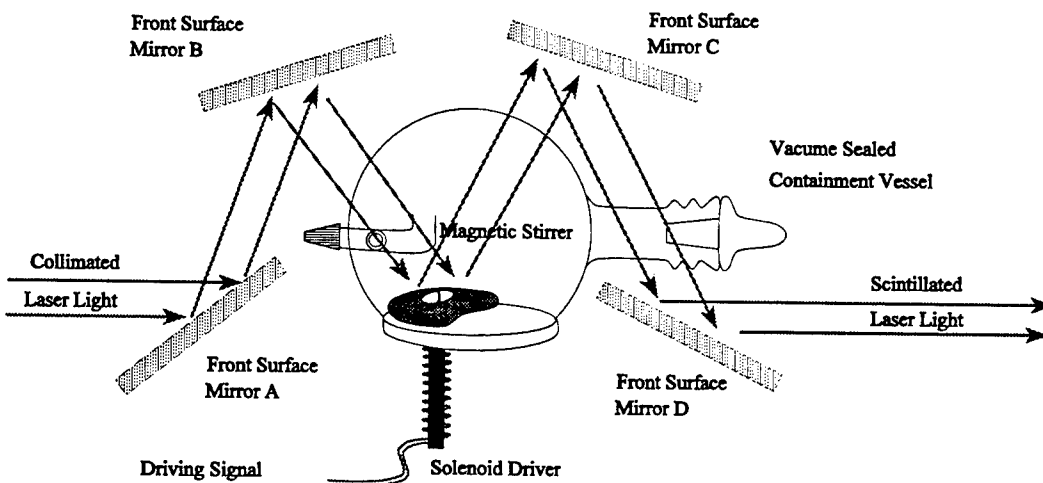
PROTOTYPE DESIGN #3

Figure 4: Liquid Mercury Optical Scintillator (LMOS)

Since liquid mercury has high surface tension and low viscosity, the fluid surface disturbances responsible for energy redirection are quite small and generate a scintillated beam profile that is too minuscule to work with directly. Therefore, an additional beam ladder arrangement steers the reflected beam into a beam expander, allowing for variable pathlength working distances. Then the beam is recollimated by a spherical mirror to simulate far-field angle of arrival statistics while maintaining the same spatial irradiance redistribution, see **Figure 5**. The beam expander accelerates the natural divergence of the laser and allows arbitrary magnification; this is equivalent to allowing the beam to diverge naturally over some arbitrary pathlength and measuring the statistics at that distance.

Statistics of the beam energy distribution depend significantly on the applied solenoid vibration frequency spectrum, amplitude, and the mercury boundary conditions. To prevent forced resonant modes in the vibrating surface, the mercury pool is only a partially bound by the side and bottom of the containment vessel. The free flowing edge of mercury and its high surface tension allows small turbulent random fluctuations in the mercury surface. Vibrations induced by the moving magnet modulate the reflected beam. We filter the solenoid's driving signal to allow control of the electronic white noise and the statistics of the beam's energy distribution.
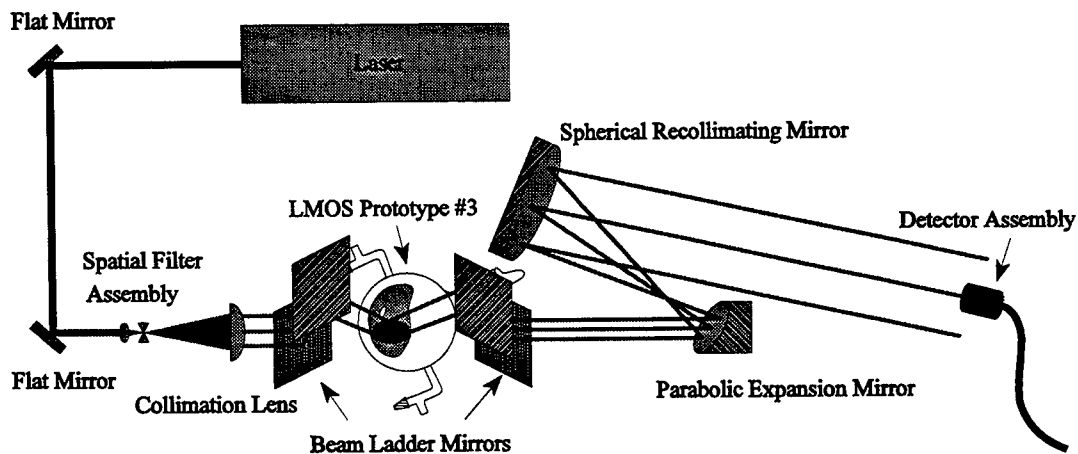
Figure 5: Liquid Mercury Optical Scintillator Experimental Setup

Optical beam analysis requires using a silicon PIN detector to measure the irradiance of the scintillated laser beam. If the intensity fluctuations are smaller than the exposed area of the detector they will be averaged. To allow for observation of various size intensity fluctuations we attach a variable aperture to the detector. The detector assembly has a bandpass filter to discriminate against detecting light not produced by the laser, see **Figure 6**.

Variable Aperture   Bandpass Filter
    Detector Holder   Silicon PIN Detector   Mounting Bracket
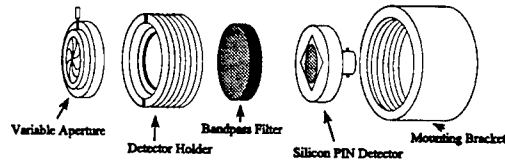
Figure 6: Detector Assembly

There are many parameters that affect the operation of LMOS. These parameters change the statistics, angle of arrival and beam divergence of the scintillated beam. To help us understand just how each parameter effect the operation of LMOS we need to record and analyze a large amount of test data. To collect this large data base we incorporate the collection and control of a computer equip with data collection hardware and software. We found it necessary to control several digital devices to allow for computer controlled data collection. This we accomplished by utilizing the RS232 communication ports and programming with Testpoint Software. We designed and implemented computer control modules for the Digital Equalizer which modifies the solenoids driving signal and the detector's Low Noise Current Amplifier, see **Figure 7**. We also developed a data analysis module used to analyze the data collected from the detector. The control and analysis modules help to automate the experiments with LMOS. These modules will be valuable in the final implementation of LMOS. We wish to be able to specify the desired scintillation level and the computer will modify LMOS controls to automatically acquire this level of scintillation. The end goal is a black box device that we can specify the desired scintillation level and the computer will modify LMOS parameters to achieve this level of scintillation. This working LMOS device will provide a valuable instrument for development and testing of optical receivers in a variety of scintillation levels.

Detector Signal   Digital
Low Noise   Equalizer
Current PreAmp   Display
                                                              Computer
                   Audio Amplifier   Control &
                                                              Analysis

Digital Signal Analyzer   Digital Equalizer
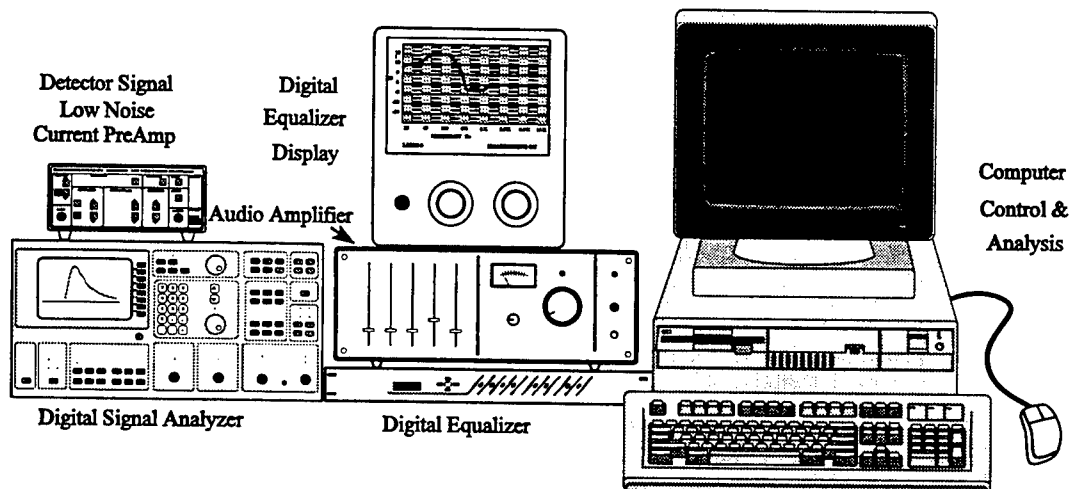
Figure 7: LMOS experimental testing and control equipment

RESULTS

We determined that the low frequency components of the driving signal, less than 200 Hz, are coupled into LMOS much more strongly than higher frequencies. However, LMOS requires some higher frequencies components, up to 2 kHz, to maintain ln-normal statistical distribution of the detected beam. The frequency distribution of the digital equalizer has a significant effect on the detected statistics from LMOS. By boosting the contributions to frequencies below 200 Hz, LMOS produced ln-normal distributions of the detected signal.

An overlay of theoretical and observed detector signal histogram distributions is shown in **Figure 8**. Chi-square null-hypothesis with significance level 0.1 alpha indicates a 99% confidence level that our detected signal matches the ln-normal distribution.

Distribution vs. Observed Histogram Ln-Normal Distribution
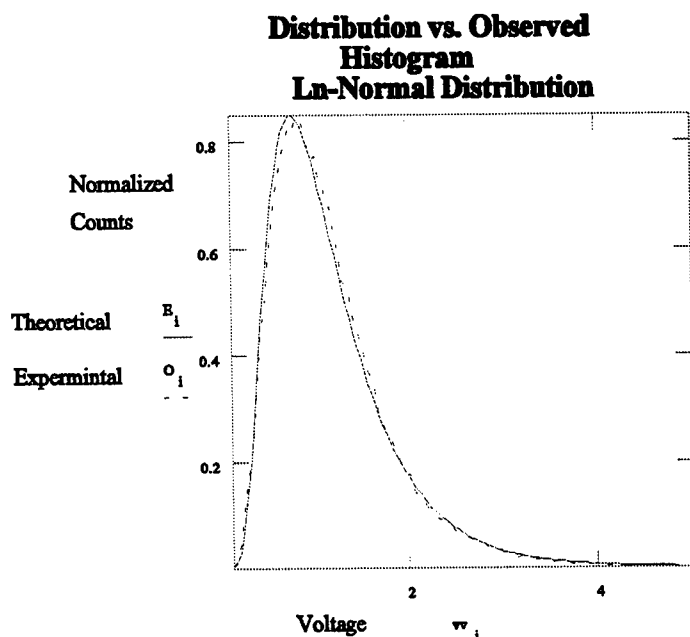
Figure 8: Experimental and theoretical ln-normal histogram distributions

The variance of the detected signal indicates the level of turbulence the beam is propagating in. By changing the driving signal amplitude, LMOS produced ln-variances that range from 0.001 to 0.8, see **Figure 9**. We did observe even larger variances, as high as 1.25, however, the signal no longer retained its ln-normal distribution. The large range of variances signifies that LMOS can simulate a wide variety of turbulence levels.
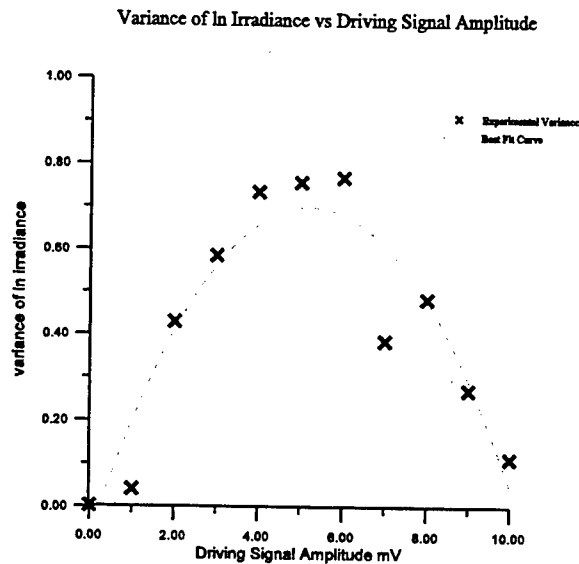
Figure 9: Variance of ln Irradiance changing with Driving Signal

The above graph demonstrates the variance increases with driving signal amplitude up to about 6 mV and then begins to fall off if we increase the driving signal above 6 mV. Above 6 mV the detected signal is very rapidly changing, indicating very strong scintillation levels.

LMOS prototype #3 has already been implemented in the testing of an optical receiver. LMOS provided a scintillated laser beam to test the receivers stability in measuring irradiance levels.

CONCLUSION

Laboratory simulation of atmospheric laser scintillation has been accomplished through a Liquid Mercury Optical Scintillator (LMOS). LMOS demonstrated spatial irradiance variations in the reflected beam exhibit probability distributions matching atmospheric ln-normal statistics. LMOS can simulate a wide range atmospheric turbulence levels, indicated by its ability to produce a large range of variance levels for the ln irradiance. We determined that low frequency components of the white noise driving signal are coupled into surface vibrations more strongly than high frequency components are. We have developed some of the computer control modules to provide dynamic control of LMOS and aid in further development of LMOS. While we have made progress in characterizing the parameters of LMOS further experimentation is necessary to produce a fully controllable LMOS device.

17-12

SUGGESTION FOR FURTHER RESEARCH

There were several characteristics of the LMOS design prototype #3 which are undesirable. Much of this is due to the containment vessel itself. The containment vessel was made from a stock boiler flask, therefore the glass is not optical quality and the spherical top has a nonuniform thickness causing a collimated laser beam to interfere with itself, which produces bright and dark fringes. The interference makes it difficult to separate the effects of LMOS from the effects of the nonuniform glass containment vessel. Another drawback is the difficulty in fastening a magnetic stirrer to the bottom of the containment vessel. To accomplish this task an epoxy that we felt would not react with mercury was used. This epoxy did form a good bond and did not seem to react with mercury, however over time it began to break down and contaminate the surface of the mercury. This contamination degrades the surface reflection ability of the mercury and alters the operation of LMOS.

We proposed a new prototype design for LMOS with flat optical windows where the beam enters and exits the vessel. Instead of a Teflon coated magnet we will enclose the magnet in glass and use a different attaching mechanism. The containment vessel for this new design is already under construction.

We plan to expand the computer control and analysis software to help automate the data collection process. We will utilize Analog to Digital conversion board in a computer to make direct measurement of the signal and analyze the output with the same program. Additional control of the driving signal can be accomplished by using a Digital to Analog conversion and computer software. After further examination of this new design we will use the computer control to modify the operation of LMOS to provide the desired level of turbulence for actual testing of laser receivers.

REFERENCES

1. J. Parker, M. DeLong, "Reflective Membrane Scintillation for Laser Receiver Diagnostics," SPIE Proceedings, v999, Laser Radar III (1988), 281-298.

2. A. K. Majumdar, H. Gamo, "Statistical Measurements of Irradiance Fluctuations of a Multipass Laser Beam Propagated through Laboratory-Simulated Atmospheric Turbulence," Applied Optics, v21 (1982), 2229-2235.

3. K. Schatzel, "K-Distributed Phase Differences in Turbulent Random Phase Screens," J. Opt. Soc. Am., v73 (1983), 269-276.

4. L. R. Bissonnette, "Atmospheric Scintillation of Optical and Infrared Waves: A Laboratory Simulation," Applied Optics, v16 (1977), 2242-2251.

5. J. W. Strohbehm, Laser Beam Propagation in the Atmosphere, Springer-Verlag, New York (1978)

6. J. W. Goodman, Statistical Optics, John Wiley & Sons, New York (1985)

The Concept of a Model within Model-based Automated Target Recognition

Paul B. Losiewicz

Department of Philosophy

The University of Texas at Austin

Austin, TX 78712

The Concept of a Model within Model-based Automated Target Recognition

Paul B. Losiewicz

Department of Philosophy

The University of Texas at Austin

Austin, TX 78712

Abstract

The concept of what constitutes a model within model-based applications is not clearly understood nor are the advantages of their employment clearly explained. An attempt is made to elucidate the formal nature of a model within the confines of Automated Target Recognition (ATR), specifically as it is invoked by the Model-Driven Automatic Target Recognition Report of the ARPA/SAIC System Architecture Study Group for the Moving and Stationary Target Acquisition and Recognition project (MSTAR). It is shown that within model-based vision applications a model is primarily a feature data structure and a set of transforms for generating and evaluating correspondence hypotheses, but that within the larger context of model-based inference applications a model is nominally an unrestrained declarative data structure and a decision-theoretic mechanism for generating and evaluating target hypotheses.

"Models are ubiquitous. From metaphors, similes, and analogies to habits, paradigms, and learned behavior; from heuristics and statistical distributions to expert systems and causal descriptions; from superstition, myth, and folklore to physical laws and engineering approximations; from empirical data to differential and logical equations - models are an integral part of all human physical and intellectual activities. Without models there would be no science, because hypotheses are models; without models there would be no yesterday, because memories are models. Thus it is surprising that the signal processing disciplines, particularly those concerned with vision, have made such limited use of models."

<div align="right">
Hatem N. Nasr and Rodney M. Larson

Introduction to the SPIE Proceedings vol 1827 on Model Based Vision
</div>

I. Introduction - Model-Based Vision in ATR

Given the above statement it is no surprise that questions have arisen as to the meaning and function of a model in computational systems. We might better ask what is *not* a model than what is. Model Based Vision (MBV) as practiced in Automated Target Recognition (ATR) employs models of prospective targets to aid in generation of anticipated features in order to facilitate matching of an observed image to a synthetic hypothesized image. In order to advance the understanding of the role of the model in ATR, a survey is provided of model based applications both within and without model based vision. My focus will be one MBV project of interest, MSTAR, the Moving and Stationary Target Acquisition and Recognition project currently being funded by ARPA.

MSTAR is conceived to:

"...take in SAR images and output target reports. For each mission, the
ATR system also needs a set of target and environmental models that
describe the target's geometry and other attributes. Models are developed
in an off-line process and then used in an on-line hypothesize and test
manner to compare predicted target signatures with image derived data. [1]

The ATR system within MSTAR has the following intended characteristics (p.11):

---

[1]From Model-Driven Automatic Target Recognition Report of the ARPA/SAIC System Architecture Study Group, 14 October, 1994, p. 6. All further references to MSTAR will be from this source.

- Use of explicit models of target, sensor, and image information.
- Use of target models that specify the three-dimensional (3-D) geometry of targets and their functional organization, e.g. what parts correspond to a "turret" that can rotate with respect to some other part.
- Use of geometric target models to accumulate and organize the evidence for or against hypotheses about a target's identity.
- Incorporation of a *model-driven* approach that works from coarse to fine predictions.

The information described above is intended to be used in an evidential reasoning , e.g. Bayesian, calculus that will produce a synthetic image that best matches a given input image which will indicate a correct classification.

The motivation for model-based approaches is not explicitly explained in the MSTAR System Architecture Study Group report, it is merely stated that the study group limited their activities to model-based vision techniques as "the method of choice" (p9). Increase of computational ease is intimated but not clearly claimed as an intrinsic element of model based vision, as the following indicates:

> "The computational complexity of the ATR problem grows rapidly with the number of targets to be considered, variability within each target type (for example, variant configurations, articulating parts), image acquisition geometry (range of aspect, depression, and squints to be covered), and viewing conditions (for example, obscuration, camouflage, netting). A brute force approach that attempts to store complete signatures for every possible view and viewing condition can not feasibly scale to handle complex targeting problems. Model driven systems *also* need to address the computational complexity and the ability to scale feasibly with the problem size"(p.18). [italics mine]

To provide insight into the motivation for model-based applications is another goal of this review, and positive evidence is given from different sources as to the benefits of employing model-based applications.

In order to simplify the investigation of how this is to be accomplished resort will be made to a key distinction in the MSTAR study:

18-4

A key to understanding the job of Match Features is the distinction between a *target hypothesis* and a *correspondence hypothesis*... The major element of a correspondence hypothesis is an assignment of extracted features to predicted features. In general this assignment will be many to many... Match Features assumes that target and background object types are fixed - Search will generate and test changes to these... Match is a separate function from Search... Search explores the space of target hypotheses. Match Features does not go back and repredict features -Search take[s] responsibility for that as it has broader knowledge of what competing target hypotheses look like (p. 114ff).

II. Models as used in Correspondence Hypothesis

The Match module within MSTAR is limited to specific target hypothesis and feature sets, and has as its role the generation and evaluation of a specific correspondence hypotheses, with the added requirement of letting a supervisory module, the Search module, know where the mismatches occur, in order to facilitate hypothesis revision (p. 113). Match has some currently operating MBV exemplars. Hsu and Reeves (1992) describe their model based vision system as follows:

> The task of model based vision is to perform object recognition by matching known object models against images that contain these objects. Detection of an occurrence of an object in an image involves finding a consistent set of corresponding image and object features. Model based systems are thus only able to recognize objects for which they have precomputed models. The recognition problem then becomes how to find the best possible mapping from prestored models in a database and a set of image features.

The following general MBV sequence of steps is provided by Hsu and Reeves:

1. Select a candidate model.
2. Detect the corresponding image features over the image.
3. Hypothesize the object from a subset of image features detected.
4. Estimate the transform from a model view to a scene view.
5. Establish a correspondence between the hypothesized scene object and the model object.

6. Verify the hypotheses according to the correspondence mapping.

Their vision system only accounts for steps 4-6 however, as no information is forthcoming as how to create select, detect and predict modules. However, their treatment of feature representation and matching is instructive. The search for a match in the recognition system is presented as a mapping problem employing one of two strategies: data-driven, or model-driven. In the data driven approach, the search sequence is controlled by the features of the scene or input data, while in model-driven searches the sequence is controlled by the sequence of model features invoked. As mentioned above, MSTAR is conceived to be model driven. Hsu and Reeves present a formalism for the model that is intended to drive the correspondence search and evaluation.

A model object is represented by:
$O_M = \{M_i \mid i = 1, ..., m\}$, where M_i are model features.

An image object is represented by:
$O_S = \{S_j \mid j = 1, ..., n\}$ where S_j are scene features.

T is a transform, $S_i = \mathbf{T}(M_{c(j)})$, that maps an object from a model coordinate system to a world or scene coordinate system

C is a correspondence relation for all S_i in O_S where **C**: $O_S \to O_M$, that is, a mapping of each s_i into a transform of a model feature set.

Hypothesis generation requires one to find *all possible sets* **P**,
$\mathbf{P} = \{(M_j, S_i) \mid C(i) = j, M_j \in O_m, S_i \in O_S, d(T(M_j), S_i) \leq \varepsilon\}$ where ε is the largest possible mismatch.

The specific model-driven nature of the hypothesis testing is explained as invoking a mapping of scene features into every possible transform of a preselected model's features, with some constraint of mismatch, that is the mapping must be constrained by

some measurement of acceptable distance between the observed values and those predicted by the model. Hsu and Reeves make no use of uncertainty in the representation of the feature set, and as stated before, no account is given of model preselection criteria. Nonetheless we see that within the correspondence hypothesis evaluation described by Hsu and Reeves, a model is represented as a *basis set of model object features and every possible transform on those features.*

Another example of MBV matching is provided by Ravichandran and Sanderson (1992) using a set of features composed of vertices and edges to model 2D and 3D objects. They provide a similar formalization of the model-based matching problem, where:

The model is represented by a set of features $M = (M_i, 1 \leq i \leq M_n)$.

The scene is represented by $D = (D_j, 1 \leq j \leq D_n)$.

A matching between each set of features in D and M is specified by a correspondence C and a transformation T that maps a set of model features onto a set of scene features. The correspondence or the mapping of the transformation set and scene set, will return either a *model, missing* or a *spurious* value in a listing for all $M_i \in M$ and $D_j \in D$. They note that the parameters for the transform T can be derived from any two correspondence pairs $(M_i, Dc_{(i)})$ and $(M_j, Dc_{(j)})$ in a linear fashion and that the number of parameters required varies from four to six depending upon whether we are mapping 2D into 2D or 3D into 2D.

The match is accomplished through a search and evaluate architecture. Evaluation is based on a minimum representation size criterion, e.g. the smallest correspondence representation over all possible transforms. A correspondence representation is a table of model features and scene features in association with their equivalents, if any. The table represents a mapping between the two feature sets, nominally, vertices and edges. Spurious features caused by noise are scene features that fail to map into the model set, missing features, e.g. caused by occlusion, are model features that fail to map into the scene set. The minimum sized correspondence representation is that table whose

aggregate residual error over the entire feature set is smallest. The distances between features that do not exceed an "unmodeled" threshold are summed over the correspondence to yield the aggregate residual error. The parameters used to denote distance and failure to model are heuristically determined and are specific to the hybrid genetic algorithm employed in searching for the best correspondence.

The hybrid genetic algorithm employed by Ravichandran and Sanderson has been employed with other problems such as graph coloring and traveling salesman. While the algorithm searches for the best correspondence among all possible correspondences given the model, it is not certain that there will be a unique solution, particularly when the model description is in a 3-D space and scene is specified as 2-D. What is implicit in their position is that the search over all possible transformations is the major source of computational expense, and when the problem is ill-defined, i.e. there is no unique solution, the algorithm can produce a family of solutions. This problem occurs in other model-based applications as well. As indicated in Ravichandran and Sanderson, constraint of the search to reach a particular solution within a family of solutions is accomplished by use of *a priori* knowledge.

For Ravichandran and Sanderson a hypothesis correspondence can be represented by a *function* from pairs of feature sets into error values, with a match being the hypothesis with the lowest aggregate error. Ideally, the Match module should provide the superset of all possible matching correspondences. However the actual module will incorporate *a priori generated constraints* on the possible correspondences and the error level allowed. The representation of a model based vision model adequate to hypothesis correspondence within the context of a CAD program for 2D to 2D mapping appears to be nothing more than a feature set basis and a set of transforms. It may even be said at this point that a working model is merely a *superset of all feature sets validated by or within error limits tolerated by the semantics* of the model. The introduction of the transforms over a basis feature set is an accident of the requirement to use a *compact representation* of the feature sets, and so is not essential to a model *per se*. Estimates of the computational complexity of a correspondence evaluation would proceed on these assumptions.

However, of interest to us at this point is the use of *a priori* knowledge in constraint of possible transforms. If we understand a model to be a feature set and set of transforms, then the transforms allowed are limited by real world knowledge. In the case of the 3D to 2D mappings described by Ravichandran and Sanderson, possible ambiguities produced by the reduction of the representation space exist, and a subset of the possible transforms are either ruled out or given preference. The appeal to *a priori* knowledge derived from the semantics of the model limits the possible transforms allowable in their model. Thus the notion of *every possible transform* is a relative one, i.e. relative to the *a priori* knowledge dictated by the semantics of the model. Another point bearing on semantics within the context of a correspondence hypothesis is the amount of error tolerated in the match. Choice of error thresholds is often attributed to heuristics, but this often means it is governed *a posteriori* by how well the correspondence relation allows us to make predictions within the world implicit in semantics of the model.

III. Models and Target Hypothesis Generation

This implicit appeal to *a priori* information to limit the possible transforms available to a Match module brings us naturally to the next level of hypothesis representation, the *target hypothesis*, for it is there we find the source of the constraints.

Within MSTAR it is envisioned that the off-line constructed models will form the major portion of the Prediction Data Base (PDB) to be used by the Predict module to provide synthetic images to Match. "At a minimum ... the predictive component database must contain a representation of the 3-D target geometry" . However, the 3-D representation has an explicit "organizational" requirement:

> "In addition to defining the geometry of target sub-components, the 3-D
> target representation must be organized to reflect the functional
> relationship between these sub-components. This is necessary to support
> subsequent generation of features corresponding to different target variants
> and articulations, as well as to support reasoning about partial target
> matches" (p.82).

The PDB is thus a necessary component in reasoning from partial matches. This is intended to be achieved by encoding the functional organization as a "hierarchical tree structure" (p.83). Thus some relational information must be included in the representation, i.e. some way of representing the relations that hold between local features in order to infer local features from other features. Furthermore, the Predict module is expected to compute uncertainty measures for the features it does predict (p.100), and pass these on to the Match module for processing.

Neither Hsu and Reeves nor Ravichandran and Sanderson have an explicit representation of hierarchical structure in their formalism, nor is there any use of uncertainties in the feature data. They focus primarily on the correspondence hypothesis problem, as found in the Match Module and the model requirements to support searching and evaluating correspondence hypotheses within their systems do not need to include hierarchical information. However, within MSTAR, the Predict module does make use of such information in creating a list of model features after the selection of a target hypothesis by the Search module. Predict employs *the same geometric model* as the Match module, but also requires *access to the hierarchical relationships* between subsets of features in order to predict features from partial feature sets. The Predict module takes in a target type hypothesis and a partial feature set from Search and returns a complete feature set to Match. Thus the model employed by Predict must be *extended* from that found in the match modules in our examples to include the information regarding functional relationships.

This extension of the model relative to the module occurs in Search as well. The Search module takes in a partial feature set and some *a priori* knowledge, e.g. force structure, mission imperatives, terrain, and, ranging over the entire hypothesis space, produces a "coarse" target hypothesis and a partial feature set for Predict. Search is given access to all previous predict/match tasks as well as has access to

> all of the models in the system. In particular, it must know what model elements i[t] can employ when constructing a hypothetical scene to offer to Predict Features. These elements may have attached attributes, which must also be specified as part of the target hypothesis. For targets, the

on-line target models define the parts, articulation variables and configuration variables to be specified. (p.139)

If here we find the on-line models being accessed by Search for possible parts, articulations and configuration variables (e.g. operational state) then again the *models are being extended* for yet another module with additional informational requirements. Search must now take these extended models as part of its domain. Thus it appears that what constitutes a model, or at least, *what implicit knowledge constrains* a model, is relative to the module that employs it. Furthermore, Search is expected to range over multiple models, whereas Predict need not, and Match is clearly intended to work with one model at a time. An observation is offered at this point: A taxonomy of what models are present in an ATR system can be either module relative or global. A module relative taxonomy would describe multiple independent of models, i.e. each model will include all and only that information necessary for the module that makes use of it. A global taxonomy would treat the entire database as a union of "partial" models, with Search ranging over the union.

A current example of a "global" target hypothesis generation is found in Ettinger, Morgan and Reinholdtsen (1991), who also apply a Bayesian inference mechanism to model-based vision, admitting that "many diverse sources of knowledge need to be exploited" for successful recognition. They characterize their system as a "general model-based recognition Bayesian modeling and reasoning paradigm" which has been applied to two model based recognition problems: battlefield scene analysis and vehicle recognition. Uncertainties enter the problem from a combination of factors, such as noisy synthetic aperture radar (SAR) imagery, loosely constrained models, and high clutter environments. Thus they have developed methods for "augmenting the target models...with additional knowledge of the sensor and contextual situation"(p74). The Bayesian modeling methodology they employ provides a "decomposition of the joint probability space into a hierarchical Bayesian network that parallels the structure of the models" (p. 76). The inference actions they describe include evidential accrual actions that incorporate direct probabilistic evidence from imagery and contextual sources. "The probability models used by the evidential accrual actions consist of empirical feature value distributions that

18-11

are derived from...actual data as well as knowledge elicitation of the domain" (p.80). The inference mechanism in the system provides *contextual model refinement* to:

> Apply external constraints to refine nominal formation models to reflect the particular underlying situation. Thus the contextual constraints are reflected in the beliefs of the corresponding hypothesis via a re-evaluation of the match of the refined model against the hypothesis. The principle constraints used are terrain features, both local and global in nature (p.79).

There is a related reference in the MSTAR study to the capacities of Search that bears on the employment of models in inference. Part of the desired capability of the Search Module is "to be able to deal with the complexity of the search space caused by complex target shapes and obscuration...[and]...move from rule-based approaches that rely on humans accumulating expertise to more rigorous, but computationally expensive, off-line analysis of target characteristics to derive search guidance." (p153).

Newton Lee (1990) casts some light on the role of models in inference mechanisms by contrasting model-based and rule-based inference applications. He notes that rule based expert systems work well in simple applications but in complex domains associational knowledge may be too much to represent. A possible solution is an explicit modeling of the basic principles invoked in expert problem solving, which makes use of the information about the structures and the behaviors of domain entities. What constitutes a model for Lee is that a model describes a structure and provides a behavior for that structure, i.e. *a structure and a behavior that can be represented as a functional definition* (p. 139). A model must then be conceived as composed of a structural definition and a function describing the behavior of the structural elements. This definition appears consistent with our previously stated understanding of a model as used in model based correspondence hypothesis evaluation as a feature set and a set of transforms.

On the other hand, rule-based expert systems are intrinsically *syntactic*, e.g. that production rules in Prolog, for example, proceed by a process of syntactic pattern matching that allow formulas to unify through a process of variable substitution in

isomorphic *formulas* within a formal language. Deduction proceeds only if a variable substitution can be carried out between knowledge representations that are isomorphic with respect to their syntactic form. Lee proposes a hybrid system that is both rule-based and model based. Lee augments a logic program by employing a system of *semantic unification* whereby nonisomorphic formulas can unify if they can be demonstrated via *semantic* transformation rules to be rewritable in isomorphic formulas that are capable of syntactic unification. Explicit in Lee's position is that model-based reasoning can provide semantic information to augment syntactic transformation rules and thus allow simplification of a deduction in a hybrid system.

Judea Pearl (1988) provides further insight into the distinction between syntactic and semantic representations. He bifurcates all AI methods for dealing with uncertainties as either *extensional* or *intensional*, classifying model-based reasoning approaches as intensional or semantic whereas proof theoretic or rule-based approaches are termed extensional or syntactic (p. 3). One of the properties of syntactic approaches is *locality* which means that whenever a rule can apply to a datum, it is discharged regardless of what else may be in the data set. This is another way of saying that extensional approaches are monotonic and classically compositional, for the uncertainty of a formula is treated solely as a function of its subformulas. Pearl indicates that semantic approaches are different, e.g. that a local inference can have a global effect on the values of other elements in the model data set, and thus are non-monotonic[2]. Uncertainties in model-based systems attach to an entire "state of affairs" or "possible world" in which interrelations bearing on uncertainty may be global rather than local. The syntax of the knowledge base is purely declarative, and, as the syntax of a model-based system does not "point to any useful procedures" to answer a query, solutions to a query must be achieved by *mechanisms* such as *belief networks* (p.12). The concept of a model within this context is at minimum a data set composed of declarative "sentences" with an associated truth value or confidence factor and a mechanism for answering a query about the data set. As Pearl points out, the essential difference is not in the notation or the

---

[2]There is room for criticism of his taxonomy. Default Logics, in some sense combine the semantics in the syntax by defining its inference rules over the possible states of the system, which still seems to qualify as rule based but not monotonic, i.e. a model using default rules is a structure that is *not* closed under classical deduction.

range of the truth values, e.g. whether the truth values are binary or multi-valued, but in the method of answering a query. A syntactically driven rule-based approach assumes:

- *locality* - that discharge of a rule is oblivious to everything else in the database except the antecedent of the rule
- *detachment* - that the source of derivation of an antecedent of a rule is irrelevant to the discharge of a rule.
- *modularity* - that a syntactic or rule based system exhibits both locality and detachment

Pearl declares the limit of modularity to be a blindness to sources of information, with a corresponding failure to recognize and exploit independent corroborative evidence. Furthermore, *update* of certainty weights in a modular system can remain coherent if and only if the rules form a *directed* tree, that is modular systems can allow only one rule per antecedent (p.11) in order to allow coherent update. It is thus a non-modular "mechanism" for query coupled with a declarative database that is taken to be what constitutes model-based reasoning for Pearl. Pearl indicates that the advantages of model-based reasoning over rule-based systems is that a model-based knowledge network is encoded in such a way "that the unignorable is quickly identified and readily accessible" e.g. via the connections between neighboring nodes in a graph (p.13). The nodes represent the data and their values, the edges represent dependency relations between nodes. The update of a system will proceed via the edges using four "axioms" of relevance that constitute a "structure common to all of these [intensional] formalisms" i.e. Bayesian, Dempster-Shafer, and Qualitative Markov methods (p.13). Pearl's description of these intensional formalisms is consistent with a model using a non-syntactic representation , i.e. a (data) structure such as a graph, and a behavior, as given in the particular mechanism that instantiates the axioms of relevance[3]. Ettinger *et al*'s system description is also consistent with Pearl's characterization of intensional model-based reasoning insofar as the empirical features that are derived from both imagery and

---

[3] Pearl offers the following interpretation of the four axioms: *Symmetry* -that in any state of knowledge Z if Y tells us nothing new about X then X tells us nothing new about Y. *Decomposition* - that if two combined items are irrelevant to X then each separate item is irrelevant. *Weak union* - that the learning of irrelevant information about Y will not make Y become relevant to X if Y was previously irrelevant. *Contraction* - if W is deemed irrelevant to X after learning some irrelevant information Y then W must have been irrelevant before we learned Y (p.85).

contextual sources can be considered declaratives that are arranged in nodes with edges representing the relevance relations that hold among them.

Halpern and Vardi (1991) provide a more general theory of model-based reasoning and reject rule-based reasoning for slightly different reasons than Pearl. The use of an "interpreted symbolic structure" i.e. a logicist rule-based formalism, to represent a knowledge base involves one in two problems - designing the appropriate formal language in which to represent the compositional nature of a knowledge base, and the need to develop a very "expressive" logic by which to prove theorems (p.325). They thus explicitly point out the advantage of model based reasoning implicit in Newton Lee's hybrid approach. They reject the use of a rule-based representation plus theorem proving in favor of a model-based representation using *model checking* to answer queries.

> "The theorem proving approach requires us to represent the agent's knowledge by a collection of formulas in some language. The model-checking approach instead represents the agent's knowledge as a local state in some structure" (p.327).

They counter that the proper question is not "does an assertion *p* follow from a knowledge base *k* using some nonmonotonic logic?", but "does *p* holds in the *Kripke* structure[4] represented by *k*?", *k* being a "data structure representing some semantic model" (p. 328). Model-checking allows *complete freedom in the form of the representation* of the local state, thus integration of the parametrics of disparate "features" into a uniform formulaic language is not a requirement of the representation.

According to Halpern and Vardi any model theoretic approach asks two basic questions:

- What is the appropriate semantic model?
- How can we check if a formula is true in the model?

---

[4]A Kripke structure is a data structure that makes explicit the possible relation between propositions, i.e. declaratives, and truth values, thus creating what is called a set of *possible worlds* for a local state.

Answering the first question goes hand in hand with what one decides to include in a data set that characterizes a local state or that *can* characterize a local state. If one wishes to include contextual information with a geometric model feature set then that intended data structure is what determines the appropriate semantic model. Halpern and Vardi choose to represent a general data structure as an *n*-tuple known as a Kripke structure. The mechanism to be employed for the update of declaratives, using binary truth values or posterior probabilities in a Bayesian approach, is described as a global state description composed of a union of an environment state of general knowledge and a local state of an agents knowledge and a *transition function* over that union that describes how the system changes from one global state to another[5]. Halpern and Zuck (1987) is recommended as a detailed example of a modeling process.

King Sun Fu (1982) also divides all pattern recognition techniques into two general groups, *decision-theoretic* and *syntactic*. It is generally accepted that Bayesian techniques fall within the purview of decision theory. The distinctions between the them are presented as follows:

> In the decision theoretic approach, a set of characteristic measurements, called features, are extracted from patterns; the recognition of each pattern (assignment to a pattern class) is usually made by partitioning the feature space (p. 1).

> The syntactic approach to pattern recognition provides a capability for describing a large set of complex patterns by using small sets of simple pattern primitives and of grammatical rules... one of the most attractive aspects of this capability is the use of the recursive nature of a grammar. A grammar (rewriting) rule can be applied any number of times, so it is possible to express in a very compact way some basic structural characteristics of an infinite set of sentences (p. 3).

> The feature selection problem in the decision theoretic approach and the primitive selection problem in the syntactic are similar in nature, except

[5]Halpern and Vardi note that the description of the state space becomes "unclear" if they try to represent not just what an agent knows, but that a particular agent knows it.

that the primitives in the syntactic part represent subpatterns, and, on the other hand, the features in the decision-theoretic approach may be any set of numerical measurements taken from the pattern. As a matter of fact it appears that there is no distinction between the two approaches at this level, since it is intended that the pattern primitives selected should contain no significant syntactic information with respect to the recognition problem....When explicit structural information about the patterns is not considered important and the problem is primarily one of classification rather than classification and description, there appears to be no real need for using syntactic methods. When, on the other hand, patterns are very rich in structural information and the recognition problems require classification and description, the syntactic approach seems to be necessary (p.43).

Fu goes on to espouse a *hybrid* approach to complex recognition tasks that require representation of structural relations, i.e. a decision-theoretic technique at the lower feature levels where the hierarchic relations between feature sets plays no role, and a syntactic technique at higher levels of representation where relational information between feature sets can be manipulated via some recursive grammar. From Fu's perspective, syntactic or rule-based approaches are *necessary* to efficiently represent hierarchical relationships. Model-based reasoning would be confined to the lower representational levels as found in correspondence hypothesis generation and evaluation.

Within MSTAR, the incorporation into Search of Model-based reasoning is still under development. Insofar as Search uses *a priori* knowledge of such things as force structure to establish a coarse hypothesis, it can be assumed that Search itself constructs a restricted model set or set of "possible worlds" adequate to the input data and that Predict operates over the restricted model set to provide a model for Match to check. That Search is expected to output a target type and configuration estimates with posterior probabilities (p.147), supports the thesis that a Bayesian net will most likely be the model-based reasoning technique employed at some level within MSTAR. However, if hierarchical information is to be manipulated, an additional representational structure e.g. a tree structure or syntax-based propositional structure seems to be called for (Fu 1982). This is a topic for further research. A Bayesian network is constructed to depict *influence* relations using a directed acyclic graph (DAG), which normally incorporates

both *converging* and diverging edges, in order to represent plausible causal influences or conditional dependencies (Charniak 1991). Thus there is some question as to the suitability of a Bayesian net for displaying hierarchical relations. An example of an attempt to integrate hierarchical models into a Baysian diagnostic inference algorithm is given in (Srinivas 94).

Of more general interest is the understanding of what a model is conceived to be within the context of model-based reasoning, that is, a non-syntactic based data structure with a correlated mechanism or transform function for answering queries over the data. All sources indicate that the bare notion of a data structure does not have any implicit commitment to the form of the representation of the data nor does it require a logical formalism for manipulating declarative or propositional data, though it does require a mechanism for extracting data if the data representation is compact. This very general understanding of a model is consistent with 3D geometric models as employed in Model-based Vision matching modules doing correspondence hypothesis evaluation. It is also general enough to be consistent with decision-theoretic techniques of model-based reasoning that would be incorporated into supervisory modules doing target hypothesis generation and testing.

Areas of interest for future research along these lines include:

- The application of functional decomposition techniques to correspondence hypothesis model behavior to explore additional possibilities of complexity reduction.

- Investigation of the feasibility of incorporating hierarchical information into models that are manipulated via decision-theoretic methods.

- Investigation of decision-theoretic methods for dealing with queries that do not produce unique solutions.

- Summary

Within the bounds of model-based vision applications models can be seen to be comprised of a *feature data structure*, e.g. a data structure that represents a model set of vertices and /or edges, and *a set of transforms* over the structure, which is used in *correspondence hypothesis* generation and evaluation with a set of scene features. This is consistent with Newton Lee's comment that a model is *a structure and a behavior*, if we take the behavior to be the set of transforms over the data structure due to changes in the basis of the feature set or changes in object orientation. In its widest sense the model is a data structure composed of a feature set and every possible transform over the data. Correspondence hypothesis generation and evaluation ideally takes the form of a mapping from every possible transform and a given scene feature set into an error value. However, in practice, every possible transform is neither required nor desired. Constraint of the feature space is accomplished via *a priori* information represented implicitly in the geometric model or explicitly through the process of *target hypothesis* generation and evaluation. Target hypothesis generation accesses global information such as sensor performance, terrain, and force structure, and operates *over* geometric models. Target hypothesis generation is also intended to perform *plausible inference* from feature sets in case of occlusion or in calculating degrees of confidence. Target hypothesis knowledge bases coupled with hypothesis inference *mechanisms* such as Bayesian nets are considered *Decision-theoretic* as opposed to Proof-theoretic, insofar as they do not require a formal logic and a syntactic representation of the data. Constrained *model checking* provides a computational complexity advantage to model-based reasoning in addition to lacking the requirement for a compositional formal language within which to perform rule-based reasoning.

References

Charniak, E. 1991 Bayesian Networks without Tears in *AI Magazine*, Winter 1991 pp. 50-63

Ettinger, Morgan and Reinholdtsen 1991 *Bayesian inference for model-based vision* SPIE Vol. 1609 Model-Based Vision Development and Tools (1991) pp.74-86

Fu, K.S. 1982 *Syntactic Patttern Recognition and Applications* Prentice-Hall Inc. Englewood Cliffs, NJ

Halpern J. and Vardi M. 1991 Model Checking vs. Theorem Proving: a Manifesto *Principles of Knowledge Representation and Reasoning, Proceedings of the Second International Conference* 1991 pp. 325

Halpern J. and Zuck L. 1987 A little knowledge goes a long way: Simple knowledge-based derivations and correctness proofs for a family of protocols. In *Proceedings, 6th ACM Symposium on Principles of Directed Computing,* pp 269-280.

Lee. N. 1990 A Computational Paradigm that Integrates Rule-based and Model-based Reasoning in Expert Systems. *International Journal of Intelligent Systems*, v 5 135-151

Hsu P. and Reeves A. 1992 Recognition of Partially Occluded Objects Using Macro Features *SPIE Vol. 1827 Model based Vision (1992)* pp. 105-116.

Model-Driven Automatic Target Recognition Report of the ARPA/SAIC System Architecture Study Group, 14 October, 1994

Srinvas, S. 1994 A probabalistic approach to hierarchical model-based diagnosis. In *Proceedings, Tenth conference on Uncertainty in Artificial Intelligence* Morgan Kaufman Pub. Inc. : San Francisco CA

Pearl J. 1988 *Probabilistic Reasoning in Intelligent Systems: Networks of Plausible Inference* Morgan Kaufman Pub. Inc. : San Francisco CA

Ravichandran B. and Sanderson A. 1992 Model based matching using a minimum representation size criterion and a hybrid genetic algorithm *SPIE Vol. 1827 Model based Vision (1992)* pp. 76-87

MICROSTRUCTURAL EFFECT OF TI-22AL-23NB
ON ISOTHERMAL FATIGUE PROPERTIES

Stephanie Luetjering
Graduate Student
Department of Materials Engineering

University of Dayton
300 College Park
Dayton, OH 45469-0240

MICROSTRUCTURAL EFFECT OF TI-22AL-23NB
ON ISOTHERMAL FATIGUE PROPERTIES

Stephanie Luetjering
Graduate Student
Department of Materials Engineering
University of Dayton

Abstract

The effect of modification in microstructure, obtained by post-consolidation heat treatment, on the fatigue performance of the titanium alloy Ti-22Al-23Nb (at. %) in neat matrix form (unreinforced consolidated foils) was investigated.

Isothermal fatigue tests were conducted at room temperature and at 650 °C and the resulting fatigue properties were correlated with the microstructural variations by means of metallography and fractography.

MICROSTRUCTURAL EFFECT OF TI-22AL-23NB
ON ISOTHERMAL FATIGUE PROPERTIES

Stephanie Luetjering

Introduction

Titanium matrix composites (TMCs) are of considerable interest for advanced aerospace applications due to their high specific strength and stiffness. Research efforts have focused on high temperature titanium aluminide alloys as possible matrix materials, especially those based on Ti_3Al (α_2). /1 - 3/

Severe problems in these composite systems such as high reactivity between the reinforcing SiC-fibers and the matrix and poor environmental resistance have led to the investigation of other matrix systems. A new class of titanium aluminides based on the ordered orthorhombic (O) phase, Ti_2AlNb, has demonstrated benefits compared to titanium alloys based upon Ti_3Al. These advantages are: reduced fiber/matrix reactivity, improved room temperature ductility and toughness, increased tensile strength, and improved creep performance. /4 - 8/

Microstructural modifications can have a significant effect on the material's mechanical properties. Previous studies by Smith et al. /9/ showed, that both monotonic tensile and creep performance of the orthorhombic titanium alloy Ti-22Al-23Nb (at. %) in neat matrix form can be further improved by post-consolidation heat treatments. These heat treatments were initially selected in such way that they can be incorporated in the consolidation process of the composite fabrication and that the reaction between the fibers and the matrix as well as residual stresses in the composite are minimized.

The objective of the present study was to investigate the cyclic behavior of "neat" Ti-22Al-23Nb. The microstructure, which had given the best balance of mechanical properties in /9/, was generated and its isothermal fatigue properties were compared with those of the as-fabricated condition.

Experimental Procedure

The material used for this investigation was the orthorhombic titanium alloy Ti-22Al-23Nb (at. %) in neat matrix form, a five-ply laminate. Consolidation of the 0.09 mm thick foils was performed by Textron Specialty Materials (Lowell, MA) using hot isostatic pressing. Dog-bone specimens were machined according to Figure 1.

A post-consolidation heat treatment in vacuum (10^{-6} torr) incorporated a sub-transus solution treatment at 1050 °C for 2 hours with a cooling rate of 28 °C/min down to 815 °C and a subsequent aging treatment at the latter temperature for 8 hours followed by a furnace cooldown. Prior to testing the specimens were polished, unless otherwise indicated, to produce the same surface condition for every specimen.

Fatigue testing was performed on a servohydraulic test system featuring a rigid horizontal design with precisely-aligned hydraulic friction grips, quartz lamps as heating device, forced air cooling, four-zone temperature control, high temperature extensometry and computer automation. The system is described in detail by Hartman and Buchanan /10/ and Hartman and Russ /11/. Difficulties arose with regard to the temperature measurement of the specimen, necessary to achieve a homogeneous temperature distribution throughout the gage section. A common method to spot-weld thermocouples onto the specimen's surface could not be applied to the thin specimens: fatigue crack initiation would preferentially be induced at the weld locations. Temperature measurement was therefore accomplished with the help of a dummy specimen placed next to the tested specimen.

Isothermal fatigue tests were conducted in load control with a triangular waveform at a stress ratio of 0.1 and a frequency of 0.1 Hz. The maximum applied stress lay at 825 MPa for room temperature testing and at 300 MPa for testing at 650 °C. All tests were performed in laboratory air. To assess the variability inherent in the fatigue data, at least 2 tests per condition were carried out.

Materials' characterization included chemical analysis of the bulk material as well as microstructural analysis. Metallographic samples, etched with Kroll's reagent (90 H_2O : 9 HNO_3 : 1 HF), were studied using a Leica 360 FE scanning electron microscope (SEM). Quantitative phase analysis was accomplished by applying an NIH image analysis program to digitally stored backscattered electron SEM micrographs at 750x and 2000x magnification.

Fracture surfaces of the fatigue specimens were examined using the SEM, failure locations and secondary cracks were determined and correlated to microstructural features.

Results and Discussion

Chemistry

Table 1 provides the results of the chemical analysis of the bulk material. The actual composition is close to the nominal one, showing only a slightly lower aluminum content.

Microstructure

The as-fabricated microstructure in its short transverse direction is displayed in Figure 2. It consists of three ordered phases, α_2, beta (β_0) and orthorhombic (O). The discontinuous dark phase is α_2 and represents approximately 36 vol. % of the structure. The two phase mixture is comprised of 39 vol. % gray O platelets in a continuous light gray colored β_0 matrix. The orthorhombic phase also appears as a thin case that surrounds the primary α_2 phase, however, it is still unknown whether the α_2 phase surrounding O phase is exactly the same as the O platelets with regard to its formation and its crystallographic orientation relationship. /9/

Figure 3 shows the effect of the heat treatment on the microstructure. Compared to the as-fabricated microstructure the α_2 phase volume fraction is decreased by half, whereas the O phase volume fraction is increased by 15 %, the β_0 volume fraction is increased only slightly. Table 2 summarizes the phase contents of the two microstructures. The average size of the primary α_2 phase as well as the orthorhombic platelets is increased in the heat treated material and its variance is decreased compared to the as-fabricated condition. The heat treated condition does not show O phase surrounding the α_2 phase, a typical feature found in the as-fabricated microstructure.

Isothermal Fatigue

A total of 9 fatigue tests were performed in this study. Table 3 provides the fatigue lives in number of cycles to failure of both material conditions, obtained through room temperature and elevated testing. Comparing the fatigue lives it appears that the as-fabricated condition shows a better fatigue resistance at room temperature than the heat treated one, whereas at 650 °C the trend reverses. The variance of the data within each test condition though can be extremely high, with a maximum value of about 130000 cycles for the room temperature data of the as-fabricated condition.

One primary reason for these high differences in fatigue lives is probably the initial surface condition of the specimens.

Crack initiation of these flat, thin specimens should occur dominantly at the edges of the specimens. Any scratches or other damages on the specimen surface enhance crack formation; therefore the initial surface condition as well as handling of the specimens are of great importance and influence the test results.

Polishing the specimens with grinding paper in longitudinal orientation was mainly done to remove the through the heat treatment oxidized surface layer. It might have resulted in a surface condition not as good as the unpolished one, since the lives of the polished specimens were either about equal to or smaller than the ones of the unpolished material. But other possible reasons for these results must also be considered, as for example machining marks or other damage due to processing along the 0.4 mm thick sides or the edges, or inclusions within the specimen as well as improper consolidation of the foils.

The fracture surfaces, examined with the SEM, give insight as to where the cracks have initiated. As expected, all formation sites, except for specimens 1 and 2, were located at the edges. Crack initiation site of specimen # 1, which represented the highest number of cycles to failure, was located on the flat surface. The fracture surface of specimen # 2 indicated failure initiation within the material, close to the flat surface, Figure 4. This obviously severe damage in the material resulted in an extremely early failure. Bad consolidation of foils, Figure 5, could have enhanced fatigue failure of specimen # 5.

Further analysis of the crack formation sites, by sectioning the specimen perpendicular to the fracture surface and the crack propagation direction right next to the location of the initiation, is necessary to achieve a better understanding of possible failure reasons.

The fracture surface always showed tensile overload regions for at least half of the surface area, which was characterized by ductile fracture, Figure 6, as opposed to brittle cleavage failure, typical for crack growth regions, Figure 7.

Secondary cracking on the specimen surface, here referred to as cracks normal to the loading direction but not responsible for final fracture, were observed only at elevated temperature testing. Cracking occurred throughout the gage sections, being more severe close to the actual fracture, Figure 8. No difference in the nature of secondary cracks was found between the two material conditions. Initial analysis on correlation between microstructure and crack propagation through the material has indicated that the crack doesn't follow any microstructural features but instead runs right through the different phases as presented in Figure 9 for a secondary crack in an as-fabricated specimen tested at 650 °C.

Similar observations were made with regard to the heat treated material. More information should be obtained by looking at the samples sectioned to study the failure site. If there are microstructural effects on fatigue crack propagation then following the crack path starting at the location of crack formation should be of importance. These investigations definitely have to be performed in near future.

Conclusions

The fatigue data shows differences in fatigue lives between the two studied microstuctures at both room temperature and elevated temperature. This gives indication of a possible effect of microstructure on the isothermal fatigue behavior of Ti-22Al-23Nb. Fatigue life can typically be devided into crack initiation and propagation. Crack initiation is governed by its resistance to crack formation. It is therefore of importance to look at the correlation between fatigue crack initiation and propagation and the microstructural features of the material. In the present state of analysis though, no signs of correlation have been determined.

Furthermore the initial surface condition of specimens of these dimensions is a major criterion to produce reliable test results.

References

/1/   *J. M. Larsen, W. C. Revelos and M. L. Gambone*: " An overview of potential titanium
        aluminid matrix composites in aerispace applications ", Intermetallic Composites II,
        edited by D. B. Miracle, D. L. Anton and J. A. Graves, Mat. Res. Soc., pp. 3 - 16, (1992)

/2/   *R. A. MacKay, P. K. Brindley and F. H. Froes*: " Continuous fiber-reinforced titanium
        aluminide composites ", JOM, vol 43, no 5, pp. 23 - 29, (1991)

/3/   *T. Nicholas and S. M. Russ*: " Elevated temperature fatigue behavior of SCS-6/Ti-24Al-
        11Nb ", Mat. Sci. Eng., vol A 153, pp. 514 - 519, (1992)

/4/   *R. G. Rowe:* " Ti$_2$AlNb-based alloys outperform conventional titanium aluminides ", Adv. Mater. Processes, vol 141, pp. 33-35, (1992)

/5/   *R. G. Rowe:* " Recent developments in TiAlNb titanium aluminide alloys ", High Temperature Aluminides and Intermetallics, edited by S. H. Whang, C. T. Liu, D. P. Pope and J. O. Stiegler, TMS, pp. 375-401, (1990)

/6/   *P. R. Smith, J. A. Graves and C. G. Rhodes:* " Evaluation of a Ti-22Al-23Nb orthorhombic alloy for use as the matrix in a high temperature Ti-based composite ", Mat. Res. Soc. Symp. Proc., 273. pp. 31-42, (1992)

/7/   *P. R. Smith, J. A. Graves and C. G. Rhodes:* " Comparison of orthorhombic and alpha-two titanium aluminides as matrices for continuous SiC-reinforced composites ", Met. Trans., A., vol 25A, pp. 1267-1283, (1994)

/8/   *P. R. Smith and J. A. Graves:* " Monotonic behavior of "neat" high temperature titanium alloys for use as composite matrices ", Scripta Met., vol 32, no 5, pp. 685-700, (1995)

/9/   *P. R. Smith, W. J. Porter, W. J. Kralik and J. A. Graves:* " The effect of heat treatment on tensile and creep response of "neat" Ti-22Al-23Nb ", presented at ICCM-10 Conference, Vancouver, BC, (1995)

/10/   *G. A. Hartman and D. J. Buchanan:* " Methodologies for thermal and mechanical testing of TMC material ", Characterization of fiber reinforced titanium matrix composites, AGARD Report 796, pp. 12-1 - 12-9, (1994)

/11/   *G. A. Hartman and S. M. Russ:* " Techniques for mechanical and thermal testing of Ti3Al/SCS-6 metal matrix composites ", Metal Matrix Composites: Testing, Analysis and Failure Modes, ASTM STP 1032, edited by W. J. Johnson, pp. 43-53, (1989)

	Ti	Al	Nb	N	O
wt. %	bal	10.34	39.2	0.0195	0.168
at. %	bal	20.8	22.6	0.069	0.522

Table 1: Chemical analysis of bulk material

	α_2	orthorhombic	β_0
as-fabricated [%]	35.8	39.0	25.2
heat treated [%]	17.2	54.0	28.8

Table 2: Volume fractions of the three ordered phases contained in the as-fabricated and the heat treated material

		specimen #	N_f [cycles]	comments
as-fabricated	room temperature	1	136601	unpolished
		2	3705	
		3	20882	
	650 °C	4	16006	unpolished
		5	8937	
heat treated	room temperature	6	10200	unpolished
		7	9342	
	650 °C	8	77048	
		9	21871	

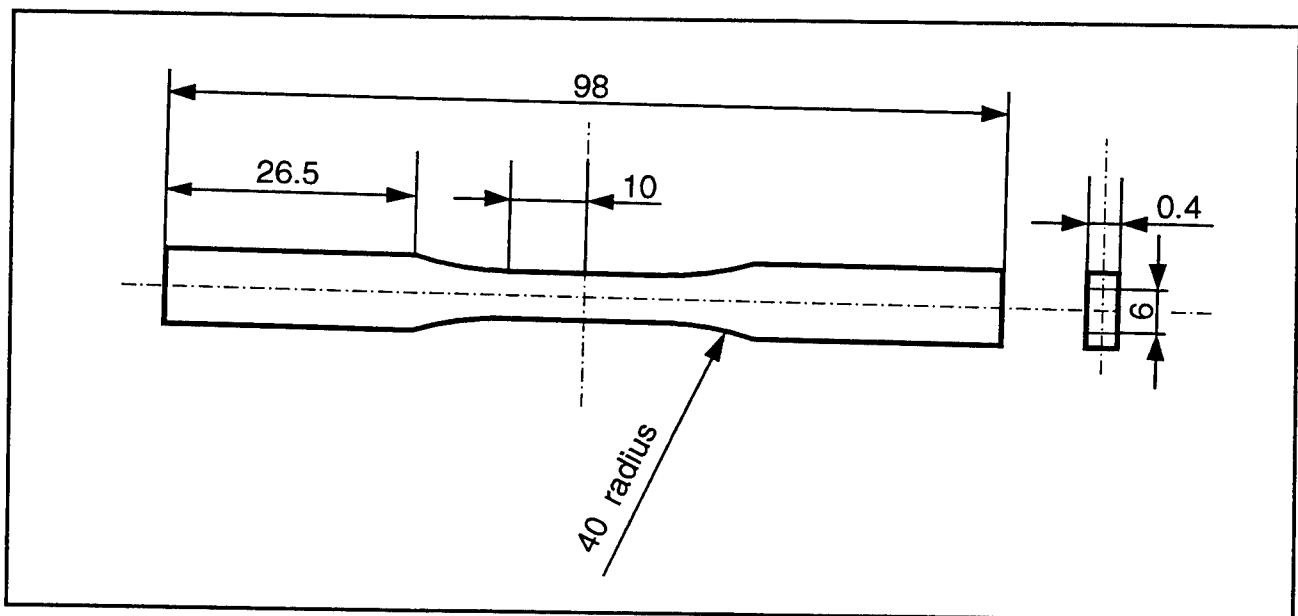Table 3: Number of cycles to failure N_f for all conducted isothermal fatigue tests
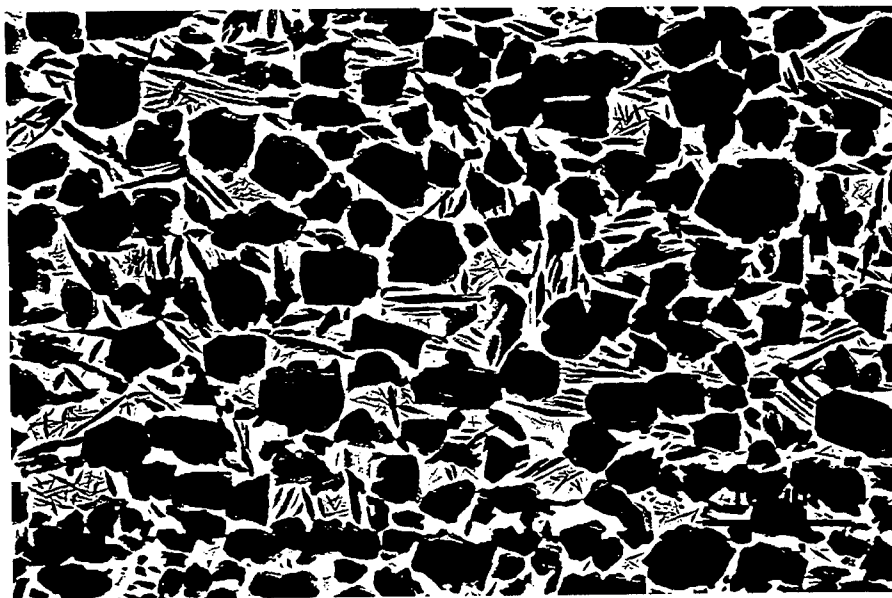

Figure 1: Schematic drawing of the fatigue specimen

Figure 2: Backscattered electron SEM micrograph of the as-fabricated micostructure, featuring the ordered phases α_2 (dark), O (gray) and β_0 (light gray), 2000x magnification
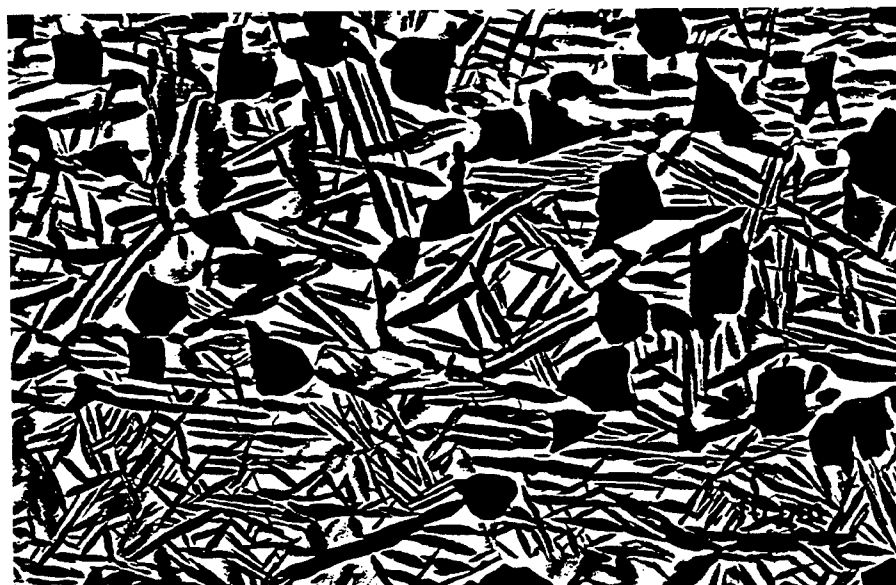

Figure 3: Backscattered electron SEM micrograph of the heat treated micostructure, featuring the ordered phases α_2 (dark), O (gray) and β_0 (light gray), 2000x magnification
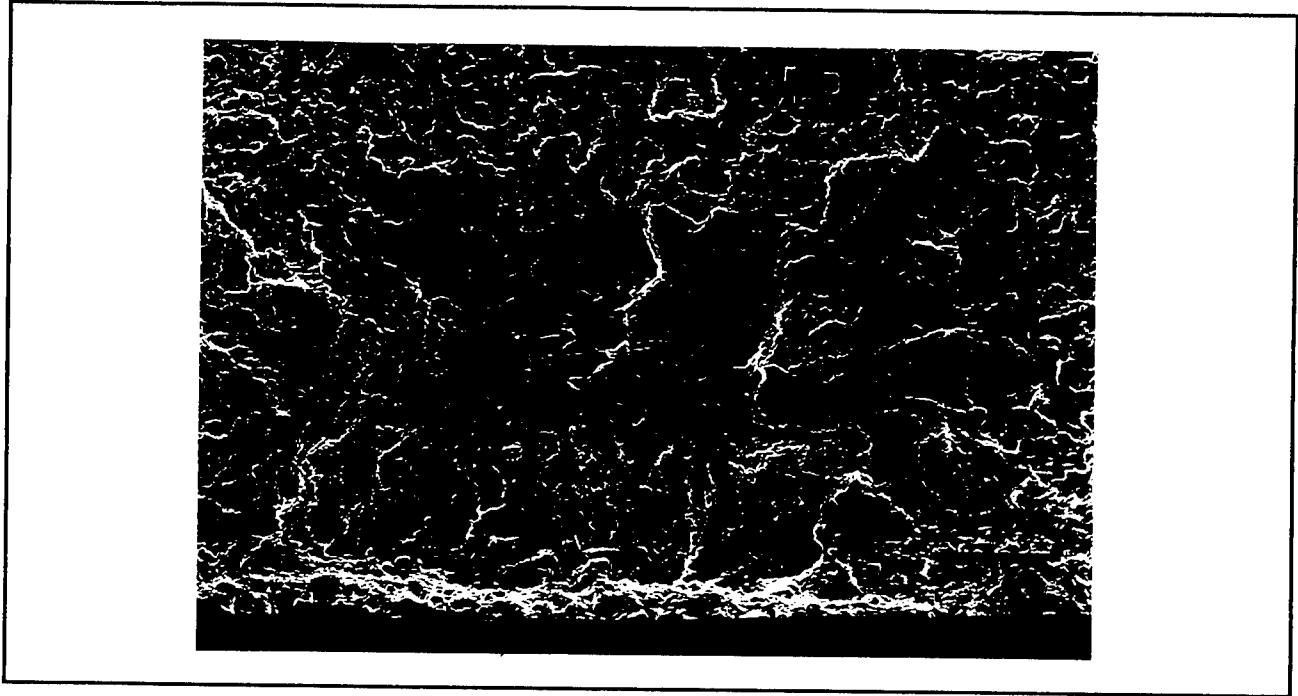
Figure 4: Secondary electron SEM micrograph of specimen #2, showing crack initiation site, 350 x magnification
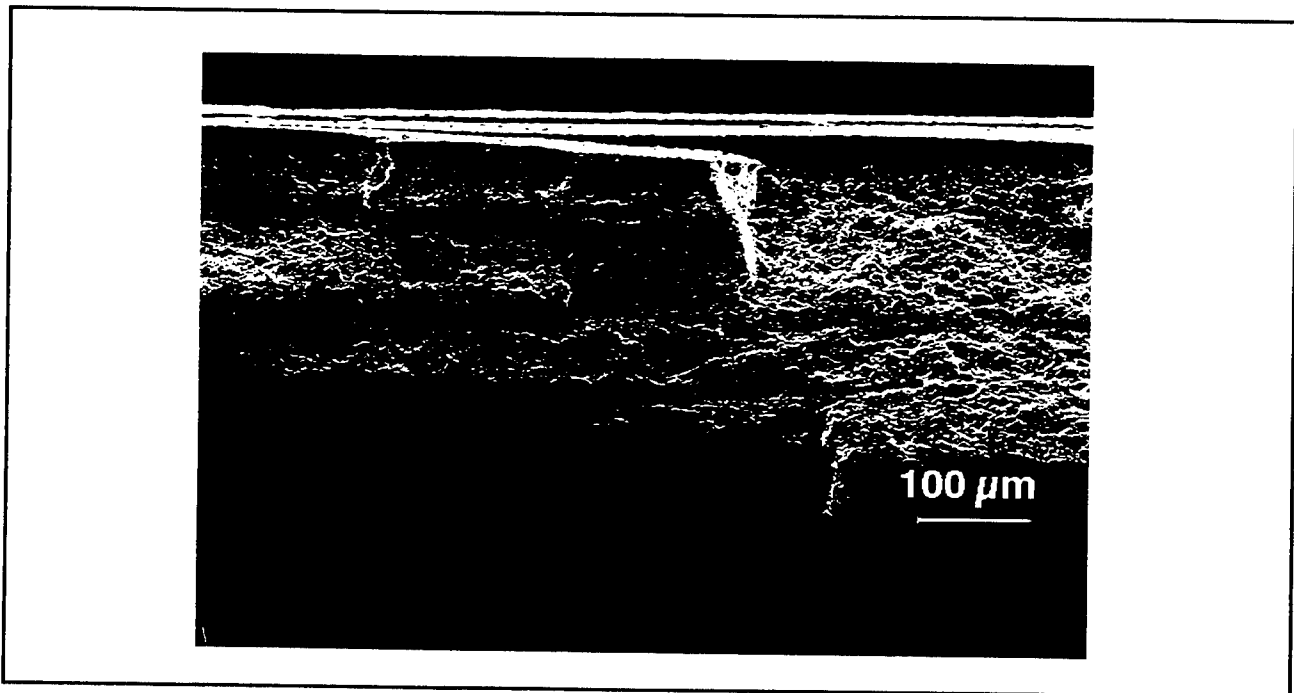

Figure 5: Secondary electron SEM micrograph of specimen # 5, showing improper consolidation of the 5 foils, 150 x magnification
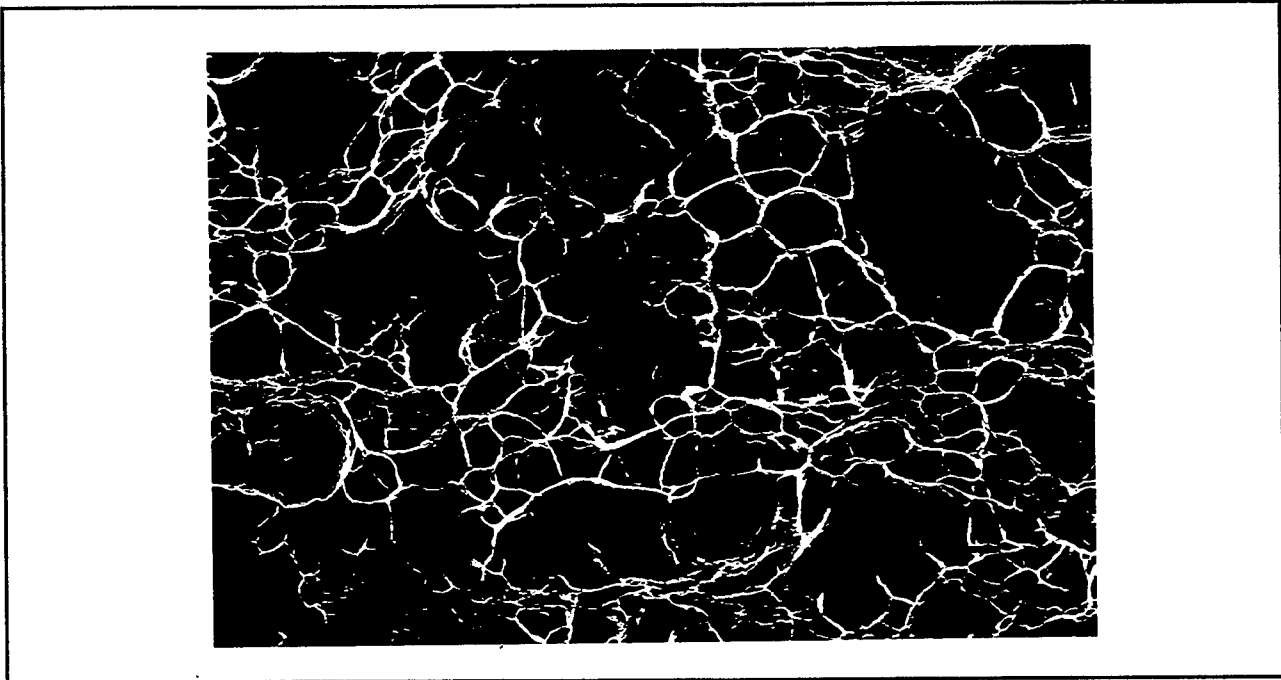
Figure 6: Secondary electron SEM micrograph of the fracture surface of specimen # 8, showing ductile failure, 2000x magnification

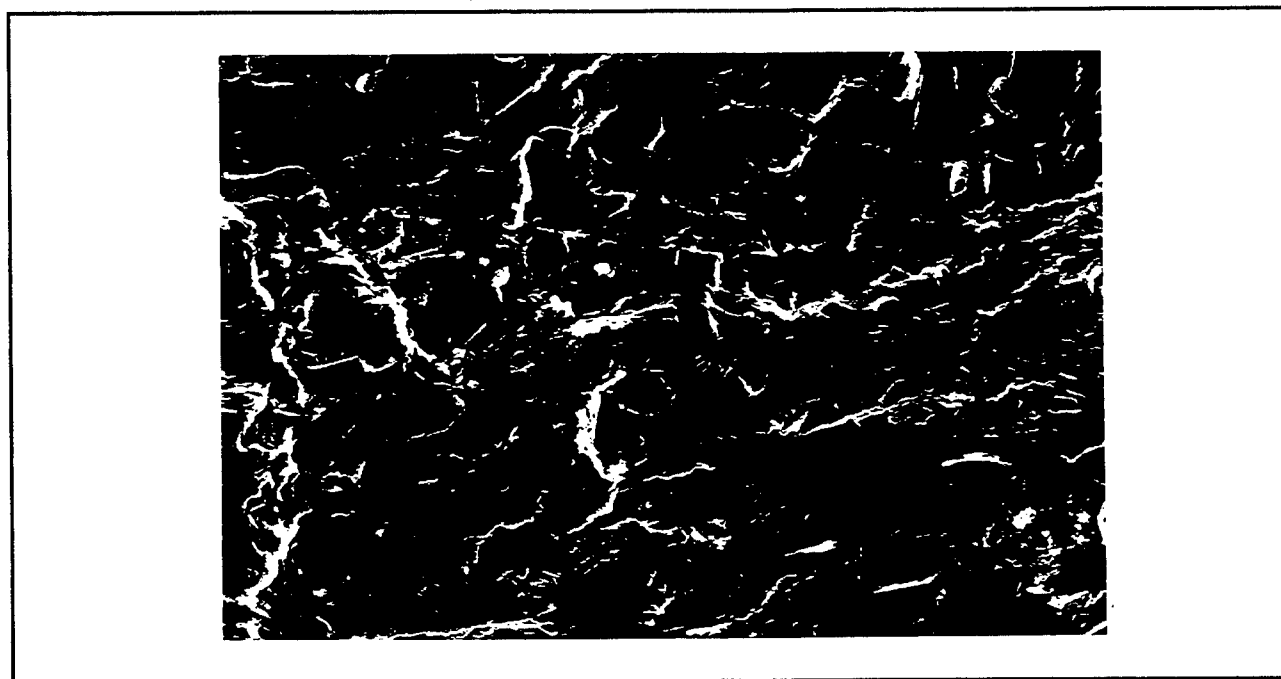Figure 7: Secondary electron SEM micrograph of the fracture surface of specimen # 8, showing brittle failure, 2000x magnification
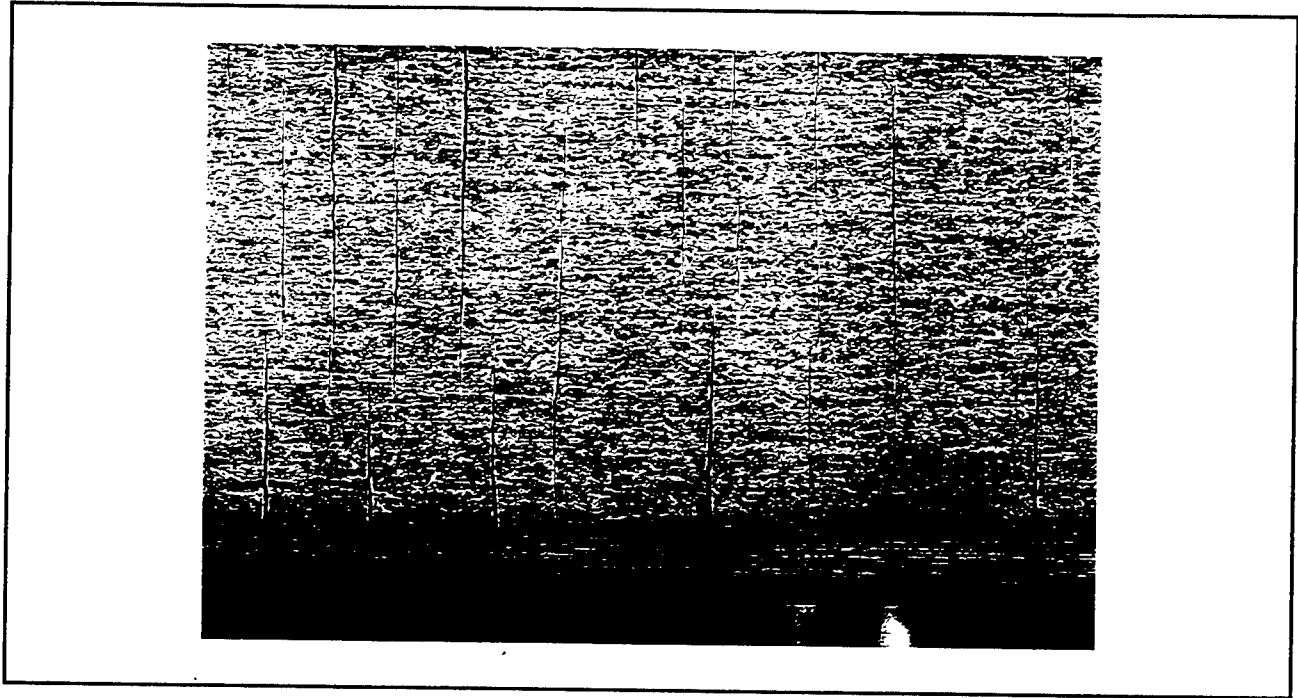
Figure 8: Secondary electron SEM micrograph of specimen # 5, showing secondary cracking, 100x magnification

Figure 9: Secondary electron SEM micrograph of specimen # 4, showing a secondary crack and its propagation path through the microstructure, 2000x magnification

The Feasibility of Using Microwave/Electron Beams
for Hypersonic Flow Ionization

John D.H. Mai

Doctoral Student

Mechanical, Aerospace and Nuclear Engineering Department

University of California, Los Angeles

420 Westwood Blvd. Engineering IV

Los Angeles, CA 90095

The Feasibility of Using Microwave/Electron Beams for Hypersonic Flow Ionization
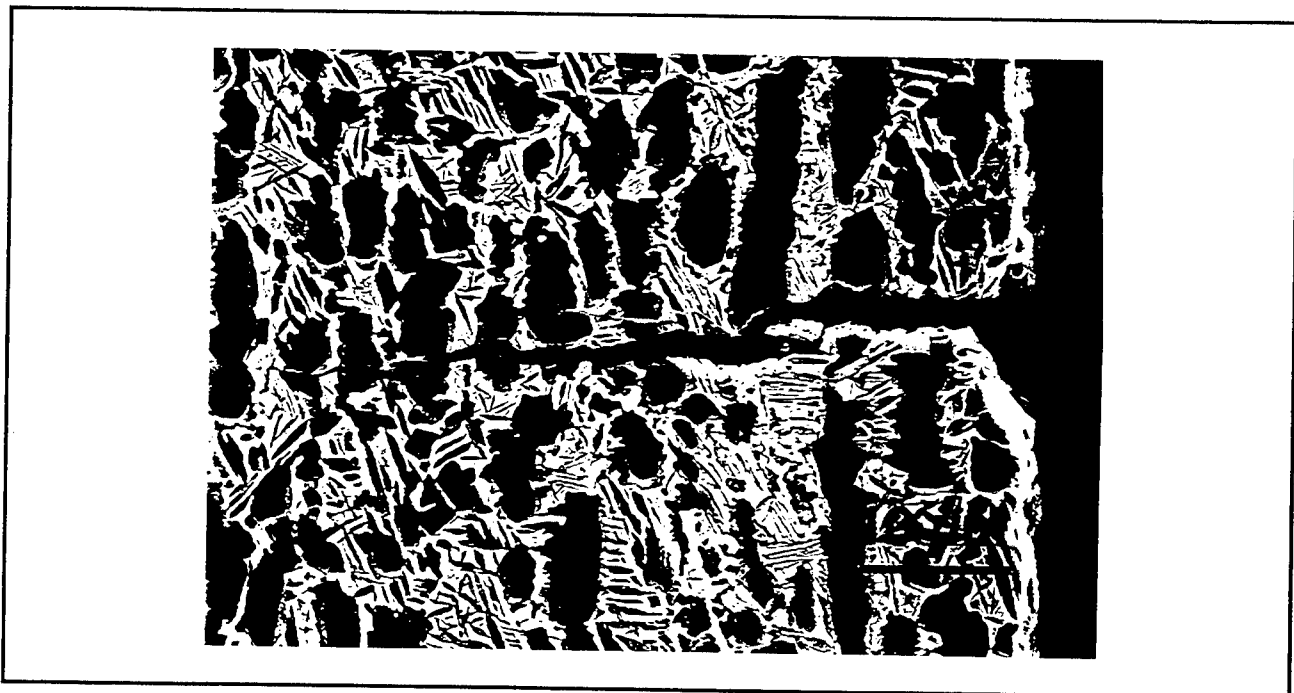
John D.H. Mai

Doctoral Student

Mechanical, Aerospace and Nuclear Engineering Department

University of California, Los Angeles

Abstract

This paper attempts to give a preliminary overview of the physics which occurs during the ionization of a fluid and how to ionize flow in the ARL 20 inch Hypersonic Wind Tunnel. The key point of interest is the fact that electron-ion and ion-ion collisions induce the majority of the ionization processes. Microwave ionization essentially is a secondary effect and only has an effect on the ionization process due to the fact it facilitates electron-ion collisions. The Boltzmann equation is presented, but no attempt is made to explicitly solve it for the boundary and initial gonditions in the 20 in. tunnel. Instead empirical correlations based on basic research done by others is applied to this situation. A reasonable method to induce microwave ionization is to generate an electric field of approximately 22.5 kV/cm to generate microwaves of 131.8 GHz frequency that will lead to air breakdown. Another method is to use a 1.72 cm diameter electron beam, with an electron temperature above 16 eV and an initial density of at least 10^{19} electrons per m^3, and raster scan it across the tunnel test section, cross sectional area at 343 kHz in order to fully ionize the 10 inch usable core for the entire 40 inch length of the test section.

A note must be made about the various discrepancies presented in this paper. First many of the empirical correlations used in this paper did not have adequate documentation. The problems were usually that certain parameters were not well defined or that there were slight variations in parameter definitions from one paper to the next, so errors initially appeared when comparing results from one paper to the next. (such as in the case of collisional cross sectional area and ionization frequency). Additionally, many of the papers detailed the quantum mechanical aspects of ionization, which means the data is referenced per electron. Therefore, scaling errors probably appeared as I multiplied these values so that the units would be consistent with the macroscopic correlations presented by other authors. Finally, no attempt was made to compensate for real gas effects such as electron quenching, electron scattering, and multiple ionizations of a single molecule or molecular dissociation due to heating.

The Feasibility of Using Microwave/Electron Beams
for Hypersonic Flow Ionization

John D.H. Mai

Introduction

In order to obtain a preliminary understanding of the physics which occurs when a flow field is ionized, a concurrent discrete and continuum examination of the flow is necessary. The discrete analysis, which begins with quantum-level, gas theory, imparts a fundamental understanding of the ionization process. The continuum approach allows one to view air as a fluid continuum which allows the derivation and description of standard fluid dynamics quantities such as Mach number and structures such as a boundary layer. The flow regime can be identified via a calculation of the Knudsen number. The Knudsen number is defined as $Kn = l/d$, where "l" is the mean molecular free path and d is a characteristic dimension of the flow. It is generally accepted that when the Knudsen number is less than 0.01 the flow is considered inviscid, and a flow greater than 100 is approaching the free molecular limit. From the perspective of continuum models the Euler Equation is valid for Kn less that approximately less than 0.05 and the Navier-Stokes Equations are valid between $Kn = 0.05$ and 0.5. From the point of view of discrete particle models, the Boltzmann equation is valid over the entire range between inviscid flows and free molecular flows. However, close form analytical solutions for both these models exist only for certain, limited situations, so time consuming computational techniques must be used to fully discretize and solve theses equations. Hopefully, the discrete particle model will shed insight into the mechanism behind the process of molecular ionization, while continuum analysis will assist in predicting the behavior of ionized flow structures.

Flow Ionization Characteristics

Wind Tunnel Objective

The goal of this paper is to address the feasibility of using a microwave (or another practical directed energy) source to ionize flow in the ARL Twenty-Inch Hypersonic Wind Tunnel at Wright Laboratory. Easily accessible literature on this tunnel gives comprehensive baseline data on its operation at Mach number equal to twelve and fourteen. [1] When a Ma = 12 flow in the test section is required,

the throat diameter is 0.407 inch which equates to a 0.130 in.^{2} circular area. From the available reports, the most rigorous, nominal test conditions were at Ma = 12, with a throat temperature of 1960 °R (3528 K) and a pressure of 814 psia (5.61 MPa). Using these values to calculate the mass flow rate yields a maximum throat flow rate of approximately 0.04 slugs per second (0.58 kg/s). This means that the proposed ionization system must be able to ionize flow at least at a rate of 0.58 kg/s. The aforementioned flow parameters are for the severe conditions at the throat. However, flow conditions are more favorable after expanding into the test section. For the purpose of this report, the nominal flow conditions in the test section are static pressure equal to 2.50 torr (332 Pa), static temperature of 50 °R (90 K), and a velocity of 4500 ft/s (1372 m/s). Inserting these pressure and temperature values into the perfect gas equation, solving for density (1.29 kg/m^3) and using a molecular conversion based on Avogadro's number for air (6.02 x 10^{23} molecules per 29 x 10^3 kg), this means that approximately 2.67 x 10^{19} molecules/m^3 must be ionized. This value is less than Nasser's density value of 3.52 x 10^{22} molecules/m^3 at 273 K and at a pressure of 1 torr, but the calculated value is on the order of 10^{19} for which hypersonic electron beam fluorescence equations are valid.

A practical matter must now be taken into consideration. It is known that a fluorite window does not pass radiation shorter than 125 nm, and quartz has a wavelength cut-off at 145 nm; therefore, the energy source, and the energy required to ionize air must be at a wavelength greater than these values to make any directed flow energizing scheme practical and physcially viable. The ionization potential for O_2 is 12.06 eV, and the value for N_2 is 15.58 eV. Using 6.64 x 10^{-34} for Plank's constant and 3.0 x 10^8 for the speed of light, simple calculations yield a wavelength of 503 nm for N_2 and 649 nm for O_2. Therefore, it is physically possible to use a directed energy source to ionize STP air through a fluorite or quartz winɑow.

The Boltzmann Transport Equation

The standard derivation procedure encountered in the literature survey for calculating the energy necessary to ionize a substance proceeds in the following manner. Since ionization is basically an electron-energy transfer phenomena, the Boltzmann equation is the usual starting point. The Boltzmann equation embodies the microscopic kinetic theory of electron behavior and must be solved with the appropriate boundary and initial conditions for the experimental situation. An exact analytical solution seldom results for complex situations, but by using some simplifying assumptions, selecting an appropriate coordinate system, and by coupling it with macroscopic momentum equations which model the

electromagnetic wave-fluid interactions, certain closed form solutions are possible. The final step in most derivations using the Boltzmann equation is to obtain values for the rate constants which inevitable appear in the solution.

In certain simplified situations, the behavior of gases can be described using the **average** values of certain quantities (such as velocity and position). However, when more exact calculations are required, the **distribution functions** associated with each quantity must be considered. If the ionization characteristics of air moving at hypersonic speeds is to be accurately described, the Boltzmann equation must be solved. The Boltzmann equation specifies the phase-space distribution function for a given assembly of particles. The term phase space refers to the two vectors (position and velocity) needed to describe the characteristics of each particle. Each vector has three components, making a total of six terms: x, y, z in Cartesian physical space, and u, v, w in the associated velocity space.

The Boltzmann equation can be quickly derived in the following manner: Assuming negligible interaction among gas particles (a viable assumption as illustrated by Chandler and MacCormack's work), the number of particles occupying a infinitesimally small volume is given by: (in phase space)

$$dV = dx\ dy\ dz\ du\ dv\ dw \tag{1}$$

at any given time, the number of particles in this space at a given time is described by

$$(dn/n)_t = f(\mathbf{r}, \mathbf{v}, t)\ dV \tag{2}$$

where the distribution function f is a function of a position vector $\mathbf{r}$ (which in turn is a function of x, y, and z) and the velocity vector $\mathbf{v}$ (which is a function of u, v, and w components). After a time dt, the particles will be displaced, which can be expressed as thus

$$(dn/n)_{t+dt} = f(\mathbf{r}+\mathbf{v}dt, \mathbf{v}+\mathbf{a}dt, t+dt)\ dV \tag{3}$$

Therefore, the change in the number of particles within the infinitesimal volume over time dt can be calculated by subtracting (2) from (3),

$$(dn/n)_{t+dt} - (dn/n)_t = (df/dt)_c\ dVdt \tag{4}$$

where $(df/dt)_c$ is a constant term. By substituting (2) and (3) into the left hand side of (4), applying Taylor's expansion theorem, and ignoring any higher order terms, the following partial differential equation results, and is commonly known as the Boltzmann Equation

$$\frac{\partial f}{\partial t} + v\frac{\partial f}{\partial r} + a\frac{\partial f}{\partial v} = \left(\frac{\partial f}{\partial t}\right)_c \tag{5}$$

If the boundary and initial conditions are known, the resulting solution will yield information about:

1. Particle motion/drift in physical space

2. Changes in particle velocity due to externally applied forces (such as ionization energy, in this case.)

For the purpose of this report, there will be no attempt to analytically solve the Boltzmann equation for our wind tunnel conditions. Instead, empirical correlations and graphs will be used to estimate energy requirements for ionizing flow in the 20 inch Hypersonic Wind Tunnel.

Photoionization/electron-ion collisions

Photoionization is the general term used to describe all phenomena associated with ionization by radiation. For a photon, or a packet of electromagnetic (EM) radiation, to ionize a neutral atom it must satisfy the relation: $h\nu > E_i$ where ν is the frequency, h is Planck's constant, and E_i is the ionization potential. It is important to note that photoionization does not generally occur as a result of external radiation but rather, takes place as a result of the radiation emitted from the gas itself when already excited atoms return to their ground states or when ionized atoms combine with negative ions to form neutral molecules. Therefore, ionization is usually initiated by ion or electron collisions. Keeping this point in mind, it will be later argued that using an electron beam instead of a microwave source is a vastly more efficient method for ionizing air.

The following process occurs when microwave energy is used to ionize flow. First, the microwave energy is used to initiate ionization by supplying enough energy to free an electron from an excite molecule. Then subsequent ion collisions propagate the ionization. Therefore, the majority of the physical process of ionization is due to ion collisions. The prominence of ion collisions is illustrated by the fact that gas ionization continues for a considerable time after the termination of a microwave pulse (due to further electron-ion and ion-ion collisions). For example, for N_2 at standard conditions, a radiation pulse of 0.05 µs will initiate a ionization collision cascade lasting for 0.5 µs. This leads to a need for a collision cross section analysis in order to quantify the ionization phenomena.

A collision cross section roughly describes the probability of an atom or molecule being ionized by an atomic or electron impact. For a beam of mono-energetic electrons of density n, moving through a gas with velocity v, the number of electrons undergoing collisions per unit area per unit time in distance dx is

$$dn/dt = -N \, [\pi(r_1 + r_2)^2]nv \qquad (6)$$

where N is the density of the gas molecules, and r_1 and r_2 are the radii of the gas molecule and an electron, respectively. By integrating the above equation, remembering that $v = dx/dt$ and that the ionization cross section is given by

$$\sigma_{ion} = \pi(r_1 + r_2)^2 \qquad (7)$$

results in the following exponential relation for electron density after the beam has traveled a distance x

(and fully ionizing anything it the beam path), given the initial electron density.

$$n = n_o \exp(-N\,\sigma_{ion}\,x) \qquad (8)$$

Conservatively estimating that the beam must travel then entire diameter of the tunnel (20 in. or 0.502 m), and taking spatial ionization cross section, σ_{ion}, data from Fig 9 from Jelenkovic and Phelp's paper (as approximately 10^{-20} for an electric field to gas density ratio, E/N of 1000 Td, where 1 Td = 10^{-21} Vm^2) yields a necessary initial concentration of 1.05×10^{19} electrons/m^3(also assuming that each electron will ionize only one gas molecule, hence $n_o = N$). In Jelenkovic and Phelp's paper, they use an electric field to induce electron-ion collisions which results in gas breakdown and ionization. In order to generate the field for our situation, a potential difference between a cathode and anode ranging from E = 26.7 V/m to 35.2 kV/m is necessary (using gas density values at 2.50 torr and 760 torr).

From Samaras, the efficiency of ionization computed from the collision cross section is expressed as a function of gas velocity, v, electric field strength, E, and ion and electron charge, q, and mass, M

$$\eta_{ion} = n\left(\frac{M_i}{M_e}\right)\frac{q_e q_i^2}{16\pi\varepsilon^2 V_i E_i} \qquad (9)$$

which represents the number of ionizing collisions per unit length per electron. This relation can also be used to estimate how many electrons are necessary to totally ionize a gas of a known density.

Another important aspect of collision analysis is the role of electron quenching. This adverse phenomena is a result of ion collisions with background gas which depopulates the excited ion states, thus reducing ionization density and subsequent ionizing collisions. The quenching cross section for N_2 is approximately 15 A; however, the effects of quenching can be ignored for gas densities less than 2×10^{15} molecules/cm^3. [2] A qualitative example of the effects of electron quenching is apparent in electron beam fluorescence applications. Given a hypersonic flow with a density of 3×10^{16} /cm^3, collisional quenching reduces α (which is known as the ionization coefficient by electron collision, also known as Townsend's first ionization coefficient) by 15%. Table I of Jelenkovic and Phelp's paper shows that 50% of the radiation is lost to quenching when the N_2 density is greater than 10^{23} molecules/m^3.

Finally, in order to present a better picture of ionization intensity relative to other well known phenomena, Samaras states that the general relation between relative intensities for heat, light, and ionization is the following ratio- $10^4 : 10^2 : 1$. This means that for a given energy input, the heat produced will be approximately 1000 times more dominant that the level of ionization.

Microwave ionization

Some preliminary estimates about the energy requirements necessary to ionize air can be obtained from Woo and DeGroot's paper, "Microwave Adsorption and Plasma Heating Due to Microwave Breakdown in the Atmosphere." It should be noted that the term "breakdown" is analogous the ionization of air in the context of this report. They state that near room temperature, and neglecting any electron diffusion effects, the electric field necessary to initiate breakdown is proportional to

$$E_{rms} \propto 32(P_t^2 + 2f^2) \tag{10}$$

where E_{rms} is in units of V/cm and P_t is pressure in torr and f is frequency in Giga-Hertz. Note that there are three types of frequencies mentioned in the literature associated with microwave ionization. There is a frequency associated with the radiation needed to free an electron and induce ionization. There is a frequency associated with the excess energy emitted after an electron-ion collision. Finally, there is an extraneous pulsed beam frequency if non-continuous beam energy is used for ionization. From this, when P_t is much greater than f, they calculate that the power flux necessary for breakdown at standard conditions is approximately 1.5 MW/cm^2.

In Kroll and Watson's paper, they too present a simple equation for estimating the electric field necessary to initiate air breakdown at room temperature. Their relation is

$$E_s \propto (30 \text{ V/cm}) \times P_t \tag{11}$$

where E_s is again in V/cm. Based on this, they give a relation between the power, P in MW/cm^2, needed to generate this electric field as

$$E = (1.94 \times 10^4) P_s^{1/3} \tag{12}$$

In terms of pressure, in atmospheres, and the frequency, in Giga-Hertz, the power is empirically given by

$$P_s = 1.44 (P_r^2 + 2.4 \times 10^{-6} f^2) \tag{13}$$

There are some discrepacies in calculations using the relations in the previous section, when compared to calculations using the relations in this paragraph.

A numerical estimate of the values necessary for ionization come from an analysis of the combined works of Kroll and Watson (1972), Woo and DeGroot (1983), and Kuo and Zhang (1991). Using Woo and DeGroot's STP breakdown power value of 1.5MW/cm^2 in equation (12) yields 22.2 kV/cm. This result agrees well with the value obtained when inserting atmospheric pressure into equation (11), which is 22.8 kV/cm. Inserting this power value into equation (13), at atmospheric pressure, give a necessary ionization frequency of 131.8 GHz. Although these values correlate well with each other and with atmospheric ionization research, which will be mentioned later, they are two orders of

magnitude greater than the results obtained in the previous section. This discrepancy appears again with further analysis of Ali's work.

This validity of this value is compared to the ionization frequency equation given by Ali as a function of E/P

$$v/P = 54.08 \times 10^6 \ (E/P)^{1/2} \ \exp(-359 \ P/E) \tag{14}$$

this yields a frequency of 1.21 MHz. (with E = 22.5 kV/cm and P = 760 torr). This value does not agree with the previous frequency values, however, my interpretation of the equation's meaning might be incorrect since the value is within an order of magnitude of the frequency of the microwave energy emitted after an electron-ion collision.

When a microwave propogates in air, the phenomena of microwave ionization occurrs when the breakdown threshold field of the background air is lower than the field intensity of the pulse. Woo and DeGroot state that ionization occurs when the microwave breakdown strength reaches $\alpha = 32$. Inserting this value into their equation for the microwave frequency as a function of pressure and α

$$v/P = 5.14 \times 10^{11} \ \exp(-73\alpha^{-0.44}) \tag{15}$$

yields a frequency of 49.2 MHz at 760 torr. This frequency corresponds to the frequency emitted by the excess microwave energy after an electron -ion collision; therefore, it shows that internal microwave emission is insufficient to sustain ionization propogation in air. Additionally, inserting the threshold ionization value of α into their equation for electron temperature yields approximately 8 eV, which is less than the energy values necessary to ionize O_2 and N_2 .(approximately 12 eV and 16 eV, respectively)

Other discrepancies occur when using equations presented in the available literature to calculate the electric field necessary to induce microwave ionization. From Figure 1 in Yee, Ali, and Bollen's paper, if the the time required for an electron to gain enough energy to ionize the gas, τ_B is estimated to equal 2.0 x 10^{-8} sec. (from 49 MHz) then the resulting E/Nm is approximately 2.0 x 10^{-15} V/cm^2. Using the N_2 concentration given by Nasser at 273 K and 1 torr gives a required electric field of 70.4 V/cm (or 7.04 kV/m) based on the graphical values.

The values calculated in the previous section can be compared to results obtained from other theoretical and empirical research. The Soviets initiated research into the ionizationg of the atmosphere using microwaves. They modelled microwave pulses beamed from Earth bound antennas to produce an electric field in the atmosphere that is sufficiently strong enough to accelerate local electrons to energies greater than the neutral ionization potential. These excited electrons would then collide with other atoms, producing more electrons. If the production rate of electrons is greater than the electron loss rate due to recombination then ionization occurs due to the increase in electron density.

Babat (1957) originally proposed using intersecting microwave beams to create an artificially ionized layer (AIL) in the higher atmosphere. In 1979, Gurevich calculated that an AIL could be produced at 10 km to 60 km altitude using a microwave pulsed at 10 to 100 ns, with a beam frequency of 0.3 to 40 GHz. The mechanism to create the AIL is that a microwave pulse beamed from an Earth bound antenna produces an electric field sufficient to accelerate an electron to energies greater than the ionization potential, so as the electron density increases, a net ionization effect results. The obvious simplification is to ionize air directly using an electron beams as an electron source instead of a microwave source.

Milikh, Hinds and Duncan (1993) developed a computer model simulating the formation of an artificially ionized layer in the atmosphere using a series of microwave pulses. They modeled a converging ionizing microwave pulse propogation through the atmosphere using a modified version of the kinetic theory of the breakdown of air by powerful microwave emissions and coupling it with a model of electromagnetic propogation through the atmosphere. This model consideres radio wave self action as well as energy absorption. In their experiments they considered the effects due to varying the shape of the ionization pulsed, the influence of ambient electron concentration, and they examined the effects of a single pulse versus a series of pulses with varying duration and energy concentration. Their results show that ionization between 40 km and 70 km is possible with microwave pulses of 2.38 GHz frequency, and power between 1 MW to 4 MW. These pulses lasted 0.1 to 0.15 microseconds at 103 Hz intervals.

Microwave Devices

Microwave devices generally fit into one of two categories: oscillator or amplifier. All oscillator type devices have a feedback mechanism where, as the amplitudes of the modes of the eigenfrequencies grows, they feedback to contribute to a more organized and coherent beam. An amplifier type device does not use feedback but requires an interaction space. Both category of devices operate on the principle of velocity modulation of electrons. The devices differ on how they achieve this velocity modulation.

The simplest amplifier is a klystron. It is essentially a gun that injects a linearly propagating electron beam through a circuit consisting of two resonant cavities, which are separated by a drift tube. Inside of these cavities is where velocity modulation occurs. Physically, this phenomena is when faster electrons overtake slower electrons in the first cavity (the bunching cavity). This electron spatial bunching leads to an excited microwave emission from the electron bunch/packet as they exit the second cavity (the output cavity).

The second general type of microwave devices, oscillators, uses a phenomena known as *Bremsstrahlung*, or breaking radiation, to induce electron velocity modulation and the subsequent

microwave emission. *Bremsstrahlung* occurs when an electron interacts with a slow electromagnetic wave propagating near the surface of a slow wave structure, e.g. a waveguide with a periodic perturbation. The classical example of a microwave oscillator is the gyrotron, which is part of the family of electron cyclotron masers. In a gyrotron an electron beam provides an electron source with a significant perpendicular velocity component. Then an applied magnetic field guides the beam through a cavity where adjustments to the magnetic field or electric field of the beam causes bunching and allows tuning of the electron oscillating frequency which results in microwave emission. Another type of microwave oscillator tube is the magnetron. In the magnetron, a layer of electrons are rotated azimuthally, by a combined radial d.c. electric field and an axial magnetic field, in the co-axial space between the inner cathode and the outer anode of the device. The anode has periodically arranged coupled resonant cavities in the azimuthal direction, and the interaction between a traveling wave emitted from these cavities and the synchronous rotating electron layer leads to electron velocity modulation (bunching), which results in microwave power generation.

High powered microwave devices can also be grouped by geometric configuration (M or O type), and subgrouped by the type of interacting wave (slow or fast). O-type slow wave devices include the backward wave oscillator (BWO), the traveling wave tube (TWT), Cerenkov masers, and the relativistic klystron. O-type fast wave devices include the free electron laser and gyrotron. M-type devices are variations of the magnetron. Not fitting into these two general categories are the space charge devices- the vircator and reflex triode. However, it must be noted that all of these microwave devices require an electron source. Back to the problem at hand, it seems that using microwaves to ionize a hypersonic flow is not as efficient as applying a direct electron beam. It has already been shown that electron-ion collisions are the dominant ionization mechanism. Therefore, it seems inefficient to use an electron beam to generate microwaves, which in turn will be used to ionize neutral molecules by causing a release of more electrons.

Electron Beam Devices

Section II shows that ionization is mostly an electron-ion or ion-ion collision induced phenomena. Therefore, it is more efficient to use electrons to directly ionize a fluid, instead of a direct method using microwaves. This section presents simple calculations showing the requirements necessary for flow ionization using an electron beam.

Cattolica gives the following relation for electron beam scattering in N_2:

$$L = (1.5 \times 10^{19} \, 1/Nm)^{1/2} \qquad (16)$$

where L is the beam length (20 inches for this application), Nm is the gas density (set at 10^{16} molecules/cm^3) and l is the half width beam diameter. Keeping in mind that this relation is only valid for low density flows (less than 10^{16} cm^{-3}) where quenching is ignored, this calculation shows that an electron initially along the beam centerline will be deflected 1.72 cm by the time it travels 20 in. in this nominal hypersonic flow. This infers that the electron beam necessary for this application must be at least 1.72 cm in diameter to effectively sweep and ionize the entire test sectional area without gaps due to beam deflection. Therefore, when an electron beam of 1.72 cm diameter, with an electron density of 1.05 x 10^{19} per m^3 is fired at a gas sample, the entire sample enveloped by the beam should be fully ionized, and thus by rastering the beam across the test sectional area the entire flow should be ionized. Next, the rastering frequency will be estimated.

Earlier it was stated that an electron beam pulse of 0.05 μs will initiate an ionization cascade lasting for 0.5 μs. Assuming this one to ten ratio is constant and that ionized particles are convected downstream at the free stream velocity of 1372 m/s, this means that a 1.0 mm diameter electron beam must be raster scanned at a pulsed rate of 343 kHz to keep the tunnel's 10 inch useable core of hypersonic flow fully ionized for the 40 inch test section length.

Inviscid Hypersonic Flow Theory

A characteristic of all hypersonic flows is the formation of thin shock layers when a solid boundary is encountered. The major interactions in hypersonic flows occur in the region between the shock and the viscous boundary layer near the boundary surface. The flow behind the shock is effectively inviscid.

Before going further, it is necessary to introduce the parameter ε, known as the density ratio, which is defined as $\varepsilon = \rho_\infty / \rho_s$ where ∞ refers to upstream flow conditions, and s refers to conditions downstream of any shock structure which inevitably forms in hypersonic conditions. For a perfect gas with a constant specific heat ratio ε_∞ is equal to ε_{lim}. A dramatic decrease in εlim only occurs when some physical mechanism appears whcih causes a large contribution to $h_s + e_s$ without a corresponding large contribution to P_s/ρ_s. As a side note to clarify the nomenclature, h is the specific enthalpy, which is defined as

$$h = e + P/\rho \qquad (17)$$

where e is the specific internal energy, P is the pressure and ρ is the density. Continuing, dissociation of molecules and ionization are examples of two mechanisms which can absorb energy from the dynamic degress of freedom of a gas. The effects of ionization are similar to the effects of dissociation. which is addressed more often in the literature. Ionization causes an energy contribution to h + e but no relative corresponding increase in temperature or the P/ρ term. Therefore, in air at elevated temperatures, εlim can

20-12

drop to 0.07 or less due to ionization. Thus, by having an estimate of the density ratio, relations for other flow conditions can be derived. For example, from the Rankine-Hugoniot relation

$$h_s - h_\infty = \frac{P_s - P_\infty}{2\rho_\infty}(1+\varepsilon)$$ (17)

knowledge about the thermodynamic states of a gas in front and behind a shock can be deduced. Straightforward algebra and substituting the definition for specific enthalpy gives the Rankine-Hugoniot relation in form of the density ratio

$$\varepsilon = \frac{P_s/\rho_s}{(h_s - e_s) - (h_\infty - e_\infty) + P_\infty/\rho_s}$$ (18)

Additionally, the pressure ratio across a shock can be obtained as a function of density ratio and upstream Mach number by

$$P_s / \rho_\infty = 1 + \gamma M_\infty^2 (1+\varepsilon)$$

Ionization and shock formation

There are three possibilities for how ionization energy can physically affect shock formation and its subsequent analysis. These possibilities result from variables in the flow conditions and test geometry. First, if the energy transfer from the flow to the shock lies within a small area, e.g. within the thin shock layer itself, then only the shock will be affected although due to conservation of energy there must be a decrease in the total enthalpy of the system. Second, if only a neglibible portion of the ionization energy is transfered to the shock then a "frozen flow" analysis is possible. The term frozen flow refers to a model where the mass fractions of all the fluid molecular or atomic species remains fixed at free-stream conditions. However, for many hypersonic flow situations the third possibility occurs. In the third situation, a significant portion of the ionization energy transfer occurs within the thickness of the shock **and** behind the shock. This non-equilibrium process makes analysis difficult due to the varying thickness/strength of the shock which affects the resulting upstream and downstream flowfield.

For standard test conditions in the 20 inch hypersonic tunnel, without flow energization, one might have to worry about species dissociation. This is due to the fact that oxygen dissociation ($O_2 \rightarrow 2\,O$) occurs in the temperature range from 2000 K to 4000 K. Additionally, at sea level, nitrogen dissociation ($N_2 \rightarrow 2\,N$) occurs from 4000 K to 9000 K. Finally, ionization at sea level, for both dissociated species, does not normally begin until the temperature is greater than 9000 K. In terms of discrete energy, approximately

12.1 eV is necessary to ionize O_2 and 16 eV is necessary to ionize N_2.

Chandler and MacCormack (1988) generated numerical solutions for a two dimensional hypersonic flow field that is ionized and in thermochemical non-equilibrium. Their calculations compared surface pressure for a seven species reacting-gas flow model with a perfect gas flow model at conditions at 71 km altitude and at Ma = 25.9. They discovered that the surface pressure is almost identical for each case and concluded that the stagnation point pressure is essentially the same whether or not flow equilibrium is achieved.

Conclusion

The preliminary results from this report give an estimate of the electric field necessary to induce microwave ionization in the ARL 20 inch hypersonic tunnel. Due to the large electric fields required, it seems impractical at this point to pursue microwave ionization methods. An alternative method using an electron beam has also been presented. However, a caveat must be kept in mind. Since the Boltzmann equation was not solved for this specific situation and empirical results from other authors were used to extrapolate results for our situation, it must be kept in mind that the results presented in this paper are only preliminary estimates. Various secondary quantum mechanical effects, as well as flow interactions, have been ignored in this analysis.

Acknowledgements

References

[1] G.M. Gregorek, "Initial Calibrations and Performance of the ARL Twenty-inch Hypersonic Wind Tunnel," ARL 62-393., August 1962.

[2] E. Nasser, *Fundamentals of Gaseous Ionization and Plasma Electronics*, Wiley-Interscience, New York, 1971.

[3] Cattolica, R. J. "Electron-Beam Fluorescence Measurements in Hypersonic Flows," Hypersonic Flow Measurement Techniques, von Karman Institute Lectures, 1989.

[4] S.P. Kuo, Y.S. Zhang, "A Theoretical Model for Intense Microwave Pulse Propogation in an Air Breakdown Environment," Phys. Fluids B, vol. 3, no. 10, pp. 2906-2912, Oct. 1991

[5] W. Woo, J.S. DeGroot, "Microwave Absorption and Plasma Heating Due to Microwave Breakdown in the Atmosphere," Phys. Fluids, vol. 27, no. 2, pp. 475-487, Feb. 1984.

[6] N. Kroll, K. Watson, "Theoretical Study of Ionization of Air by Intense Laser Pulses," Physical Review A, vol. 5, no. 4, pp. 1883-1905, April 1972.

[7] D.G. Samaras, *Theory of Ion Flow Dynamics*, Prentice-Hall, Inc., Englewood Cliffs, NJ, 1962.

[8] A.W. Ali , "Nanosecond Air Breakdown Parameters for Electron and Microwave Beam Propogation," Laser and Particle Beams, vol. 6, part 1, pp. 105-117, 1988

G.A. Tirsky, "Up-to-Date Gasdynamic Models of Hypersonic Aerodynamics and Heat Transfer with Real Gas Properties," Ann.Rev. Fluid Mech., vol 25, pp. 151-181, 1993.

H.K. Cheng, "Perspectives on Hypersonic Viscous Flow Research," Ann. Rev. Fluid Mech., vol. 25, pp. 455-484, 1993.

T.J. Bartel, S.J. Plimpton, "Direct Monte Carlo Simulation of Ionized Rarefied Flows on Large MIMD Parallel Supercomputers," 16th. International Symposium on Rarefied Gas Dynamics, vol. 118, AIAA, pp.155-164, Pasadena, CA, 1988.

E.W. Miner, C.H. Lewis, "Hypersonic Ionizing Air Viscous Shock-Layer Flows over Sphere Cones," AIAA Journal, vol. 13, p.80-88, Jan. 1975.

V.A. Lyutomskii, V.M. Polyakov, V.G. Testov, "Experimental Investigation of Microwave Radiation Produced by Hypersonic Flows," Sov. Phys. Tech. Phys., vol. 19, no. 4, Oct. 1974.

W.S. Liu, K.Takayama, I.I. Glass, "Coupled Interactions of Shock-wave Structure with Laminar Boundary Layers in Ionizing-argon Flows," J.Fluid Mech., vol. 97, part 3, pp. 513-530, 1980.

W.S. Liu, I.I. Glass, "Ionizing Argon Boundary Layers. Part 2. Shock-tube side-wall boundary-layer flows," J.Fluid Mech., vol 91, part 4, pp.679-696, 1979.

R.Miles, G. Brown, et al. "Radiatively Driven Hypersonic Wind Tunnel," 18th AIAA Aerospace Ground Testing Conference, AIAA 94-2472, Colorado Springs, CO, June 1994.

G.M. Gregorek, J.D. Lee, "Design Performance and Operational Characterisitics of the ARL Twenty-inch Hypersonic Wind Tunnel," ARL 62-392, August 1962.

J.J. Bertin, R. Glowinski, J. Periaux, ed., *Hypersonics, Volume* I, Birkhauser, Boston, 1989.

G.V. Marr, *Photoionization Processes in Gases*, Academic Press Inc., New York, 1967.

M. Gavrila, *Atoms in Intense Laser Fields*, Academic Press, Inc., San Diego, CA, 1992.

W.D. Hayes, R.F. Probstein, *Hypersonic Flow Theory*, Academic Press, Inc., New York, 1966.

A.V. Gaponov-Grekhov, V.L. Granatstein, ed., *Applications of High-Power Microwaves*, Artech House, Boston, 1994.

J. Benford, J. Swegle, *High-Power Microwaves*, Artech House, Boston, 1992.